

# **Regulation of the pancreatic K<sub>ATP</sub> channel**

Samuel Usher

Green Templeton College  
University of Oxford

*A thesis submitted for the degree of  
Doctor of Philosophy*

Trinity 2021

## **Abstract**

ATP-sensitive potassium (K<sub>ATP</sub>) channels are present in many tissues, most notably pancreatic islets and cardiac cells, where they couple the metabolic state of a cell to its electrical activity by regulating the flow of K<sup>+</sup> across the membrane in response to the intracellular ATP/ADP ratio. K<sub>ATP</sub> channels are an octameric complex, comprised of four inwardly-rectifying potassium channel (Kir) subunits, each of which is associated with a sulphonylurea receptor (SUR) subunit. In pancreatic islets, K<sub>ATP</sub> channels are formed by Kir6.2 and SUR1.

The physiological regulation of K<sub>ATP</sub> activity by the ATP/ADP ratio is the summed contribution of activation by Mg-nucleotides binding to SUR1, and inhibition by nucleotides binding to Kir6.2. Mutations in either Kir6.2 and SUR1 which lead to diseases of insulin secretion are frequently observed to disrupt the nucleotide regulation of the channel.



# Regulation of the pancreatic K<sub>ATP</sub> channel



Samuel Usher  
Green Templeton College  
University of Oxford

A thesis submitted for the degree of

*Doctor of Philosophy*

Trinity 2021



# Statement of Authorship

I hereby certify that this is the original work of the author. Data that has been previously published is declared here:

- The data presented in Figures 3.3 to 3.12, Figures 5.1 to 5.5 and Figures 6.1, 6.6 and 6.7 are reanalysed data that have been previously published in Usher *et al.* (1).
- The data presented in Figures 5.6 to 5.12 are reanalysed data that have been previously published in Pipatpolkai *et al.* (2).
- Part of the data presented in Figure 7.2A are reanalysed data that have been previously published in Puljung *et al.* (3).

Contributions from others are declared here:

- The ATP concentration-response curves in Figure 5.6C and Figure 5.9B are constructed from data collected by Dr. Natascia Vedovato.

No part of this thesis has been submitted for any other degree at this or any other university.



# Acknowledgements



## Abstract

ATP-sensitive potassium ( $K_{ATP}$ ) channels are present in many tissues, most notably pancreatic islets and cardiac cells, where they couple the metabolic state of a cell to its electrical activity by regulating the flow of  $K^+$  across the membrane in response to the intracellular ATP/ADP ratio.  $K_{ATP}$  channels are an octameric complex, comprised of four inwardly-rectifying potassium channel (Kir) subunits, each of which is associated with a sulphonylurea receptor (SUR) subunit. In pancreatic islets,  $K_{ATP}$  channels are formed by Kir6.2 and SUR1.

The physiological regulation of  $K_{ATP}$  activity by the ATP/ADP ratio is the summed contribution of activation by Mg-nucleotides binding to SUR1, and inhibition by nucleotides binding to Kir6.2. Mutations in either Kir6.2 and SUR1 which lead to diseases of insulin secretion are frequently observed to disrupt the nucleotide regulation of the channel.



# Contents

<b>List of Figures</b>	<b>xiii</b>
<b>List of Abbreviations</b>	<b>xvii</b>
<b>1 Introduction</b>	<b>1</b>
1.1 Pancreatic islets and the $\beta$ -cell . . . . .	1
1.2 Architecture of the pancreatic $K_{ATP}$ channel . . . . .	3
1.3 Ligand-independent regulation of the pancreatic $K_{ATP}$ channel . . . . .	6
1.3.1 Assembly and trafficking . . . . .	6
1.3.2 Regulation of intrinsic gating . . . . .	9
1.4 Ligand dependent regulation of the pancreatic $K_{ATP}$ channel . . . . .	15
1.4.1 Nucleotide regulation of the pancreatic $K_{ATP}$ channel . . . . .	17
1.4.2 $PIP_2$ regulation of the pancreatic $K_{ATP}$ channel . . . . .	20
1.5 Fluorescence applications for ion channels . . . . .	22
1.5.1 Labelling techniques . . . . .	24
<b>2 Methods</b>	<b>27</b>
2.1 Molecular biology . . . . .	27
2.2 Cell culture and channel expression . . . . .	28
2.3 Western blots . . . . .	29
2.4 Confocal microscopy . . . . .	30
2.5 Surface expression assays . . . . .	31
2.6 Epifluorescence imaging and spectroscopy . . . . .	32
2.7 Electrophysiology . . . . .	32
2.8 FRET calculations . . . . .	33
2.9 Unroofed binding measurements. . . . .	34
2.10 Patch-clamp fluorometry. . . . .	35
2.11 Bayesian data analysis . . . . .	36
2.12 Concentration response processing and presentation . . . . .	42
2.13 MWC model equations and fitting . . . . .	43
2.14 Computational docking. . . . .	44
2.15 Chemicals and stock solutions. . . . .	44

<b>3 Measuring nucleotide binding to K<sub>ATP</sub></b>	<b>47</b>
3.1 Designing a nucleotide binding assay . . . . .	47
3.1.1 Criteria for a useful assay for nucleotide binding to Kir6.2 . . . . .	47
3.1.2 Choosing a site to incorporate ANAP . . . . .	50
3.2 Incorporating ANAP into the Kir6.2 binding site . . . . .	53
3.2.1 The Amber stop codon expression system . . . . .	53
3.2.2 ANAP incorporation into Amber stop codon containing constructs	55
3.3 Testing for functional membrane expression . . . . .	56
3.3.1 Surface expression of HA-epitope labelled Kir6.2 constructs . . . . .	56
3.3.2 Electrophysiology of Kir6.2 constructs . . . . .	58
3.3.3 Unroofed membrane binding assay of Kir6.2 constructs . . . . .	58
3.3.4 Patch-clamp fluorometry of Kir6.2 constructs . . . . .	61
3.4 Discussion . . . . .	62
<b>4 MWC modelling</b>	<b>75</b>
4.1 Modelling nucleotide regulation of the K <sub>ATP</sub> channel . . . . .	75
4.1.1 Restricting the subset of possible models . . . . .	77
4.2 Implementing an MWC model . . . . .	79
4.2.1 A simple case . . . . .	79
4.2.2 The role of PIP <sub>2</sub> . . . . .	79
4.2.3 Determining open probability . . . . .	84
4.2.4 Comparing models . . . . .	89
4.2.5 Discussion . . . . .	94
<b>5 Nucleotide regulation of Kir6.2</b>	<b>95</b>
5.1 Introduction . . . . .	95
5.2 Nucleotide binding . . . . .	96
5.2.1 G334D abolishes nucleotide binding . . . . .	96
5.3 Channel gating . . . . .	97
5.3.1 C166S alters inhibition without affecting binding . . . . .	97
5.3.2 Mutations at E179 alter both inhibition and binding . . . . .	99
5.3.3 Mutations at K39 alter both inhibition and binding . . . . .	101
5.4 Discussion . . . . .	102
<b>6 Regulation of Kir6.2 by SUR1</b>	<b>119</b>
6.1 Introduction . . . . .	119
6.2 Intrinsic effects of SUR1 . . . . .	120
6.2.1 SUR1 dramatically alters nucleotide inhibition, but only subtly effects nucleotide binding at Kir6.2 . . . . .	120
6.2.2 Presence of SUR1-TMD0 alone does not dramatically alter nucleotide binding at Kir6.2 . . . . .	123

6.3	SUR1 and nucleotide regulation . . . . .	125
6.3.1	Mutations at SUR1-K205 alter nucleotide binding and inhibition at Kir6.2 . . . . .	125
6.4	Discussion . . . . .	126
<b>7</b>	<b>Discussion</b>	<b>135</b>
7.1	Summary of findings . . . . .	135
7.2	Inhibition in the context of K <sub>ATP</sub> regulation . . . . .	138
7.3	Nucleotide inhibition of the K <sub>ATP</sub> channel in the context of other ligand- gated ion channels . . . . .	140
<b>Appendices</b>		
<b>A</b>	<b>Appendices</b>	<b>145</b>
<b>References</b>		<b>161</b>

*xii*

# List of Figures

1	hKir6.2 and hSUR1 constructs and their abbreviations . . . . .	xix
1.1	Electrical excitability of pancreatic beta cells . . . . .	2
1.2	Structure of Kir6.2 . . . . .	4
1.3	Structure of SUR1 . . . . .	5
1.4	K <sub>ATP</sub> architecture and nucleotide regulation . . . . .	8
1.5	Intrinsic regulation of Kir6.2 gating . . . . .	12
1.6	Modes of regulation of K <sub>ATP</sub> . . . . .	16
1.7	Contrasting sizes of fluorophores . . . . .	25
2.1	Flipping a coin - illustrating Bayesian analysis . . . . .	37
2.2	Credible intervals of a probability distribution . . . . .	39
2.3	Multilevel modelling of coinflips . . . . .	40
2.4	Multilevel modelling of coinflips - fitting the model . . . . .	41
3.1	ANAP and TNP-nucleotides as FRET pairs . . . . .	51
3.2	TNP-ATP is predicted to bind with a similar pose to ATP . . . . .	54
3.3	ANAP incorporation . . . . .	64
3.4	Confocal imaging . . . . .	65
3.5	ANAP construct surface expression assay . . . . .	66
3.6	WT-GFP and W311*-GFP electrophysiology . . . . .	67
3.7	Unroofed membranes spectral images . . . . .	68
3.8	Unroofed membranes bleaching correction . . . . .	69
3.9	Numerical analysis of FRET efficiency in tetrameric Kir6.2 . . . . .	70
3.10	W311*-GFP unroofed membrane binding . . . . .	71
3.11	PCF bleaching correction . . . . .	72
3.12	ANAP is not quenched by ATP . . . . .	73
4.1	Simple ion channel model . . . . .	76
4.2	Generating data from MWC model schemes . . . . .	80
4.3	Parameter retrieval from MWC models . . . . .	82
4.4	Parameter retrieval from MWC models . . . . .	83
4.5	Systematic underestimation of single channel currents . . . . .	87
4.6	Simulated multibinomial currents . . . . .	89

4.7	Estimating open probability from stationary noise analysis . . . . .	90
4.8	Full model diagrams . . . . .	91
4.9	A concerted model explains the data better than an independent model	92
4.10	Comparing the states and weights of concerted and independent models	93
5.1	G334D abolishes nucleotide binding at Kir6.2 . . . . .	106
5.2	C166S does not alter nucleotide binding . . . . .	107
5.3	C166S alters sensitivity to nucleotide inhibition . . . . .	108
5.4	C166S alters transduction of nucleotide binding to Kir6.2 . . . . .	109
5.5	TEA <sub>+</sub> inhibits K <sub>ATP</sub> channels at high concentrations . . . . .	110
5.6	Functional effects of E179 mutations . . . . .	111
5.7	E179 mutations EC <sub>50</sub> parameters . . . . .	112
5.8	E179 mutations affect gating and nucleotide binding . . . . .	113
5.9	Functional effects of K39 mutations on ATP inhibition . . . . .	114
5.10	Functional effects of K39 mutations on TNP-ATP binding and inhibition	115
5.11	K39 mutations EC <sub>50</sub> parameters . . . . .	116
5.12	K39 mutations affect gating and nucleotide binding . . . . .	117
5.13	K39 is in close proximity to the TNP moiety of bound TNP-ATP . . . . .	118
6.1	SUR1 dramatically alters inhibition but only subtly alters binding at Kir6.2 . . . . .	128
6.2	SUR1-mO associates with WT-GFP and W311*-GFP . . . . .	129
6.3	TMD0 and TMD0-LO associate with WT-GFP and W311*-GFP . . . . .	130
6.4	TMD0 and TMD0-LO subtly alter TNP-ATP binding to Kir6.2 . . . . .	131
6.5	TMD0 and TMD0-LO subtly alter the effect of nucleotides on Kir6.2 . . . . .	132
6.6	Functional effects of mutations at K205 . . . . .	133
6.7	K205 mutations affect gating and nucleotide binding . . . . .	134
7.1	Modes of regulation of K <sub>ATP</sub> - reprinted . . . . .	138
7.2	TNP-ATP inhibits K <sub>ATP</sub> more strongly than MgTNP-ADP activates it . . . . .	142
A.1	ATP inhibition population hill fits . . . . .	146
A.2	ATP inhibition sample hill fits . . . . .	147
A.3	TNP-ATP inhibition population hill fits . . . . .	148
A.4	TNP-ATP inhibition sample hill fits . . . . .	149
A.5	Nucleotide inhibition IC <sub>50</sub> posterior distributions . . . . .	150
A.6	Unroofed membrane quenching population hill fits . . . . .	151
A.7	Unroofed membrane quenching sample hill fits . . . . .	152
A.8	Excised patch quenching population hill fits . . . . .	153
A.9	Excised patch quenching sample hill fits . . . . .	154
A.10	Fluorescence quenching EC <sub>50</sub> posterior distributions . . . . .	155

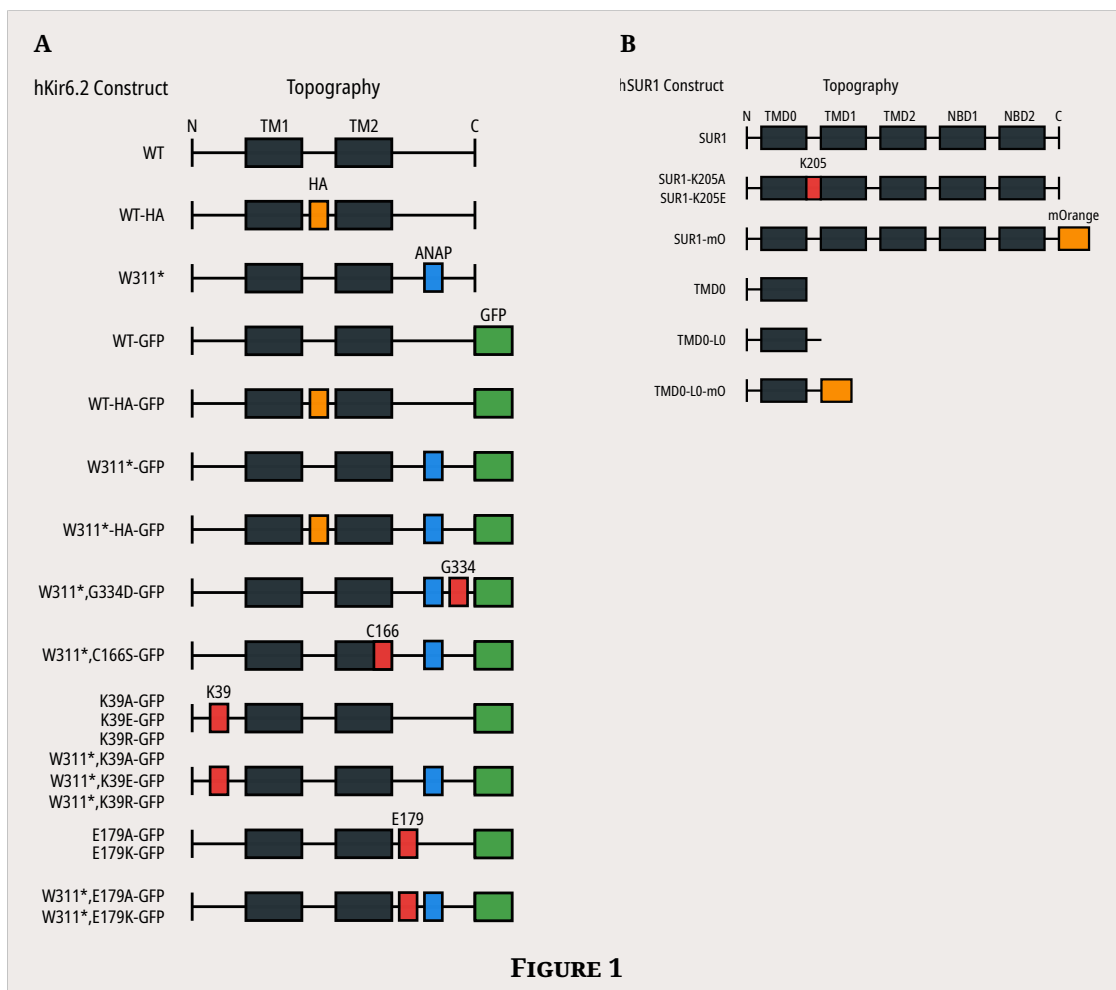
A.11 MWC population fits . . . . .	156
A.12 MWC sample fits . . . . .	157
A.13 MWC parameter posterior distributions . . . . .	158
A.14 MWC parameter cross-correlation - inhibition . . . . .	159
A.15 MWC parameter cross-correlation - inhibition and activation . . . . .	160



# List of Abbreviations

<b>aaRS</b>	Aminoacyl-tRNA synthetase
<b>ABC</b>	ATP-binding cassette
<b>ADP</b>	Adenosine diphosphate
<b>ATP</b>	Adenosine triphosphate
<b>ANAP</b>	L-3-(6-acetylnaphthalen-2-ylamino)-2-aminopropionic acid
<b>BK channel</b>	Large conductance K <sup>+</sup> channel
<b>CFTR</b>	Cystic fibrosis transmembrane conductance regulator
<b>CNG channel</b>	Cyclic nucleotide gated channel
<b>Cryo-EM</b>	Cryo-electron microscopy
<b>DEND syndrome</b>	Permanent neonatal diabetes mellitus with neurological complications
<b>EC<sub>50</sub></b>	Half maximal effective concentration
<b>ELPD</b>	Expected log pointwise predictive density
<b>ER</b>	Endoplasmic reticulum
<b>FRET</b>	Förster resonance energy transfer
<b>GFP</b>	Green fluorescent protein
<b>HA</b>	Human influenza hemagglutinin
<b>HEK293T</b>	Human embryonic kidney 293 cells containing the SV40 T-antigen
<b>HRP</b>	Horseradish peroxidase
<b>IC<sub>50</sub></b>	Half maximal inhibitory concentration
<b>K<sub>ATP</sub> channel</b>	ATP-sensitive potassium channel
<b>Kir</b>	Inward rectifier potassium channel
<b>L0</b>	Loop zero
<b>LOO-CV</b>	Leave-one-out cross-validation
<b>mO</b>	mOrange fluorescent protein

<b>MWC</b> . . . . .	Monod-Wyman-Changeaux
<b>nAChR</b> . . . . .	Nicotinic acetylcholine receptor
<b>NBD</b> . . . . .	Nucleotide binding domain
<b>PCF</b> . . . . .	Patch-clamp fluorometry
<b>PDB</b> . . . . .	Protein data bank
<b>PIP</b> <sub>2</sub> . . . . .	Phosphatidylinositol 4,5-bisphosphate
$P_O$ . . . . .	Open probability
<b>SUR</b> . . . . .	Sulphonylurea receptor
<b>TEA</b> <sup>+</sup> . . . . .	Triethylammonium ion
<b>TMD</b> . . . . .	Transmembrane domain
<b>TNP-ADP</b> . . . .	Trinitrophenyl adenosine diphosphate
<b>TNP-ATP</b> . . . .	Trinitrophenyl adenosine triphosphate
<b>tRNA</b> . . . . .	Transfer RNA
<b>UAA</b> . . . . .	Unnatural amino acid
<b>WT</b> . . . . .	Wild-type

**FIGURE 1**



# 1

## Introduction

### Contents

---

1.1	Pancreatic islets and the $\beta$ -cell . . . . .	1
1.2	Architecture of the pancreatic K <sub>ATP</sub> channel . . . . .	3
1.3	Ligand-independent regulation of the pancreatic K <sub>ATP</sub> channel . . . . .	6
1.3.1	Assembly and trafficking . . . . .	6
1.3.2	Regulation of intrinsic gating . . . . .	9
1.4	Ligand dependent regulation of the pancreatic K <sub>ATP</sub> channel . . . . .	15
1.4.1	Nucleotide regulation of the pancreatic K <sub>ATP</sub> channel . . . . .	17
1.4.2	PIP <sub>2</sub> regulation of the pancreatic K <sub>ATP</sub> channel . . . . .	20
1.5	Fluorescence applications for ion channels . . . . .	22
1.5.1	Labelling techniques . . . . .	24

---

### 1.1 Pancreatic islets and the $\beta$ -cell

Pancreatic islets are endocrine cells which are responsible for maintaining glucose homeostasis. It has been estimated that there are between  $3 \times 10^6$  to  $1.5 \times 10^7$  islets in a human pancreas, constituting 1 % to 2 % of the total pancreatic mass (4). Islets consist of three principal cell types; insulin secreting  $\beta$ -cells, glucagon secreting  $\alpha$ -cells and somatostatin secreting  $\delta$ -cells (5). Islets respond to increases in blood glucose by releasing insulin, which acts on peripheral tissues to increase glucose uptake and reduce blood glucose levels. Conversely, decreases in blood glucose

leads to the release of glucagon, which acts on those tissues to stimulate glucose production and increase blood glucose.

Insulin secretion in beta cells - and indeed in all three cell types of pancreatic islets - is induced by the firing of action potentials, which leads to the influx of  $\text{Ca}^{2+}$  ions and the activation of secretory granule exocytosis (Figure 1.1A) (5). This electrical excitability is controlled by the ATP-sensitive potassium ( $K_{\text{ATP}}$ ) channel. At rest,  $K_{\text{ATP}}$  channel activity results in a leak current of  $\text{K}^+$  ions out of the cell, hyperpolarising the membrane. Glucose metabolism in beta cells increases the ATP:ADP ratio, closing  $K_{\text{ATP}}$  channels and releasing their hyperpolarising clamp on the membrane potential (6, 7). When  $K_{\text{ATP}}$  channels are closed and membrane resistance is high, even small currents are sufficient to induce large membrane potential depolarisations and action potential initiation (Figure 1.1B).

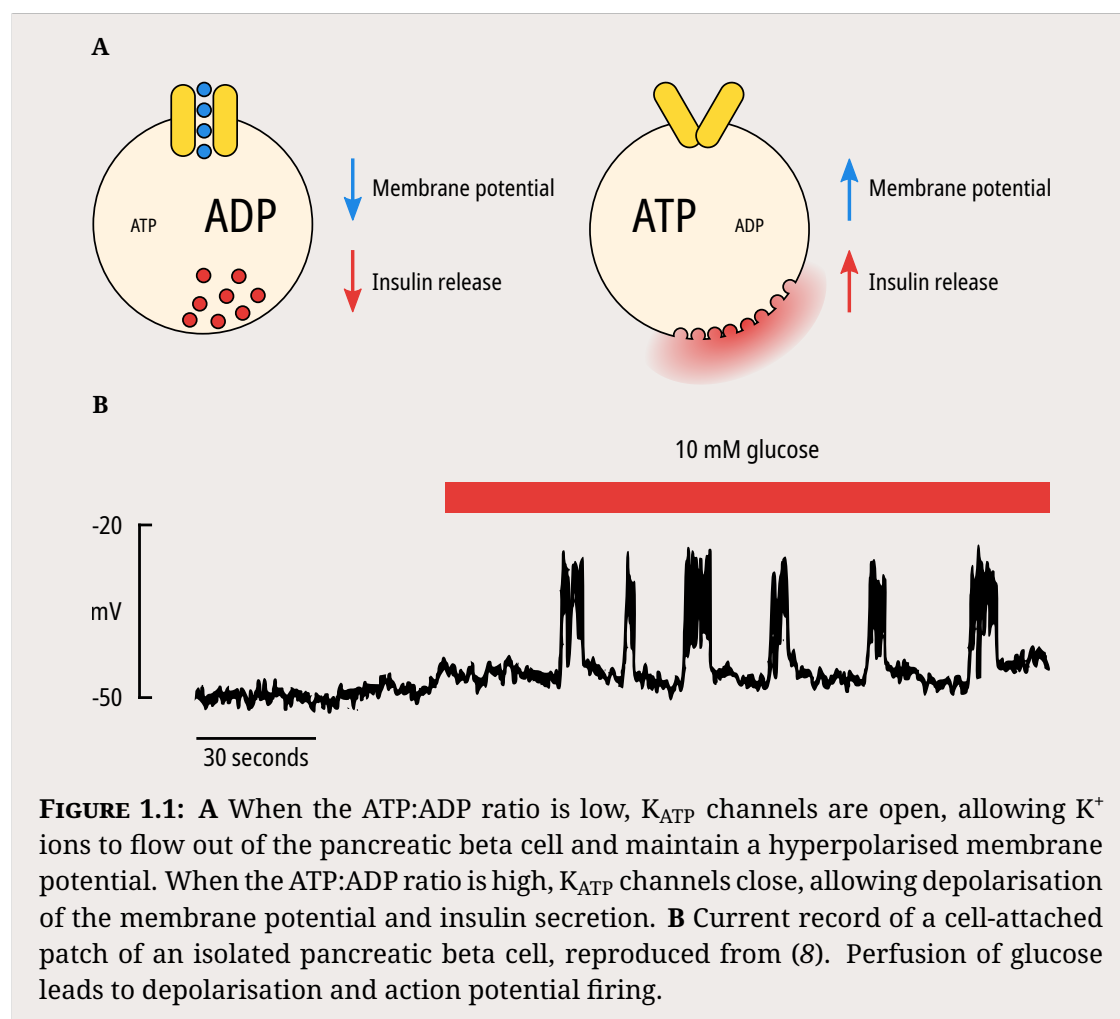


**FIGURE 1.1:** **A** When the ATP:ADP ratio is low,  $K_{\text{ATP}}$  channels are open, allowing  $\text{K}^+$  ions to flow out of the pancreatic beta cell and maintain a hyperpolarised membrane potential. When the ATP:ADP ratio is high,  $K_{\text{ATP}}$  channels close, allowing depolarisation of the membrane potential and insulin secretion. **B** Current record of a cell-attached patch of an isolated pancreatic beta cell, reproduced from (8). Perfusion of glucose leads to depolarisation and action potential firing.

## 1.2 Architecture of the pancreatic K<sub>ATP</sub> channel

K<sub>ATP</sub> channels are present in many tissues, where they couple the metabolic state of a cell to its electrical activity by regulating the flow of K<sup>+</sup> across the membrane (9). K<sub>ATP</sub> channels are an octameric complex, comprised of four inwardly-rectifying potassium channel subunits (Kir6.1 or Kir6.2), each of which is associated with a sulphonylurea receptor subunit (SUR1, SUR2A or SUR2B) (10–13). In pancreatic β-cells, the K<sub>ATP</sub> channel isoform is composed of Kir6.2 and SUR1 (14). Together, Kir6.2 and SUR1 form a complex nearly a megadalton in size and over 15 nanometres across (Figure 1.4A, 1.4B).

Inwardly-rectifying potassium channels are so named because they allow K<sup>+</sup> to flow more easily into the cell than out of it (Figure 1.2A) (15, 16). This phenomenon is a consequence of voltage-dependent pore blockade by intracellular divalent cations (especially Mg<sup>2+</sup>) and polyamines. At depolarising membrane potentials, blockers are driven into the pore and K<sup>+</sup> current is blocked, while at hyperpolarising potentials the blockers are cleared and K<sup>+</sup> current can flow. Strongly rectifying Kir channels display drastically reduced conductance at potentials more positive than the K<sup>+</sup> reversal potential. In contrast, Kir6.2 is a weak rectifier, and allows substantial current to flow at more positive potentials.

In addition to voltage, Kir6.2 is regulated by two endogenous ligands; phosphatidylinositol 4,5-bisphosphate (PIP<sub>2</sub>) and adenine nucleotides (Figure 1.2B) (17, 18). The binding of adenine nucleotides to Kir6.2 leads to closure of the channel pore, while the binding of PIP<sub>2</sub> promotes the opening of the pore (Figure 1.2C). Activation by PIP<sub>2</sub> is a mechanism common to the whole Kir family, whereas inhibition by nucleotides is unique to the Kir6 subfamily (19).

SUR1 is a member of the ATP-binding cassette (ABC) family of transporters. While other ABC proteins transport substrate across the membrane, SUR1 does not appear to do so; instead it acts to modulate the function of its associated ion channel (22, 23). The cystic fibrosis transmembrane conductance regulator (CFTR) is another member of the ABC family, and is an ion channel in its own right, capable of conducting

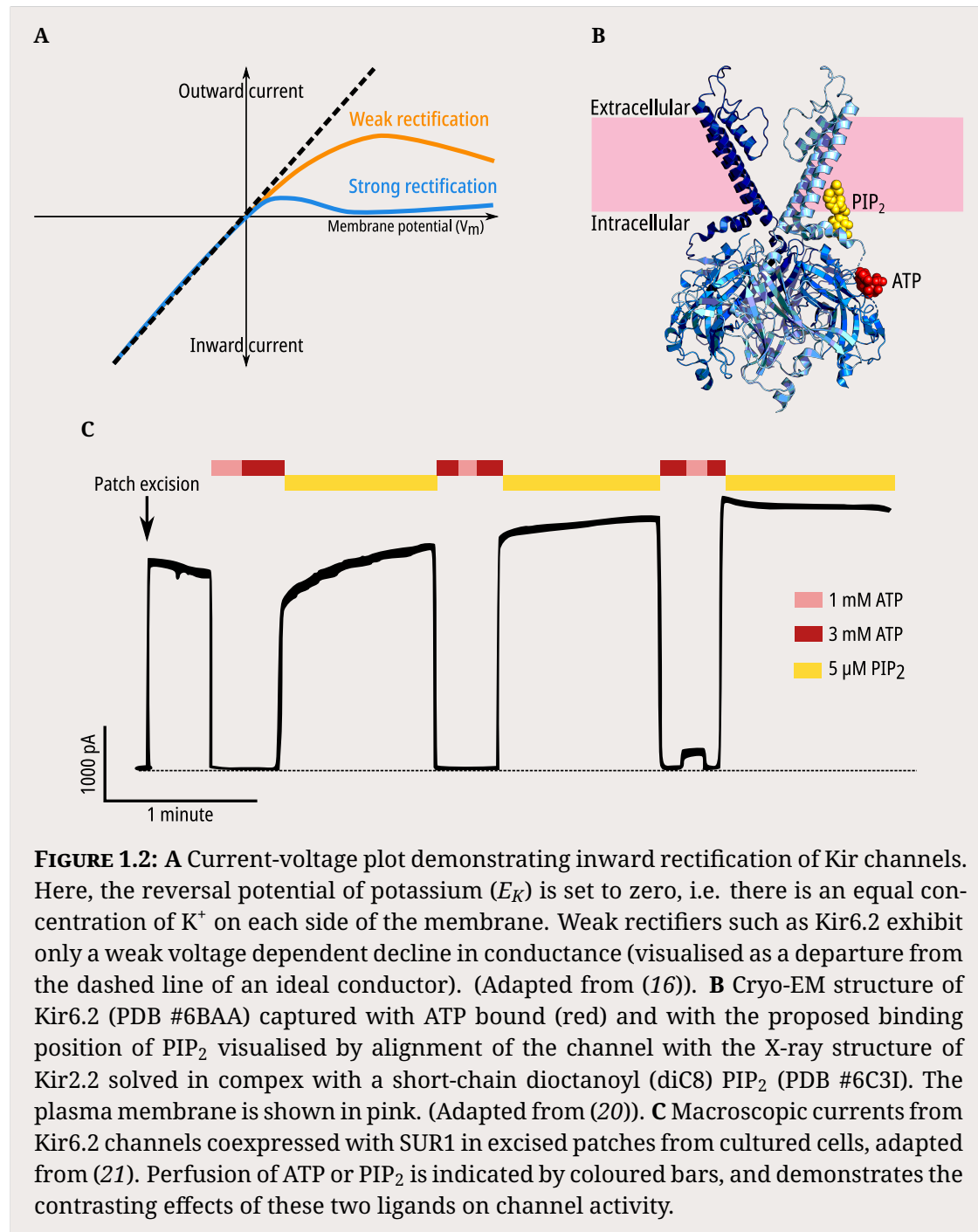
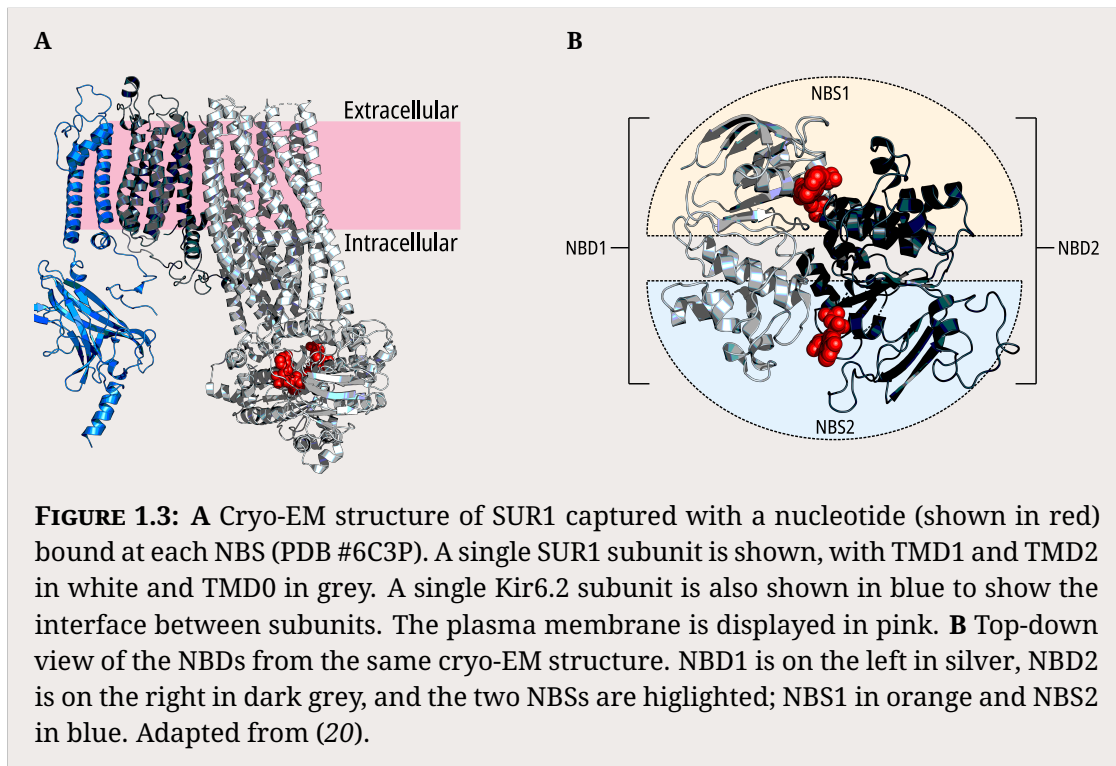


**FIGURE 1.2:** **A** Current-voltage plot demonstrating inward rectification of Kir channels. Here, the reversal potential of potassium ( $E_K$ ) is set to zero, i.e. there is an equal concentration of  $K^+$  on each side of the membrane. Weak rectifiers such as Kir6.2 exhibit only a weak voltage dependent decline in conductance (visualised as a departure from the dashed line of an ideal conductor). (Adapted from (16)). **B** Cryo-EM structure of Kir6.2 (PDB #6BAA) captured with ATP bound (red) and with the proposed binding position of PIP<sub>2</sub> visualised by alignment of the channel with the X-ray structure of Kir2.2 solved in complex with a short-chain dioctanoyl (diC8) PIP<sub>2</sub> (PDB #6C3I). The plasma membrane is shown in pink. (Adapted from (20)). **C** Macroscopic currents from Kir6.2 channels coexpressed with SUR1 in excised patches from cultured cells, adapted from (21). Perfusion of ATP or PIP<sub>2</sub> is indicated by coloured bars, and demonstrates the contrasting effects of these two ligands on channel activity.

chloride across the membrane (24). Like other ABC proteins, SUR1 contains two sets of transmembrane domains (TMD1 and TMD2) and two cytosolic nucleotide binding domains (NBD1 and NBD2) (22, 25). Unique to SUR is the presence of an additional transmembrane domain (TMD0) N-terminal to the core of the protein, and this domain forms the primary contact between SUR1 and Kir6.2 (26–29).

The NBDs of ABC transporters are highly conserved, and consist of two subdomains: a larger RecA-like subdomain found in other P-loop ATPases, and a smaller  $\alpha$ -helical subdomain which is unique to ABC transporters (20, 25). There are three key structural motifs present in these subdomains: the RecA-like subdomain contains the Walker A ( $W_A$ ) and B ( $W_B$ ) motifs, while the  $\alpha$ -helical subdomain contains the ABC signature motif (typically LSQQQ).

The two domains come together to form an antiparallel dimer with two nucleotide binding sites (NBS1 and NBS2) at the interface, such that NBS1 is formed from the  $W_A$  and  $W_B$  motifs of NBD1 and the signature motif from NBD2, whereas NBS2 is formed from the  $W_A$  and  $W_B$  motifs of NBD2 and the signature motif from NBD1. NBS2, also known as the consensus site as it is more similar in sequence to other ABC family members, is catalytically competent and able to hydrolyse ATP (30–32). In contrast, NBS1 is the degenerate site, with a less conserved sequence and an inability to catalyse hydrolysis of ATP (20, 25).



## **1.3 Ligand-independent regulation of the pancreatic K<sub>ATP</sub> channel**

### **1.3.1 Assembly and trafficking**

Biogenesis of K<sub>ATP</sub> channels occurs in the endoplasmic reticulum (ER), and is an important checkpoint in determining surface expression and channel stoichiometry (33, 34). The precise nature of the events which occur between subunit translation and insertion of octameric K<sub>ATP</sub> into the cell membrane are not fully mapped out, but studies have highlighted some important quality control steps in this process which regulate K<sub>ATP</sub> channel expression. When Kir6.2 or SUR1 are expressed alone in heterologous systems, they are retained in the ER (33). This mechanism is achieved through the exposure of a three amino acid ER-retention motif (RKR) in the cytoplasmic domains of both Kir6.2 and SUR1. Only upon complete assembly of the channel complex are the RKR motifs masked, allowing forward trafficking of K<sub>ATP</sub> to the cell surface. Deletion of the RKR motif (35), or mutation of the motif to AAA (33), results in unregulated surface expression of individual subunits and/or partially assembled channel complexes. Addition of a GFP label to the C-terminus of Kir6.2 is also sufficient to allow trafficking of tetrameric Kir6.2 to the cell surface in the absence of SUR1 (36).

In addition to the RKR motif, there are two N-linked glycosylation sites on SUR1 (N10 and N1050) which are required for cell surface expression (37). Mutation of these sites to glutamines results in retention in the ER and drastically reduced expression of K<sub>ATP</sub> on the cell surface. This mechanism is thought to be separate to that for the ER-retention motif, as mutation of RKR to AAA is not sufficient to drive surface expression of the glycosylation mutants (37).

A putative third site of trafficking regulation is in the C-terminus of SUR1. Mutation or deletion of a dileucine motif 16 amino acids distal to the C-terminal of SUR1 results in reduced surface expression of K<sub>ATP</sub> channels in COSm6 cells (38). This reduction in expression is not rescued by C-terminal truncation of Kir6.2, indicating that this result is not due to masking of the RKR retention motif. The

dileucines are therefore suggested to promote forward trafficking of assembled channel complexes to the cell membrane (38). Expression of K<sub>ATP</sub> channels expressed in *Xenopus* oocytes is also dramatically reduced by truncation of the C-terminal 42 amino acids of SUR1 (39). However, longer deletions of the SUR1 C-terminus did not reduce surface expression of channels in HEK293 cells (40), and other modifications of the SUR1 C-terminus do not exhibit effects on surface expression (41). In fact, a splice variant of SUR1 missing the entirety of the NBD2 domain (truncated at residue 1355) was found to successfully traffic to the cell membrane of *Xenopus* oocytes (42). The precise role of the dileucine motif remains unclear, and is potentially confounded by the use of expression system (34, 40)

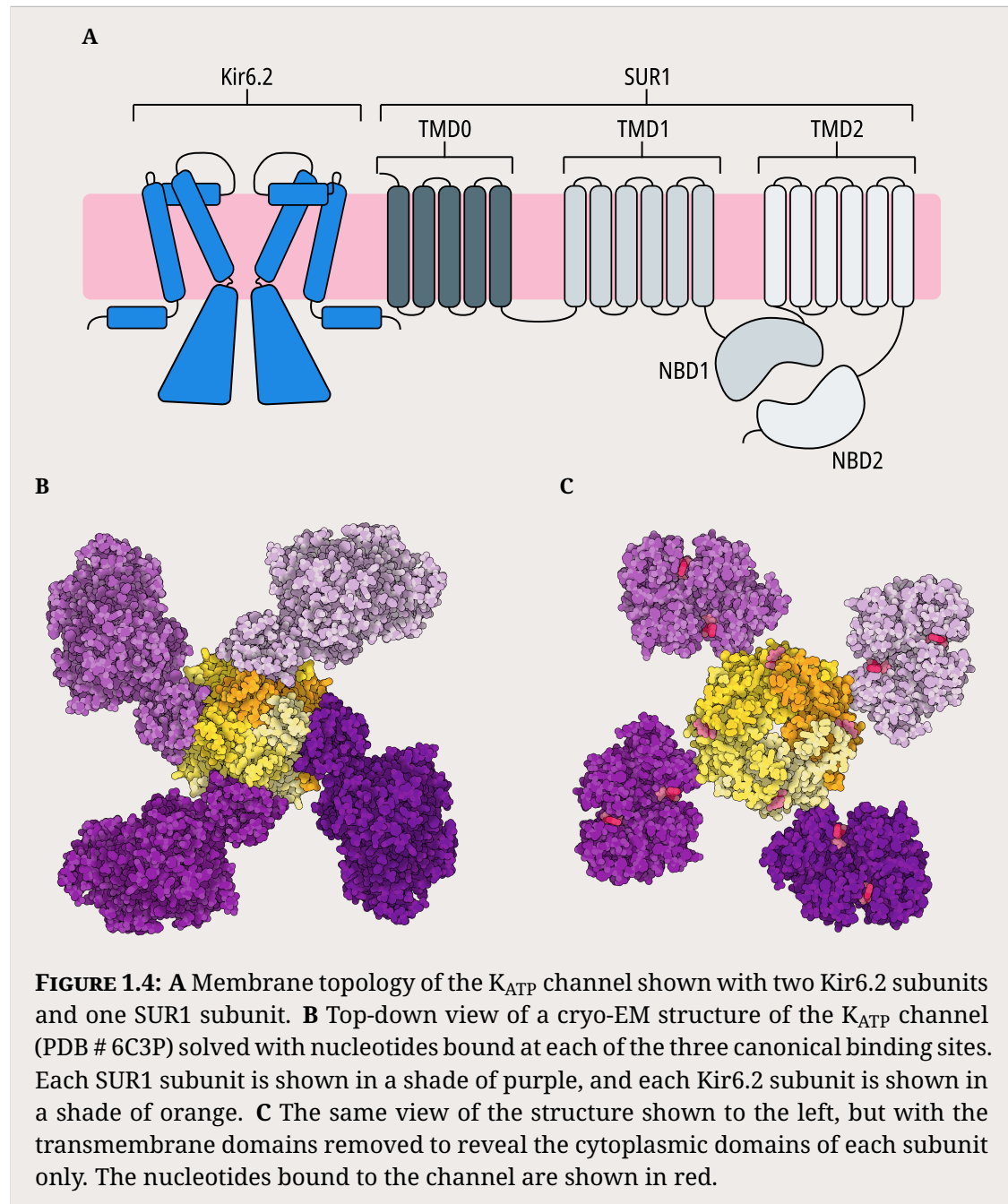
Failure of the channel complex to pass these three checkpoints results in ER-associated degradation (ERAD), a common pathway shared by most membrane and secretory proteins (43, 44). Both SUR1 and Kir6.2 are substrates for polyubiquitination, both when heterologously expressed and in INS-1 cells (44). Application of proteasome inhibitors both reduces the rate of degradation for Kir6.2 and SUR1, and increases the surface expression of K<sub>ATP</sub> channels by increasing their biogenesis efficiency (44).

The surface expression of K<sub>ATP</sub> channels is therefore controlled by a variety of different quality control mechanisms to ensure that only correctly assembled octameric channel complexes reach the cell membrane. Mutations which lead to defects in assembly and trafficking are therefore a common cause of congenital hyperinsulinemia (HI) as they result in permanent membrane depolarisation and unregulated insulin secretion. These mutations are found throughout both Kir6.2 and SUR1, although they are more commonly found in SUR1 (34).

Interestingly, sulphonylureas are able to act as pharmacological chaperones and rescue surface expression of several mutations which would otherwise not traffic to the cell surface (45–49). Sulphonylureas bind directly to the channel during biogenesis, as mutation of residues in SUR1 which are critical for sulphonylurea binding abolished or reduced the effectiveness of expression rescue (46). Pharmacological chaperoning requires full assembly of the channel complex, as the presence

### 1.3. Ligand-independent regulation of the pancreatic $K_{ATP}$ channel

of Kir6.2 was required to rescue expression of trafficking mutants even when the SUR1 RKR motif was mutated to AAA (46). In addition, reducing the temperature at which cells are cultured can rescue some trafficking defects (50).



### 1.3.2 Regulation of intrinsic gating

In the absence of nucleotides, K<sub>ATP</sub> channels are spontaneously active. This can be seen at a macroscopic level in excised patches. Upon excision of a patch from a cell membrane containing K<sub>ATP</sub> channels, the magnitude of current dramatically increases when voltage is applied (Figure 1.2C), reflecting the relief from inhibition of cytoplasmic nucleotides. While this macroscopic time course is smooth and graded, it consists of hundreds or thousands of individual channels which exhibit binary behaviour, switching between a nonconducting closed state and a conducting open state (15). The summed activity of these individual channels constitutes the large currents observed in macroscopic excised patches.

Single K<sub>ATP</sub> channels exhibit bursts of brief openings, separated by long interburst closures (51–54). Thus, the open probability ( $P_O$ ) of the channel is determined both by the kinetics of the burst (open and closed durations within a burst) and the duration of the long interburst closures. The intrinsic gating of K<sub>ATP</sub> can therefore be separated into two separate 'gating' processes; fast (responsible for intraburst closures) and slow (responsible for interburst closures). While it is helpful to distinguish between fast and slow gating processes to characterise channel regulation, doing so does not require the existence of separate structural gates (15, 54).

Gating is a property intrinsic to Kir6.2, which is able to open and close in the absence of SUR1 (35, 55) (Figure 1.5B); albeit with very different kinetic properties as will be discussed later. The open and intraburst closed time of single channels is dependent on the electrochemical gradient across the cell membrane, otherwise called the K<sup>+</sup> driving force (56). As the name implies, the electrochemical gradient depends on two things: the voltage across the membrane, and the K<sup>+</sup> concentration gradient. Increasing hyperpolarisation decreases the amount of time channels remain in the open state and increases the amount of time channels remain in the closed state within bursts (57, 58). This is a characteristic feature shared by other inwardly-rectifying K<sup>+</sup> channels (57, 59). In addition, altering the K<sup>+</sup> gradient across the membrane by changing the K<sup>+</sup> concentration in the pipette or bath solution has the same effect on fast gating kinetics (56, 60). As the driving force for K<sup>+</sup> increases,

the open lifetime of the  $K_{ATP}$  channel decreases. This is in contrast to other  $K^+$  channels such as  $Kv2.1$ , which exhibits the opposite relationship (61).

There are a number of domains within Kir6.2 that regulate the intrinsic gating of the channel. Firstly, the P-loop is a conserved feature across  $K^+$  channels (62). In Kir channels, the P-loop connects the two transmembrane domains, and dips into the plasma membrane to form the  $K^+$  selectivity filter. While the P-loop is broadly conserved between Kir family members, there are key residues which differ. Notably, the  $K^+$  selectivity filter signature sequence (TxGYG) is identical across all other Kir subtypes (TIGYG), but in Kir6.1 and Kir6.2 the tyrosine is replaced by a phenylalanine at position 133 (TIGFG), a feature shared only by eag-like  $K^+$  channels (63). Another particularly interesting residue is V127, which is unique to Kir6.1 and Kir6.2 within the Kir family - all other Kir channels possess a threonine at this location (64).

Proks *et al.* (64) investigated a range of substitutions at these two residues. Mutation of V127 to the conserved threonine (V127T) dramatically increases the open time of  $K_{ATP}$ , while also increasing the intraburst closed time. There is also some suggestion of an additional open state existing in this mutant construct, evidenced by the appearance of a second peak in the open time histograms. Mutation of F133 to the conserved tyrosine (F133Y) did not produce expression of functional channels; however combining the two mutations (V127T,F133Y) resulted in functional channels with a further increase in the open time when compared to the single mutant V127T. In addition, substitutions at other residues in the P-loop of Kir6.2 lead to a range of effects on the intraburst kinetics of  $K_{ATP}$ . Crucially, none of the substitutions affected the slow gating of the channel; i.e. burst duration and interburst closed times remained similar despite the varied alterations in the intraburst kinetics. Proks *et al.* (64) concluded that the P-loop is instrumental in regulating the fast gating of  $K_{ATP}$ , and suggested that the lack of correlation between perturbations of inter- and intra-burst kinetics is evidence for independence between the fast and slow gating processes.

Other domains of Kir6.2 are involved in the regulation of slow gating. The cytosolic end of the second transmembrane domain of Kir6.2 has been implicated

in regulation of  $K_{ATP}$  slow gating by a number of mutational studies (58, 65–67). Substitution of C166 with a more bulky or hydrophobic residue dramatically reduces the frequency of the channel entering the long, closed interburst state, and increases the open time of the channel in the bursts (58). However, no effect is seen on the length of the intraburst closed times, which is additional evidence for the independence of the fast and slow gating processes. Substitutions at N160 (65), L164 (68), I167 (66), and T171 (66, 69) also increase channel open time and decrease the rate of entry into the interburst closed state, further implicating this region of Kir6.2 in modulating the slow gating of  $K_{ATP}$ .

The slide-helix of Kir6.2 is the interface between the transmembrane domain and the cytoplasmic domain, and mutations in this region result in changes in the single channel kinetics and  $P_O$  of  $K_{ATP}$  (70–74). Mutations examined at the single channel level show changes in burst duration (70–72) but unaltered intraburst kinetics. Interpretation of the mechanism underlying these single channel kinetics alterations is complicated by the proximity of this region of Kir6.2 to the putative PIP<sub>2</sub> binding site (75). Perturbations of this region could be affecting intrinsic gating directly, or indirectly by altering PIP<sub>2</sub> regulation, both of which would lead to changes in slow gating.

While Kir6.2 is able to gate intrinsically when expressed alone, coassembly with SUR1 alters the intrinsic gating of the channel in a number of ways. Compared to the single channel kinetics of Kir6.2ΔC or Kir6.2-GFP alone, coexpression of Kir6.2 with SUR1 increases the open time of the channel within the bursts, and increases their duration, while the intraburst closed times are unaffected (36, 58, 76). This suggests that interactions of SUR1 with Kir6.2 serve to regulate the slow gating of the channel, rather than the fast gating. The mechanisms by which SUR1 regulates intrinsic gating of the  $K_{ATP}$  channel are complex and not yet fully understood. Structurally, the primary contacts between the two subunits are formed between the N-terminus and first transmembrane domain of Kir6.2 and TMD0 and L0 of SUR1 (Figure 1.3A) (28, 77, 78). The contributions of the interactions of these regions have been studied in a variety of ways.

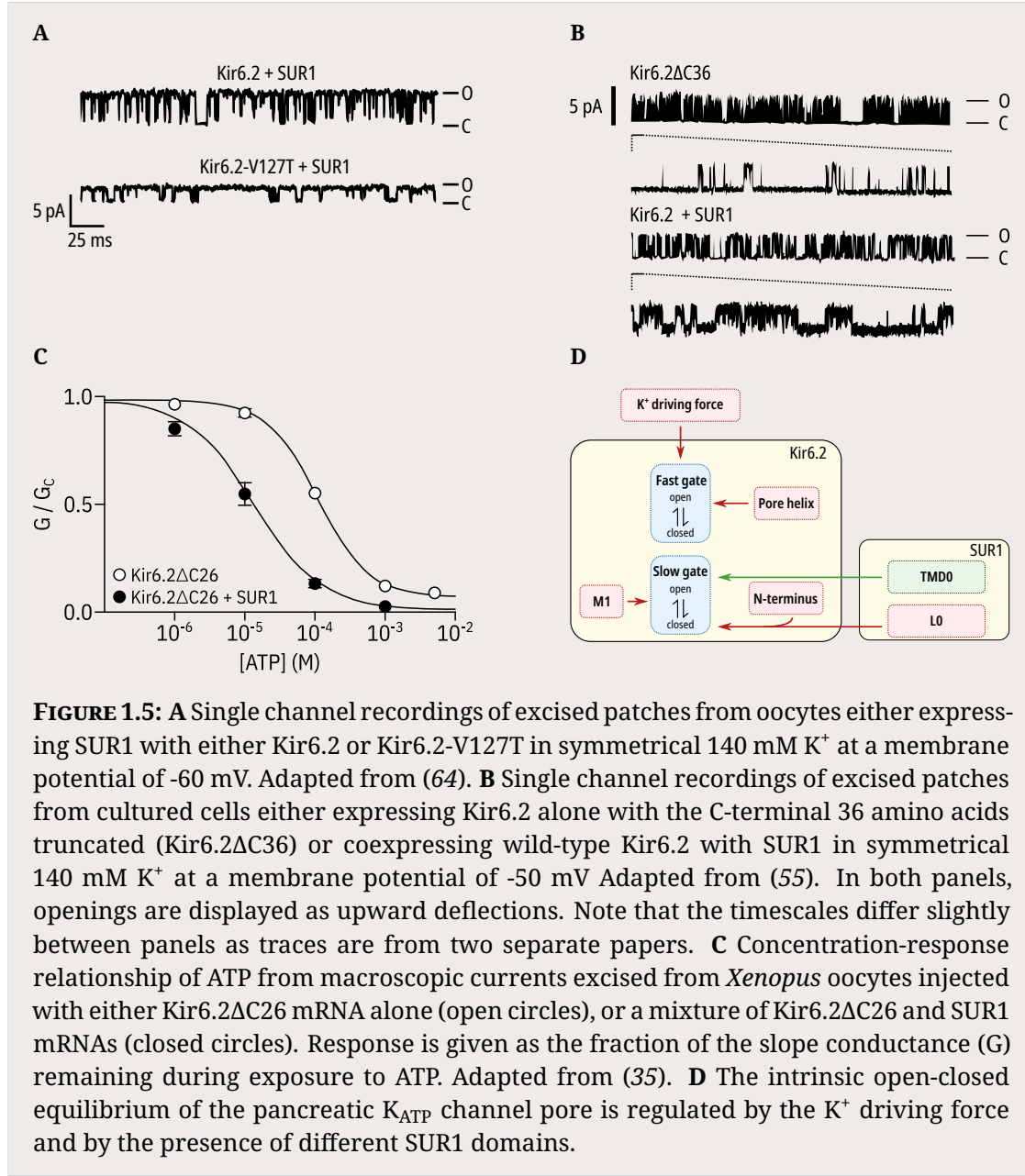


**FIGURE 1.5:** **A** Single channel recordings of excised patches from oocytes either expressing SUR1 with either Kir6.2 or Kir6.2-V127T in symmetrical 140 mM  $K^+$  at a membrane potential of -60 mV. Adapted from (64). **B** Single channel recordings of excised patches from cultured cells either expressing Kir6.2 alone with the C-terminal 36 amino acids truncated (Kir6.2ΔC36) or coexpressing wild-type Kir6.2 with SUR1 in symmetrical 140 mM  $K^+$  at a membrane potential of -50 mV Adapted from (55). In both panels, openings are displayed as upward deflections. Note that the timescales differ slightly between panels as traces are from two separate papers. **C** Concentration-response relationship of ATP from macroscopic currents excised from *Xenopus* oocytes injected with either Kir6.2ΔC26 mRNA alone (open circles), or a mixture of Kir6.2ΔC26 and SUR1 mRNAs (closed circles). Response is given as the fraction of the slope conductance ( $G$ ) remaining during exposure to ATP. Adapted from (35). **D** The intrinsic open-closed equilibrium of the pancreatic  $K_{ATP}$  channel pore is regulated by the  $K^+$  driving force and by the presence of different SUR1 domains.

Babenko *et al.* (52) constructed a series of SUR1/SUR2A chimeras and characterised the changes in single channel kinetics that resulted from swapping different domains between the two isoforms of SUR. They found that Kir6.2+SUR2A channels exhibited a far higher single channel  $P_O$  than Kir6.2+SUR1 channels (0.91 and 0.64 respectively). This difference could be attributed to increased burst durations and decreased interburst periods, while fast gating was indistinguishable. They found that a chimerical construct replacing the N-terminal 291 amino acids of SUR1 with

those of SUR2A was sufficient to recapitulate the single channel kinetics of full-length SUR2A, suggesting that this region is critical for specifying the intrinsic gating of K<sub>ATP</sub>.

Later work established that truncations of SUR1 to TMD0 or TMD0-L0 fragments allowed expression of "mini-K<sub>ATP</sub>" channels at the cell membrane (79–81). The first two studies showed that expression of Kir6.2 with TMD0 alone (residues 1–195 or 1–196 of SUR1) essentially recapitulates the intrinsic gating characteristics of Kir6.2 expressed with full-length SUR1, restoring the increased open time duration and burst duration as compared to expression of Kir6.2 alone (79, 80). Fang *et al.* (81) later found that in their hands, mini-K<sub>ATP</sub> channels formed from Kir6.2ΔC and SUR1-TMD0 were similar to full-length K<sub>ATP</sub> but they consistently observed differences in the burst durations. This discrepancy may be, at least in part, due to differences in the heterologous expression system (COSm6 cells in Babenko and Bryan (79), *Xenopus* oocytes in Fang *et al.* (81)). Otherwise, the remaining difference between K<sub>ATP</sub> and mini-K<sub>ATP</sub> channels could either be due to differences in structural interactions due to the truncation, or could implicate a role for the ABC core domain in regulating slow gating (81).

Increasing the length of the SUR1 fragment to include the first section of the L0 linker (residues 1–232 of SUR1) results in a nearly constitutively open channel, with dramatically increased open time duration and few observable interburst closures (79). The resulting  $P_O$  of 0.93 reflects a near saturation of the slow gating process; as without changes to the fast gating there can be limited further increases in  $P_O$  due to the flickery closure. Increasing the length of the L0 linker included in the SUR1 truncation fragment results in a progressive decrease in the open time duration, burst length and  $P_O$ , although it never regresses to the kinetics observed in Kir6.2 expressed alone (79). These findings suggest that while the TMD0 and the initial segment of L0 help to stabilise the open state of K<sub>ATP</sub> channels, other sections of the L0 linker act to destabilise the open state in some fashion (79, 82).

One hypothesis for this destabilisation is that parts of the L0 linker interact with the N-terminus of Kir6.2 to regulate the intrinsic gating of K<sub>ATP</sub> channels (83–86).

When Kir6.2 $\Delta$ C is expressed alone, deletion of the first 14 amino acids of the N-terminus of Kir6.2 does not affect the single channel kinetics (85). However, in the presence of SUR1, truncations of up to the first 44 amino acids of the N-terminus reduce the frequency of transitions to the long closed state, increasing the  $P_O$  (83–85). This effect increases with progressive truncations from  $\Delta$ N4 to  $\Delta$ N30, but increasing the truncation past this point does not appear to have additional effects.

Cukras *et al.* (87) conducted an alanine scan of positively charged residues in the N-terminus of Kir6.2. They identified two residues in the proximal 30 amino acids which reduced  $P_O$  when substituted (R4A, K5A) and two residues which increased  $P_O$  when substituted (R16A, R27A).

Application of a synthetic peptide which contains the first 33 amino acids of the N-terminus of Kir6.2 to full-length  $K_{ATP}$  channels decreases the frequency of transitions to the closed state, in a manner comparable to truncation of the N-terminus (86). This effect was dependent on the presence of SUR1, as with the N-terminal truncation experiments. This finding suggests that the synthetic peptide competes with the endogenous N-terminus of Kir6.2 for an interaction within the  $K_{ATP}$  channel complex.

Finally, Craig *et al.* (88) investigated an in-frame deletion of five amino acids (28 $\Delta$ 32) identified in neonatal diabetes patients. This deletion resulted in  $K_{ATP}$  channels with increased  $P_O$  only in the presence of SUR1; single Kir6.2 $\Delta$ C and Kir6.228 $\Delta$ 32, $\Delta$ C channel currents were indistinguishable. The authors then made use of the 1-195 and 1-288 truncated SUR1 constructs described by Babenko and Bryan (79), and determined that only when the L0 linker was present (i.e. SUR1 residues 1-288) was there a difference in intrinsic gating upon the 28 $\Delta$ 32 deletion.

Together, these results provide evidence for interactions between SUR1 and the N-terminus of Kir6.2 which facilitate transitions to the long closed state of the channel (79).

Of course, when measuring currents from hundreds or thousands of  $K_{ATP}$  channels, it is not possible to distinguish between perturbations which alter fast gating and perturbations which alter slow gating; the current measured reflects the sum of both of these processes. At a macroscopic level, anything which increases single

channel open time or burst duration, or decreases the intraburst closed time or frequency of entering the interburst state will be indistinguishable.

## 1.4 Ligand dependent regulation of the pancreatic K<sub>ATP</sub> channel

K<sub>ATP</sub> channels are regulated by two classes of endogenous ligands (nucleotides and phosphoinositides) and a range of exogenous ligands (predominantly sulphonylureas and glinides) (Figure 1.6). Thus far, the action of each of these ligands appears to exclusively affect the slow gating of channel (54). While the binding of adenine nucleotides to the Kir6.2 binding site leads to closure of the pore, binding of nucleotides to the NBSs of SUR1 in the presence of Mg<sup>2+</sup> activates the channel (89, 90). The interplay between the action of nucleotides at these distinct sites (Figure 1.4C) determines the response of the K<sub>ATP</sub> channel to metabolic changes, and therefore even subtle mutations or modifications to these sites can lead to diseases of insulin secretion. Phosphoinositides present in cell membranes are also regulators of K<sub>ATP</sub> function, a property which is shared amongst the Kir family of channels (9, 91, 92). PIP<sub>2</sub> stimulates the opening of K<sub>ATP</sub>, and excision of membrane patches results in a decline of channel activity due to the loss of PIP<sub>2</sub> in the excised membrane over time (93).

Proteins are inherently dynamic and sample a vast ensemble of accessible conformations (94). Techniques with high temporal resolution such as NMR spectroscopy have revealed the breadth of the energy landscape of macromolecules, and highlighted the ability of molecules at equilibrium to adopt a variety of conformational states (95). The K<sub>ATP</sub> channel is no exception. The ability of the channel to open and close in the absence of ligand (i.e. after channel rundown due to loss of PIP<sub>2</sub>) shows that at equilibrium, the K<sub>ATP</sub> channel is able to exchange between open and closed states, albeit with a much higher occupancy of closed states (93, 96). One mechanism by which ligands are proposed to regulate the equilibrium of K<sub>ATP</sub> channels (and macromolecules in general) is by being selective for particular conformations. For example, PIP<sub>2</sub> will exhibit a higher binding affinity for the open state of the channel

that it will for the closed state; and thus the presence of  $PIP_2$  will selectively stabilise the open state of  $K_{ATP}$  channels. This mechanism is the cornerstone of the MWC model of allostery (97–100), and its assumptions and implications will be discussed in more detail in 4. In this framework, the link between ligand binding and channel gating, sometimes called transduction, is the factor by which a ligand preferentially stabilises a particular conformation. Figure 1.6 is a simplified diagram of how ligands interact to regulate the  $K_{ATP}$  channel. Briefly,  $L$  describes the unliganded equilibrium between open and closed states, while ligands which bind with affinity constants  $K_X$  preferentially stabilise the open state by a factor  $D_X > 1$  or the closed state by a factor  $D_X < 1$  (where  $X$  is the general term for a particular ligand interaction).

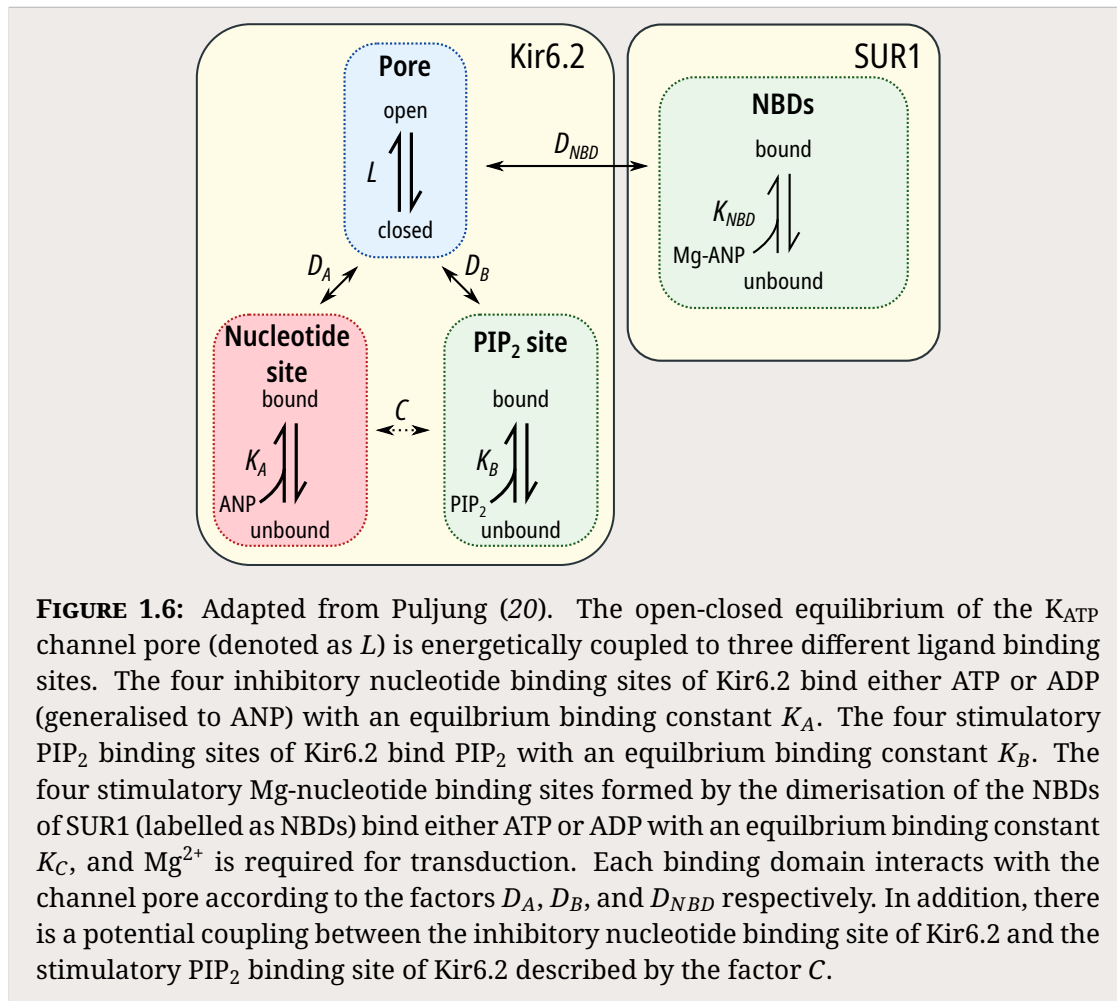


**FIGURE 1.6:** Adapted from Puljung (20). The open-closed equilibrium of the  $K_{ATP}$  channel pore (denoted as  $L$ ) is energetically coupled to three different ligand binding sites. The four inhibitory nucleotide binding sites of Kir6.2 bind either ATP or ADP (generalised to ANP) with an equilibrium binding constant  $K_A$ . The four stimulatory  $PIP_2$  binding sites of Kir6.2 bind  $PIP_2$  with an equilibrium binding constant  $K_B$ . The four stimulatory Mg-nucleotide binding sites formed by the dimerisation of the NBDs of SUR1 (labelled as NBDs) bind either ATP or ADP with an equilibrium binding constant  $K_C$ , and  $Mg^{2+}$  is required for transduction. Each binding domain interacts with the channel pore according to the factors  $D_A$ ,  $D_B$ , and  $D_{NBD}$  respectively. In addition, there is a potential coupling between the inhibitory nucleotide binding site of Kir6.2 and the stimulatory  $PIP_2$  binding site of Kir6.2 described by the factor  $C$ .

### 1.4.1 Nucleotide regulation of the pancreatic K<sub>ATP</sub> channel

The physiological regulation of channel activity by nucleotides is the summed contribution of activation by Mg-nucleotides binding to the NBSs of SUR1, and inhibition by nucleotides binding to Kir6.2 (101). To study these contributions experimentally, most research to date has relied on electrophysiological recordings of K<sub>ATP</sub> currents. Separating the contributions of the different classes of site has been achieved through a variety of methods. Firstly, activation of the channel by Mg-nucleotides can be eliminated by removing Mg<sup>2+</sup> ions from the solutions used to perfuse excised patches by inclusion of high concentrations of chelators such as EDTA or EGTA (102, 103). While it may still be possible that nucleotides bind to the NBDs in the absence of Mg<sup>2+</sup> ions and affect channel inhibition, it is widely assumed that the absence of Mg<sup>2+</sup> ions allows for the measurement of inhibition at Kir6.2 alone. Secondly, activation of the channel by Mg-nucleotides can be isolated by introducing mutations which abolish nucleotide binding to Kir6.2 (102, 103).

Mutation of residues which are involved in nucleotide inhibition of the K<sub>ATP</sub> channel can result in one of two functional effects. In the first category are residues which, when substituted, reduce the sensitivity of the channel to nucleotide inhibition (i.e. increase the IC<sub>50</sub> for nucleotide inhibition) while not perturbing the intrinsic gating of the channel. Mapping these residues to the cryo-EM structures of ATP-bound K<sub>ATP</sub> channels reveals that the residues in this category are invariably located close to the nucleotide binding site of Kir6.2. The binding site is composed of part of the N-terminal region of one Kir6.2 subunit, and part of the C-terminal region of its neighbouring subunit. Well characterised mutations of residues in this region of the N-terminus (e.g. R50 (87, 104–108), and G53 (71)) and the C-terminus (e.g. I182 (69, 109, 110), K185 (105–107), F333 (111), and G334 (69, 103, 111, 112)) have no effect on the single channel kinetics in the absence of nucleotide. However, they are far less sensitive to inhibition by nucleotides. The simplest hypothesis to explain this data given the location of the residues in the structures is that mutations of these residues perturb interactions between K<sub>ATP</sub> and nucleotides,

reducing the direct binding affinity of nucleotides for the inhibitory binding site (i.e. a reduction of  $K_A$  in Figure 1.6).

Alternatively, mutations which do not affect intrinsic gating but reduce sensitivity to nucleotide inhibition may be decreasing the efficacy of nucleotides, rather than the affinity, causing nucleotide binding to no longer be as strongly coupled to the pore (i.e.  $D_A$  approaches unity in Figure 1.6). R201 was hypothesised to form part of the binding site as a cysteine (70, 113) or histidine (114) substitution at this site results in reduced inhibition of  $K_{ATP}$  channels by nucleotides, without any changes in intrinsic gating. Curiously, an alanine at this position results in  $K_{ATP}$  channels which exhibit both reduced sensitivity to ATP inhibition and reduced activation by PIP<sub>2</sub> (115). Examining the cryo-EM structures suggests that this residue does not form direct contacts with bound ATP, and would therefore have to alter the nucleotide binding site allosterically - potentially by stabilising the short helix containing the critical F333 and G334 residues (20). John *et al.* (105) and Ribalet *et al.* (106) proposed that mutating R201 to an alanine instead acts by perturbing the preference of nucleotides for the closed state of the channel, increasing  $D_A$ .

The second category of residues are those which, when mutated, increase the  $P_O$  of the channel and also affect the sensitivity of the channel to nucleotide inhibition. This category is far larger, and these residues are found across both Kir6.2 and SUR1 structures. Within the MWC framework in Figure 1.6, mutations which increase  $L$  (and therefore increase the observed  $P_O$ ) reduce the ability of nucleotides to inhibit the channel. By increasing the stability of the open state, the selectivity of nucleotides for the closed state ( $D_A < 1$ ) results in a decreased probability of nucleotide binding, and thus reduces inhibition. Mutations within this category are difficult to fully characterise in the cell membrane environment due to the presence of phosphoinositides. An observed increase in  $P_O$  in an excised patch may either stem from an increase in  $L$ , or from an increase in  $K_B$  or  $D_B$ .

Activation of  $K_{ATP}$  channels by Mg-nucleotides is not quite as trivial to measure in isolation. The most common experimental paradigm used to isolate stimulatory

effects is introduction of a mutation into Kir6.2 which renders it insensitive to inhibition by nucleotides (102, 103). Application of Mg-nucleotides to mutant channels such as Kir6.2-G334D then results in an increase in the burst duration and therefore the  $P_O$  of  $K_{ATP}$  channels (103). This stimulatory effect is conferred by the NBSs of SUR1, as mutation of the Walker A motif in either NBS1 or NBS2 results in  $K_{ATP}$  channels which are no longer activated by Mg-nucleotides (101, 116).

In ABC transporters, the conformational changes which allow substrate movement across the membrane are driven by ATP hydrolysis (117). In addition, there is strict coupling between ATP hydrolysis and channel gating in CFTR, an ABC family member which is in itself a chloride channel (118). The NBDs of SUR are capable of hydrolysing ATP at rates comparable to that of CFTR (20, 30, 119), although by necessity these studies were carried out on purified channels or purified NBD fragments and may not reflect the physiological rate. Zingman *et al.* (120) used beryllium-fluoride and orthovanadate to stabilise the pre- and post-hydrolytic states of SUR2A respectively, and suggested that the post-hydrolytic state favoured channel opening.

However, Choi *et al.* (121) analysed the microscopic reversibility of single-channel kinetics to determine whether ATP hydrolysis is coupled to channel gating. Microscopic reversibility is a property of equilibrium systems such that their dynamics are time-reversible. As ATP hydrolysis is irreversible and thus not in equilibrium, if channel gating is dependent on ATP hydrolysis it will not obey microscopic reversibility (122). Unlike for CFTR (118), Choi *et al.* (121) found no evidence for ATP-dependent violations of microscopic reversibility in  $K_{ATP}$  channel gating, supporting the conclusion that ATP hydrolysis by the NBDs of SUR1 is not directly coupled to conformational changes of the channel. In addition, Mg-ADP is sufficient to activate channel currents, obviating the need for ATP hydrolysis (103). It is most likely that the activatory function of Mg-nucleotides occurs in a similar manner as for the inhibitory function of nucleotides; via an allosteric equilibrium effect on the channel pore ( $D_{NBD}$  in Figure 1.6). It remains unclear whether Mg-ATP is

capable of activating K<sub>ATP</sub> channel currents upon binding to SUR1, or whether it first needs to be hydrolysed to Mg-ADP.

### **1.4.2 PIP<sub>2</sub> regulation of the pancreatic K<sub>ATP</sub> channel**

A conserved feature of Kir channels is that they are regulated by phosphoinositides, in particular PIP<sub>2</sub>, and Kir6.2 is no exception (17, 18, 91, 92). Studying the nature of the regulation of K<sub>ATP</sub> by PIP<sub>2</sub> is difficult experimentally due to the lack of control over PIP<sub>2</sub> concentrations, and our inability to precisely measure them. Firstly, while the contaminating effects of intracellular nucleotides are removed by excision of a patch, the same is not true for PIP<sub>2</sub>. The rundown of channel currents is largely attributable to dissociation and/or degradation of PIP<sub>2</sub> from the membrane patch, but rundown is a complex phenomenon and the relative amounts of PIP<sub>2</sub> in the membrane varies between patches and experimental conditions (93). The hydrophobicity of PIP<sub>2</sub> means that perfusing a membrane patch with it results in accumulation of lipid in the membrane; it is impossible to reach an equilibrium with a known concentration. An alternative is using analogs of PIP<sub>2</sub> with increased solubility due to shortening of the acyl chain length, such as dioctanoyl (diC<sub>8</sub>) PIP<sub>2</sub> (123). While more soluble analogs are easier to work with and an experimenter can reach a quasi-equilibrium, we still do not know how the concentration of diC<sub>8</sub> PIP<sub>2</sub> applied to the membrane equates to the concentration achieved in the membrane; nor do we know if soluble analogs such as diC<sub>8</sub> PIP<sub>2</sub> modulate the channel in exactly the same manner as PIP<sub>2</sub>. Another alternative is using polyamines such as neomycin as negative charge chelators; screening the negatively-charged phospholipid head groups present in the membrane away from their normal binding sites (91, 124). This approach runs into the problems of both methods previously outlined; we do not know the precise correlation between the concentration of neomycin applied and the concentration of active, un-chelated PIP<sub>2</sub> in the membrane; and due to rundown it is impossible to reach a true equilibrium. It also remains possible that neomycin may have additional effects independent of PIP<sub>2</sub> screening.

Despite all these complexities, there is still a great deal of research exploring how PIP<sub>2</sub> regulates K<sub>ATP</sub> channel gating. Many researchers have shown that PIP<sub>2</sub> stimulates K<sub>ATP</sub> channel currents by increasing channel open time and burst duration, and reduces the sensitivity of K<sub>ATP</sub> channel currents to inhibition by nucleotides (17, 18, 125, 126). The stimulatory effect occurs in the absence of SUR1, as the  $P_O$  of Kir6.2ΔC or Kir6.2-cGFP expressed alone is still enhanced by perfusion of PIP<sub>2</sub> (125, 126). However, the presence of SUR1 appears to enhance the ability of PIP<sub>2</sub> to stimulate channel currents (17, 18, 125, 126). This enhancement has been proposed to occur through the interaction between the N-terminus of Kir6.2 and TMD0 of SUR1, and may account (at least in part) for the increase in 'intrinsic'  $P_O$  observed when Kir6.2 and SUR1 are coexpressed (21). Pratt *et al.* (21) introduced a mutation (E128K) into the TMD0 region of SUR1 and found that K<sub>ATP</sub> channels formed either with full-length mutant SUR1 or mutant TMD0 exhibited drastically reduced  $P_O$  when compared to their wild-type counterparts. In addition, the E128K mutation reduced the activation of channel currents by PIP<sub>2</sub>, and exposure to PIP<sub>2</sub> did not reduce the sensitivity of E128K channels to nucleotide inhibition. These findings highlight the complexity of the regulatory role of SUR1, and also the difficulty in separating effects on intrinsic channel gating from effects on PIP<sub>2</sub> regulation, given the difficulty in measuring and controlling the latter.

The second important functional aspect of PIP<sub>2</sub> modulation is its effects on the sensitivity of K<sub>ATP</sub> channels to nucleotide inhibition. Application of PIP<sub>2</sub> reduces the ability of nucleotides to inhibit K<sub>ATP</sub> channels, and reduction of PIP<sub>2</sub> activity from rundown or application of neomycin increases the ability of nucleotides to inhibit K<sub>ATP</sub> channels (17, 18, 125, 126). In addition, photoaffinity labelling of Kir6.2 by ATP analogs is reduced in the presence of phosphoinositides (127). This phenomenon can be explained by the allosteric effects of increasing channel  $P_O$ , which would result in a corresponding decrease in nucleotide binding and inhibition due to the energetic coupling of the nucleotide binding site and the channel pore ( $D_A$  in Figure 1.6) (54). However, it has also been hypothesised that there is an additional interaction between nucleotides and PIP<sub>2</sub> which is not mediated through energetic

coupling to the channel pore ( $C$  in Figure 1.6) (54, 125, 128, 129). This interaction could be due to direct competition between  $\text{PIP}_2$  and nucleotides for the same site, or by local allosteric interactions which energetically disfavour binding of one ligand when the other is already bound.

While the cryo-EM structures of  $\text{K}_{\text{ATP}}$  were not able to capture a  $\text{PIP}_2$ -bound state, there is a crystal structure of Kir2.2 complexed with  $\text{PIP}_2$  which suggests that the Kir6.2  $\text{PIP}_2$  binding site is not the same as the nucleotide binding site (130). This is supported by mutagenic electrophysiological studies, which show that substitutions at residues which alter nucleotide sensitivity but not  $P_O$  also do not affect activation of channel currents by  $\text{PIP}_2$  (with the notable exception of R201, which is discussed previously) (91, 115, 124, 129). This does not rule out the possibility of separate but overlapping sites for nucleotide and  $\text{PIP}_2$  binding, and whether nucleotides and  $\text{PIP}_2$  are able to simultaneously bind to the same subunit remains an open question (54, 131).

## **1.5 Fluorescence applications for ion channels**

Electrophysiological studies of ion channels allow recordings with high temporal resolution and exquisite sensitivity to protein energetics. However, while current recordings give detailed functional information even at a single protein level, it is difficult to reconcile function with structural "snapshots" obtained with X-ray crystallography or cryo-EM. Fluorescence techniques offer a window into the structural dynamics of ion channels in their native environments which can be correlated with functional data (16). The simultaneous measurements of current and fluorescence are often referred to as voltage-clamp fluorometry (VCF, when the electrophysiological configuration is two-electrode voltage clamp or cut-open oocyte clamp) or patch-clamp fluorometry (PCF, when the electrophysiological configuration is patch-clamp).

There are two main features of fluorophores which make them attractive for dynamic structural studies. Firstly, some fluorophores are sensitive to their local environments and can be used to detect movements of protein domains. For

example, Cha and Bezanilla (132) labelled residues in the S4 helix of Shaker K<sup>+</sup> channels with a variety of fluorophores to investigate the structural dynamics of the voltage-sensing domain (VSD) during channel gating. They labelled two residues (M356C and A359C) with tetramethylrhodamine (TMRM) and captured the fluorescence spectra of the labelled Shaker channel in cut-open oocytes at a series of different membrane potentials. TMRM exhibits a characteristic shift in the peak of its emission spectra according to the hydrophobicity of its environment, with a decrease in wavelength of 7 nm from solvation in methanol to solvation in isopropanol (132). Thus, when Cha and Bezanilla (132) observed a constant peak in the emission spectrum over a range of voltages, they were able to conclude that it was unlikely that the labelled residues move from a buried, purely hydrophobic environment to an external aqueous environment as the voltage changes.

The second feature is that fluorescence can be quenched, which occurs when the excited state of the fluorophore is dissipated through interaction with a different molecule (16). Quenching can be static, with the fluorophore and quencher forming a non-fluorescent pair, or quenching can be collisional, with the fluorophore transferring energy to the quencher upon the pair colliding with each other. Cha and Bezanilla (132) introduced potassium iodide (KI) into the extracellular solution as a collisional quencher to determine the accessibility of the labelled residues. Consistent with their spectral observations, the proportion of fluorescence quenched by KI did not change on depolarisation of the membrane, indicating that the residues were equally exposed to the iodide in the external solution at different voltages.

More commonly, quenchers are residues in the surrounding protein, with tryptophan being the strongest quencher followed by tyrosine (133, 134). Relative movements of fluorophore and quencher which result in overlap of the van der Waals radii of the pair result in quenching, the efficiency of which depends on the species of quencher and the nature of the fluorophore. Bimane and its derivatives are particularly sensitive to quenching by tryptophans (135), but are otherwise remarkably environmentally insensitive (136). Priest *et al.* (137) used the positively

charged bimane derivative monobromo(trimethylammonio)bimane (qBBr) to replace arginine residues in the S4 helix of Shaker K<sup>+</sup> channels. By substituting a cysteine for a native gating charge and then covalently attaching qBBr to this site, the authors produced a fluorescent analogue of a discrete charge in the voltage sensor of the channel. Voltage induced conformational changes of the fluorescent gating charge could then be detected by quenching from either a native tryptophan, or site-specific insertions of tryptophan.

### 1.5.1 Labelling techniques

The examples described above both used thiol-reactive fluorophores which can be covalently linked to cysteine residues in the protein of interest. Cysteine residues are relatively scarce in the extracellular domains of most transmembrane proteins, which enables the insertion of cysteines into extracellular loops of ion channels for labelling (132, 138–140). However, the relative abundance of cysteine residues on the intracellular side of proteins and the inaccessibility of many residues in transmembrane domains to solution restricts the wider applicability of this method. In addition, the presence of cysteines in other membrane proteins makes it difficult to eliminate background fluorescence from fluorophore conjugation to off-target proteins.

Genetically encoded fluorescent labels are an alternative to chemical conjugation which avoid the problems of off-target labelling. Initial fluorescence studies of ion channels used fluorescent proteins such as GFP (141), which are typically used to label the N- or C-termini of proteins (although there are exceptions (142, 143)). While fluorescent proteins are bright and photostable, their large size (Figure 1.7) results in limited utility for investigating subtle conformational dynamics.

An alternative to fluorescent proteins are fluorescent unnatural amino acids (UAAAs). UAAAs expand the available palette beyond the 20 naturally occurring amino acids and enable the site-specific insertion of more exotic side chains to explore protein function (16, 139, 140, 144, 145). One particularly hard-working fluorescent UAA is L-3-(6-acetylnaphthalen-2-ylamino)-2-aminopropionic acid (ANAP), which

was developed in the Schultz laboratory (146, 147). Kalstrup and Blunck (148) were the first to realise the potential of ANAP for the study of ion channels, incorporating ANAP into a number of strategically chosen locations in the Shaker K<sup>+</sup> channel to investigate its conformational dynamics. This work built on the previously described findings of Cha and Bezanilla (132) by labelling previously inaccessible residues in the lower part of the S4 helix and the intracellular loops of the channel. Since then, 32 primary research articles published (or pre-printed) as of March 2021 include the use of ANAP, and 21 of those are ion channel studies (145).

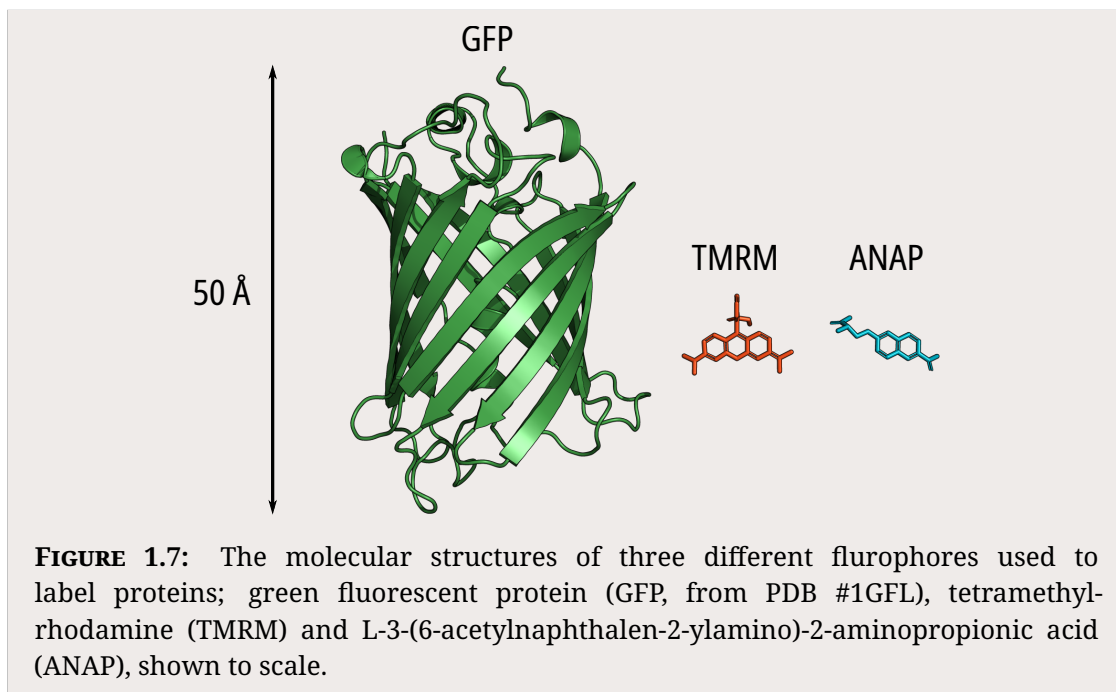


**FIGURE 1.7:** The molecular structures of three different fluorophores used to label proteins; green fluorescent protein (GFP, from PDB #1GFL), tetramethylrhodamine (TMRM) and L-3-(6-acetylnaphthalen-2-ylamino)-2-aminopropionic acid (ANAP), shown to scale.

Finally, ligands and toxins can be fluorescently labelled to investigate the ion channels they regulate (16, 140). A good illustration of this approach is the use of a fluorescent analogue of cAMP (fcAMP) to study hyperpolarisation-activated cyclic nucleotide-modulated (HCN) pacemaker channels, which are regulated by membrane voltage and the endogenous ligand cAMP. Binding of fcAMP to HCN channels in membrane patches leads to increased fluorescence at the membrane and activation of channel current, which can be measured simultaneously to correlate ligand binding to channel gating (149–151). The authors measured the increase

in fluorescence and channel current in response to step changes in cAMP to discriminate between possible models of HCN channel function, and found that their measurements were most consistent with asymmetric contributions of the four subunits of the channel (150). Curiously, conformational states of the channel appeared to be most stable with zero, two or four ligands bound, with the first and third binding steps exhibiting negative cooperativity.

While this series of studies illustrates the power of patch-clamp fluorometry, measuring the fluorescence intensity in membrane patches is not without its pitfalls. Firstly, the correlation between fluorescence intensity and ligand binding is not perfect. A necessary assumption is that at saturating fluorescence intensities, the binding sites are fully occupied. Secondly, careful controls are required to ensure that fluorescence increases are specific to ligand binding to the channel of interest. Kusch *et al.* (149) achieved this as described in a previous study (152), by including free fluorescent dye (DY647) in the bath solution, which allowed the authors to separate the specific bound fraction. Finally, this method is unsuitable for channels with more than one class of binding site for the fluorescent ligand, as it is not possible to assign an increase in fluorescence to ligand binding to one site over another.

# 2

## Methods

### Contents

---

2.1 Molecular biology . . . . .	27
2.2 Cell culture and channel expression . . . . .	28
2.3 Western blots . . . . .	29
2.4 Confocal microscopy . . . . .	30
2.5 Surface expression assays . . . . .	31
2.6 Epifluorescence imaging and spectroscopy . . . . .	32
2.7 Electrophysiology . . . . .	32
2.8 FRET calculations . . . . .	33
2.9 Unroofed binding measurements . . . . .	34
2.10 Patch-clamp fluorometry . . . . .	35
2.11 Bayesian data analysis . . . . .	36
2.12 Concentration response processing and presentation . . . . .	42
2.13 MWC model equations and fitting . . . . .	43
2.14 Computational docking . . . . .	44
2.15 Chemicals and stock solutions . . . . .	44

---

### 2.1 Molecular biology

Human Kir6.2 and SUR1 were subcloned into pcDNA4/TO and pCGFP\_EU vectors for expression of wild-type and GFP-tagged constructs, respectively. pcDNA4/TO and pANAP were obtained from Addgene. peRF1-E55D and pCGFP\_EU were kind gifts from the Chin Laboratory (MRC Laboratory of Molecular Biology, Cambridge, UK)

and the Gouaux Laboratory (Vollum Institute, Oregon, USA) respectively. Amber stop codons and point mutations were introduced using the QuikChange XL system (Stratagene; San Diego, CA). All constructs were confirmed by DNA sequencing (DNA Sequencing and Services, University of Dundee, Scotland).

## 2.2 Cell culture and channel expression

HEK-293T cells were obtained from and verified/tested for mycoplasma by LGC standards (ATTC CRL-3216, Middlesex, UK). Our working stock tested negative for mycoplasma contamination using the MycoAlert Mycoplasma Detection Kit (Lonza Bioscience; Burton on Trent, UK). Cells were plated onto either poly-L-lysine coated borosilicate glass coverslips (VWR International; Radnor, PA) or poly-D-lysine coated glass-bottomed FluoroDishes (FD35-PDL-100, World Precision Instruments). ANAP-tagged Kir6.2 constructs were labelled using amber stop codon suppression as described in reference (147). Transfections were carried out 24 hours after plating using TransIT-LT1 (Mirus Bio LLC; Madison, WI) at a ratio of 3 µl per µg of DNA. Unless specified otherwise, all transfections included a Kir6.2 construct with an amber stop codon (TAG) at position 311 (Kir6.2-W311<sup>TAG</sup>), SUR1, pANAP and eRF1-E55D in the ratio 0.5:1.5:1:1. Transfected cells cultured in Dulbecco's Modified Eagle Medium (Sigma; St. Louis, MO) + 10 % foetal bovine serum, 100 U ml<sup>-1</sup> penicillin and 100 µg ml<sup>-1</sup> streptomycin (Thermo Fisher Scientific; Waltham, MA) supplemented with 20 mM ANAP (free acid, AsisChem; Waltham, MA). Cells were incubated at 33 °C and in the presence of 300 µM tolbutamide to enhance protein expression and channel trafficking to the plasma membrane (34, 45). eRF1-E55D was included to increase efficiency of ANAP incorporation. Experiments were carried out 2-4 days after transfection. We also expressed constructs labelled with ANAP at positions I182, F183, F198, and I210. Kir6.2-F183\*, Kir6.2-F198\*, and Kir6.2-I210\* co-expressed with SUR1 did not produce sufficient currents for subsequent experimentation. Mutations at I182 are known to produce profound effects on nucleotide inhibition of K<sub>ATP</sub>. Thus, we did not consider this site for further experimentation.

## 2.3 Western blots

Transfected HEK-293T cells grown in 6-well plates were harvested in cold PBS (Life Technologies Limited; Paisley, UK), pelleted at 0.2 x g for 2.5 minutes and resuspended in lysis buffer containing 0.5 % Triton X-100, 100 mM potassium acetate, and a cOmplete protease inhibitor tablet (1 tablet/50 ml, Roche; Basel, Switzerland), buffered to pH 7.4. After a 30-minute benzonase (Sigma) treatment at room temperature, samples were mixed with a DTT containing reducing agent and loading buffer (NuPAGE, Invitrogen; Carlsbad, CA) and run on a precast Bis-Tris 4 % to 12 % poly-acrylamide gel at 200 V for 40 minutes. Proteins were wet transferred overnight onto polyvinylidene difluoride (PVDF) membranes (Immobilon P, Merck Millipore; Burlington, VT) in 25 mM Tris, 192 mM glycine, 20 % methanol, and 0.1 % SDS at 10 V on ice. Membranes were blocked with 5 % milk in TBS-Tw (150 mM NaCl, 0.05 % Tween 20, 25 mM Tris, pH 7.2) before staining for 30 minutes with a 1:1000 dilution of rat anti-HA monoclonal antibody in TBS-Tw (clone 3F10, Roche). After washing with TBS-Tw, membranes were incubated for 30 minutes with a 1:20,000 dilution of HRP-conjugated goat anti-rat polyclonal antibodies in TBS-Tw (Jackson ImmunoResearch; Ely, UK). Detection was performed using the SuperSignal West Pico Chemiluminescent Substrate (Thermo Fisher) and a C-DiGit Blot Scanner (Licor Biosciences; Lincoln, NE). Analysis was performed using custom code written in Python.

To confirm our ability to express full-length W311\*-GFP, we performed Western blots for HA-tagged Kir6.2 constructs in detergent-solubilized HEK-293T cells (Figure ??). The HA tag plus a short linker (YAYMEKGITDLAYPYDVPDY) was inserted in the extracellular region following helix M1 of Kir6.2 between L100 and A101. Transfection of WT-HA or WT-HA-GFP resulted in two bands on the Western blots. The upper bands were close to the expected sizes for full-length WT-HA and WT-HA-GFP (46 kDa and 77 kDa, respectively).

We consistently observed a lower molecular weight band as well. This band must correspond to an N-terminally truncated Kir6.2 product, as the apparent molecular weight shifted with addition of the C-terminal GFP tag. Based on the molecular

weight, we predict that the truncated protein product initiated from a start codon in the first transmembrane domain. Therefore, we believe it is unlikely that this protein would form functional channels or traffic to the plasma membrane. When W311\*-HA or W311\*-HA-GFP were co-transfected with SUR1, pANAP, and eRF1-E55D, and cells were cultured in the presence of ANAP, the Western blots were similar to wild-type Kir6.2-HA or Kir6.2-HA-GFP. Over 90 % full-length W311\*-HA-GFP was produced under these conditions. We were unable to quantify the percentage of full-length W311\*-HA produced as the C-terminally truncated band resulting from termination at the TAG codon was very similar in size to the N-terminally truncated band. Co-expression with SUR1 increased the percentage of full-length W311\*-HA-GFP produced. In the absence of ANAP, we did not observe any full-length Kir6.2, indicating that there was no read-through of the amber (TAG) stop codon.

## 2.4 Confocal microscopy

Confocal imaging was performed using a spinning-disk system (Ultra-VIEW VoX, PerkinElmer; Waltham, MA) mounted on an IX81 microscope (Olympus; Southend-on-Sea, UK) with a Plan Apo 60x oil immersion objective (NA = 1.4), provided by the Micron Advanced Bioimaging Unit, Oxford. Transfected HEK-293T cells were incubated for 15 minutes with 1 nM CellMask Deep Red (Thermo Fisher) to stain plasma membranes before washing with PBS and imaging. ANAP was excited with a solid-state laser at 405 nm. GFP and CellMask were excited with an argon laser at 488 nm and 633 nm respectively. Images were captured on an EMCCD camera (ImagEM; Hamamatsu Photonics; Welwyn Garden City, UK) binned at 2 x 2 pixels and analysed using Python. A median filter with a box size of 5 x 5 pixels was applied to improve the signal-to-noise ratio by reducing background fluorescence.

We examined the surface expression of our ANAP-labelled constructs using confocal microscopy. When Kir6.2-W311<sup>TAG</sup>-GFP was co-transfected with SUR1 along with pANAP and eRF1-E55D in the presence of ANAP, the ANAP and GFP fluorescence were co-localized at the plasma membrane. When wild-type Kir6.2-GFP was transfected under the same conditions, only GFP fluorescence was observed

at the plasma membrane. ANAP fluorescence was diffuse and confined to the cytoplasm or intracellular structures. Thus, the plasma-membrane ANAP signal was specific for W311\*-GFP.

## 2.5 Surface expression assays

We measured surface expression of HA-tagged Kir6.2 subunits using an approach outlined by Zerangue *et al.* (153). Cells were plated on 19 mm coverslips coated with poly-L-lysine and transfected as described above. Following incubation, cells were rinsed with PBS before fixation with 10 % formalin for 30 minutes at room temperature. After washing again, cells were blocked with 1 % BSA in PBS for 30 minutes at 4 °C before a 1-hour incubation at 4 °C with a 1:1000 dilution (in PBS) of rat anti-HA monoclonal antibodies. Cells were then washed 5 times on ice with 1 % BSA in PBS followed by a 30-minute incubation at 4 °C with a 1:2000 dilution of HRP-conjugated goat anti-rat polyclonal antibodies. Cells were washed 5 times in PBS + 1 % BSA and 4 times in PBS. Coverslips were removed from the culture dishes and placed in clean, untreated dishes for measurement. 300 µl of SuperSignal ELISA Femto Maximum Sensitivity Substrate (Thermo Fisher) was added to each sample and the luminescence was measured using a Glomax 20/20 Luminometer (Promega; Madison, WI) after a 10 second incubation.

HEK-293T cells were transfected with Kir6.2 constructs with or without a TAG stop codon corresponding to position 311. Cells were co-transfected with pANAP and eRF1-E55D in the presence or absence of SUR1 and cultured with or without ANAP. WT-HA and WT-HA-GFP in the presence of SUR1 were included as positive controls. Kir6.2 constructs with no HA tag served as negative controls. In the presence of ANAP, we observed strong trafficking of W311\*-HA-GFP to the plasma membrane, but much less trafficking of W311\*-HA (Figure 3.5A). When cells were cultured in the absence of ANAP, we observed little to no Kir6.2 surface expression from cells that were transfected with Kir6.2-W311<sup>TAG</sup>-HA or Kir6.2-W311<sup>TAG</sup>-HA-GFP, suggesting that prematurely truncated constructs did not traffic to the plasma membrane. In the absence of SUR1, surface expression was weak for both wild-type and tagged

constructs, despite the reported ability of Kir6.2 with a C-terminal GFP tag to traffic to the plasma membrane in the absence of SUR1 (36).

## **2.6 Epifluorescence imaging and spectroscopy**

Epifluorescence imaging and spectroscopy were performed using a Nikon Eclipse TE2000-U microscope with a 60x water immersion objective (Plan Apo VC, NA = 1.2, Nikon; Kingston upon Thames, UK) or a 100x oil immersion objective (Nikon, Apo TIRF, NA = 1.49). Imaging of ANAP was performed using a 385 nm LED source (ThorLabs; Newton, NJ) with a 390/18 nm band-pass excitation filter, an MD416 dichroic and a 479/40 nm band-pass emission filter (all from ThorLabs). GFP was imaged using a 490 nm LED source (ThorLabs) with a 480/40 nm band-pass excitation filter, a DM505 dichroic, and a 510 nm long-pass emission filter (all from Chroma; Bellows Falls, VT). Fluorescence spectra were collected by exciting ANAP as above but using a 400 nm long-pass emission filter (ThorLabs), then passing emitted light through an IsoPlane 160 Spectrometer (Princeton Instruments; Trenton, NJ) with a  $300\text{ g mm}^{-1}$  grating. Images were collected with 1 s exposures on a Pixis 400BR\_eXcelon CCD (Princeton Instruments).

## **2.7 Electrophysiology.**

Patch pipettes were pulled from thick-walled borosilicate glass capillaries (GC150F-15, Harvard Apparatus; Holliston, MA) to a resistance of  $1.5\text{ M}\Omega$  to  $2.5\text{ M}\Omega$  when filled with pipette solution. Currents were recorded at  $-60\text{ mV}$  from excised inside-out patches using an Axopatch 200B amplifier equipped with a Digidata 1322A digitizer and using pClamp 10 software (Molecular Devices; San Jose, CA). Currents were low-pass filtered at 5 kHz and digitized at 20 kHz. The bath solution (intracellular) contained 140 mM KCl, 10 mM HEPES, 1 mM EDTA and 1 mM EGTA (pH 7.3 with KOH). The pipette solution (extracellular) contained 140 mM KCl, 10 mM HEPES and 1 mM EDTA (pH 7.4 with KOH). All experiments were carried out in  $\text{Mg}^{2+}$ -free conditions. Currents were leak corrected using the current remaining in bath

solution containing 5 mM barium chloride at 60 mV, assuming a linear leak with a reversal potential of 0 mV. Inhibition was calculated and corrected for rundown by alternating test concentrations of nucleotide solution with nucleotide-free solution, and then expressing the test currents as a fraction of the average of the control currents before and after the test solution.

## 2.8 FRET calculations

We calculated the expected FRET efficiency between ANAP incorporated at amino acid position 311 and a docked TNP-ATP (fluorescent analogue of ATP) molecule. The efficiency of energy transfer is exquisitely distance-dependent, and can be calculated with the following formula:

$$E = \frac{1}{1 + \frac{R^6}{R_0^6}} \quad (2.1)$$

where  $R$  is the distance between donor and acceptor fluorophores and  $R_0$  is a characteristic distance at which 50 % of the energy is transferred. We calculated the  $R_0$  of the ANAP:TNP-ATP FRET pair using the following equations from Selvin (154):

$$R_0 = (8.79 \times 10^{-5} J q_D n^{-4} \kappa^2)^{1/6}$$

$$J = \frac{\int \epsilon_A(\lambda) f_D(\lambda) \lambda^4 d\lambda}{\int f_D(\lambda) d\lambda} \quad (2.2)$$

where  $J$  (in  $M^{-1} \text{cm}^{-1} \text{nm}^4$ ) is the normalised spectral overlap of the donor emission ( $f_D$ ) and acceptor extinction ( $\epsilon_A$ ),  $q_D$  is the quantum efficiency of the donor measured in the absence of the acceptor,  $n$  is the refractive index for the medium the experiment is performed in, and  $\kappa^2$  is a geometric factor related to the relative orientation of the two transition dipoles of donor and acceptor that can take values between 0 and 4.

For our purposes, we measured the overlap between donor emission measured from the averaged spectra from multiple unroofed membranes containing W311\* without the C-terminal GFP tag, and acceptor extinction spectra measured from TNP-ATP in solution using a Beckman Coulter DU800 spectrophotometer (Pasadena,

CA). We did not measure the  $q_D$  of ANAP ourselves, instead using the quantum yield of 0.22 measured by Zagotta *et al.* (155). As our experiments were performed in a water-based medium, we used the refractive index of water ( $n = 1.33$ ). We used a  $\kappa^2$  value of  $\frac{2}{3}$ , which is the case when the orientation of dipoles of donor and acceptor are able to rotate freely within the excited state donor lifetime.

The equivalency between FRET efficiency (measured as ANAP quenching) and nucleotide binding is based on two main assumptions. Firstly, we assume that the observed quenching from a bound nucleotide does not differ dramatically between open and closed states of the channel. As there is no open-state structure of K<sub>ATP</sub>, we do not know exactly how much relative movement would occur between a bound TNP-ATP and Kir6.2-W311. However, based on cryo-EM structures of apo and nucleotide-bound Kir6.2 we do not expect to see a change in the distance between these two positions. Secondly, we assume that the orientation of the ANAP and TNP-ATP dipoles can be well described by a  $\kappa^2$  value of  $\frac{2}{3}$ . This assumption is commonly made in FRET assays, and reference (156) shows that uncertainty introduced by this assumption is relatively small (typically less than 20 %). Empirically, our results showing FRET occurs to a similar extent as predicted by formula 2.1 supports this assumption as reasonable.

## 2.9 Unroofed binding measurements.

Unroofed membranes which have their intracellular surface exposed to the bath solution were prepared as follows. A coverslip plated with transfected HEK-293T cells was removed from the culture media and rinsed with PBS. The coverslip was then briefly sonicated using a probe sonicator (Vibra-cell; Newtown, CT) leaving behind adherent plasma membrane fragments. Cells cultured on FluoroDishes were rinsed and sonicated directly in the dish. Unroofed membrane fragments were nearly invisible in bright-field images and identified by the presence of GFP and ANAP fluorescence. Fluorescent TNP-nucleotides (Jena Bioscience; Jena, Germany) were diluted in bath solution and perfused onto unroofed membranes using a valve

controlled microvolume superfusion system ( $\mu$ Flow, ALA Scientific Instruments; Farmingdale, NY).

Fluorescence spectra were collected as described above. A region of interest corresponding to the membrane fragment was manually selected and line-averaged for each wavelength. A similarly sized region of background was selected and averaged, then subtracted from the spectrum of interest. After subtraction, ANAP intensity was calculated by averaging the fluorescence intensity measured between 469.5 nm and 474.5 nm. Concentration-response experiments were conducted by alternating perfusion of nucleotide-free solution and perfusion of test nucleotide solutions of different concentrations, allowing 60 s of equilibration time before capturing a fluorescence spectrum. Bleaching was corrected by fitting the normalised ANAP intensity of exposures taken during perfusion with nucleotide-free solution to a single exponential decay of the form

$$\frac{F}{F_{max}} = ae^{kt} + (1 - a) \quad (2.3)$$

then using the fit to correct the intensity of exposures taken during perfusion with test nucleotide solutions.

Some experiments were excluded from further analysis due to obvious cross-contamination between different solutions within the  $\mu$ Flow superfusion system. These were identified by noticeable colour changes in the solution in the delivery tubes.

## 2.10 Patch-clamp fluorometry.

The tip of the patch pipette was centred on the slit of the spectrometer immediately after patch excision. Currents were measured as described above. Fluorescence emission spectra from the excised patch were acquired concurrently with current measurements, both during test solution application as well as nucleotide-free solution. Background subtraction was slightly imperfect due to the exclusion of TNP-ATP from volume of the glass of the pipette, resulting in spectra that have negative intensities at the TNP-ATP peak at high nucleotide concentrations. However,

this over-subtraction does not affect the size of the ANAP peak, which we used to quantify nucleotide binding.

Some experiments were excluded from further analysis due to low fluorescence intensity, as we were concerned about a low signal to noise ratio influencing our results.

## 2.11 Bayesian data analysis

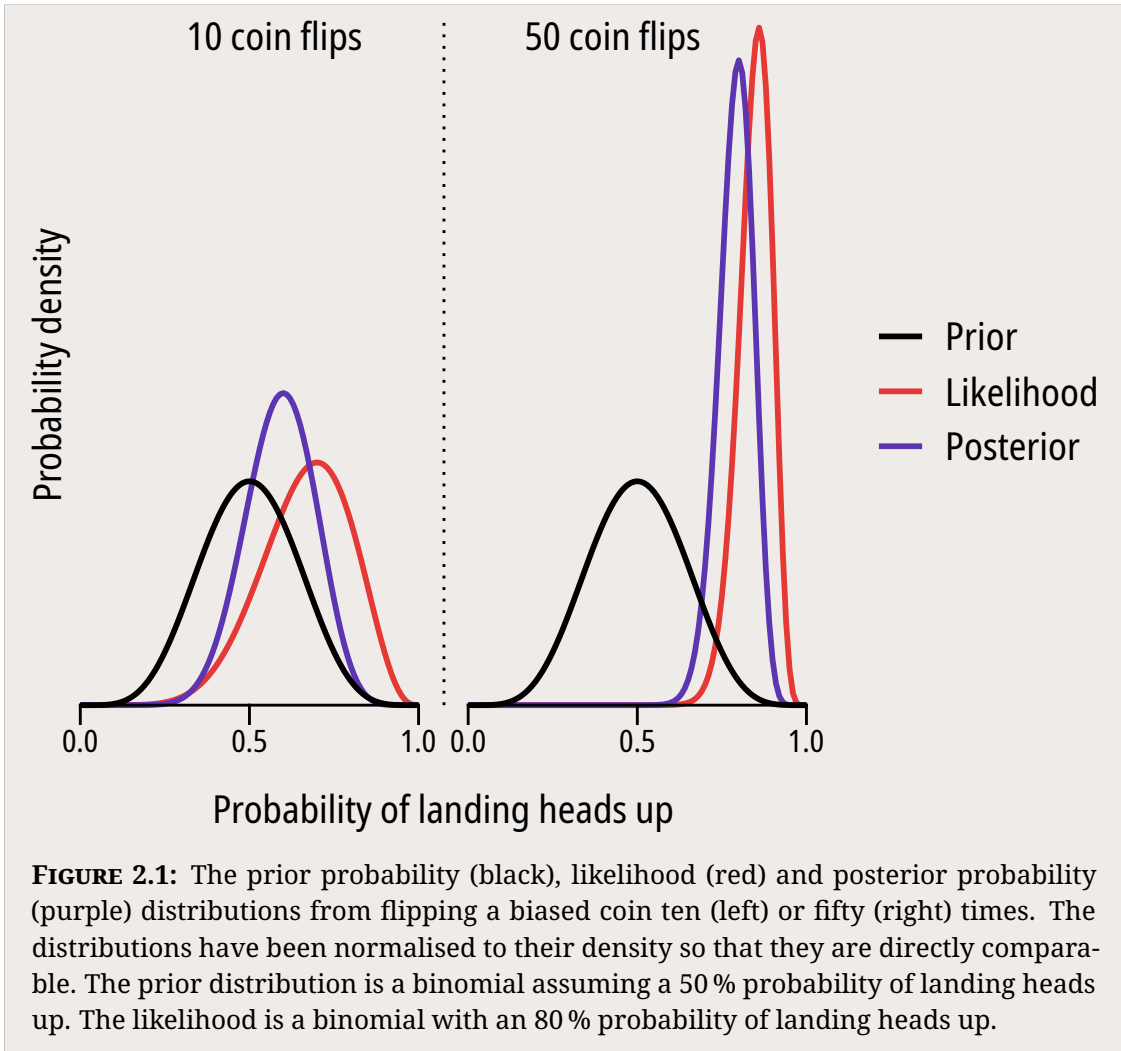
"Statistical evidence is part of the hot mess that is science, with all of its combat and egotism and mutual coercion." - McElreath (157). Bayesian data analysis is the process of fitting a probability model to a set of data, and summarising the result with a probability distribution of the parameters of the model (158). At its most basic level, Bayesian data analysis is no more than counting the numbers of ways the data could happen, according to our assumptions. The more ways in which something can happen, the more plausible it is (157). Frequentist statistical approaches (such as t-tests and ANOVAs) can be thought of as special cases of Bayesian data analysis, which requires all probabilities to be defined by connection to the frequencies of events in very large samples.

We can use Bayes' theorem to evaluate model  $m$  given our observed data  $d$  as follows:

$$P(m | d) = \frac{P(d | m) \cdot P(m)}{P(d)} \quad (2.4)$$

where

- $P(m)$  is the prior probability - how plausible is our model  $m$  before we collect any data?
- $P(m | d)$  is the posterior probability - in light of the data  $d$  we have collected, how plausible is our model  $m$ ?
- $P(d | m)$  is the likelihood - the probability of observing the data  $d$  if our model  $m$  describes the true underlying data generating process.



Building and fitting a Bayesian model to data involves setting a prior probability for each parameter included in the model, and then updating the posterior probability based on the likelihood of the collected data. What does this look like in practice?

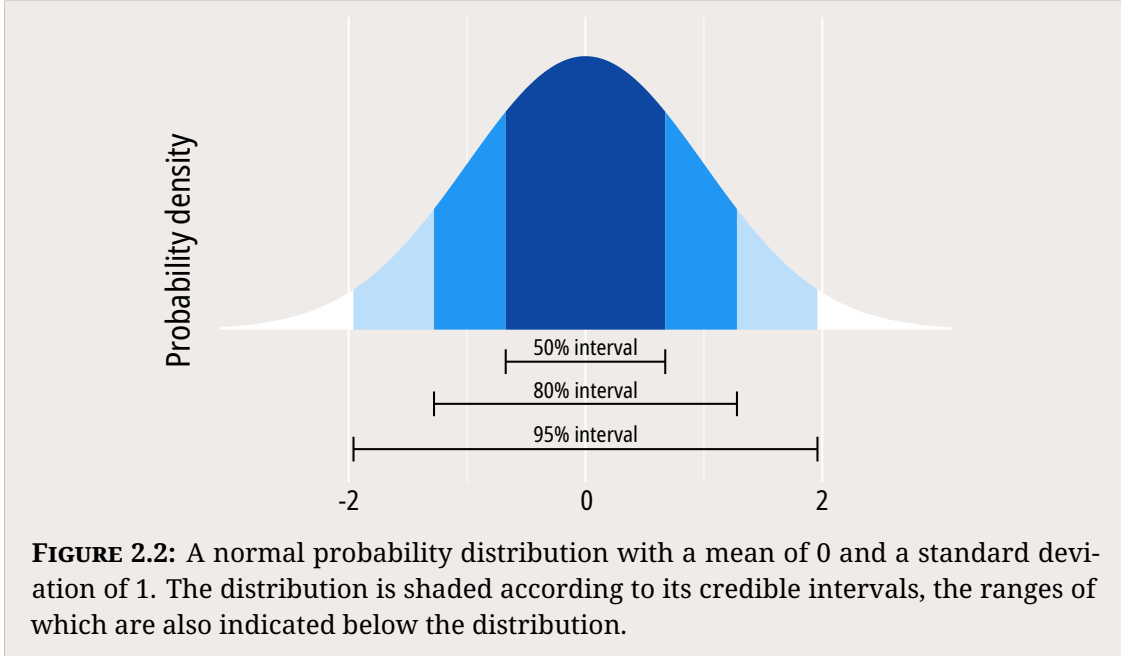
Imagine we have a coin, and we want to know if it is fair - that when we flip it, there is a 50 % chance that it will land heads up. Most coins are fair, which we can describe with a prior probability distribution which gives most weight to a 50 % chance of landing heads up (Figure 2.1, black line). After flipping our coin ten times, we find that it landed heads up eight times, giving rise to the likelihood shown in red. When we calculate our posterior probability distribution, which is proportional to the product of the prior and the likelihood, we see it falls midway between the prior and the likelihood (purple line). Why? Ten coin flips is not particularly strong

evidence, so even though our coin landed heads up eight times out of ten, there is still a good chance that the coin is fair - especially starting from the assumption that most coins are! However, if we flip the coin forty more times for a total of fifty coin flips, the likelihood begins to dominate our posterior probability distribution, pulling it away from the prior. It is now clear that this is not a fair coin; the 95<sup>th</sup> percentiles of our posterior probability distribution fall between a 65 % to 87 % chance of landing heads up. In actuality, the coin we have been flipping has an 80 % chance of landing heads up, well within our posterior probability distribution.

A lot of ink has been spilled on Bayesian methods and how they differ from frequentist approaches, but fundamentally they are more similar than they are different. In both approaches, the likelihood is the most important component of the analysis, and as samples sizes grow larger the likelihood becomes increasingly influential. However, they differ in two key ways. Firstly, instead of calculating a point estimate and a confidence interval, Bayesian analysis gives us the full probability distribution of our parameters of interest. Throughout this thesis, I have presented the full posterior probability distributions and expressed them in terms of their credible intervals (an example is given in Figure 2.2. The credible interval is intuitive - it is simply the range containing a particular percentage of probable values. For example, the 95 % credible interval is the central portion of the posterior distribution that contains 95 % of the values. We can say that given the observed data, the parameter we are estimating has a 95 % probability of falling within this range.

The second difference is the flexibility Bayesian analysis offers for incorporation of uncertainty from different sources, through a method known as multilevel or hierarchical modelling. Multilevel models seek to describe datasets which consist of clusters or groups of measurements that may differ from one another (157, 158). As opposed to fitting each group individually, multilevel models allow for 'pooling' of information between groups to give improved estimates and avoid averaging over experimental variability. Again, it is easiest to appreciate this with an example.

Imagine that instead of testing just one coin as in Figure 2.1, we are interested in the differences between batches of coins. Instead of just modelling the variability



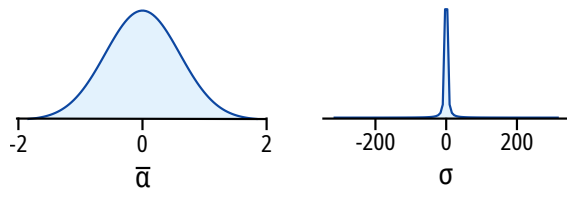
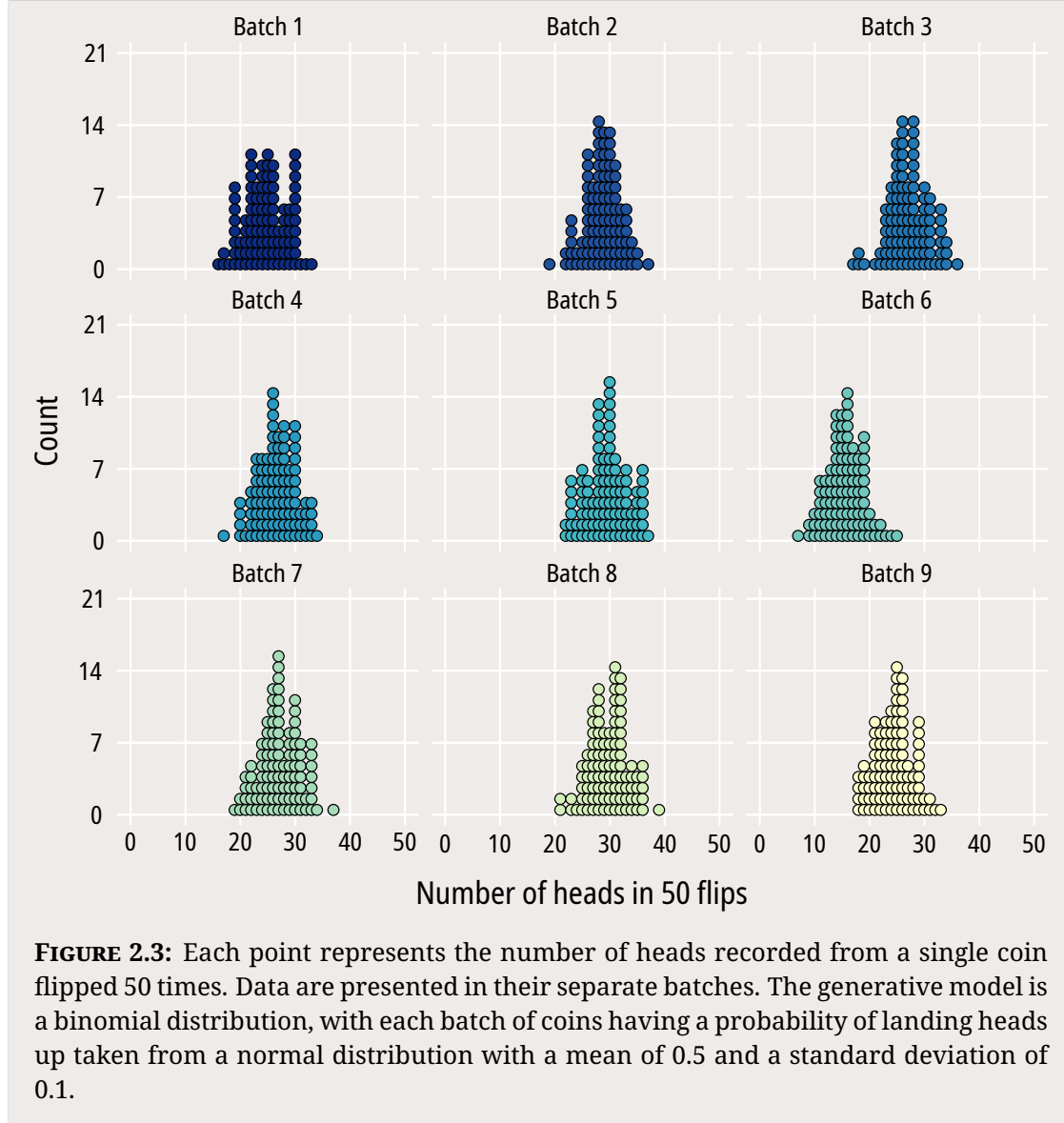
inherent in the coin flip, we now need to capture any additional variability from batch to batch. We collect our data by flipping 100 different coins from 9 separate batches 50 times each, recording the number of heads in Figure 2.3.

We could fit this dataset with a single or fixed-level model by estimating the probability of a coin landing heads up individually for each batch as below:

$$\begin{array}{ccc}
 \text{prior: } \alpha_j & \sim & \text{Normal}(0, 1) \\
 \text{likelihood: } nheads_i & \sim & \text{Binomial}(50, p_i) \\
 \text{logit transformation: } \text{logit}(\alpha_j) & = & \alpha_{batch[i]} \quad (2.5)
 \end{array}$$

where  $nheads_i$  is the number of times coin  $i$  lands heads up,  $\alpha_{batch[i]}$  is the unique log-odds for landing heads up for each batch of coins  $j$ , and  $\alpha_j$  is our prior. This would give us a separate posterior probability distribution for each batch, but would not be able to tell us anything about the global population of all nine batches. The logit transformation here converts the prior from real values to probabilities between zero and one.

Instead, in addition to estimating the probability separately for each batch, we can estimate a population parameter (across batches) and a parameter which corresponds to the variability between batches. We can do this with the multi-level model below:



$$\begin{aligned}
 nheads_i &\sim \text{Binomial}(50, p_i) \\
 \text{logit}(p_i) &= \alpha_{batch[i]} \\
 \alpha_j &\sim \text{Normal}(\bar{\alpha}, \sigma) \\
 \bar{\alpha} &\sim \text{Normal}(0, 1) \\
 \sigma &\sim \text{Cauchy}(0, 1)
 \end{aligned} \tag{2.6}$$

where  $\alpha_j$  is again our prior probability, but this time it has two separate parameters: one for the population average probability of landing heads up  $\bar{\alpha}$ , and one for the standard deviation of that probability between batches  $\sigma$ .

Fitting this model to the data in Figure 2.3, we can see that while the overall

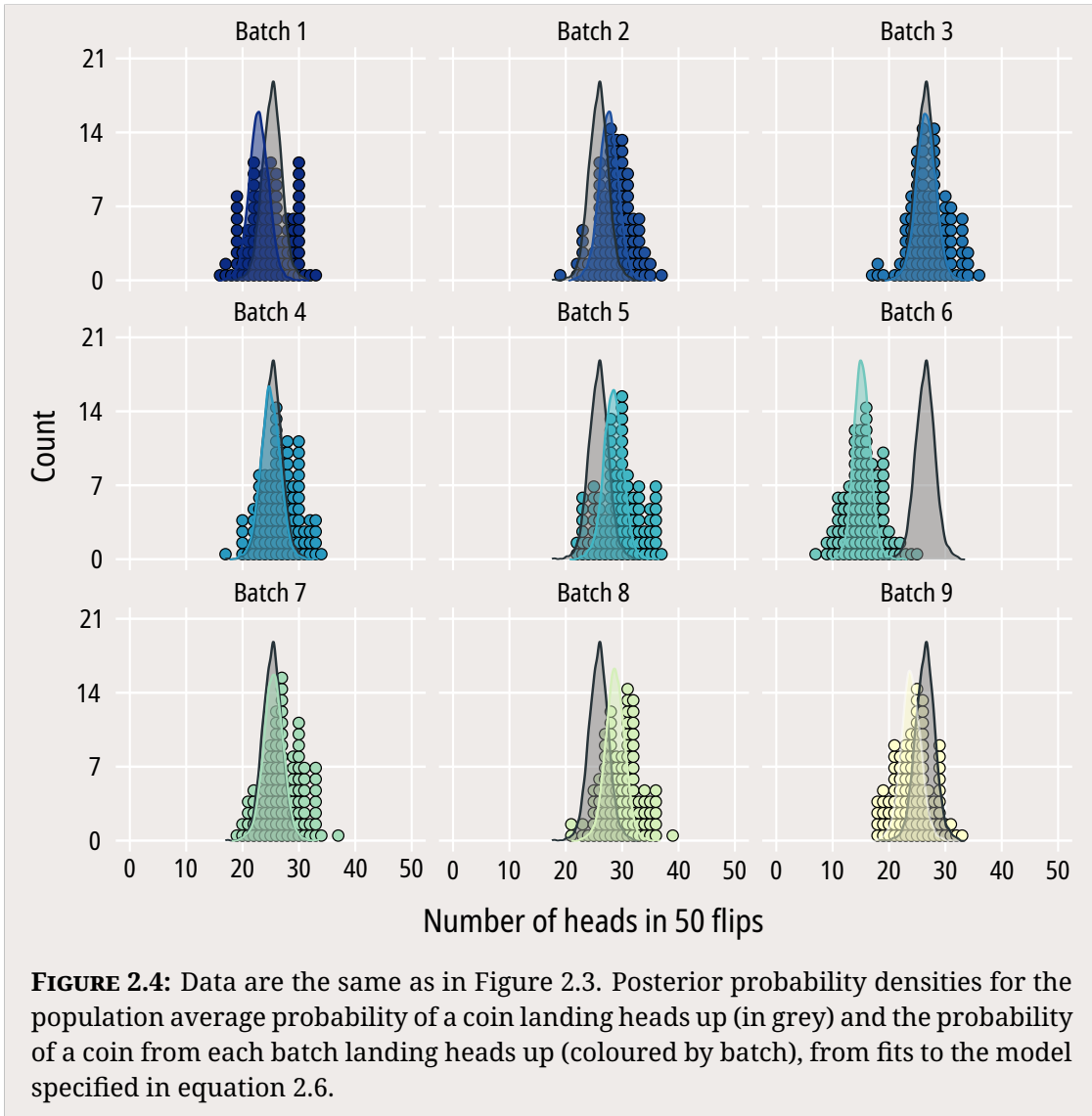


**FIGURE 2.4:** Data are the same as in Figure 2.3. Posterior probability densities for the population average probability of a coin landing heads up (in grey) and the probability of a coin from each batch landing heads up (coloured by batch), from fits to the model specified in equation 2.6.

population average probability of a coin landing heads up when we flip it is very close to 50 %, there is between group variability which we are able to capture using a multilevel model. For a more detailed - and eloquent - overview of Bayesian data analysis and multilevel modelling, Chapter 1 of McElreath (157) is an excellent introduction.

## 2.12 Concentration response processing and presentation

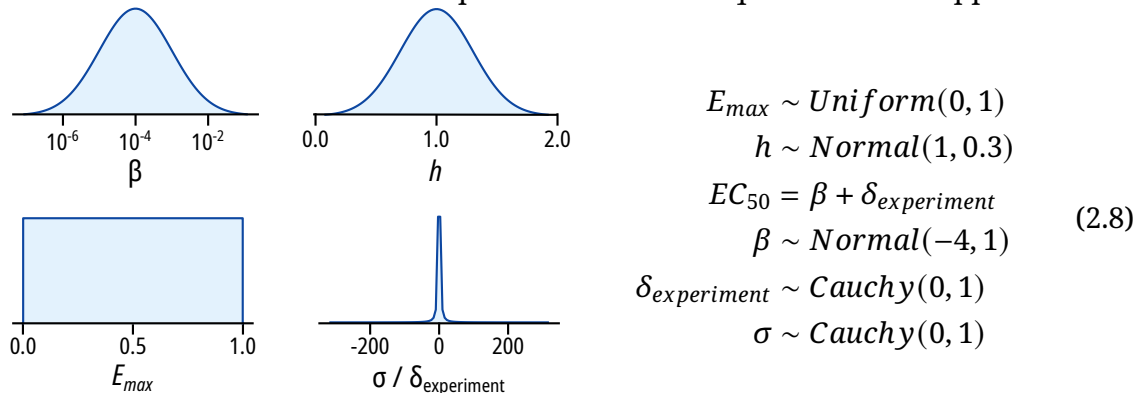
Raw spectrographic images and current traces were pre-processed in Python and Clampfit (Axon) before analysis with R. Where applicable, all experimental data points are displayed in each figure. To help visualise uncertainty and prevent some data points being hidden, they are arranged with a small amount of horizontal jitter; the vertical position remains unaffected.

We fit our fluorescence quenching data with the following equation:

$$\frac{y}{y_{max}} = 1 - E_{max} + \frac{E_{max}}{1 + 10^{(EC_{50}-[TNPATP]) \cdot h}} + \sigma \quad (2.7)$$

where  $y$  represents corrected fluorescence intensity,  $EC_{50}$  and  $[TNPATP]$  are  $\log_{10}$  values, and  $\sigma$  is the remaining variance. For the fluorescence quenching data,  $E_{max}$  was fixed to the value obtained from W311\*-GFP+SUR1 unroofed experiments (0.1) as explained in more detail in chapter 4. Current inhibition data were fit to the same equation but with  $y$  representing normalised current magnitude,  $IC_{50}$  instead of  $EC_{50}$ , and  $I_{max}$  instead of  $E_{max}$ .

We used the brms package in R to perform a non-linear fit to equation 2.7 reformulated as a multilevel model. The parameters in the equation were supplied as:



In this case, each group of measurements is the set of current inhibition or fluorescence quenching values obtained from a single excised patch or unroofed membrane. Essentially, the  $EC_{50}$  (or  $IC_{50}$ ) parameter for each concentration-response experiment can be described as the combination of a population parameter that is an estimate of the construct-specific value ( $\beta$ ), and an additional 'random' component that varies between experiments on the same construct ( $\delta_{experiment}$ ).

## 2.13 MWC model equations and fitting

The concerted MWC-type model fitted to the patch-clamp fluorometry data was formulated as follows:

$$\frac{F}{F_{max}} = \frac{K_A[TNPATP](1 + K_A[TNPATP])^3 + LD_AK_A[TNPATP](1 + D_AK_A[TNPATP])^3}{(1 + K_A[TNPATP])^4 + L(1 + D_AK_A[TNPATP])^4} + \sigma \quad (2.9)$$

$$\frac{\text{open channels}}{\text{total channels}} = \frac{L(1 + D_AK_A[TNPATP])^4}{(1 + K_A[TNPATP])^4 + L(1 + D_AK_A[TNPATP])^4} + \sigma \quad (2.10)$$

When no ligand is present (i.e. when  $[TNPATP] = 0$ ), equation 2.10 becomes:

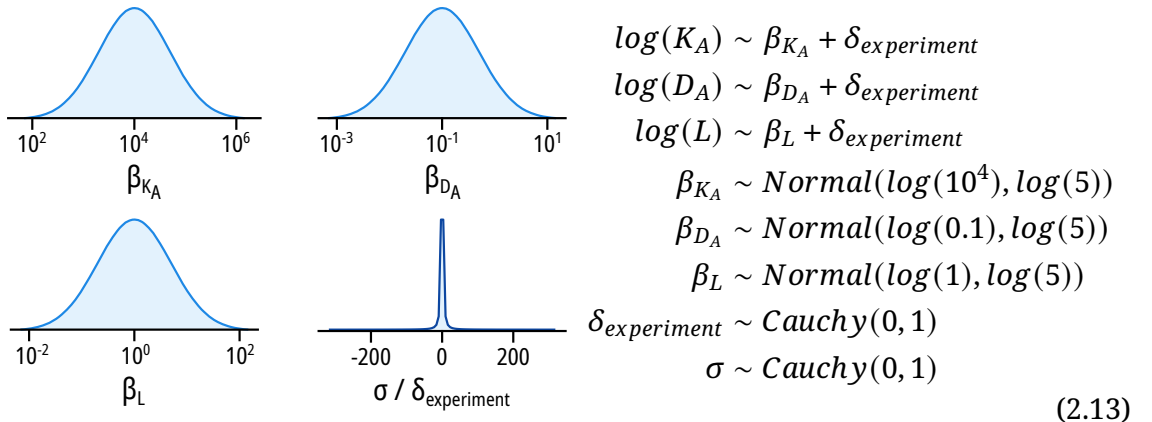
$$\frac{\text{open channels}}{\text{total channels}} = \frac{L}{1 + L} + \sigma \quad (2.11)$$

We can use this to normalise the predicted changes in the open fraction to an observed change in current:

$$\frac{I}{I_{max}} = \frac{L(1 + D_AK_A[TNPATP])^4}{(1 + K_A[TNPATP])^4 + L(1 + D_AK_A[TNPATP])^4} \cdot \frac{1 + L}{L} + \sigma \quad (2.12)$$

We used the brms package in R to fit a multilevel model to equations 2.9 and 2.12. First, we normalised the fluorescence quenching data by the  $E_{max}$  determined from W311\*-GFP+SUR1 unroofed experiments (0.1). We then corrected it by transforming each data point as  $\log_2(\frac{F}{F_{max}+1})$  as described in more detail in Chapter 3.

The parameters in the equation were supplied as:



Each of the three parameters was modelled as a combination of a population parameter  $\beta_x$  and an additional random component  $\delta_{\text{experiment}}$ . Each combined

set of current inhibition and nucleotide binding measurements from one excised patch was grouped as one experiment. The remaining variance  $\sigma$  was allowed to vary between fluorescence and current data.

The alternate single-binding model was formulated as follows:

$$\frac{F}{F_{max}} = \frac{LD_A K_A [TNPATP] (1 + 3K_A [TNPATP] + 3K_A^2 [TNPATP]^2 + K_A^3 [TNPATP]^3) + K_A [TNPATP] (1 + K_A [TNPATP])^3}{L(1 + 4D_A K_A [TNPATP] + 6D_A K_A^2 [TNPATP]^2 + 4D_A K_A^3 [TNPATP]^3 + D_A K_A^4 [TNPATP]^4) + (1 + K_A [TNPATP])^4} \quad (2.14)$$

$$\frac{I}{I_{max}} = \frac{L(1 + 4D_A K_A [TNPATP] + 6D_A K_A^2 [TNPATP]^2 + 4D_A K_A^3 [TNPATP]^3 + D_A K_A^4 [TNPATP]^4)}{L(1 + 4D_A K_A [TNPATP] + 6D_A K_A^2 [TNPATP]^2 + 4D_A K_A^3 [TNPATP]^3 + D_A K_A^4 [TNPATP]^4) + (1 + K_A [TNPATP])^4} \cdot \frac{1 + L}{L} \quad (2.15)$$

The extra length of these formulas when compared to equations 2.9 and 2.12 do not represent any additional complexity; just an unfortunate consequence of the lack of exponents of  $D_A$  which make it impossible to simplify further. Parameters were supplied and fitted as in equation 2.13.

## 2.14 Computational docking.

Computational docking of TNP-ATP into the nucleotide binding site of Kir6.2 was performed using AutoDock-Vina and Pymol (Schrödinger, LLC; New York, NY). 11 TNP-ATP structures from the Protein Data Bank (PDB accession #s 1I5D, 3AR7, 5NCQ, 5SVQ, 5XW6, 2GVD, 5A3S, 2PMK, and 3B5J) were used as starting poses and a 15x11.25x15 Å box was centred on the ATP bound to Kir6.2 in PDB accession #6BAA. Protonation states for each residue were assigned using PDB2PQR and PROPKA 3.0. The modal highest-scoring pose from the docking run was selected (PDB accession #5XW6) and distances were measured from a pseudo atom at the centre of the fluorescent moiety. TNP-ATP (PDB #3AR7) was positioned into the first nucleotide binding site of SUR1 (PDB #6PZI) using the alignment tool in Pymol.

## 2.15 Chemicals and stock solutions.

Unless otherwise noted, all chemicals were obtained from Sigma. TNP-ATP was obtained as a 10 mM aqueous stock from Jena Bioscience and stored at -20 °C. 1 mM aqueous stocks of ANAP-TFA were prepared by dissolving the free acid in 30 mM

NaOH, and were stored at –20 °C. Tolbutamide stocks (50 mM) were prepared in 100 mM KOH and stored at –20 °C.



# 3

## Measuring nucleotide binding to K<sub>ATP</sub>

### Contents

---

<b>3.1 Designing a nucleotide binding assay . . . . .</b>	<b>47</b>
3.1.1 Criteria for a useful assay for nucleotide binding to Kir6.2 . . . . .	47
3.1.2 Choosing a site to incorporate ANAP . . . . .	50
<b>3.2 Incorporating ANAP into the Kir6.2 binding site . . . . .</b>	<b>53</b>
3.2.1 The Amber stop codon expression system . . . . .	53
3.2.2 ANAP incorporation into Amber stop codon containing constructs . . . . .	55
<b>3.3 Testing for functional membrane expression . . . . .</b>	<b>56</b>
3.3.1 Surface expression of HA-epitope labelled Kir6.2 constructs . . . . .	56
3.3.2 Electrophysiology of Kir6.2 constructs . . . . .	58
3.3.3 Unroofed membrane binding assay of Kir6.2 constructs . . . . .	58
3.3.4 Patch-clamp fluorometry of Kir6.2 constructs . . . . .	61
<b>3.4 Discussion . . . . .</b>	<b>62</b>

---

### 3.1 Designing a nucleotide binding assay

#### 3.1.1 Criteria for a useful assay for nucleotide binding to Kir6.2

Previous approaches to measuring nucleotide binding directly to the different binding sites of K<sub>ATP</sub> have relied on isolating binding to individual classes of site by disrupting protein function; either by introducing mutations which abolish binding to a particular site, by measuring binding to Kir6.2 or SUR1 alone, or by measuring

binding to fragments of the two subunits.

Two key studies have attempted to measure nucleotide binding to the inhibitory site on Kir6.2 directly. The first relied on photoaffinity labelling of Kir6.2 by the radionucleotide 8-azido-[ $\gamma$ -<sup>32</sup>P]-ATP (159). In these experiments, Kir6.2 with an N-terminal FLAG-tag was expressed in COS-7 cells, and membranes were separated by centrifugation. After incubating the membrane fractions with 8-azido-[ $\gamma$ -<sup>32</sup>P]-ATP, application of UV light results in a covalent linkage between the bound 8-azido-[ $\gamma$ -<sup>32</sup>P]-ATP and Kir6.2. After separation of the membrane fraction proteins on a gel, the quantity of bound radionucleotide can then be quantified by counting the radioactivity of the band corresponding to Kir6.2. These experiments were able to definitively establish that the inhibitory nucleotide binding site of K<sub>ATP</sub> was on Kir6.2, and suggested that the Kir6.2 binding site possessed a lower affinity toward the radionucleotide than the SUR1 binding sites.

The second made use of a fluorescent congener for ATP, trinitrophenyl (TNP)-ATP. TNP-ATP has previously been used in binding measurements of purified proteins due to its increased quantum yield (and thus increase in observed fluorescence) upon binding (160, 161). TNP-ATP is most commonly used as an antagonist of P2X receptors, which are regulated by extracellular ATP. The authors measured binding of TNP-ATP to the purified carboxyl terminal of Kir6.2 (residues 169 to 354) solubilised by linking it to mannose binding protein (MBP) (162). The increased fluorescence of TNP-ATP when bound to the Kir6.2-MBP construct could be measured in a spectrometer, and allowed for equilibrium measurements of nucleotide binding. These experiments were able to establish an initial estimate for the binding affinity of the Kir6.2 site for TNP-ATP at 5  $\mu$ M. These findings were replicated in a similar study, which used fusion proteins constructed from residues 170 to 390 of Kir6.2 fused to glutathione-S-transferase (GST) and estimated a binding affinity of 5  $\mu$ M (163).

These studies were hampered by the need to isolate the Kir6.2 binding site from the two SUR1 binding sites, which leads to unphysiological experimental conditions. To improve on these methods, an ideal assay measuring nucleotide binding to the K<sub>ATP</sub> channel needs to fulfill a number of criteria.

1. We need sufficient spatial sensitivity to distinguish between different classes of binding site; i.e. the assay should be capable of distinguishing binding to Kir6.2 from binding to NBS1 or NBS2 of SUR.
2. We should be able to measure binding to a channel which we know is functional, so our experimental conditions cannot be drastically different from those used to measure channel function.
3. There should be minimal perturbation of the channel in order for binding measurements to be physiologically relevant.
4. For accurate measures of affinity, binding should be at equilibrium so we cannot use covalent interactions or other forms of non-equilibrium labelling.
5. We should be able to achieve a higher temporal resolution.

To fulfill these criteria, we used an approach involving a fluorescent unnatural amino acid, ANAP. ANAP has been used increasing widely in the study of ion channel structure and function due to several desirable qualities.

1. It is smaller than traditional fluorescent labels such as fluorescent proteins or rhodamine derivatives. Therefore, it should be less perturbing to the function of the protein it labels.
2. As it is an amino acid, it can be site-specifically inserted into any protein. This avoids the issues of other small chemical dyes which are targeted to a site via post-translational covalent modifications, typically by reacting with a cysteine residue. While this can be avoided in some proteins by mutating each cysteine residue to an alternative residue to avoid off-target labelling, there are functionally important cysteines in the  $K_{ATP}$  channel which cannot be mutated. In addition, this does not solve the problem of off-target labelling of other membrane proteins

3. ANAP is environmentally sensitive, which has been used to great effect in other studies. Notably, the peak emission ranges from ~450nm to ~490nm depending on the hydrophobicity of the surrounding environment.

Initially, we hoped that the environmental sensitivity of ANAP fluorescence might be sufficient for the peak of the emission spectrum of an ANAP residue inserted into an ATP binding site to measureably change when ATP was bound. Unfortunately, when we introduced ANAP directly into the Kir6.2 binding site in place of residues I182 or F183 we were not able to observe any functional  $K_{ATP}$  channels at the cell membrane.

Instead, we turned to Förster resonance energy transfer (FRET) as a reporter for ATP binding. As ATP itself is not fluorescent, and has no intrinsic fluorescence quenching, we turned to TNP-ATP (Figure 3.1A). TNP-ATP is an excellent FRET partner of ANAP, as evidenced by the good overlap in the TNP emission spectra and the ANAP extinction spectra (Figure 3.1B). This leads to a theoretical distance-dependency of FRET which is most sensitive between 20 Å to 60 Å (Figure 3.1C) with a calculated R<sub>0</sub> of 38.4 Å.

### **3.1.2 Choosing a site to incorporate ANAP**

The theoretical R<sub>0</sub> of 38.4 Å for FRET between ANAP and TNP-ATP allowed for flexibility when choosing a site to incorporate ANAP. Ideally, a residue should be chosen to maximise the following aims:

1. The incorporated ANAP needs to be close enough to the nucleotide binding site of interest to report a quantifiable change in FRET when TNP-ATP is bound. This would not have to be close enough for 100 % FRET to occur, but the greater the efficiency achieved the higher the signal-to-noise ratio would be for measuring binding.
2. It also needs to be far enough from each other class of nucleotide binding site to avoid quenching by TNP-ATP bound to other sites.

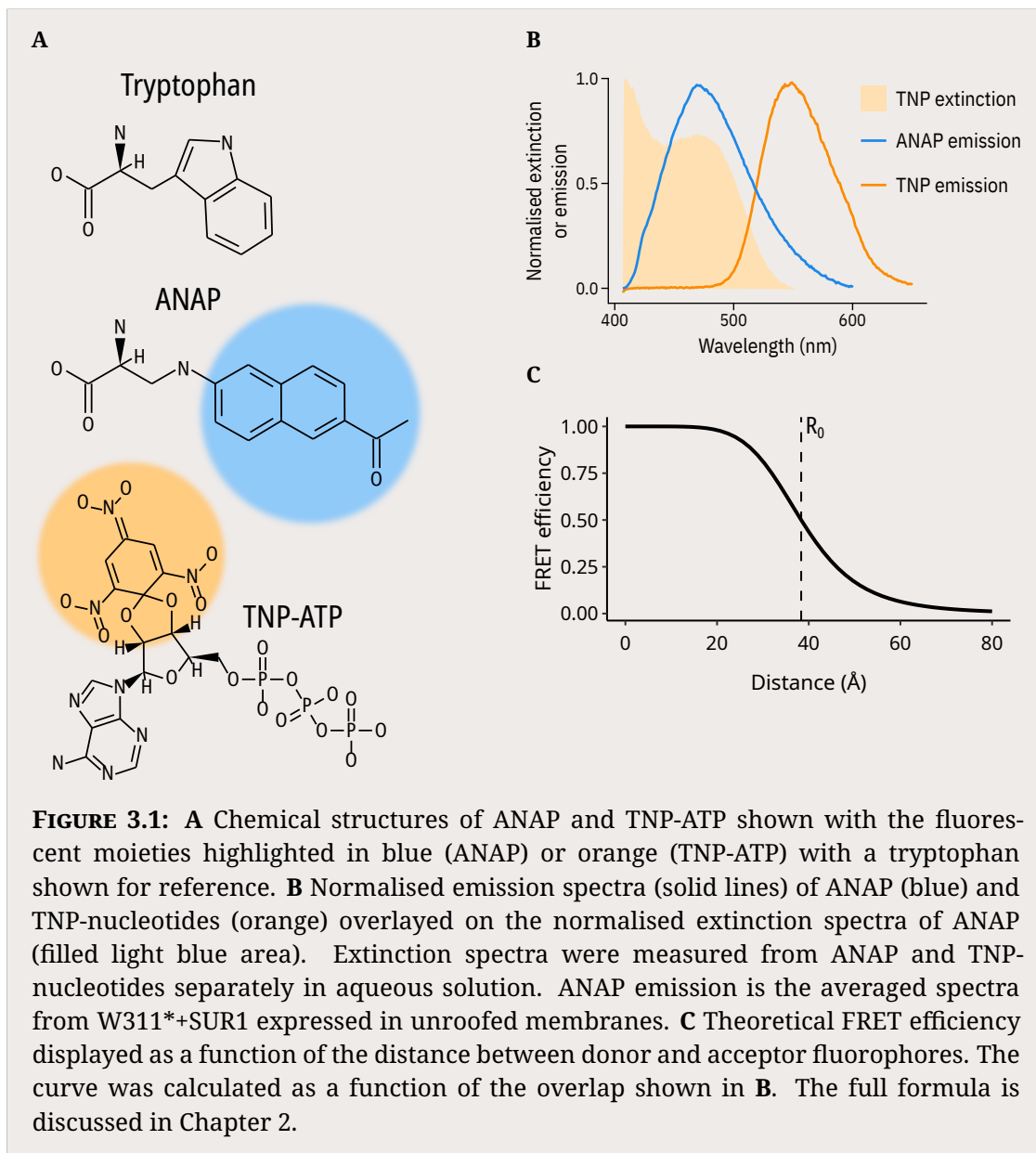


**FIGURE 3.1:** A Chemical structures of ANAP and TNP-ATP shown with the fluorescent moieties highlighted in blue (ANAP) or orange (TNP-ATP) with a tryptophan shown for reference. B Normalised emission spectra (solid lines) of ANAP (blue) and TNP-nucleotides (orange) overlayed on the normalised extinction spectra of ANAP (filled light blue area). Extinction spectra were measured from ANAP and TNP-nucleotides separately in aqueous solution. ANAP emission is the averaged spectra from W311<sup>\*</sup>+SUR1 expressed in unroofed membranes. C Theoretical FRET efficiency displayed as a function of the distance between donor and acceptor fluorophores. The curve was calculated as a function of the overlap shown in B. The full formula is discussed in Chapter 2.

3. In addition to avoiding interference from other classes of binding site, we also need to avoid cross-talk between nucleotide binding sites of the same class on different subunits, as this would lead to difficulty interpreting the measured quenching. The ideal theoretical solution would be labelling only one nucleotide binding site per ion channel, but without using a concatemer this is not so easy in practice.
4. More practically, incorporation of ANAP should not lead to drastic changes

in nucleotide binding or channel gating properties, and the complete K<sub>ATP</sub> channel needs to be expressed on the cell surface membrane.

To narrow down which residues could be candidates for ANAP incorporation to measure binding at Kir6.2, we took three cryo-EM structures of K<sub>ATP</sub> with ATP bound and computationally docked TNP-ATP into the nucleotide binding pocket (Figure 3.2). To assess the validity of computationally docking a ligand to each structure, we first attempted to dock ATP into the inhibitory binding pocket of Kir6.2 to check that the highest-scoring binding poses were similar to those observed in the cryo-EM structures. Docking ATP to both #6C3P and #6C3O yielded binding poses which were very similar to the pose found in the cryo-EM structures (Figures 3.2B, 3.2C). However, docking ATP to #6BAA resulted in binding poses which were in a flipped orientation relative to the pose found in the cryo-EM structure (Figure 3.2A).

We then took TNP-nucleotide structures from eleven different X-ray diffraction and cryo-EM structures published on RCSB to dock to the Kir6.2 binding site of K<sub>ATP</sub>. For both #6BAA and #6C3P we observed that the three highest scoring binding poses for TNP-nucleotides closely resemble those of the ATP solved in complex with the channel (Figures 3.2A, 3.2B). It is not so clear for #6C3O, for which the highest scoring poses are not in agreement with each other or the solved structure of ATP.

Based on the predicted TNP-ATP poses for #6BAA and #6C3P, we could narrow down potential ANAP incorporation sites to within 25 Å of the centre of the TNP-moiety, at which distance we would expect to see over 90 % FRET efficiency when TNP-ATP is bound to Kir6.2. In addition, we excluded residues which fell within 45 Å of NBS1 or NBS2, as this restricts the potential FRET between TNP-ATP bound at these sites and our chosen residue to roughly 25 % or less. While we can exclude residues which fall too close to the NBS's of SUR1, the close proximity of the Kir6.2 nucleotide binding sites to each other means that we cannot exclude intersubunit FRET occurring; i.e. TNP-ATP binding to a neighbouring subunit will also be able to quench ANAP to a certain extent. However, this occurs in a predictable way that we can measure and account for.

We ended up with one residue which fulfilled these criteria and for which surface membrane expression of the ANAP-incorporated channel could be detected: W311. It is a bulky hydrophobic residue similar to ANAP, and at the time of the construct design I was not aware of mutations at this residue which had been previously identified to alter  $K_{ATP}$  function. During the writing of this thesis, I came across an experiment by Cukras *et al.* (164), in which they mutated W311 to an alanine and were unable to observe  $K_{ATP}$  currents in excised patches. It was not resolved whether this was an assembly, trafficking, or functional disruption. However, as we were able to see  $K_{ATP}$  membrane expression and currents when we mutated W311 to ANAP, it is possible that this more conservative substitution is enough to overcome the lack of currents seen in the W311A mutant.

## 3.2 Incorporating ANAP into the Kir6.2 binding site

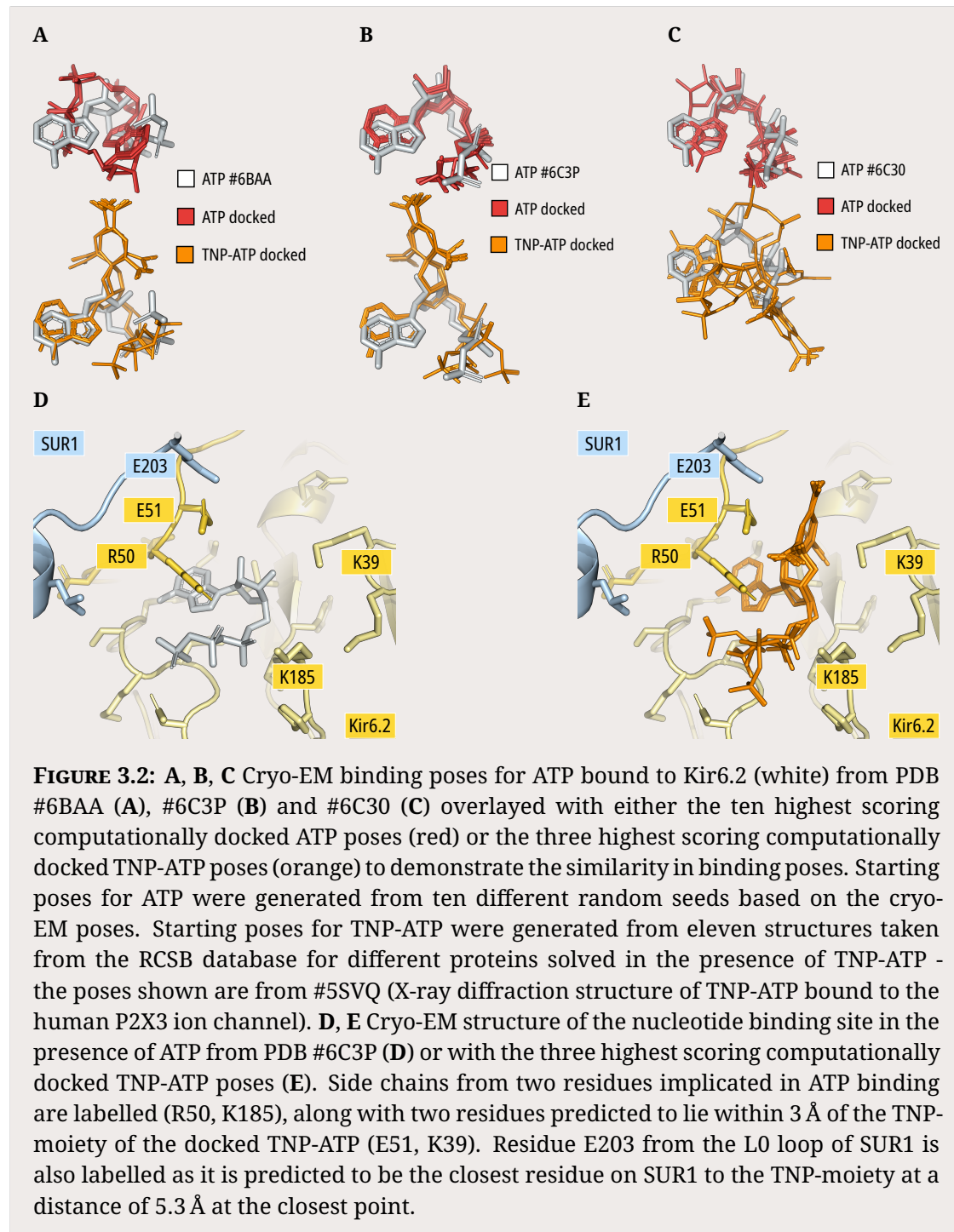
### 3.2.1 The Amber stop codon expression system

ANAP can be introduced into a protein of interest by essentially expanding the genetic code to incorporate a noncanonical amino acid (165). The Amber stop codon (TAG) is the least frequently occurring stop codon in eukaryotic cells (166), and can be repurposed to encode ANAP. This requires the introduction of two new components into the translational machinery of the chosen heterologous expression system:

- A transfer RNA (tRNA) which specifically recognises the TAG codon.
- An aminoacyl-tRNA synthetase (aaRS) which selectively attaches ANAP to the introduced tRNA (146, 147).

Lee *et al.* (146) used directed evolution to develop a tRNA/aaRS pair to encode ANAP in *Saccharomyces cerevisiae* (146). Briefly, they altered the specificity of *Escherichia coli* leucyl-tRNA synthetase so that it was able to aminoacylate the leucyl-tRNA with ANAP, and not endogenous amino acids. The coevolved tRNA/aaRS pair were built into an expression plasmid pANAP (Figure 3.3A) which is capable of driving expression in mammalian cells (147). HEK293 cells transfected with

### 3.2. Incorporating ANAP into the Kir6.2 binding site



pANAP and a plasmid encoding GFP with an Amber stop codon at residue position 40 exhibited green fluorescence only when incubated in the presence of ANAP in the culture media (147), demonstrating that ANAP can be selectively incorporated into proteins in mammalian cells.

As far as we are aware, only two other studies have incorporated unnatural amino acids into Kir6.2 (167, 168). Zhang *et al.* (167) incorporated three unnatural tryptophan variants at position W68 to highlight the necessity of a planar amino acid side-chain at this location to maintain physiological  $K_{ATP}$  channel function (167). However, in this study *Xenopus* oocytes were the heterologous expression system, so rather than transfecting a combination of plasmids, the authors injected a combination of transcribed mRNAs.

Devaraneni *et al.* (168) incorporated azidophenylalanine (AzF) at three different positions on the N-terminus of Kir6.2 (residue numbers 12, 18 and 52) (168). AzF is photocross-linkable upon exposure to UV light, and the authors used this phenomenon to investigate the extent of physical interactions between the N-terminus of Kir6.2 and SUR1, and how these interactions are mediated by pharmacological chaperones. In this study, COSm6 cells were the heterologous expression system, and expression of AzF containing constructs was found to be dramatically reduced when compared to wild-type channels.

### 3.2.2 ANAP incorporation into Amber stop codon containing constructs

The nature of the amber stop codon suppression system requires a number of careful controls to ensure the following:

1. Stop codon recognition is not perfect, and there is a chance of read-through. Instead of incorporating ANAP, it is possible that the translation machinery can insert endogenous amino acids instead, leading to production of full length, unlabelled Kir6.2. However, we found that cells transfected with W311TAG constructs and pANAP which were not cultured in the presence of ANAP did not produce full length Kir6.2 (Figure 3.3B, 3.3C), suggesting there is minimal read-through of the stop codon in our experiments.
2. Introducing a stop codon creates a risk that truncated Kir6.2 will be produced instead of ANAP labelled Kir6.2. This risk can be reduced by transfecting a

dominant negative engineered version of eukaryotic translation termination factor 1(eRF1-E55D), which does not efficiently terminate protein synthesis in response to the amber stop codon (but leaves opal and ochre stop codons nearly unaffected) and thus increases the incorporation of ANAP (169). We found that transfection of W311TAG constructs with a C-terminal GFP tag produced minimal truncated Kir6.2 (less than 10 % of the total density observed in Figure 3.3C).

3. Despite being the least frequent eukaryotic stop codon, the amber stop codon is still present in a significant number of protein sequences. We must be careful that ANAP is not incorporated into a protein which localises to the plasma membrane to an extent which would affect our ability to assign ANAP fluorescence to Kir6.2. We found that in cells transfected with GFP-tagged Kir6.2 without an amber stop codon, there was no increase in ANAP fluorescence at the cell membrane (Figure 3.4A, 3.4B). By contrast, when W311TAG-GFP was transfected, we saw a clear increase in ANAP fluorescence at the cell membrane (Figure 3.4C, 3.4D), suggesting that any observed ANAP fluorescence at the cell membrane originates from our labelled Kir6.2 construct.

### 3.3 Testing for functional membrane expression

#### 3.3.1 Surface expression of HA-epitope labelled Kir6.2 constructs

To assess the ability of ANAP-incorporating constructs to traffic to the plasma membrane, we used a luminescence-based surface expression assay (153). This assay relies on the recognition of a human influenza hemagglutinin (HA)-epitope introduced into an extracellular region of the protein of interest (in this case, the N-terminal region of Kir6.2) by an anti-HA primary antibody followed by a horseradish peroxidase (HRP)-conjugated secondary antibody. The luminescence after applying HRP substrate is then proportional to the amount of protein at the plasma membrane of the cells.

We assessed the membrane expression of N-terminally HA-tagged Kir6.2 (WT-HA) in the presence or absence of ANAP in the culture media and in the presence or absence of cotransfected SUR1. We also measured how the addition of a C-terminal GFP tag affected membrane expression under these conditions. We used untagged Kir6.2 as a control for nonspecific luminescence.

We found that for wild-type Kir6.2 (WT) there is roughly a 20-fold increase over background in observed luminescence when coexpressed with SUR1, and roughly a 100-fold increase for the C-terminally GFP tagged Kir6.2 (WT-GFP, Figure 3.5A, 3.5C). There is no difference in surface expression of these constructs when ANAP is present in the culture medium (Figure 3.5A, 3.5D). When ANAP is incorporated at either residue 183 or 311 (F183\* and W311\* respectively, F183\* included here as an example of a construct deemed unsuitable for further experiments) we see an increase over background in luminescence when coexpressed with SUR1 and with ANAP present in the culture medium (Figure 3.5A, 3.5C). The presence of the C-terminal GFP tag increases luminescence further for both constructs, dramatically so for W311\*. However, when F183\* is transfected and ANAP is not present in the culture media we still see a similar increase in fluorescence over background when compared to the luminescence when ANAP is present (Figure 3.5A, 3.5D), suggesting that a large proportion of the protein reaching the cell surface membrane does not have ANAP incorporated. In contrast, when W311\*-GFP is transfected with SUR1 in the presence of ANAP, we see a 10-fold increase in luminescence compared to when ANAP is not present, consistent with the majority of cell surface expressed protein having incorporated ANAP. We also see a consistent increase in luminescence for all constructs aside from W311\* when cotransfected with SUR1 (Figure 3.5B), suggesting that the incorporation of ANAP and the addition of a C-terminal GFP tag do not affect the role of SUR1 in forming the full  $K_{ATP}$  complex and trafficking to the cell surface membrane.

### 3.3.2 Electrophysiology of Kir6.2 constructs

To establish whether W311\*-GFP formed K<sub>ATP</sub> channels with similar function to wild-type, we excised patches from cells transfected with either WT-GFP or W311\*-GFP cotransfected with SUR1. Excision was performed in Mg<sup>2+</sup>-free solution to reduce rundown and to prevent activation of the channel by nucleotides. We observed similar magnitudes of current for both WT-GFP and W311\*-GFP, and the currents ran down at similar rates.

We fit our inhibition data with equation 2.7 (Figure 3.6A) as described in the methods. Briefly, our fitting procedure assumes that there is a population parameter for  $IC_{50}$ ,  $I_{max}$  and  $h$ , and an additional 'random' effect on  $IC_{50}$  that can differ between experiments (shown in Figure 3.6C). Our fits result in posterior probability distributions for the population  $IC_{50}$  parameter shown in blue in Figure 3.6E. These distributions reflect our confidence in the population parameter for the  $IC_{50}$ . For all  $IC_{50}$  and  $EC_{50}$  values fitted this way, in the text we will report the 95 % credible intervals of the posterior probability distribution for the fitted population parameter.

Perfusion of ATP resulted in current inhibition with an  $IC_{50}$  of 24  $\mu$ M to 45  $\mu$ M for WT-GFP+SUR1 and 75  $\mu$ M to 124  $\mu$ M for W311\*-GFP+SUR1. Thus, despite the distance from the ATP binding site, the incorporation of ANAP at W311 clearly affects some aspect of nucleotide inhibition. However, we assume that insights into the function of the ANAP-incorporating channel will still be applicable to wild-type channels despite the change in nucleotide inhibition.

Next, we established that TNP-ATP inhibits K<sub>ATP</sub> (Figure 3.6B, 3.6D). We observed current inhibition with an  $IC_{50}$  of 0.7  $\mu$ M to 1.8  $\mu$ M for WT-GFP+SUR1 and 2.9  $\mu$ M to 10  $\mu$ M for W311\*-GFP+SUR1. K<sub>ATP</sub> thus appears to be more sensitive to inhibition by TNP-ATP than by ATP. This could potentially be due to extra contacts made by the TNP moiety with Kir6.2, seen in our computational docking (Figure 3.2).

### 3.3.3 Unroofed membrane binding assay of Kir6.2 constructs

We then directly measured nucleotide binding to W311\*-GFP in unroofed membranes. Briefly sonicating transfected cells adhered to coverslips results in the

adhered lower membrane of the cell remaining stuck to the coverslip while the rest of the cell is disrupted and the contents are perfused away. This leaves the cytoplasmic domains of expressed  $K_{ATP}$  channels accessible to TNP-ATP in the perfusate. These patches of membrane are barely visible under brightfield illumination, but due to the presence of the C-terminal GFP tag and the incorporated ANAP, we can see patches of membrane expressing  $K_{ATP}$  channels light up when we excite either fluorophore (Figure 3.7A). By measuring the fluorescence spectra of patches of unroofed membrane, we can separate the fluorescence emission peaks of the C-terminal GFP tag and the incorporated ANAP (Figure 3.7B). The peak at 472 nm corresponds to ANAP emission, while the peak at 508 nm corresponds to GFP emission. We observed no change in the locations of those peaks in the presence of ATP or TNP-ATP.

Perfusing TNP-ATP results in a decrease in the peak corresponding to ANAP fluorescence, and a concomittant increase in a fluorescence peak at 561 nm which corresponds to the TNP-ATP (Figure 3.7C). This phenomenon is the result of FRET between TNP-ATP bound to the channel at the Kir6.2 binding site. The decrease in ANAP fluorescence is almost directly correlated to an increase in bound nucleotide. We chose to measure the decrease in ANAP fluorescence rather than the increase in TNP-ATP fluorescence or the change in the ratio of ANAP:TNP-ATP fluorescence as we know that the ANAP fluorescence is specific to the Kir6.2 binding site. Increases in TNP-ATP fluorescence could in part be due to direct excitation of TNP-ATP bound to other membrane proteins. We can plot the quenching of ANAP fluorescence as a concentration-response curve as in Figure 3.7D.

Before analysis, ANAP bleaching was corrected as shown in Figure 3.8A. ANAP intensities of spectra imaged during bath perfusion with TNP-ATP free solution, in between applications of TNP-ATP, were fit with Equation 2.3. We found that in all unroofed membrane experiments bleaching was well described by a single exponential fit to equation 2.3. In each experiment, there was a mean value of 49 % ANAP fluorescence remaining by the last exposure (Figure 3.8C), means we maintained a good signal-to-noise ratio for each spectra imaged.

While our measurements of ANAP quenching are proportional to nucleotide binding to  $K_{ATP}$ , the raw  $F/F_{max}$  observations are not directly equivalent to the unbound fraction of Kir6.2 subunits. This non-equivalence is due to two factors. Firstly, there is the potential for crosstalk between ANAP incorporated in one subunit and TNP-ATP bound to the adjacent subunits. To determine the extent to which this crosstalk would affect the measured FRET efficiency when ANAP is incorporated at position 311, we adapted a program described by Deplazes *et al.* (170) which uses a numerical method to model FRET in complex geometries. We implemented a simple version of this program in Python which uses a Monte Carlo simulation scheme to approximate the observed FRET efficiency for a given set of donor and acceptor fluorophores and coordinates. An overview of the program is shown in Figure 3.9A. We did not measure the fluorescence lifetimes and quantum yields of ANAP and TNP-ATP directly, instead using previously determined values (171–173). The fluorescence lifetime of TNP-ATP differs when it is bound to proteins; we ran simulations using the fluorescence lifetime of TNP-ATP in solution and the fluorescence lifetime of bound TNP-ATP and saw no difference in the FRET efficiency.

We simulated the expected FRET for a single  $K_{ATP}$  channel bound to 0–4 molecules of TNP-ATP in two different scenarios. In the idealised scenario, each ANAP molecule is only able to FRET with the TNP-ATP molecule bound at the closest inhibitory binding site (Figure 3.9B). In the actual scenario, which resembles the experimental paradigm, each ANAP molecule is able to FRET with any bound TNP-ATP molecule in a probabilistic manner dependent on the inter-fluorophore distance. We can observe that there is a systematic deviation in the FRET efficiency between these two scenarios (Figure 3.9C), which we can correct by transforming the actual values ( $F/F_{max}$ ) into adjusted values ( $\log_2(\frac{F}{F_{max}+1})$ ). This is an empirical transformation based on the observed deviation.

Secondly, we need to correct for incomplete FRET due to the distance between the donor and acceptor. Based on the results of the computational docking, we predict a maximal FRET efficiency of 91 % when a TNP-ATP molecule is bound to each Kir6.2 subunit. Fitting our adjusted data to a Hill equation results in a maximum observed

FRET efficiency ( $E_{max}$ ) of 91 %, agreeing well with our prediction. We can then constrain our Hill fits so that  $E_{max}$  is equal to this maximum FRET efficiency, so that the  $EC_{50}$  parameter we obtain is equivalent to the  $EC_{50}$  of TNP-ATP binding.

Overall, these two corrections do not dramatically alter our results (Figure 3.10A). We observed quenching of ANAP fluorescence from W311\*-GFP+SUR1 in unroofed membranes over a concentration range of TNP-ATP similar to the range in which we observed inhibition of current in excised patches expressing W311\*-GFP+SUR1 (Figure ??, 3.10B). When fit to a Hill equation, quenching ( $F/F_{max}$ ) was fit with an  $EC_{50}$  of 21  $\mu\text{M}$  to 31  $\mu\text{M}$ , while the corrected binding data (adjusted  $F/F_{max}$ ) gave an  $EC_{50}$  of 30  $\mu\text{M}$  to 45  $\mu\text{M}$ .

### 3.3.4 Patch-clamp fluorometry of Kir6.2 constructs

To ensure that the ANAP fluorescence we observe in the unroofed membranes is emitted by functional channels, we measured fluorescence quenching and current inhibition from the same excised patches (Figure 3.12A, 3.12B, 3.12C).

This experimental paradigm leads to two complications compared to performing the measurements separately. Firstly, the number of channels in an excised patch are far smaller than the number of channels in an unroofed membrane patch. This results in a much dimmer fluorescence readout, and a lower signal-to-noise ratio. Secondly, the presence of the pipette glass in the images results in some abnormalities in the background subtraction procedure. This is not due to the glass itself, but results from the occlusion of TNP-ATP from the image surrounding the patch. This leads to oversubtraction of the background TNP-ATP spectra, leading to an apparent negative peak in our corrected images. However, we find that there is no overlap of this peak and the ANAP peak, so our fluorescence quenching measurements are unaffected by this phenomenon. We were able to correct for ANAP bleaching in the same manner as we did for unroofed membranes (Figure 3.11).

Our fluorescence measurements from excised patches are right-shifted with respect to our measurements for unroofed membranes (Figure 3.12D), with an  $EC_{50}$  value of 76  $\mu\text{M}$  to 144  $\mu\text{M}$  in PCF compared to 30  $\mu\text{M}$  to 45  $\mu\text{M}$ . Our finding that

the  $EC_{50}$  for TNP-ATP binding is right-shifted compared to the  $IC_{50}$  for TNP-ATP inhibition is consistent between each experimental paradigm (Figure 3.12E). This finding has implications for how exactly the binding of nucleotides to Kir6.2 leads to closure of the  $K_{ATP}$  channel pore.

## 3.4 Discussion

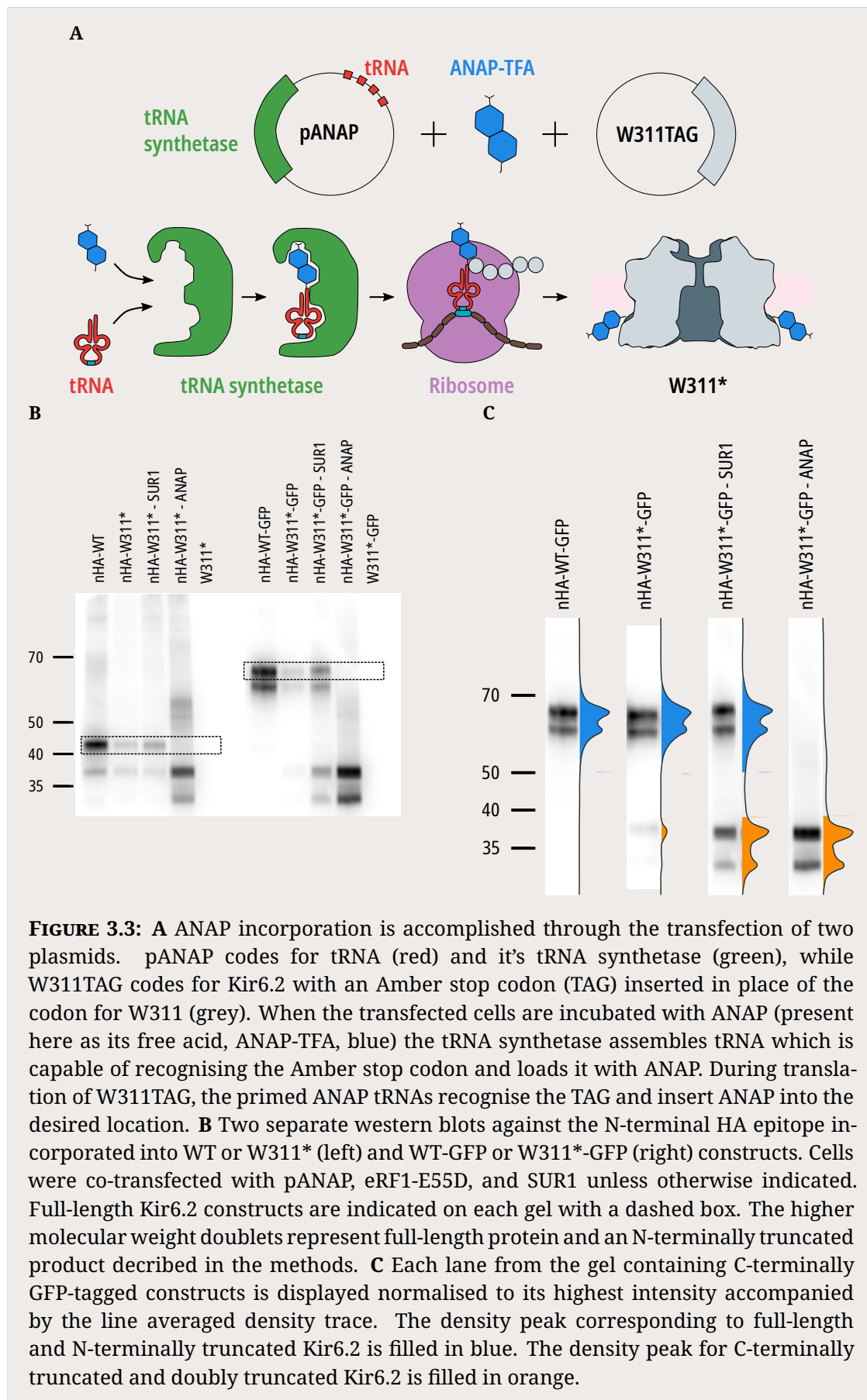
We have demonstrated that we can measure nucleotide binding to the inhibitory nucleotide binding site of Kir6.2 in intact, functional  $K_{ATP}$  channels in their native membrane environment. Measuring binding directly in either unroofed membrane patches, or in excised patches simultaneously with current recordings, reveals that nucleotide binding is right-shifted compared to nucleotide inhibition; i.e.  $K_{ATP}$  channels begin to close at nucleotide concentrations where there is very little binding. This observation rules out certain models of ion channel function, which will be explored further in chapter 4.

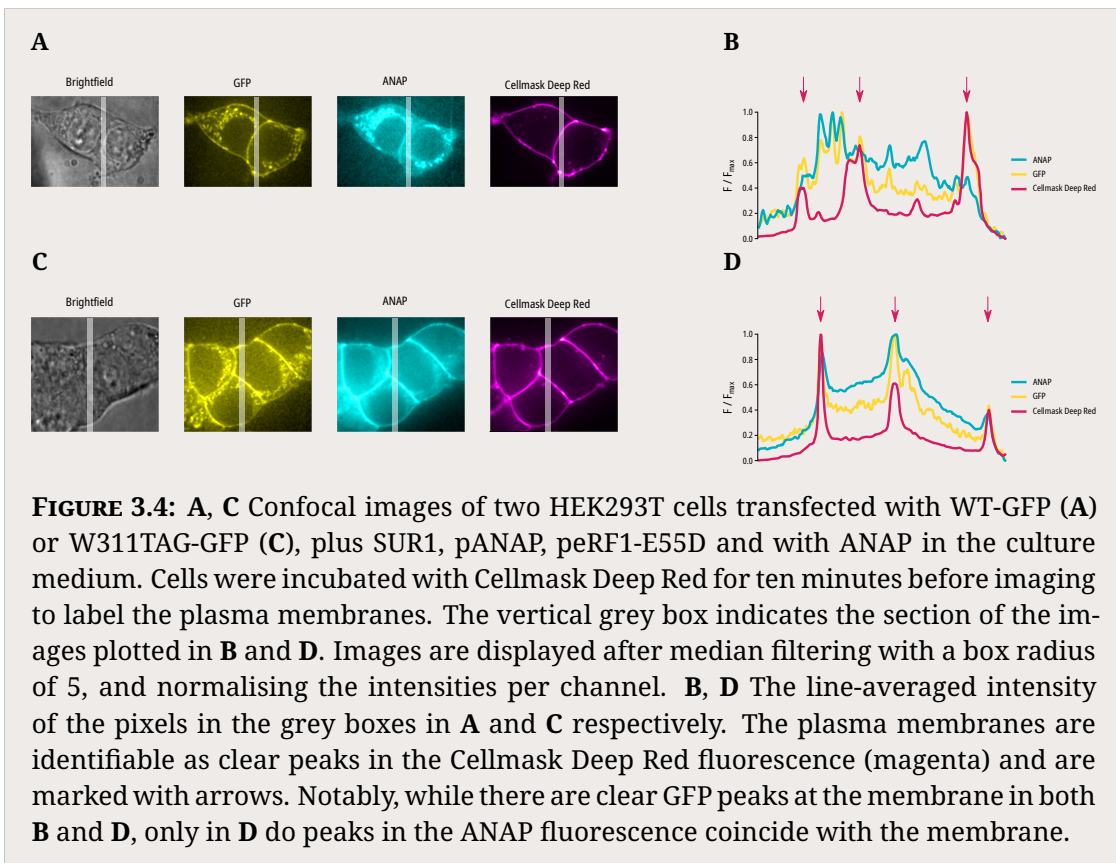
These findings come with some important caveats. Firstly, the introduction of ANAP into Kir6.2 at residue 311 clearly impacts nucleotide inhibition of the channel, increasing the observed  $IC_{50}$  values for ATP. Our analysis of nucleotide binding and inhibition is therefore predicated on this decrease in sensitivity to ATP inhibition not reflecting a disruption of the normal physiological mechanism of ATP inhibition. As all of our binding experiments are performed in the W311\* background by necessity, we hope that measurements of relative changes in binding and inhibition will still be meaningfully interpretable as they will mirror similar relative changes in inhibition observed in the WT background.

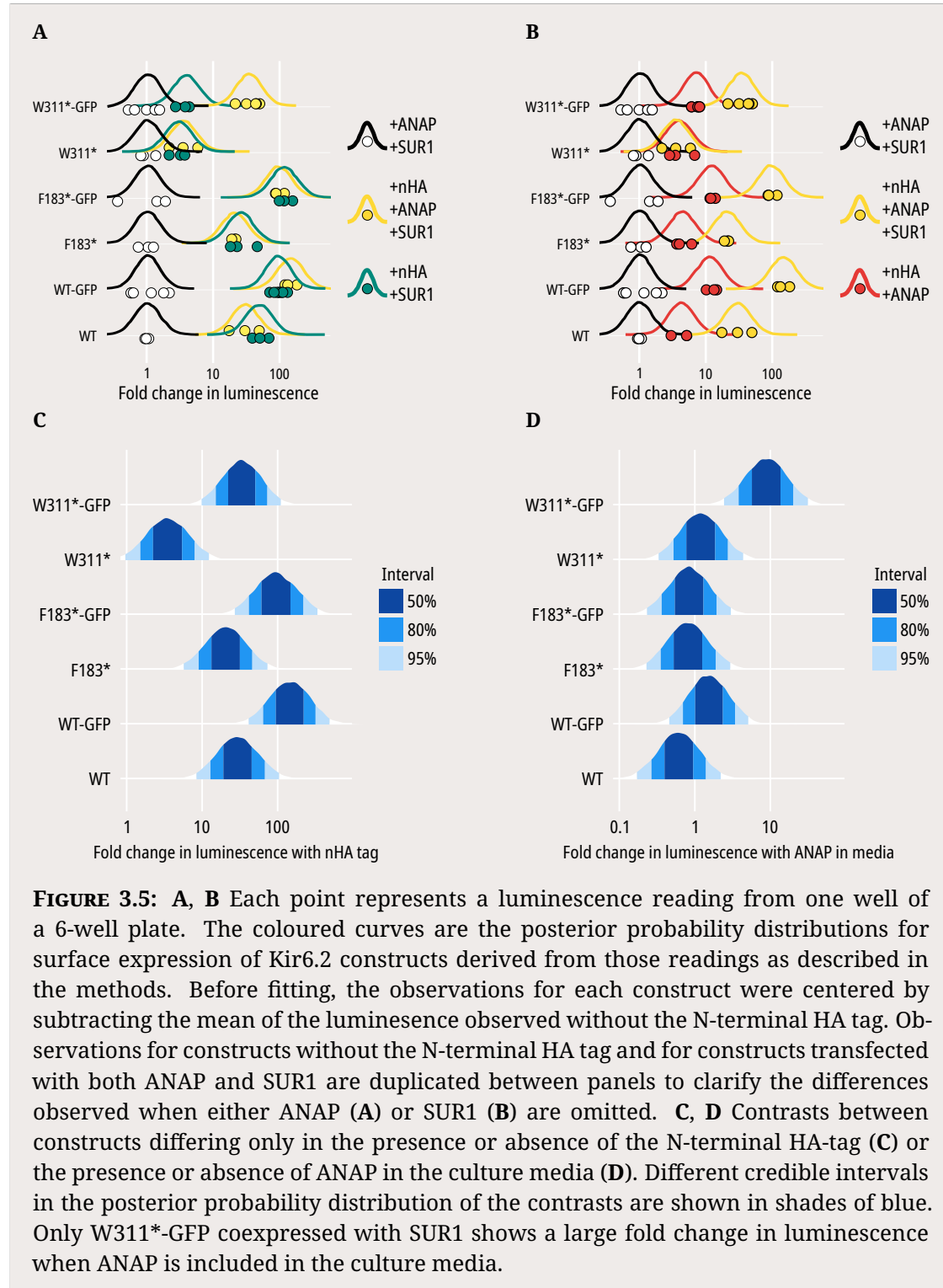
Secondly,  $K_{ATP}$  channels are more sensitive to inhibition by TNP-ATP than by ATP. Again, this means that any conclusions we draw from experiments measuring relative changes in binding and inhibition rely on those relative changes affecting ATP binding and inhibition to a similar extent as TNP-ATP. To try and ameliorate these caveats as best as we can, where possible we have performed control experiments in the WT background with ATP to ensure that introduced mutations result in similar relative effects on nucleotide inhibition despite the background of the construct or

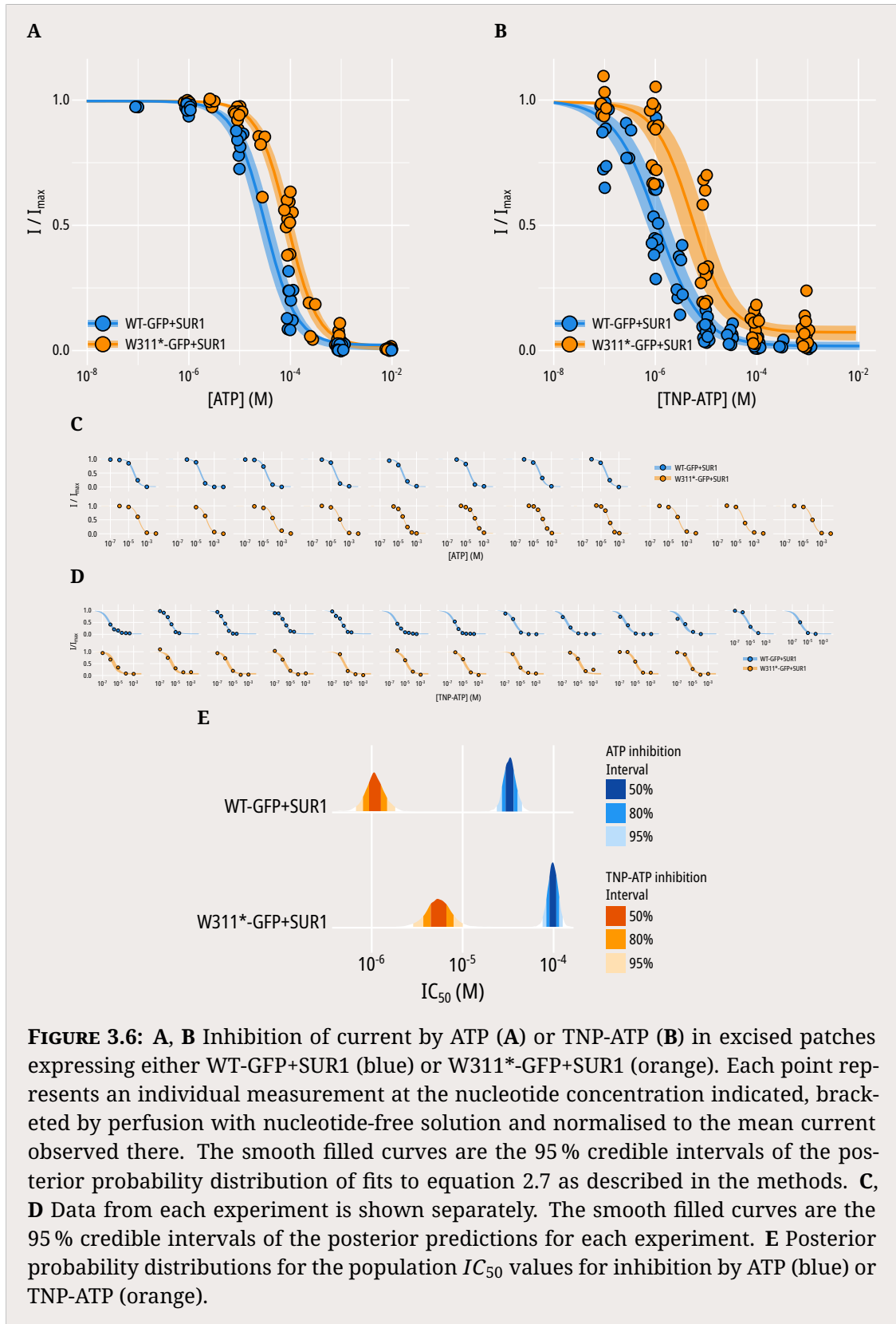
the identity of the nucleotide. As control experiments of this sort are not possible in unroofed membranes, where it is impossible to measure current inhibition, we have focused on PCF for constructs where expression is good enough to measure sufficient fluorescence.

Finally, there is a clear difference between the  $EC_{50}$  values we estimate from TNP-ATP binding in unroofed membranes and in excised patches. This may be due to increased levels of channel rundown in unroofed membranes, as the time between unroofing and measurement is longer (not measured, but around 10 minutes until first exposure) than the time between patch excision and measurement (typically less than a minute before first exposure). Rundown  $K_{ATP}$  channels with a lower  $P_O$  would be expected to have lower apparent  $EC_{50}$  values for TNP-ATP binding. An additional possibility is that our unroofing procedure does not result in all of the cell contents being disrupted, and that some of the ANAP fluorescence we are measuring is from W311\*-GFP subunits resident in ER fragments associated with the adherent membrane. Again, where possible we have tried to perform our experiments with PCF to avoid these possibilities.

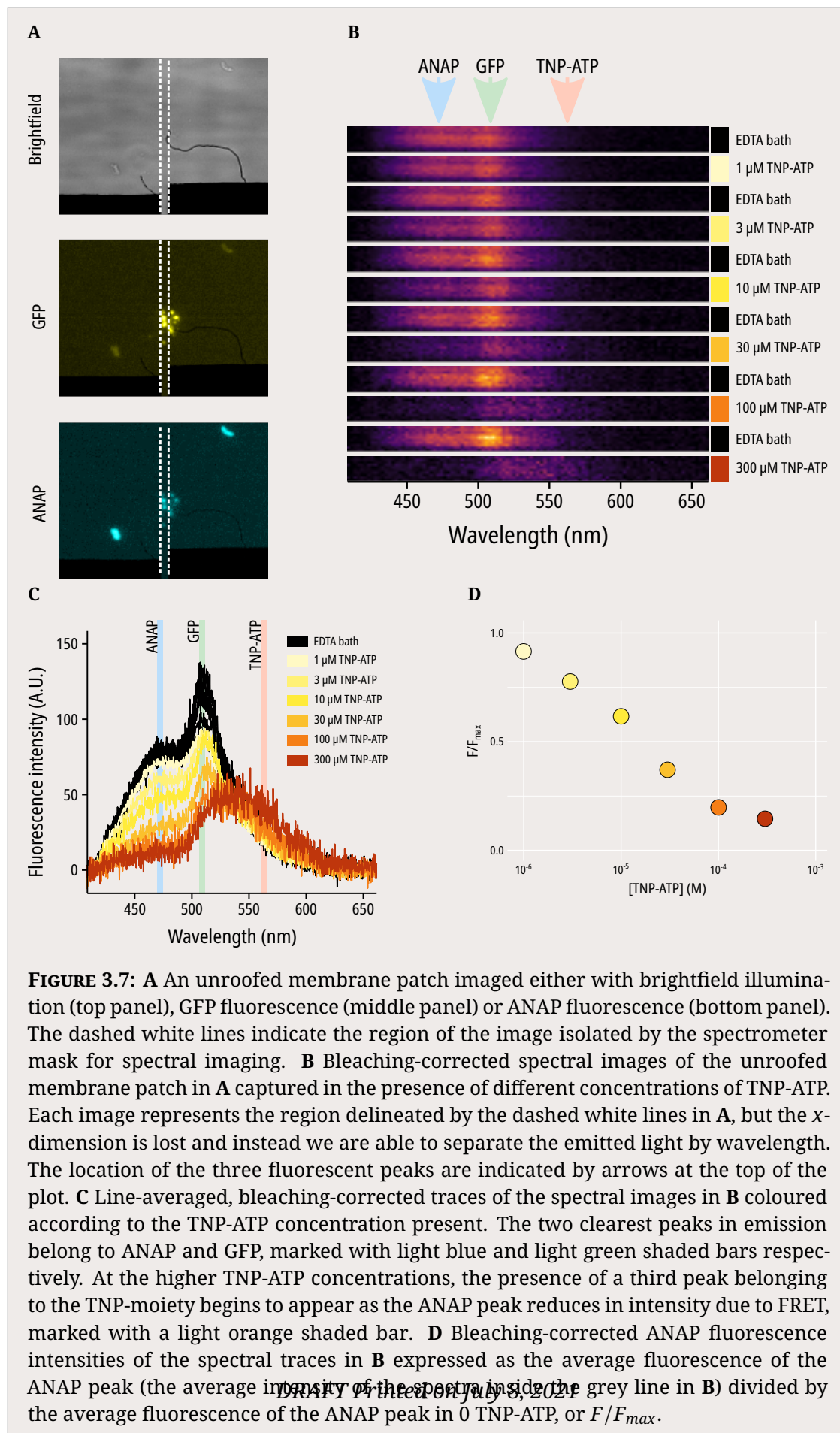


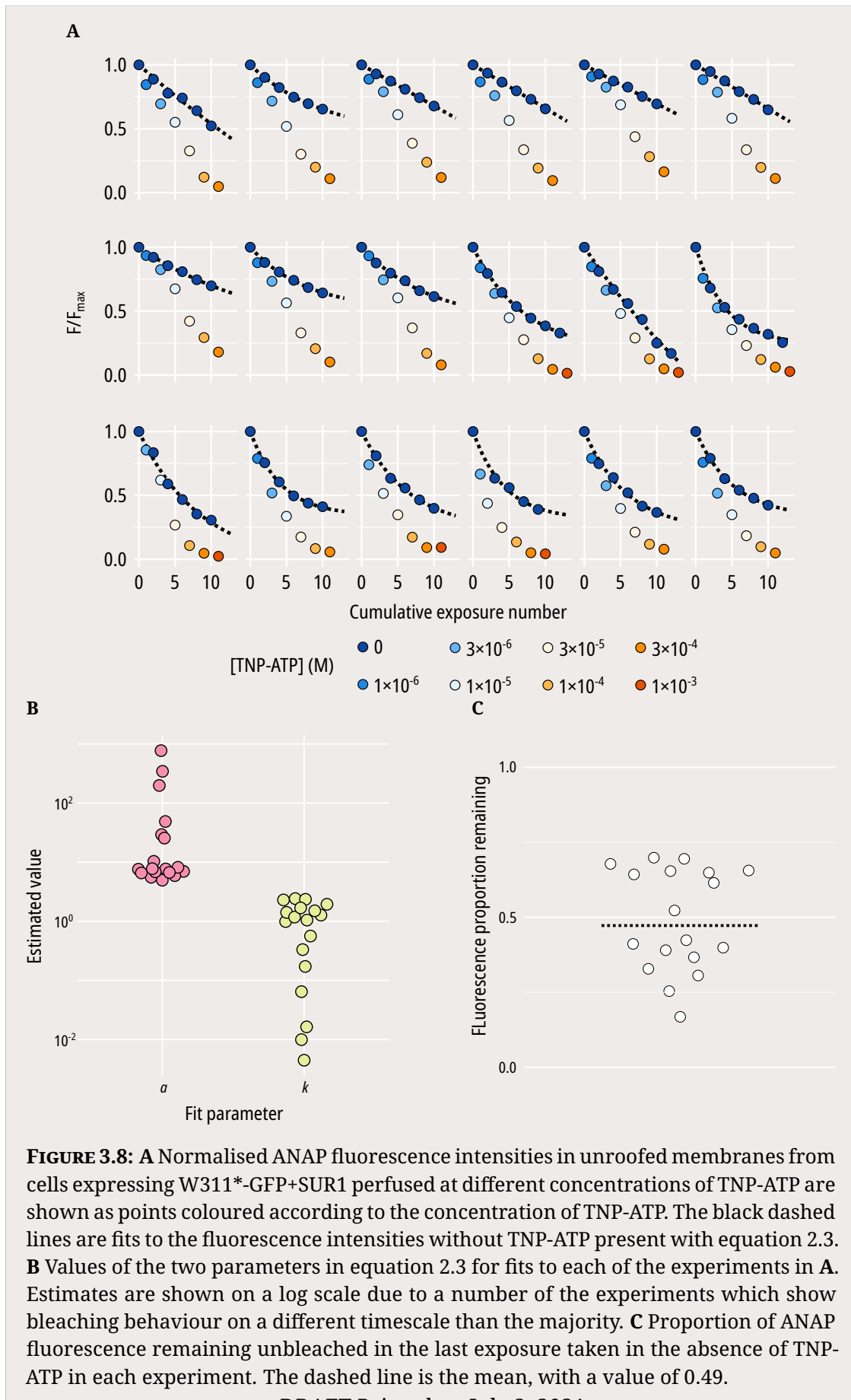


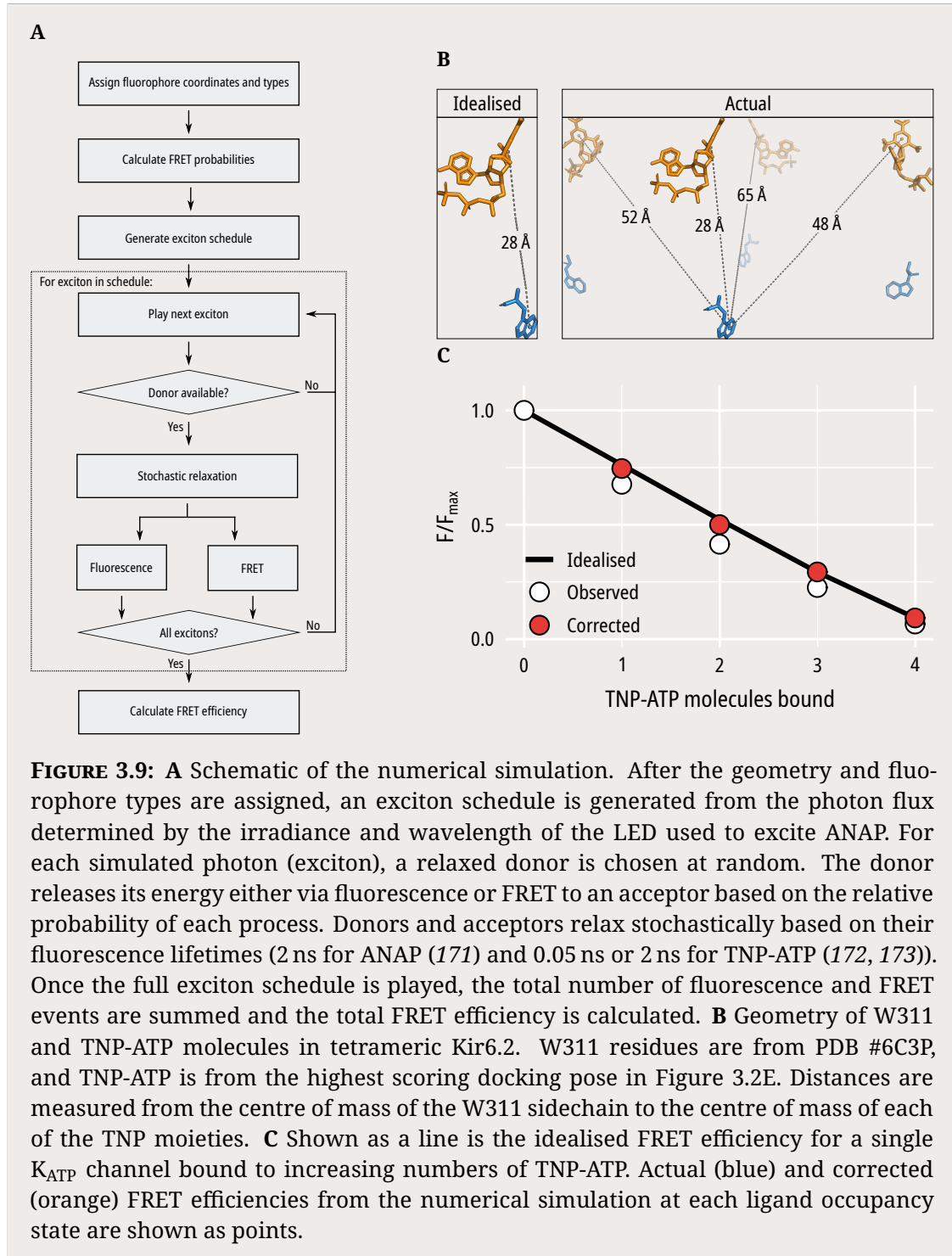


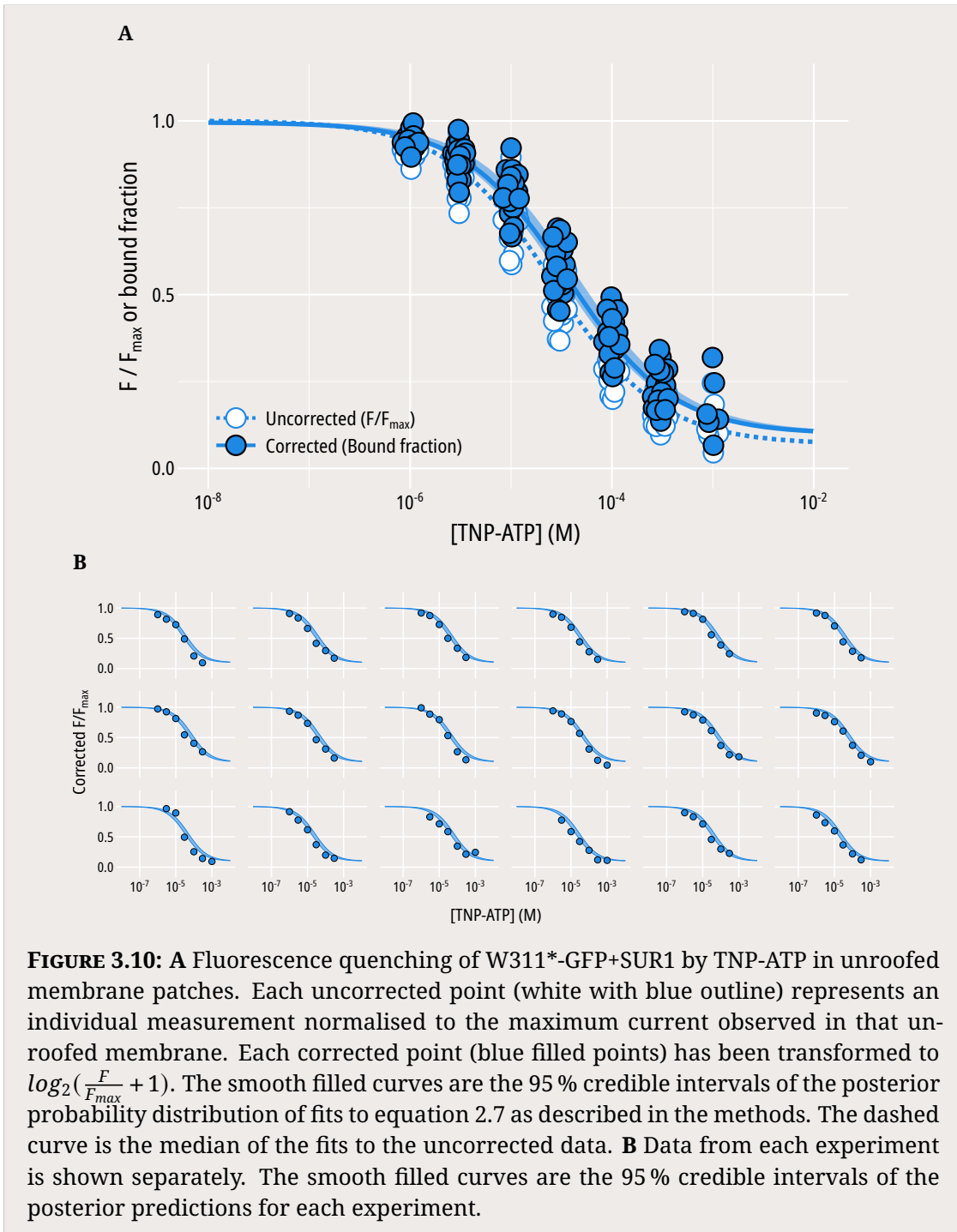


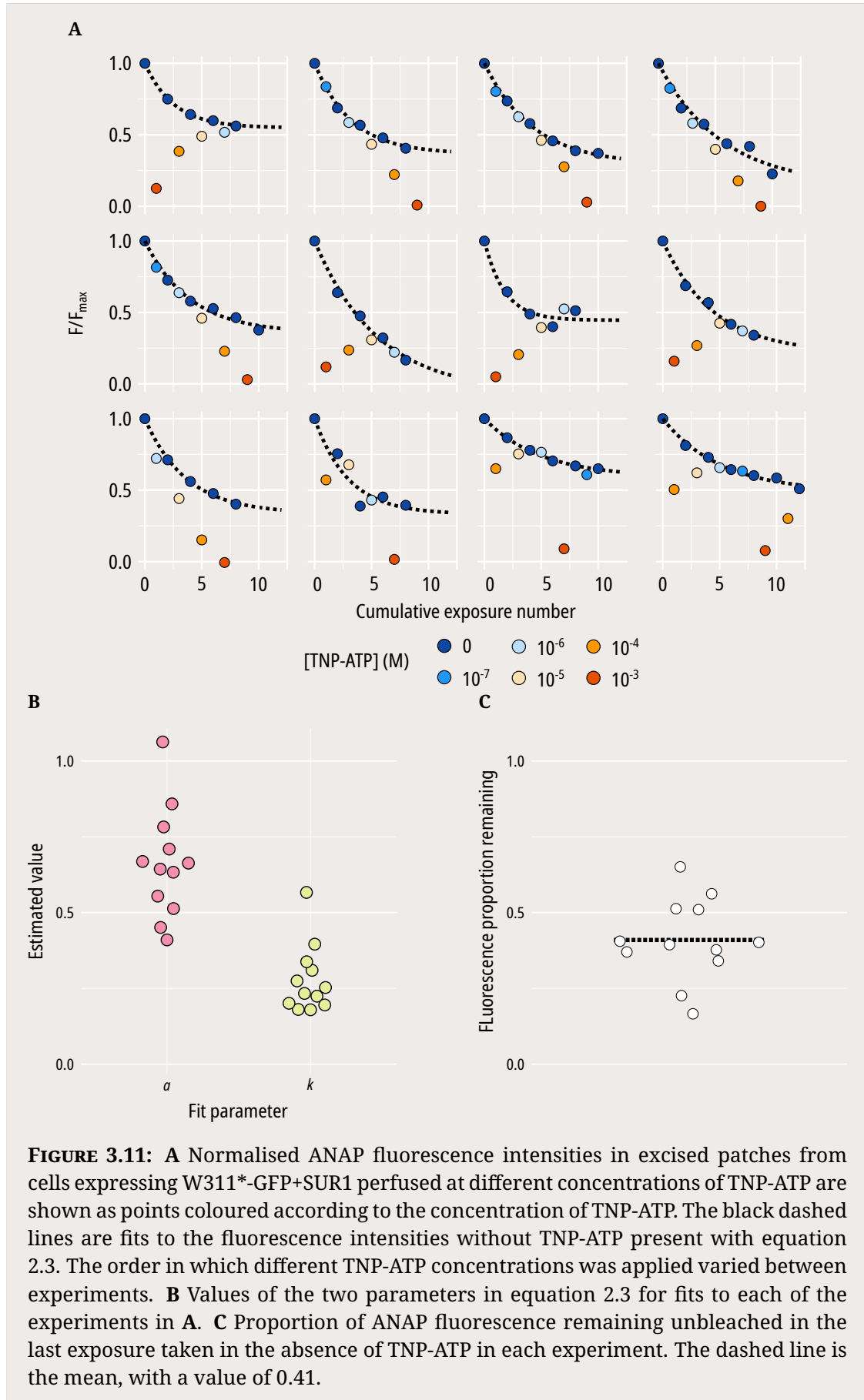
**FIGURE 3.6:** **A, B** Inhibition of current by ATP (**A**) or TNP-ATP (**B**) in excised patches expressing either WT-GFP+SUR1 (blue) or W311\*-GFP+SUR1 (orange). Each point represents an individual measurement at the nucleotide concentration indicated, bracketed by perfusion with nucleotide-free solution and normalised to the mean current observed there. The smooth filled curves are the 95 % credible intervals of the posterior probability distribution of fits to equation 2.7 as described in the methods. **C, D** Data from each experiment is shown separately. The smooth filled curves are the 95 % credible intervals of the posterior predictions for each experiment. **E** Posterior probability distributions for the population  $IC_{50}$  values for inhibition by ATP (blue) or TNP-ATP (orange).

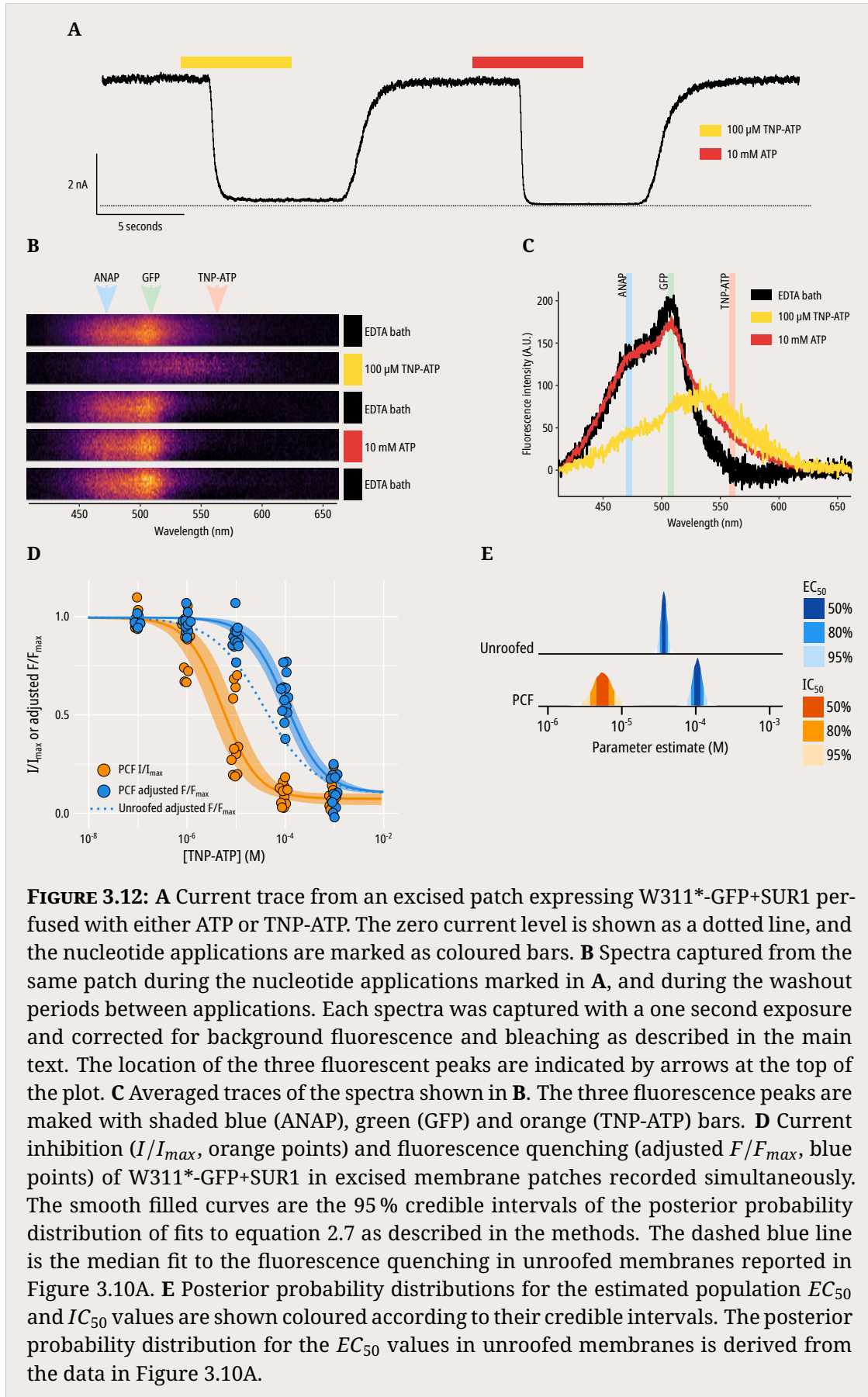














# 4

## MWC modelling

### Contents

---

<b>4.1 Modelling nucleotide regulation of the K<sub>ATP</sub> channel . . . . .</b>	<b>75</b>
4.1.1 Restricting the subset of possible models . . . . .	77
<b>4.2 Implementing an MWC model . . . . .</b>	<b>79</b>
4.2.1 A simple case . . . . .	79
4.2.2 The role of PIP <sub>2</sub> . . . . .	79
4.2.3 Determining open probability . . . . .	84
4.2.4 Comparing models . . . . .	89
4.2.5 Discussion . . . . .	94

---

### 4.1 Modelling nucleotide regulation of the K<sub>ATP</sub> channel

The complex regulation of K<sub>ATP</sub> channel activity by nucleotides and phosphoinositides has led to a wide range of scientists seeking to unify the constellation of structural and functional studies into one mechanistic framework, which is capable of explaining each aspect of channel regulation. The importance of K<sub>ATP</sub> channels in regulating insulin secretion, responding to cardiac stress, and protecting against seizures is one driving force behind the search for a functional model (54). Another aim is more holistic; hoping that increasing our understanding of how the K<sub>ATP</sub>

channel is regulated by the interplay of its ligands may shed light on other ion channels or proteins functions (174). In any case, the primary goal of constructing a mathematical model of the  $K_{ATP}$  channel is to explain as much of the diversity of channel function as possible, while keeping the model as simple and biologically relevant as possible; a balancing act between completeness and complexity.

Previous attempts at modelling the function of  $K_{ATP}$  channel regulation have primarily focused on nucleotide inhibition (96, 126, 175–182), due to the relative ease of isolating the effects of nucleotide inhibition. There have been fewer attempts at incorporating activation by Mg-nucleotides (90, 96, 103). The difficulty in quantifying phosphinositide regulation of the  $K_{ATP}$  channel means that in most cases where it is considered, it is implicitly included as a component of the intrinsic gating of the channel, rather than explicitly described (17, 125, 126), although there are some exceptions (96, 177, 183).

What does a functional model of ion channel function look like? Broadly, a model attempts to categorise discrete conformational states of the channel, and describe the transitions between those states. In the simplest case, an ion channel can be described as fluctuating between an open state and a closed state (Figure 4.1). As these states exist in equilibrium, they can be described by an equilibrium constant ( $L$ ) which is composed of the rate constant for the opening transition ( $k_O$ ) divided by the rate constant for the closing transition ( $k_C$ ).

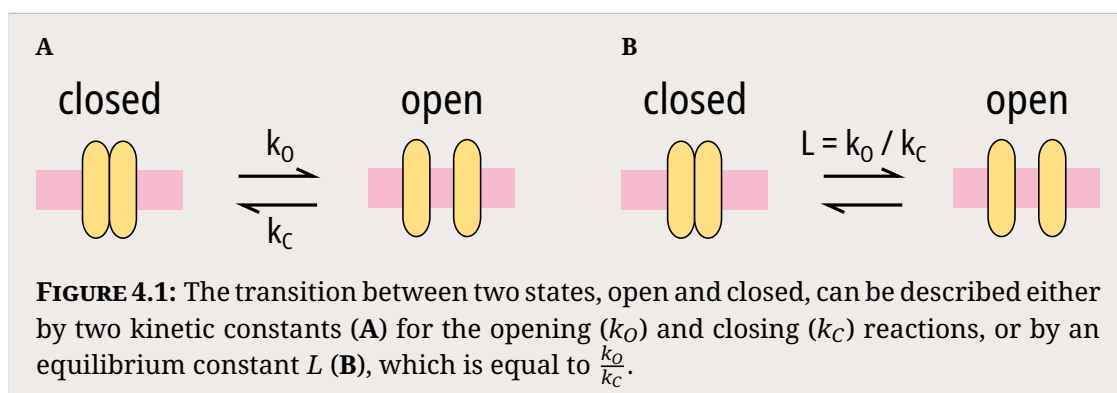


**FIGURE 4.1:** The transition between two states, open and closed, can be described either by two kinetic constants (A) for the opening ( $k_O$ ) and closing ( $k_C$ ) reactions, or by an equilibrium constant  $L$  (B), which is equal to  $\frac{k_O}{k_C}$ .

To relate this to empirical measurements of ion channel function,  $L$  is equivalent to the  $P_O$  of this two-state channel. Alternatively, in this simple two-state channel,

$k_O$  and  $k_C$  can be calculated directly by measuring the lifetimes of the closed and open states respectively from single-channel recordings (184, 185). Of course, real ion channels are more complicated and two states are not sufficient to describe the complexity of the ligand regulation of K<sub>ATP</sub> channels, which visit a multitude of conformational states. As our understanding of the channel grows, the more complex a model needs to be to fully account for all observed aspects of function.

One shortcoming of K<sub>ATP</sub> channel functional models to date is that there are limited data directly measuring binding of nucleotides to the channel, and as such the nucleotide-bound conformational states and transitions of the channel have had to be inferred from electrophysiological measurements. Here, we hope to apply our correlated measurements of nucleotide binding and channel inhibition to reconcile the predictions of existing models of K<sub>ATP</sub> channel inhibition by nucleotides.

#### 4.1.1 Restricting the subset of possible models

Functional models which have been proposed to describe K<sub>ATP</sub> channel inhibition can be categorised into two groups; models in which each Kir6.2 subunit is able to change between open and closed conformations independently, and models in which opening and closing take place via a concerted mechanism of all four subunits (54, 55, 81, 90, 178, 182, 186, 187). The independent class of models are often referred to as Hodgkin and Huxley (HH)-like models, after the original model proposed to describe voltage-gated ion channels (188). The concerted class of models are often referred to as Monod-Wyman-Changeaux (MWC)-like models, after the allosteric model formulated by Monod, Wyman and Changeaux to describe hemoglobin (189).

Conceptually, an MWC-like model is easier to reconcile with the structure of K<sub>ATP</sub> given that each inhibitory nucleotide binding site is composed of domains from two adjacent subunits; it is hard to imagine how nucleotide binding could lead to an independent conformational change in one subunit alone (182). Empirically, the two types of model make testable predictions about channel behaviour and nucleotide binding. In a concerted model, each nucleotide binding event contributes the same amount of energy towards closure of the pore, such that each subunit

binding a nucleotide will have an additive effect on the probability of the channel closing. In an independent model, as each subunit is free to change its conformation independently, the stoichiometry of nucleotide binding is less clear. Most formulations of an independent model have suggested that  $K_{ATP}$  channel behaviour is most consistent with a single nucleotide binding event being sufficient to drive closure of the channel (53, 175, 176, 190).

A number of studies have examined the kinetics of single  $K_{ATP}$  channels to determine which model best describes nucleotide inhibition (178, 182, 187, 190). (178) examined single channel currents in patches excised from *Xenopus* oocytes injected with a mixture of Kir6.2ΔC and Kir6.2ΔC-N160D,T171A subunits. The T171A mutation appears to eliminate the interburst closures of Kir6.2ΔC by dramatically slowing the rate at which the ATP-sensitive inhibitory gate closes. The authors classified the single channel stoichiometry by assessing the sensitivity of currents to inhibition by spermine, which is provided to a subunit by the N160D mutation. An exponential relationship between the mean burst time of the channel and the number of mutant subunits incorporated into it fit the predictions made by a concerted model of inhibition.

Wang *et al.* (187) and Craig *et al.* (182) constructed tetrameric concatemers of Kir6.2 subunits to precisely control the stoichiometry of the resulting channels. The authors introduced mutations which affected either nucleotide binding (K185E (182, 187)) or mutations which altered intrinsic gating (C166S, T171Y (187)) into a fixed proportion of Kir6.2 subunits in the concatemerised channels. This selective disruption of individual subunits resulted in changes in ATP-dependent inhibition which could only be explained by a concerted model of  $K_{ATP}$  channel inhibition. However, as these experiments relied on introducing an additional physical linker between Kir6.2 subunits, the observed concerted gating behaviour may in part be due to the concatemerisation.

## 4.2 Implementing an MWC model

### 4.2.1 A simple case

The simplest case of an allosteric MWC model for an ion channel is shown as Scheme I in Figure 4.2A. This simple case assumes a channel composed of a single monomer with a single binding site for ligand  $A$ . The channel is restricted to two functional states, open and closed. These two states exist in an equilibrium described by  $L$ , which is equivalent to  $\frac{[\text{open}]}{[\text{closed}]}$ . Ligand  $A$  binds to the protein with a microscopic affinity constant  $K_A$ . The ligand  $A$  differentially stabilises the open and closed states by a constant  $D_A$ . When  $D_A$  is unity, the ligand  $A$  binds equally to both states and so does not influence the conformational changes of the channel. When  $D_A > 1$ , the ligand  $A$  preferentially stabilises the open state, whereas when  $D_A < 1$  the ligand instead preferentially stabilises the closed state.  $D_A$  therefore represents *transduction* of nucleotide binding to channel gating, and vice versa.

For  $K_{\text{ATP}}$  inhibition, each monomer in Scheme I represents a subunit of Kir6.2, and in our case the ligand  $A$  is TNP-ATP. The equation describing the expansion of Scheme I to account for four identical subunits is shown in Chapter 2. Importantly, in an MWC model, cooperativity between subunits is not due to the incorporation of an additional parameter, but a phenomenon which arises naturally due to the energetic coupling between ligand binding and channel gating described by the transduction parameter  $D_A$ .

### 4.2.2 The role of $\text{PIP}_2$

Of course, nucleotide inhibition is not the only ligand regulation of  $K_{\text{ATP}}$  channels. If we assume that activation of  $K_{\text{ATP}}$  currents by Mg-nucleotides binding at the NBDs of SUR1 or by  $\text{PIP}_2$  binding to Kir6.2 are independent processes, the effects of these ligands on nucleotide inhibition can be incorporated implicitly through their effects on  $L$ . Mg-nucleotide activation of  $K_{\text{ATP}}$  channel currents is well described by assuming independence from nucleotide inhibition; i.e. there is no evidence to suggest that there is a direct interaction between binding of Mg-nucleotides to SUR1

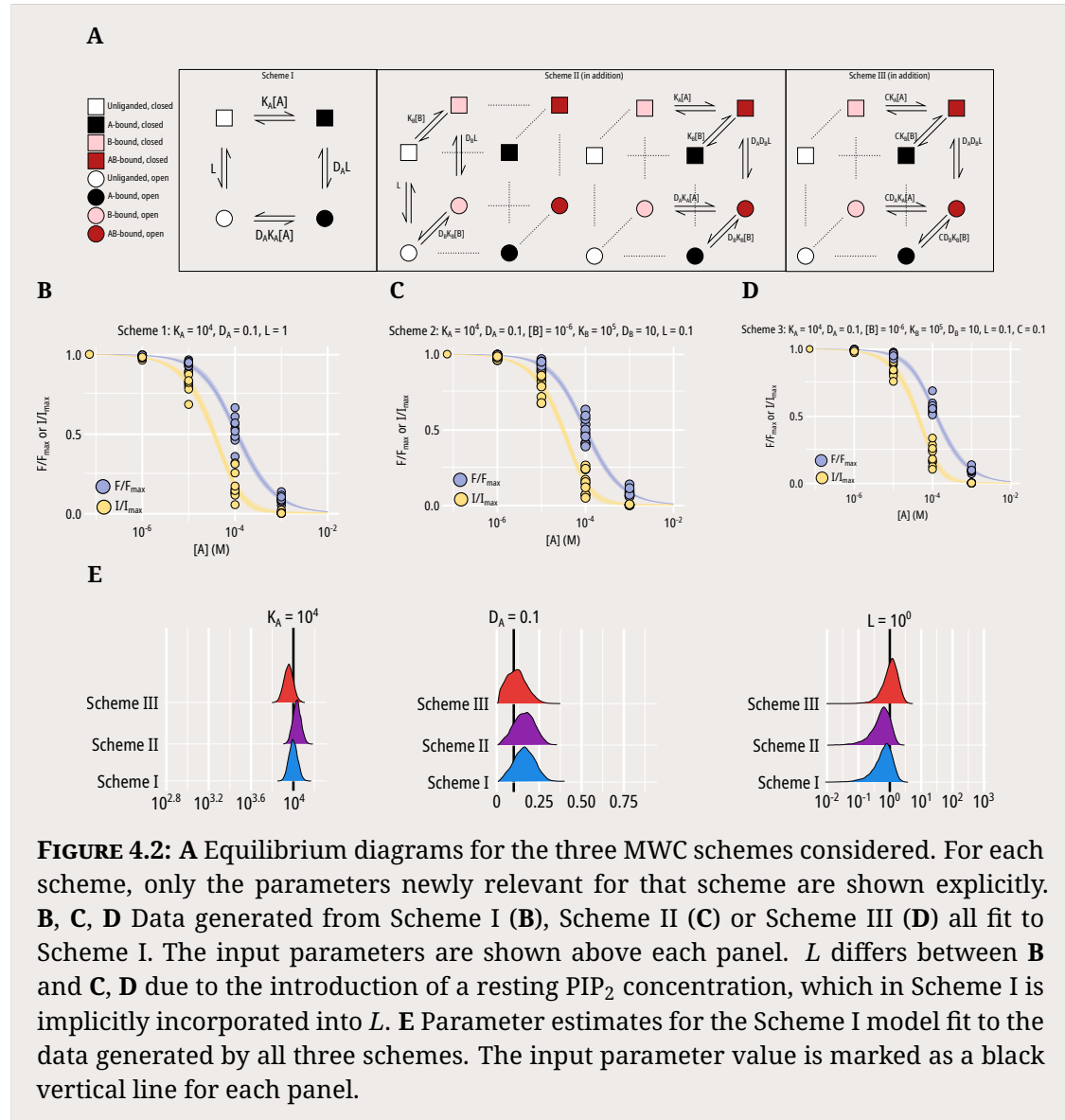


**FIGURE 4.2:** A Equilibrium diagrams for the three MWC schemes considered. For each scheme, only the parameters newly relevant for that scheme are shown explicitly. B, C, D Data generated from Scheme I (B), Scheme II (C) or Scheme III (D) all fit to Scheme I. The input parameters are shown above each panel.  $L$  differs between B and C, D due to the introduction of a resting  $\text{PIP}_2$  concentration, which in Scheme I is implicitly incorporated into  $L$ . E Parameter estimates for the Scheme I model fit to the data generated by all three schemes. The input parameter value is marked as a black vertical line for each panel.

and the ability of nucleotides to bind to Kir6.2 (90, 103). However, there is some evidence to suggest that there is a direct interaction between the nucleotide and  $\text{PIP}_2$  binding sites (54, 125, 128, 129). The existence of a direct interaction, either by competition for an overlapping binding site or through allosteric rearrangements of the two binding sites, may make it difficult to incorporate regulation by  $\text{PIP}_2$  implicitly as an effect on  $L$ . We investigated how the existence of direct interaction between the two ligand binding sites may manifest in our observations by simulating data from three progressively expanded MWC-like schemes (Figure 4.2A).

If we consider introducing a second ligand  $B$  which binds to a distinct site on the same monomer and does not directly interact with ligand  $A$ , we introduce the states shown in Scheme II of Figure 4.2A. Each ligand has its own microscopic association constant ( $K_A$  or  $K_B$ ) and its transduction factor ( $D_A$  or  $D_B$ ). Importantly, there is no interaction term between ligand  $A$  and ligand  $B$ ; the only way the binding of the ligands can impact each other is through effects on  $L$ . Scheme II is therefore a restricted form of scheme III, which explicitly introduces a term for direct interaction ( $C$ ) between binding sites for ligands  $A$  and  $B$  on the same monomer. When  $C$  is unity, Scheme III becomes Scheme II. When  $C < 1$ , binding of one ligand reduces the ability of the other ligand to bind on the same monomer. When  $C > 1$ , binding of one ligand enhances the ability of the other ligand to bind on the same monomer.

Under Scheme II, in which there is no direct interaction between ligands, changes in the parameters describing ligand  $B$  (perturbations of PIP<sub>2</sub> regulation) should manifest in the data in the same way as if there was a change in  $L$  in Scheme I (98). It is unclear whether under Scheme III, with the introduction of the direct interaction  $C$ , the same assumption is true - and if not, how much it would affect channel behaviour. To determine whether this approximation is appropriate, we generated data using each of the three schemes in Figure 4.2A as the underlying model of channel function and then fit the generated observations to Scheme I (Figure 4.2B, 4.2C, 4.2D). Ten individual sets of observations were generated using the inputs shown above each figure panel as the centre of a lognormal distribution with a standard deviation of 0.25. These observations were then fit to Scheme I and the values of the three free parameters ( $K_A$ ,  $D_A$  and  $L$ ) were estimated (Figure 4.2E).

We can show that when Scheme II or Scheme III are the underlying data generating model, with ligand  $B$  representing PIP<sub>2</sub>, we are still able to extract the true values of  $K_A$  and  $D_A$  by fitting the generated data to Scheme I (Figure 4.2). Parameter choices for Scheme II and III are such that the open probability of the channel at 0 M ATP is still 50%, equivalent to  $L = 1$  in Scheme I.

We can also show that when Scheme I is the underlying data generating model, changes in any of the three parameters are easily identified and retrieved by fitting

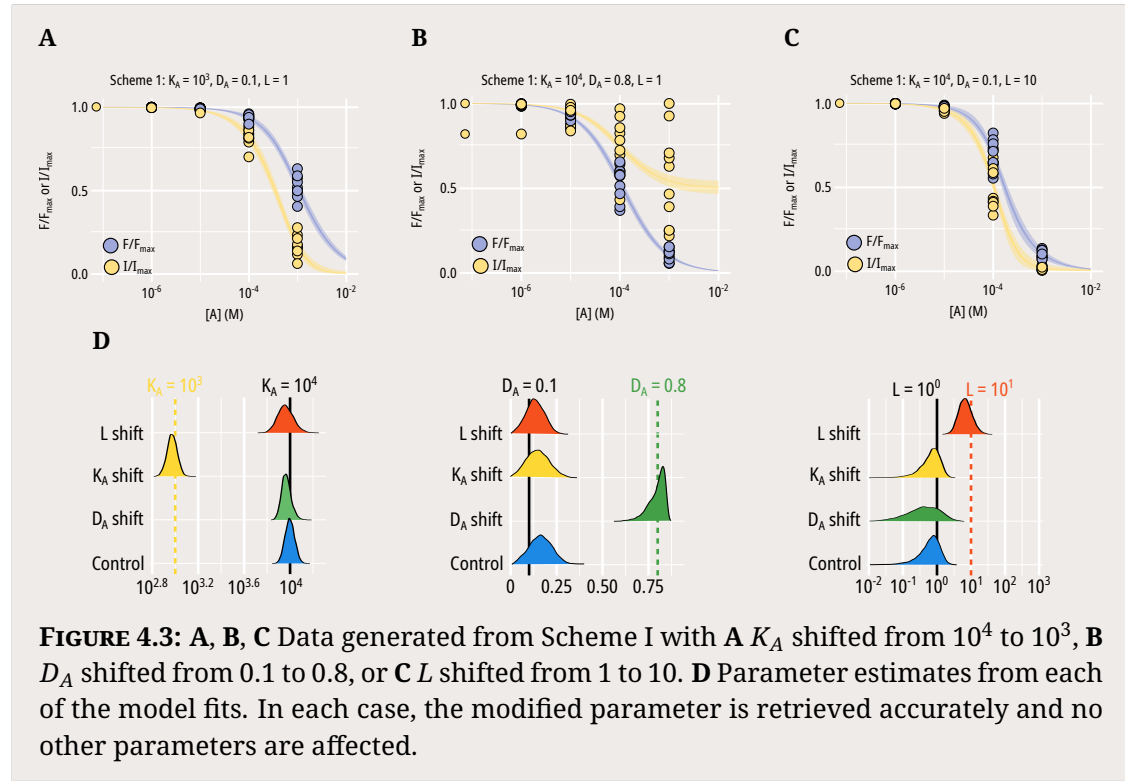


**FIGURE 4.3:** **A, B, C** Data generated from Scheme I with **A**  $K_A$  shifted from  $10^4$  to  $10^3$ , **B**  $D_A$  shifted from 0.1 to 0.8, or **C**  $L$  shifted from 1 to 10. **D** Parameter estimates from each of the model fits. In each case, the modified parameter is retrieved accurately and no other parameters are affected.

the observed data to Scheme I (Figure 4.3). This suggests that introducing mutations or perturbing nucleotide inhibition in any other way which directly affects any of the three parameters of this model would be easily identifiable if Scheme I was the true underlying model.

What if Scheme II or III were the underlying model? We would still expect changes in the three parameters which exist in Scheme I to be identifiable ( $L$ ,  $K_A$  and  $D_A$ ), although  $L$  would not represent the true unliganded open/closed equilibrium as we would be estimating an  $L$  modified by the resting PIP<sub>2</sub> concentration,  $K_B$ ,  $D_B$  and  $C$  - in this case, the estimated  $L$  parameter in fact represents the ATP-unbound open/closed equilibrium.

However, it is unclear how changes in parameters which are not explicitly modelled in Scheme I will affect the generated data and the parameter estimates obtained by fitting the data to Scheme I. Figure 4.4 shows the results of increasing  $K_B$  by tenfold on data generated from Scheme II (Figure 4.4A) or Scheme III (Figure 4.4B). The first observation of note is that the generated data closely resemble those

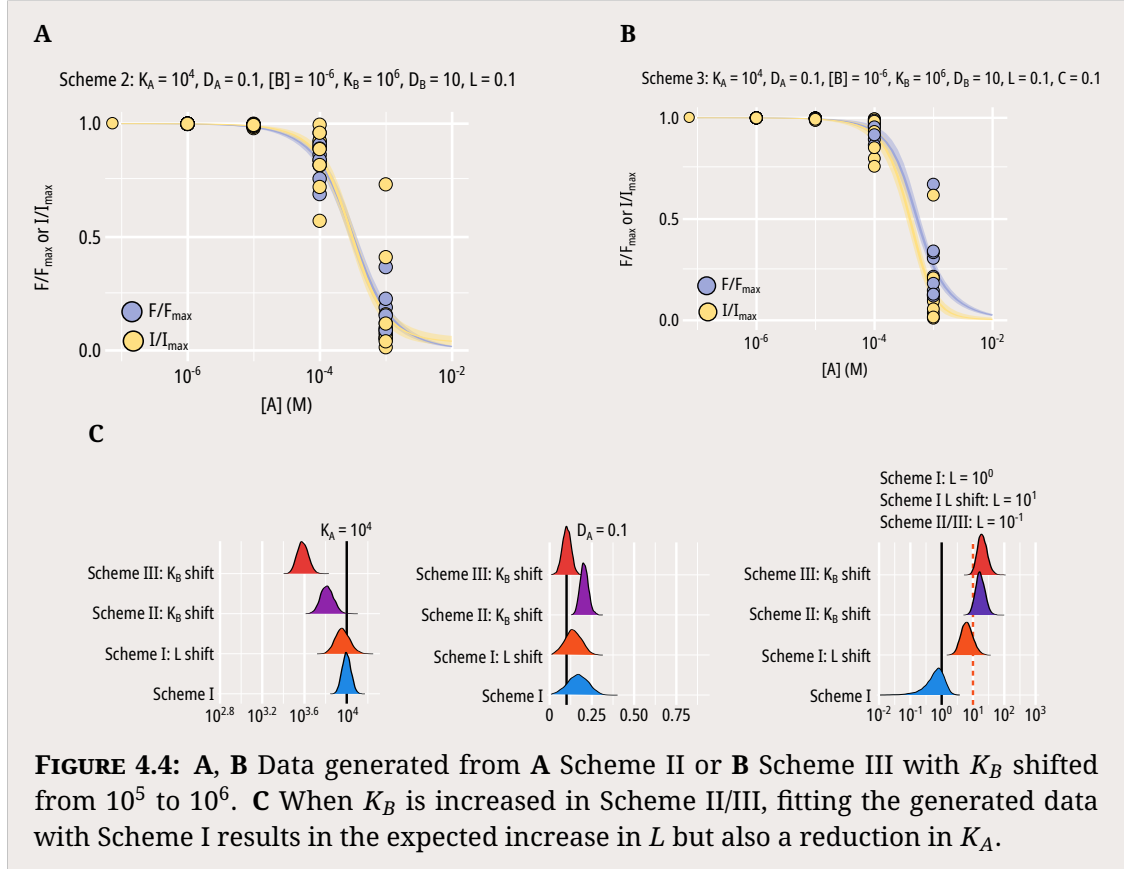


**FIGURE 4.4:** **A, B** Data generated from **A** Scheme II or **B** Scheme III with  $K_B$  shifted from  $10^5$  to  $10^6$ . **C** When  $K_B$  is increased in Scheme II/III, fitting the generated data with Scheme I results in the expected increase in  $L$  but also a reduction in  $K_A$ .

generated from Scheme I when  $L$  is increased (Figure 4.3C), and indeed when the  $L$  parameter estimates for a tenfold shift in  $K_B$  in Scheme II/III and tenfold shift in  $L$  for Scheme I are compared (Figure 4.4C, right panel) are compared they appear to be similar. So far so good, as an observed increase in  $L$  when fit with Scheme I would lead us to draw the correct inferences about changes in the underlying model (i.e. the open probability of the channel has indeed increased).

However, changes in  $K_B$  under Scheme III are not perfectly captured by changes in  $L$  when fit to scheme I. Notably, if a direct interaction exists between the nucleotide and PIP<sub>2</sub> binding site - if Scheme III is the true underlying model - then fitting the observed data to Scheme I would lead us to estimate an incorrect value for  $K_A$  (Figure 4.4A). Thus, if there is a direct interaction between the sites, then a mutation which induces an increase in the binding affinity for PIP<sub>2</sub> would not just increase our estimate of  $L$  (which would lead to a correct inference) but it would also decrease our estimate of  $K_A$  by a not-insignificant amount. This could lead to the incorrect

inference that a mutation is causing a direct change in nucleotide binding when it is in fact causing a direct change in PIP<sub>2</sub> binding, which is influencing our estimates of  $K_A$  through a direct interaction with the inhibitory nucleotide binding site.

### 4.2.3 Determining open probability

As  $L$  represents the fraction of channels in the open state, it is directly measurable by determining the channel open probability. Ideally then, to fit an MWC model to our data we would like to establish the open probability of the channels in our experiments. Measuring the open probability of an ion channel is most accurately accomplished by single-channel electrophysiological recordings, which allows direct measurement of the time a channel spends in an open state. Measuring open probability directly is not possible in macroscopic patches, which consist of hundreds or thousands of individual channels. Thus it would not be possible to determine single channel open probability simultaneously with nucleotide binding, as the fluorescence signal from a small number of channels would be impossible to resolve.

Another approach is noise analysis of currents from large populations of channels (191, 192). The 'noise' in noise analysis refers to current fluctuations which occur when recording from a population of ion channels due to the stochastic channel gating of individual channels. If there are a constant number of channels ( $N$ ) which are gated independently from each other and share a homogenous open probability ( $P_O$ ) and a single open conductance level ( $i$ ), the observed macroscopic current level  $I$  can be described by equation 4.1:

$$I = iNP_O \quad (4.1)$$

and the observed variance of the macroscopic current can be described by the variance of the binomial distribution, equation 4.2:

$$\sigma^2 = NP_O \cdot (1 - P_O) \cdot i^2 \quad (4.2)$$

where the single channel current is essentially a scaling factor. If we assume that in a given recording  $N$  and  $i$  remain constant, and it is  $P_O$  which changes in response to

any given stimuli, then we can combine equations 4.1 and 4.2 to yield equation 4.3:

$$\sigma^2 = iI - \frac{1}{N} \cdot I^2 \quad (4.3)$$

This equation yields a parabola from  $I = 0$  to  $I = Ni$ . Intuitively, there can be no variance when  $P_O$  is exactly 0 or 1, as there will be no opening or closing events which can give rise to current fluctuations. Once  $i$  and  $N$  have been determined for a given experiment, the observed current magnitude  $I$  can be converted into the  $P_O$  for the population of channels by rearranging equation 4.1 as follows:

$$P_O = \frac{I}{iN} \quad (4.4)$$

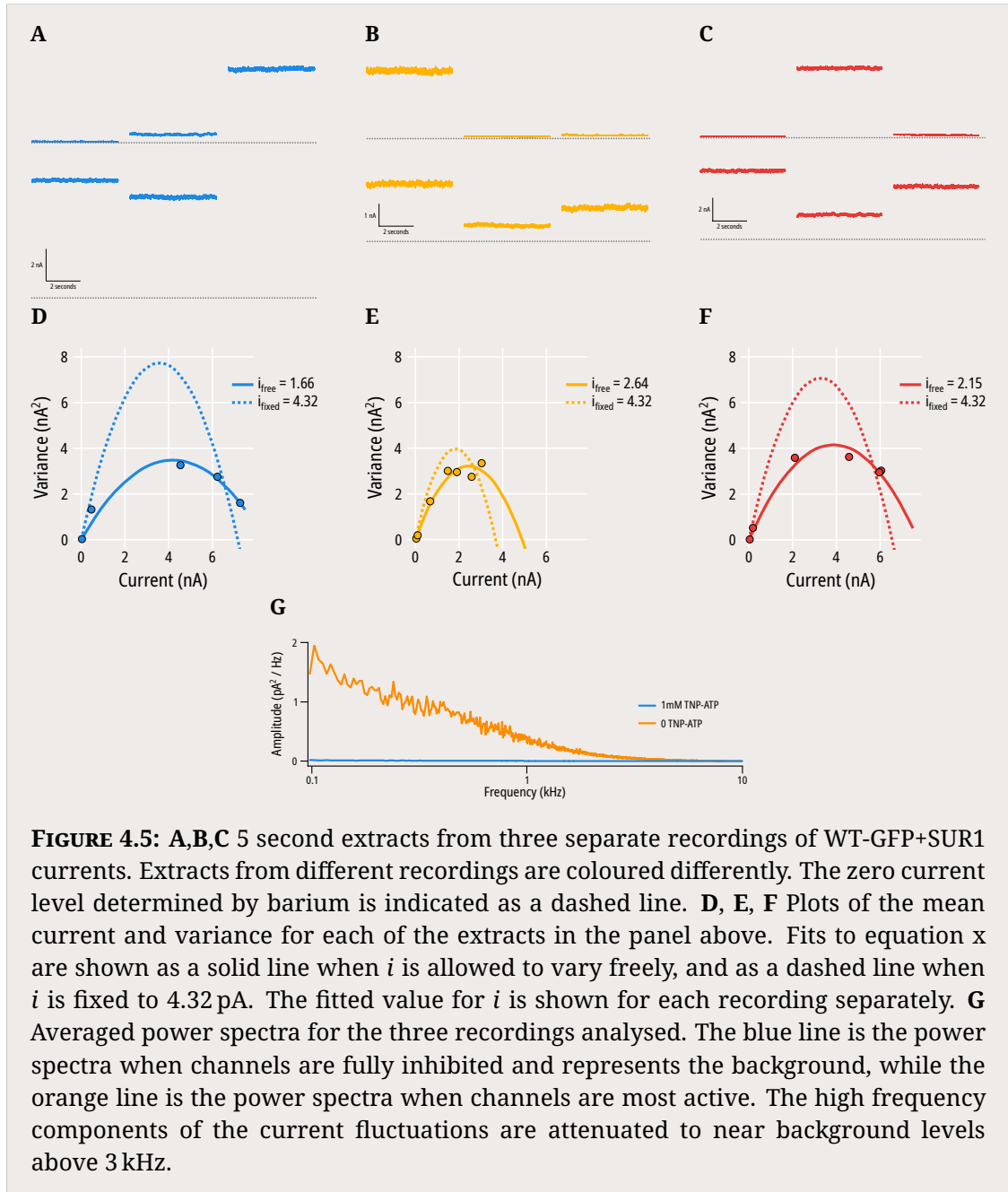
Equation 4.3 can be fit to experimental data by calculating the variance of observed current at different current magnitudes. This calculation is not exactly trivial, and has been accomplished a number of different ways for different purposes. For channels with fast inactivation such as the  $\text{Na}_V$  family, non-stationary noise analysis involves repeating a stimulus multiple times and measuring variance as the squared sum of deviations from the mean of the current magnitude calculated at the same time point across multiple stimuli, referred to in the literature as an 'isochrone' (193). For channels which do not inactivate, stationary noise analysis is possible, and variance can be measured as the squared sum of deviations from the mean current magnitude over a period of time for which  $I$  is 'stationary' (Figure 4.5A, 4.5B, 4.5C).

Stationary noise analysis has been performed for  $\text{K}_{\text{ATP}}$  channels before by a number of different researchers (65, 86, 87, 103, 194–196). Unfortunately, in most of the published research the exact procedure for extracting the parameters in equation 4.2 is described in the methods section, but the quality of the fits and the value of the fitted parameters besides the final calculated  $P_O$  is not discussed. A notable exception to this rule is in reference (194), in which two findings are discussed. Firstly, fitting equation 4.3 to the mean and variance of 200 ms sections of macroscopic currents from wild-type Kir6.2+SUR2A resulted in a systematic underestimation of the single channel current  $i$ . From single channel experiments, the single channel current was determined to be 4 pA, while the value obtained

from fitting macroscopic currents was only 2 pA. In the case of WT-GFP+SUR1, we see a similar underestimation of single channel current (Figure 4.5D, 4.5E, 4.5F), with fits yielding estimates of 1.66 pA to 2.64 pA, while measured single channel currents are at least 4 pA at a holding potential of  $-60$  mV (64, 65). This underestimate of  $i$  is most likely due to a reduction in observed channel current variance when compared to the predictions of equation 4.3.

There are two possible explanations for this reduction. Firstly, the process of filtering and digitising channel currents can lead to underestimates of variance depending on the relationship between the open time of the measured channel and the cut-off frequency of the filter used. It is unlikely that this phenomenon is responsible for our findings, as the  $K_{ATP}$  mean open time duration is close to 1 ms and therefore filtering at 5 kHz would lead to less than a 5 % underestimation of  $i$  (0). Even if the mean open time of WT-GFP+SUR1 was closer to 0.1 ms, we would expect a 20 % reduction rather than the 50 % we actually observe. Empirically, we can use the frequency power spectrum of our measured current fluctuations to determine whether there may be high frequency channel openings we are missing (Figure 4.5G). For WT-GFP+SUR1, we observe that at frequencies approaching our filter cut-off at 5 kHz there is very little observed amplitude in active channels when compared to fully inhibited channels, suggesting we are not missing high frequency current fluctuations.

Secondly, an underestimation of  $i$  could occur due to violations in the underlying assumptions of the binomial distribution. The first two assumptions are that  $N$  and  $i$  are constant throughout a recording. We know that  $i$  is unaffected by nucleotide inhibition of  $K_{ATP}$  channels, nor is it affected by  $PIP_2$  or channel rundown. Given that we are recording from excised patches, it is unlikely that there will be any change in the number of channels present in the membrane ( $N$ ) during the short time course of a recording. The third assumption in using equation 4.3 is that the channels in a patch share a homogenous  $P_o$ , which can be perturbed to a similar extent by a stimulus (in our case, application of nucleotide). This assumption is far harder to justify for our experimental condition, in which channel rundown



due to loss of  $PIP_2$  results in a complicated mixture of channel populations with different  $P_O$ s, which respond differently to nucleotide inhibition.

An extreme case in which channels transition between two states, one where  $0 < P_O < 1$  and one where  $P_O \approx 0$  can be approximated by equation 4.2, with a channel transitioning to the  $P_O \approx 0$  state essentially considered to be no longer available to open, reducing  $N$ . Thus, fitting the observed current-variance data with

4.2 would yield a straight line where the slope of the line is equal to  $i \cdot (1 - P_O)$ . This formulation of equation 4.2 has been used successfully in the analysis of currents from CRAC channels (197), VSOA channels (198, 199), and in the analysis of a specific cardiac K<sub>ATP</sub> channel mutation (194). Unfortunately, in our case channel rundown does not render the K<sub>ATP</sub> channel completely unable to open, with fully rundown channels still displaying openings. Instead of each current measurement coming from a single binomial distribution, we are instead observing a mixture of binomial distributions with different  $P_O$ . We can demonstrate how this could lead to an underestimation of  $i$  by simulating a simple case where there are two populations of channels,  $a$  and  $b$ , with a shared single channel conductance  $i$  but one with a tenfold lower  $P_O$  than the other:

$$N = 1000$$

$$N = N_a + N_b$$

$$0 < P_{O_a} < 1$$

$$P_{O_b} = \frac{P_{O_a}}{10} \tag{4.5}$$

$$i = 4$$

$$I = i * \text{Binomial}(N_a, P_{O_a}) + \text{Binomial}(N_b, P_{O_b})$$

where population  $a$  consists of  $N_a$  channels with an open probability  $P_{O_a}$ , and population  $b$  consists of  $N_b$  channels with an open probability  $P_{O_b}$ , constrained to be tenfold lower than  $P_{O_a}$ .

Comparing the mean current/variance relationship of simulated currents from a single binomial (Figure 4.6A, 4.6B) to that of simulated currents from the mixture of binomials in equation 4.5 (Figure 4.6C) reveals that equation 4.2 is no longer able to retrieve the true values of  $i$  and  $N$  when the data generating process is not a single binomial distribution. In fact, the underestimation of  $i$  from fitting to data simulated in this way is very similar to the underestimation of  $i$  we see when fitting to our measured data (Figure 4.5).

We considered whether the underestimation of  $i$  and the poor fits to equation 4.3 when  $i$  was fixed to 4.32 pA (Figure 4.5) may be due to the low number of data points

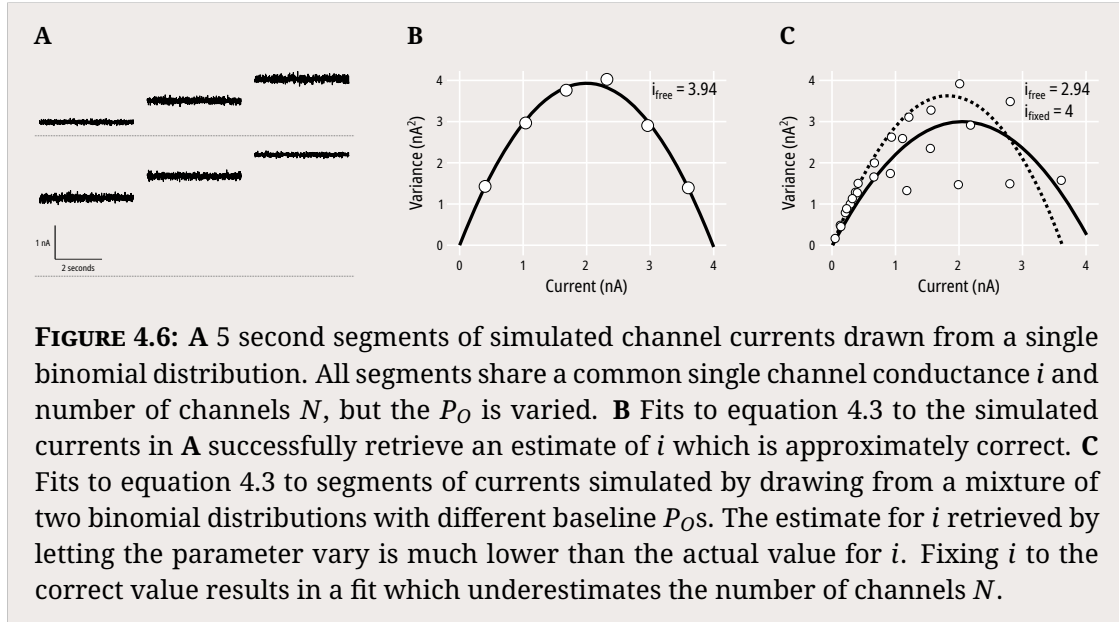


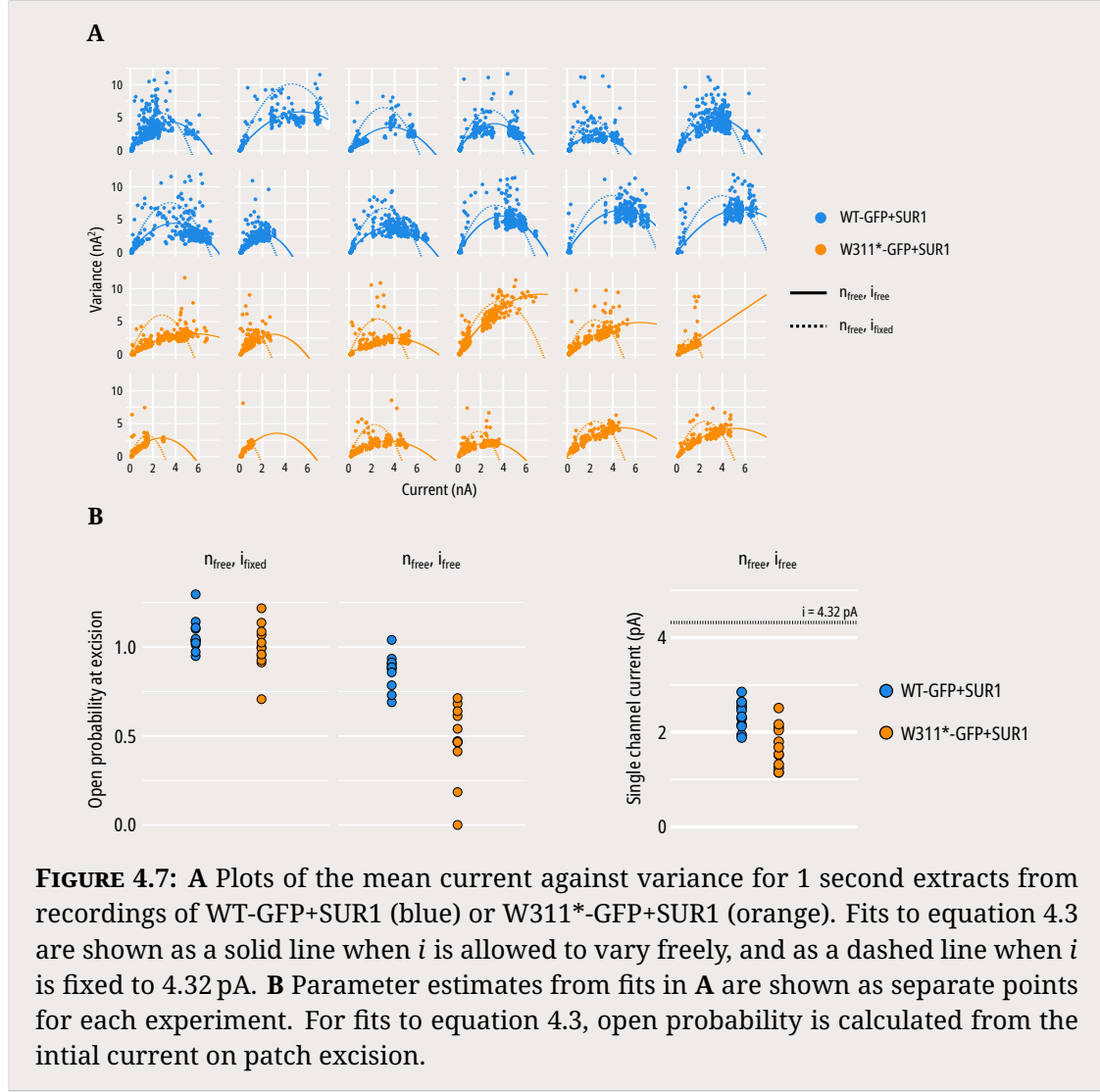
**FIGURE 4.6:** **A** 5 second segments of simulated channel currents drawn from a single binomial distribution. All segments share a common single channel conductance  $i$  and number of channels  $N$ , but the  $P_O$  is varied. **B** Fits to equation 4.3 to the simulated currents in **A** successfully retrieve an estimate of  $i$  which is approximately correct. **C** Fits to equation 4.3 to segments of currents simulated by drawing from a mixture of two binomial distributions with different baseline  $P_O$ s. The estimate for  $i$  retrieved by letting the parameter vary is much lower than the actual value for  $i$ . Fixing  $i$  to the correct value results in a fit which underestimates the number of channels  $N$ .

when selecting segments of current manually. We took our full current records from each excised patch from cells expressing WT-GFP+SUR1 or W311\*-GFP+SUR1, divided them into 1 second segments, and plotted the mean current/variance relationship for each segment (Figure 4.7A). We fit the data to equation 4.3 either with  $i$  allowed to vary freely, or with  $i$  fixed to 4.32 pA. Our estimates for  $i$  when it was allowed to vary freely were similar to our estimates from Figure 4.5, with no patch yielding a value above 3 pA (Figure 4.7B). The fits with  $i$  fixed to 4.32 pA clearly fit the data less well, and the resulting estimate for the open probability on patch excision exceeded 1 for nearly every patch, which is of course not possible.

Given these results, we chose not to use noise analysis to calculate the  $P_O$  directly for each patch. In addition, Cukras *et al.* (87) compared the  $P_O$  calculated from noise analysis and the  $P_O$  calculated by application of saturating concentrations of PIP<sub>2</sub> to a variety of K<sub>ATP</sub> channel mutants, and found only a weak correlation between the two methods (87).

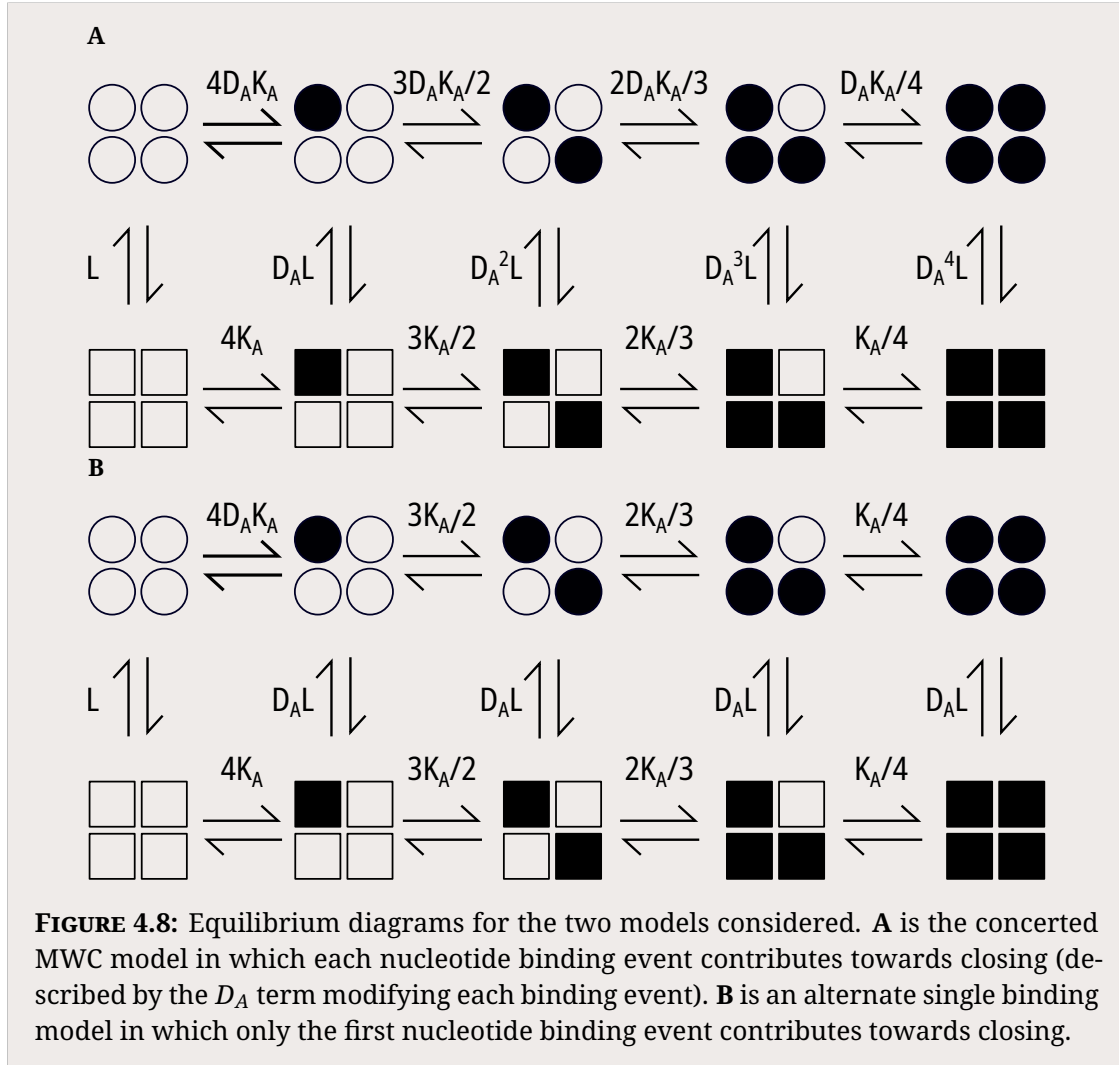
#### 4.2.4 Comparing models

We expanded Scheme I from Figure 4.2A to account for the four inhibitory nucleotide binding sites of K<sub>ATP</sub> (Figure 4.8A). In addition, we considered an alternate model



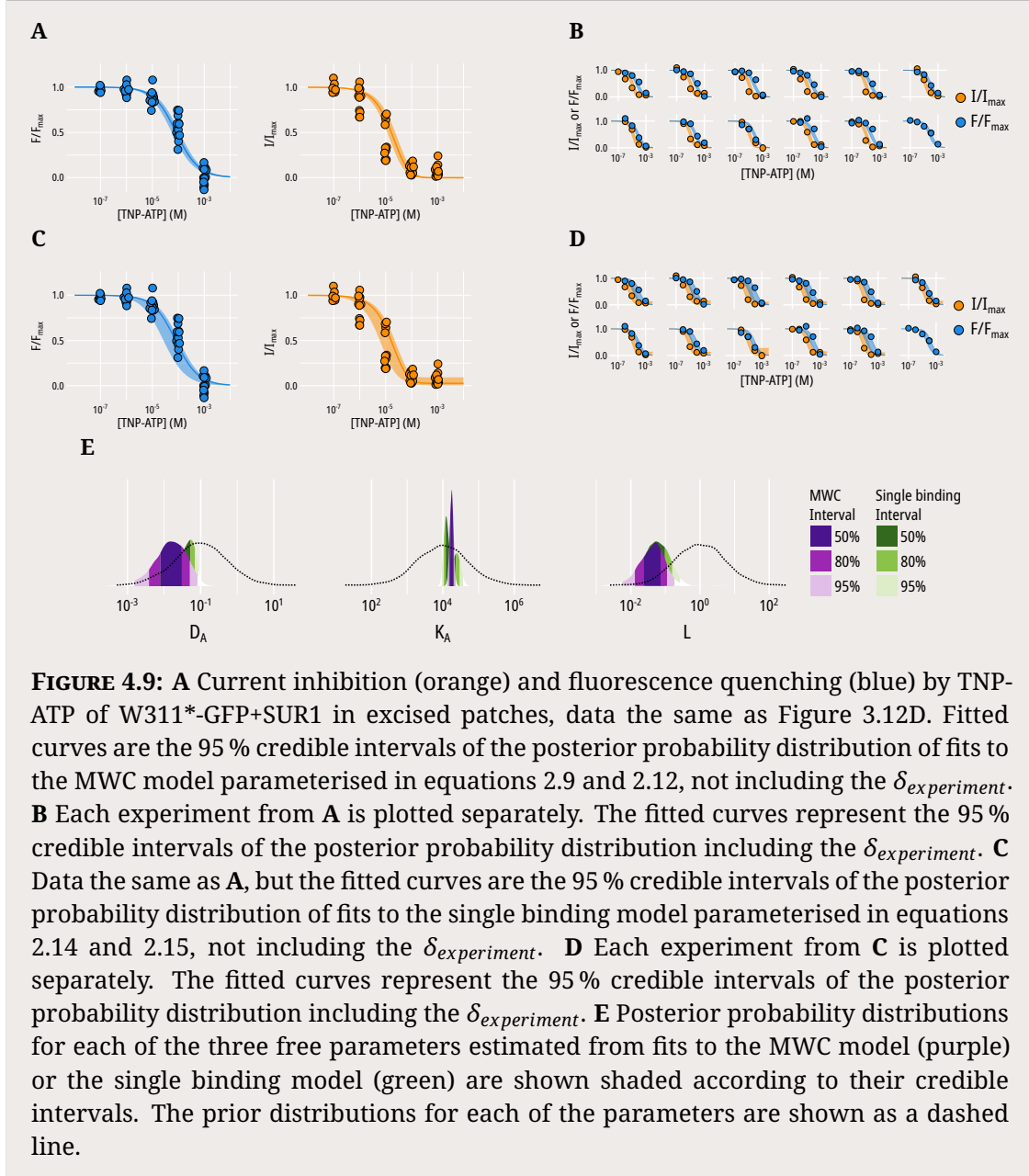
in which only the first nucleotide binding event contributes towards closure of the channel, and thus there is no cooperativity between subunits (Figure 4.8B). We then fit our observed TNP-ATP binding and current inhibition data from excised patches expressing W311\*-GFP+SUR1 to equations 2.9 and 2.12 respectively.

Both models fit our data reasonably well (Figure 4.10), although the posterior distributions of the fits to the MWC model (Figure 4.9A, 4.9B) are narrower than those for the single binding model (Figure 4.9C, 4.9D). Examining the posterior distributions for the three parameters, both models yield similar estimates, with much narrower distributions for  $K_A$  than for  $D_A$  and  $L$  (Figure 4.9E). The cross-correlation plots for the parameter estimates indicate that the model is identifiable given the



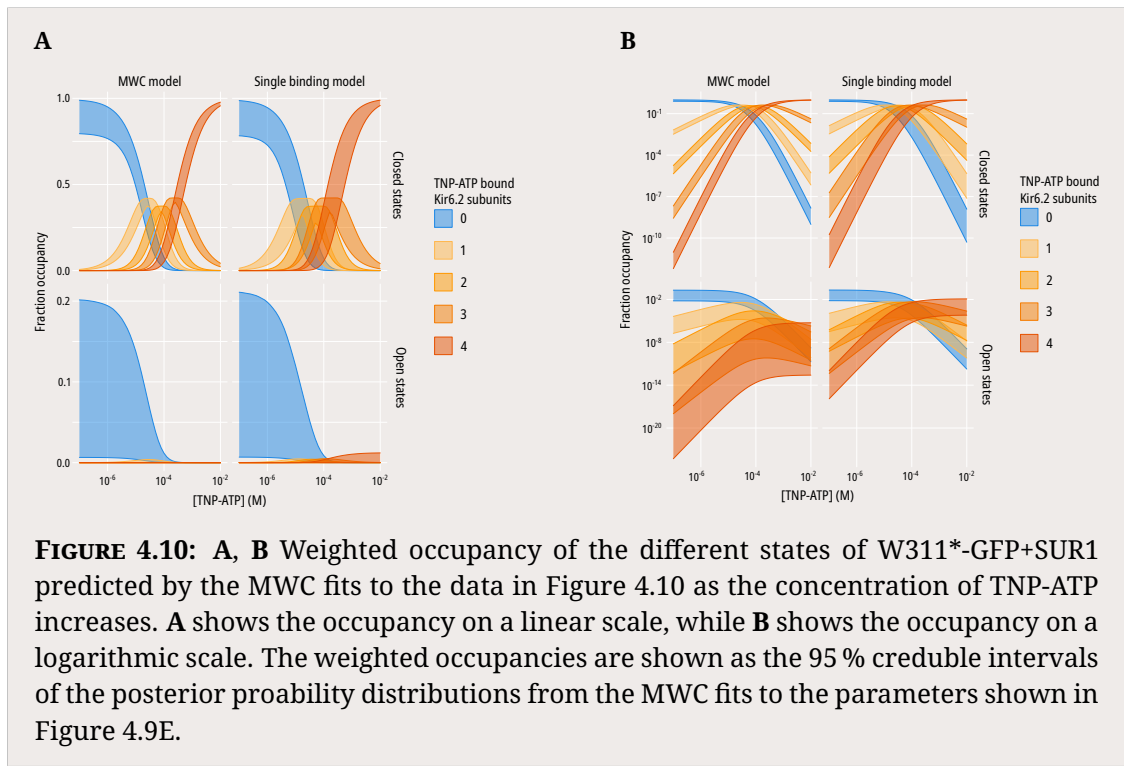
data, with well bounded ellipses clearly visible (Figure A.14A). We compared the ability of the two models to explain the data with two complimentary methods. First, we used bridge sampling to calculate a Bayes factor of  $1.1 \times 10^4$  in favor of the MWC model over the single binding model (200). The Bayes factor can be interpreted as the weight of evidence in favour of one model over another (201). Specifically, the observed data are  $1.1 \times 10^4$  more likely to have occurred under the MWC model than they are under the single binding model. In addition, we performed leave-one-out cross-validation (LOO-CV), which approximates the out-of-sample predictive accuracy of each of the fitted models (202). The MWC model fit has a higher expected predictive accuracy than the single binding model (ELPD

increase of  $27.3 \pm 6.3$ ). Together, the Bayes factor and LOO-CV scores favour a concerted MWC binding model.



The 95 % credible intervals for  $K_A$  are  $9 \times 10^3 \text{ M}^{-1}$  to  $1.7 \times 10^4 \text{ M}^{-1}$  for the MWC model, corresponding to a  $K_d$  of 56  $\mu\text{M}$  to 110  $\mu\text{M}$ . The 95 % credible intervals for  $L$  are 0.007 to 0.254, which is equivalent to an unliganded  $P_O$  of <0.01 to 0.2. This is a broad range of predicted  $P_O$ , which may reflect the variability of PIP<sub>2</sub> concentrations in the excised patches. The 95 % credible intervals for  $D_A$  are 0.002 to 0.096. This

low range for  $D_A$  indicates very strong coupling between TNP-ATP binding to Kir6.2 and  $K_{ATP}$  channel closure. Based on the fits to the data, we can illustrate how these models couple nucleotide binding to the functional state of the channel by predicting the occupancy of the different states of the  $K_{ATP}$  channel defined in Figure 4.8. Figure 4.10 shows the weighted occupancy of each of the ten states across a range of TNP-ATP concentrations as predicted by our fits to an MWC or single binding model. Qualitatively, the models make similar predictions; as nucleotide binding is so tightly coupled to pore closure, there is a vanishingly small proportion of  $K_{ATP}$  channels which exist in the open state with two or more TNP-ATP molecules bound to Kir6.2 subunits under the MWC model. Crucially however, for the single binding model to explain the data in Figure 4.8, it predicts that even at saturating nucleotide concentrations a reasonable fraction of  $K_{ATP}$  channels (up to 1 %) will be open even with all four Kir6.2 subunits bound to nucleotide.



### 4.2.5 Discussion

Measuring binding of TNP-ATP to  $K_{ATP}$  channels concurrently with measuring inhibition of channel currents has allowed us to test the predictions of prior studies about the stoichiometry of nucleotide binding, and the suitability of an MWC model to describe inhibition of the channel. We have established that a simple MWC model is capable of describing both inhibition of  $K_{ATP}$  channel currents as well as the binding of nucleotides to the Kir6.2 subunit. There has been some debate over the stoichiometry of nucleotide inhibition of the  $K_{ATP}$  channel, with some research indicating that a single Kir6.2 subunit binding to ATP is sufficient to close the channel, while other studies have suggested that further subunit binding events contribute additively to pore closure. Our data suggest that these findings can be reconciled with the observation that even within the framework of a concerted MWC model, where each nucleotide binding event is energetically coupled to the pore, the proportion of  $K_{ATP}$  channels which are in the open state with more than one TNP-ATP molecule bound to a Kir6.2 subunit is essentially nil. This is of course caveated by our assumption that TNP-ATP, while exhibiting a higher affinity for the channel than by ATP, does not alter transduction of binding to inhibition.

However, a model capable of describing  $K_{ATP}$  channel function should also be able to explain how mutations or other perturbations disrupt the regulation of channel function by nucleotide inhibition. In the following chapters, we will explore whether this method and model are capable of discerning between alterations of nucleotide binding,  $K_{ATP}$  channel gating, and transduction of nucleotide binding to the pore. In addition, these experiments should allow us to test the ability of a simple MWC model to explain the variety of functional changes we observe.

# 5

## Nucleotide regulation of Kir6.2

### Contents

---

5.1	Introduction	95
5.2	Nucleotide binding	96
5.2.1	G334D abolishes nucleotide binding	96
5.3	Channel gating	97
5.3.1	C166S alters inhibition without affecting binding	97
5.3.2	Mutations at E179 alter both inhibition and binding	99
5.3.3	Mutations at K39 alter both inhibition and binding	101
5.4	Discussion	102

---

### 5.1 Introduction

There are variety of ways in which mutations in Kir6.2 can lead to altered K<sub>ATP</sub> channel function, and often lead to diseases of insulin secretion (5, 203–208). These can be divided into two broad categories; mutations which have a ligand-independent effect, and those which affect the ligand-dependent regulation of the channel, covered in more detail in Chapter 1. Nucleotide inhibition of the K<sub>ATP</sub> channel can be altered by mutations through three separate mechanistic routes. A mutation which reduces sensitivity of the channel to nucleotide inhibition may act by (i) reducing the affinity of nucleotide binding to Kir6.2, (ii) increasing the open probability of the

channel, (iii) reducing the transduction of nucleotide binding to channel closure, or (iv) a combination of all three.

Interrogation of residues in categories (iii) and (iv) is very difficult using electrophysiological measures alone, as without measuring binding of nucleotides directly it is hard to truly separate effects on open probability from effects on binding and transduction (209). In this chapter, we aim to clarify the role of several residues implicated in regulating the inhibitory effect of nucleotides on K<sub>ATP</sub> channel function by measuring TNP-ATP binding directly to the inhibitory nucleotide binding site on Kir6.2, where possible in conjunction with simultaneous current measurements.

## 5.2 Nucleotide binding

### 5.2.1 G334D abolishes nucleotide binding

Residue G334 of Kir6.2 is located in the C-terminal region (Figure 5.1A) and has been hypothesised to form part of the ATP binding site since electrophysiological studies demonstrated a dramatic reduction in nucleotide sensitivity upon mutation of the residue (53, 69, 180). In addition, mutation of this residue to aspartic acid (G334D) results in severe DEND syndrome (permanent neonatal diabetes mellitus with neurological complications) (112). This hypothesis was confirmed by the solving of cryo-EM structures of K<sub>ATP</sub> in the presence of ATP, which revealed the close proximity of residue G334 to the bound ATP (26, 77, 82, 210). Mutating G334 to a total of 13 different amino acid substitutions led to a increase in the IC<sub>50</sub> for ATP by over an order of magnitude in excised patches (180). However, only two of those substitutions (R and K) resulted in any changes in nucleotide-independent channel gating when examined at the single-channel level, with unliganded P<sub>O</sub> remaining constant. It has therefore been suggested that while G334 forms part of the ATP binding site of Kir6.2, it does not participate in channel gating or transduction of ligand binding to the channel pore.

We sought to test this directly by measuring the binding of TNP-ATP in unroofed membranes to W311\*,G334D-GFP+SUR1. Fluorescence spectra captured

from unroofed membrane patches expressing W311\*,G334D-GFP+SUR1 were indistinguishable from those expressing W311\*-GFP+SUR1. The location of the ANAP peak and the bleaching characteristics were also identical. We found that ANAP fluorescence from W311\*,G334D-GFP+SUR1 was barely quenched by even 1 mM TNP-ATP (Figure 5.1B, 5.1C), reducing the apparent binding EC<sub>50</sub> from 30 µM to 45 µM to at least 2.8 mM (Figure 5.1D). We cannot be sure of the upper boundary of the apparent binding EC<sub>50</sub> given how little quenching we were able to achieve even with 1 mM TNP-ATP. Unfortunately, we were unable to resolve macroscopic currents from W311\*,G334D-GFP+SUR1 in excised patches despite seeing fluorescence in unroofed membranes. Thus, we were unable to measure TNP-ATP inhibition of this construct. In electrophysiological experiments on K<sub>ATP</sub> channels containing the G334D mutation, other studies have found that currents are insensitive to inhibition by as much as 10 mM ATP (69, 112). In the framework of our MWC model, the only explanation for a dramatic decrease in both nucleotide binding and inhibition is a decrease in  $K_A$ , the microscopic binding affinity. However, as we were unable to measure TNP-ATP inhibition, we were unable to determine whether the G334D substitution affected transduction in addition to this binding effect.

## 5.3 Channel gating

### 5.3.1 C166S alters inhibition without affecting binding

Residue C166 of Kir6.2 is located at the cytosolic end of the second transmembrane domain (Figure 5.2A, (26, 77, 82, 210)), and has been suggested to play a role in regulating the intrinsic gating of the channel (67, 126, 175, 211–213). Mutations at this residue lead to dramatically increased unliganded  $P_O$  in single-channel experiments (126, 175, 212), and a reduction in sensitivity to nucleotide inhibition at both single-channel and the macroscopic level (73, 126, 175, 212, 213). In addition, two substitutions at this residue (F and Y) have been found to cause severe DEND syndrome (211). Electrophysiological measurements alone are not sufficient to distinguish between the reduction in sensitivity to nucleotide inhibition being caused

by the increase in intrinsic  $P_O$  alone, whether there is an additional disregulation of transduction, or even if there is a long-distance effect on nucleotide binding.

We measured TNP-ATP binding to W311\*,C166S-GFP+SUR1 in unroofed membranes to determine how mutations at C166 reduce sensitivity to nucleotide inhibition (Figure 5.2B). We observed no real change in binding of TNP-ATP to the channel ( $EC_{50}$  of 44  $\mu M$  to 74  $\mu M$ ). If the C166S mutation solely increases the  $P_O$  of the channel, we would expect an increase in the apparent  $EC_{50}$  of nucleotide binding due to the preference of nucleotides for the closed state of the channel. This finding therefore suggests a role for C166 in the transduction of nucleotide binding to the channel pore.

To investigate this further, we excised patches expressing W311\*,C166S-GFP+SUR1 and measured current inhibition and fluorescence quenching by TNP-ATP simultaneously (Figure 5.3A). We found that the apparent affinity for nucleotide binding was indistinguishable from that for W311\*-GFP+SUR1, and similar to our observations in unroofed membranes (Figure 5.3B,  $EC_{50}$  of 26  $\mu M$  to 218  $\mu M$ ). Consistent with the literature, we did observe a large reduction in the apparent sensitivity of W311\*,C166S-GFP+SUR1 currents to inhibition by TNP-ATP (Figure 5.3C,  $IC_{50}$  of at least 155  $\mu M$ ). Intuitively, a change in nucleotide-dependent channel gating which is not accompanied by a change in nucleotide binding must be due (at least in part) to a change in the transduction of nucleotide binding to channel gating.

Fitting our data to the MWC-type model described previously (Figure 5.4A, 5.4B), we found that in addition to the effects of the C166S mutation on the intrinsic open probability of  $K_{ATP}$ , there is a striking shift in  $D_A$  (Figure 5.4C). This shift to a value much closer to unity indicates that binding of TNP-ATP to W311\*,C166S-GFP+SUR1 favours the closed state far less than binding of TNP-ATP to W311\*-GFP+SUR1. Equivalently, binding of TNP-ATP to the mutant channel is less able to induce closure of the pore. Thus, even at millimolar concentrations of TNP-ATP when all of the Kir6.2 subunits are predicted to be bound by nucleotide, the mutant  $K_{ATP}$  channels are still able to open.

Notably, the MWC fit to the current inhibition data has wide 95 % posterior probability credible intervals (Figure 5.4B). Unfortunately, we were not able to use

higher concentrations of TNP-ATP due to its purification as a TEA<sup>+</sup> salt. High mM concentrations of TEA<sup>+</sup> inhibit K<sub>ATP</sub> channels, and we determined that for W311\*-GFP+SUR1 and W311\*,C166S-GFP+SUR1 concentrations of above 1 mM TEA<sup>+</sup> began to inhibit currents to an extent that would interfere with our measurements (Figure 5.5A, 5.5B). The precise ratio of TEA<sup>+</sup> to TNP-ATP in our solutions is unknown, but is assumed to be between 1:1 and 3:1. Any additional inhibition observed at TNP-ATP concentrations greater than 1 mM for W311\*,C166S-GFP+SUR1 will therefore be (at least in part) due to the presence of TEA<sup>+</sup>. However, we do see that even at concentrations of 10 mM ATP, W311\*,C166S-GFP+SUR1 is not fully inhibited (Figure 5.4B, open circle).

Curiously, despite the wide posterior probability credible intervals for the MWC fit to the observed current inhibition data in Figure 5.4B, the probability distributions for the underlying parameter values for W311\*,C166S-GFP+SUR1 are not much wider than those observed for W311\*-GFP+SUR1 (Figure 5.4C). Thus, the variability of current inhibition observed for 1 mM TNP-ATP is not due to increased uncertainty in our MWC parameter estimates. Instead, the variability may mean that the C166S substitution alters the nucleotide regulation of the K<sub>ATP</sub> channel such that small changes in the energetics of the underlying gating mechanism result in large changes in the observed current. This may help to explain the differences in inhibition of K<sub>ATP</sub> channels with substitutions at C166 by high nucleotide concentrations observed across multiple electrophysiological studies (177, 181, 213, 214).

### 5.3.2 Mutations at E179 alter both inhibition and binding

Residue E179 of Kir6.2 is located in the C-terminal region of Kir6.2 between the inhibitory nucleotide binding site and the proposed PIP<sub>2</sub> binding site. In one early predicted structure of Kir6.2, it was theorised that E179 would form part of the nucleotide binding pocket directly, potentially coordinating the adenine ring of ATP directly through hydrogen bonding (113). In another, it was hypothesised to form part of the PIP<sub>2</sub> binding pocket instead (129). Electrophysiological experiments painted a confusing picture of the residue's role (113). Mutation to an amino

acid capable of forming hydrogen bonds (Q) resulted in no change in the IC<sub>50</sub> for nucleotide inhibition (although a separate study found that Q increased the IC<sub>50</sub> (104)), while only one of two amino acids incapable of forming hydrogen bonds tested (M and L) resulted in an increased IC<sub>50</sub>. In addition, mutation of the residue to asparagine (which is not capable of forming hydrogen bonds) not only dramatically increased the nucleotide IC<sub>50</sub>, but also increased the intrinsic open probability of the channel (113).

The cryo-EM structures of K<sub>ATP</sub> in complex with ATP revealed that bound ATP adopted a radically different conformation to that proposed in early models, and showed that the E179 side chain actually lies over 8 Å away from bound ATP (26, 77, 82, 210) (Figure 5.6A). Unfortunately, no structure has been resolved in the presence of PIP<sub>2</sub> to date. However, coarse-grained molecular dynamics simulations using the cryo-EM structures as a starting point indicate that E179 may form part of the PIP<sub>2</sub> binding pocket (75). In addition, mutation to E179K results in reduced inhibition of the channel by the sequestering agent neomycin - potentially due to an increased affinity of the mutated residue for PIP<sub>2</sub> (75).

To attempt to resolve the precise role of E179 in nucleotide binding and inhibition, we first determined how ATP and TNP-ATP inhibition of K<sub>ATP</sub> channels was affected by mutation of E179 to A or K (Figure 5.6C, 5.6B. For E179A-GFP+SUR1 and E179K-GFP+SUR1, we observed an increase in IC<sub>50</sub> for both ATP and TNP-ATP inhibition (Figure 5.7A). ATP inhibition did not seem to be influenced by the identity of the replacement amino acid (49 µM to 145 µM and 43 µM to 138 µM respectively), while TNP-ATP inhibition was less reduced by mutation to an A than a K (6.5 µM to 21 µM and 16 µM to 87 µM respectively). Introducing the mutations into the ANAP-labelled construct did not affect the relative changes in inhibition by either nucleotide, with ATP inhibition occurring at similar IC<sub>50</sub>s for A and K (162 µM to 562 µM and 191 µM to 479 µM respectively) and with A increasing the IC<sub>50</sub> for TNP-ATP less than K (14 µM to 44 µM and 42 µM to 224 µM respectively). Measurements of TNP-ATP binding mirrored our observations for current inhibition by TNP-ATP, with mutation to both A and K resulting in an increased apparent binding EC<sub>50</sub>, with A having less of

an effect than K ( $166 \mu\text{M}$  to  $417 \mu\text{M}$  and  $347 \mu\text{M}$  to  $813 \mu\text{M}$  respectively). Fitting the combined data to the MWC-type model, we found that both mutations resulted in a decreased  $K_A$  estimate, with no apparent change in  $L$ . In addition, mutation to a K led to a  $D_A$  value closer to unity than for E or the wild-type A (Figure 5.8).

### 5.3.3 Mutations at K39 alter both inhibition and binding

Residue K39 of Kir6.2 is located in the N-terminal region of Kir6.2, and is positioned between the inhibitory nucleotide binding site and the proposed PIP<sub>2</sub> binding site (Figure 5.9A). In previous studies, the mutation K39A has shown a small reduction in open probability (87), and a small reduction in sensitivity to nucleotide inhibition (66, 87). These effects are somewhat contradictory, as mutations which reduce open probability tend also to increase sensitivity to nucleotide inhibition. In each of the cryo-EM structures of K<sub>ATP</sub>, the K39 side chain appears to coordinate the bound ATP molecule (26, 77, 82, 210). These structures are presumed to represent the closed state of the channel, and no PIP<sub>2</sub> bound structure of the channel has yet been solved. However, molecular dynamics simulations using the ATP-bound structure as a starting point and introducing PIP<sub>2</sub> suggest that the K39 residue is able to contact both ligands (2). This suggests a potential role for K39 in the binding sites of both ATP and PIP<sub>2</sub>, which may explain the contradictory findings of open probability and nucleotide inhibition changes when the residue is mutated.

We tested three mutations at K39 (K39A, K39E, K39R) to examine the effects of changing the side chain characteristics on nucleotide binding and inhibition. Mutation to E (opposite charge) or R (same charge) results in an increase in IC<sub>50</sub> for ATP inhibition for both WT and W311\* backgrounds (Figure 5.9B, 5.11A). We did not see an increase in the IC<sub>50</sub> for ATP inhibition when K39 was mutated to A (neutral) in either background (Figure 5.9B, 5.11A). Inhibition by TNP-ATP displayed a different profile depending on the mutant residue (Figure 5.10A). In both WT and W311\* backgrounds, inhibition by TNP-ATP exhibited higher IC<sub>50</sub> values for K39A and K39E than we observed for K39R, which was not really distinguishable from K39 (5.11A). Our docked conformation for TNP-ATP suggests that the TNP-moiety of

the nucleotide may result in extra contacts with K39 compared to ATP, which may be the cause of the different sensitivity to inhibition between the two nucleotides when this residue is mutated. Measurements of TNP-ATP binding showed increases in the EC<sub>50</sub> estimates for each of the three mutations (Figure 5.10B, 5.11A).

Fits of the combined data to the MWC model gave parameter estimates for  $K_A$  that decreased from K>R>E>A (Figure 5.12). In addition, mutation to an E or an A resulted in  $D_A$  values closer to unity. Interpretation of these parameters for the R and A mutations is frustrated by the differences in inhibition between TNP-ATP and ATP; we cannot be sure that these differences in binding and inhibition are due to the identity of the nucleotide rather than the identity of the residue. However, the K39E mutation displayed similar inhibition for both TNP-ATP and ATP. The increase in our estimate for  $D_A$  when K39 is mutated to an A or an E, but not for R, may indicate a positive charge at the sidechain of this residue is important for transduction of nucleotide binding to the channel pore.

## 5.4 Discussion

Fitting a concerted MWC model to the combined datasets obtained by measuring TNP-ATP binding to Kir6.2 in combination with current inhibition allows us to distinguish between mutations which affect nucleotide binding, ligand-independent channel gating, and the transduction of nucleotide binding to channel gating. This is best demonstrated by our results for W311\*,C166S-GFP+SUR1, which we propose not only increases the unliganded  $P_O$  of the K<sub>ATP</sub> channel as described many times previously (illustrated in this experiment by the increase in  $L$  from the MWC fit), but also reduces the ability of TNP-ATP to induce channel closure ( $D_A$  approaches unity). Substitutions of C166 must therefore alter the structure of the channel such that in addition to the unliganded open state being more energetically favourable than in wild-type channels, nucleotides are no longer able to stabilise the closed state to the same extent as in wild type channels.

We can quantify this difference by calculating the energy contribution of nucleotide binding to the closed state of the two constructs at saturating concentrations

of TNP-ATP, given by the formula  $-RT\ln(D_A^4)$  where  $R$  is the gas constant and  $T$  is the absolute temperature (assumed to be 296 K). The free energy TNP-ATP binding contributes to the closed state of W311\*-GFP+SUR1 is 23.0 kJ M<sup>-1</sup> to 63.4 kJ M<sup>-1</sup>, while the free energy TNP-ATP binding contributes to the closed state of W311\*,C166S-GFP+SUR1 is only 20.4 kJ M<sup>-1</sup> to -3.05 kJ M<sup>-1</sup>. However, as the energy contributed is dependent on the identity of the ligand, it is possible that TNP-ATP stabilises the closed state of the channel to a different extent than ATP.

Interpretation of our findings for substitutions at E179 and K39 of Kir6.2 are not as straightforward. Mutations at these residues lead to a complex mixture of changes to both the microscopic binding affinity for TNP-ATP ( $K_A$ ) and the transduction of nucleotide binding ( $D_A$ ). Given that E179 is predicted to form part of the PIP<sub>2</sub> binding site (75, 129), we might expect mutations at this location to alter the  $P_O$  of channels in excised patches due to changes in the PIP<sub>2</sub> binding affinity. Antcliff *et al.* (113) found that mutation to asparagine increased the  $P_O$  of K<sub>ATP</sub> channels in excised patches, while Pipatpolkai *et al.* (75) observed that mutation to a lysine caused a reduction in the IC<sub>50</sub> for neomycin inhibition of the channel. Here, mutation to alanine or lysine did not result in a change in our estimate for  $L$ , which we would expect to see if there was a change in the  $P_O$  of the channel resulting from altered PIP<sub>2</sub> affinity. Instead, we observed changes in our estimates for  $K_A$ , the microscopic binding affinity for TNP-ATP, and  $D_A$ , the transduction of nucleotide binding to channel gating.

We believe there are two possible ways to interpret these findings. The first is to accept the shift in  $K_A$  at face value - a decrease in the apparent TNP-ATP binding affinity would suggest a role for residue E179 in forming the nucleotide binding pocket, and this function is abrogated by our mutations. Despite the distance of the residue from the bound ATP, there could be interactions between E179 and the sidechains of residues which do form the pocket (e.g. R54), such that mutation of E179 leads to alterations in the binding pocket which reduce nucleotide binding affinity and therefore our estimate of  $K_A$ . The additional effect on  $D_A$  caused by mutating the residue to K suggests a dysregulation of the transduction of nucleotide binding to the channel pore, making nucleotides less selective for the closed state.

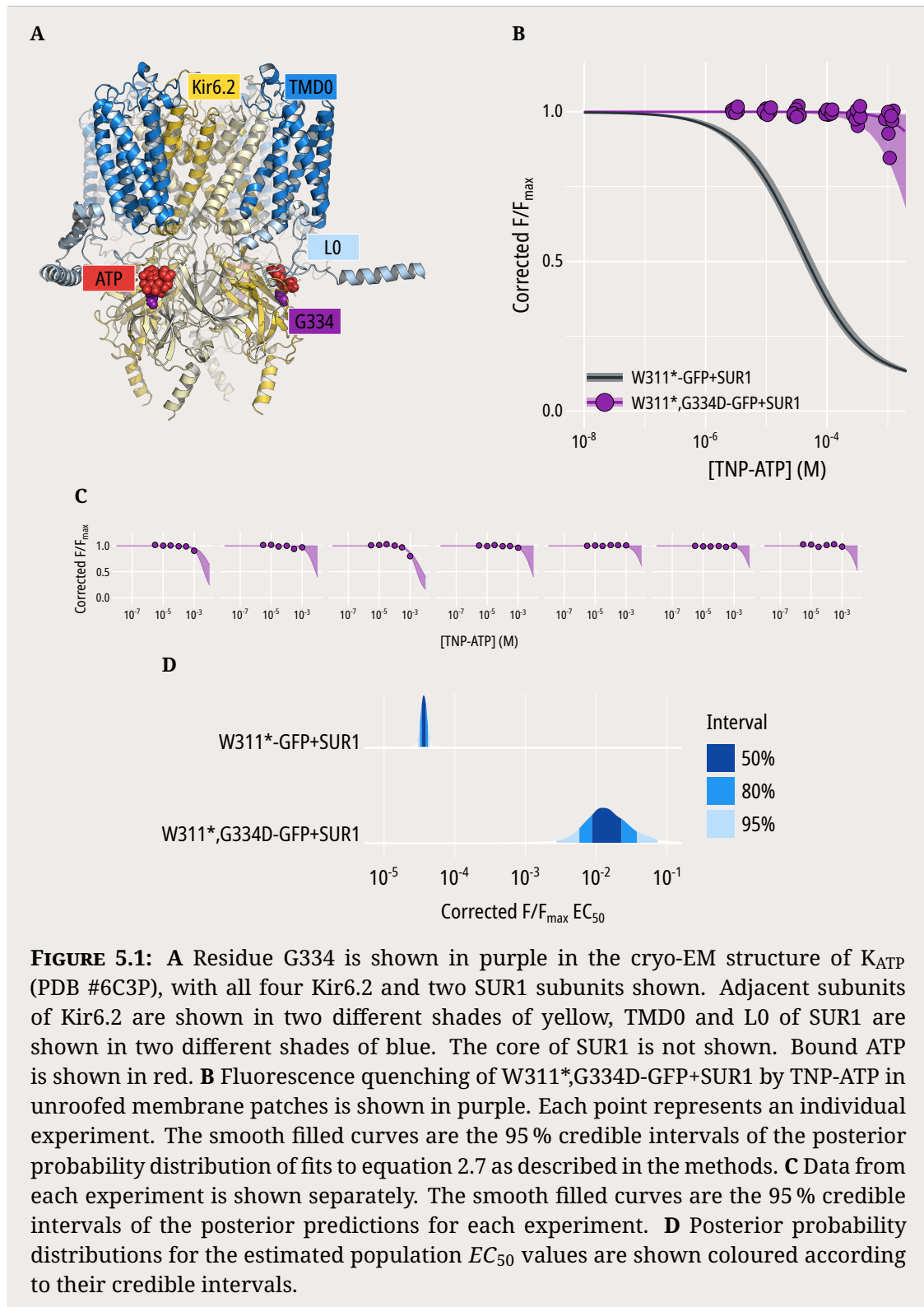
The second interpretation is possible due to the simplification of the role of PIP<sub>2</sub> in our MWC model as discussed in chapter 4. Briefly, if there is an additional allosteric interaction between nucleotide and PIP<sub>2</sub> binding to Kir6.2 which is separate to the channels open/closed state, then changes in  $K_A$  may reflect alterations in the affinity for PIP<sub>2</sub> binding in addition to, or instead of, alterations in the affinity for nucleotide binding. Thus, the decrease in  $K_A$  upon mutation of E179 may reflect an increase in PIP<sub>2</sub> affinity and demonstrate the presence of local allostery between nucleotide and lipid.

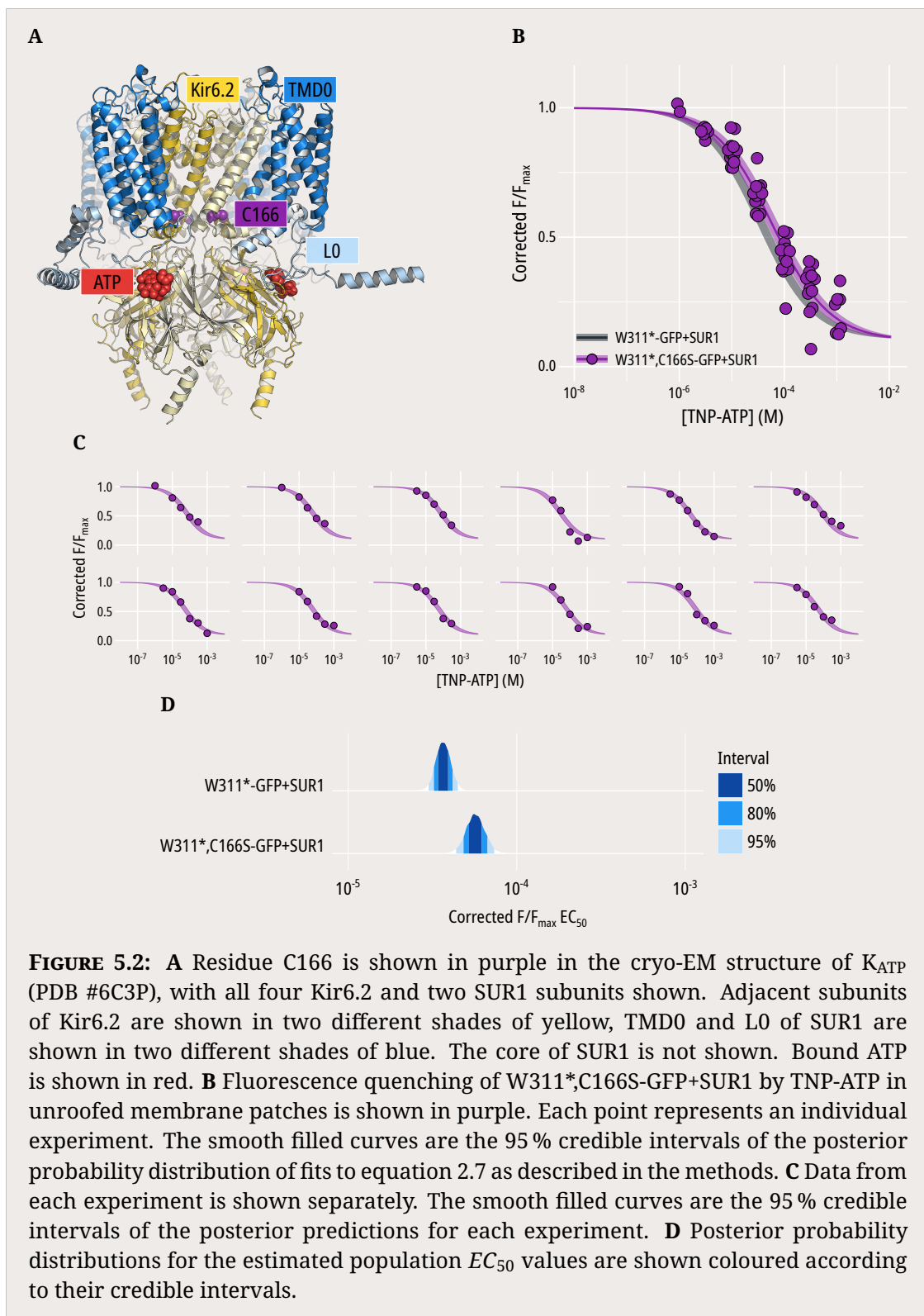
Distinguishing between these two interpretations is difficult given our current evidence, and essentially depends on the weight you place on the assumptions of each, but should be possible with one or two further experiments. Firstly, an increase in PIP<sub>2</sub> affinity should lead to an increase in channel open probability on excision (barring an effect on the relative preference of PIP<sub>2</sub> for the open state). Our inability to accurately determine the open probability of the macroscopic experiments described so far could be supplemented by single channel analysis of the mutants to test this directly. In addition, we could measure the relative affinity of PIP<sub>2</sub> for the E179 mutants directly in macroscopic patches; although as described in chapter 1 this is not as trivial as it sounds. Finally, to definitively test the existence of local allostery between the nucleotide and PIP<sub>2</sub> binding sites, we could introduce PIP<sub>2</sub> binding mutants into the C166S background. C166S channels exhibit almost no nucleotide-dependent gating; i.e. nucleotide binding is uncoupled from gating of the channel pore. Thus, any changes observed in nucleotide binding in the C166S background when PIP<sub>2</sub> affinity is changed would necessarily be due to a local allosteric interaction which does not involve the pore.

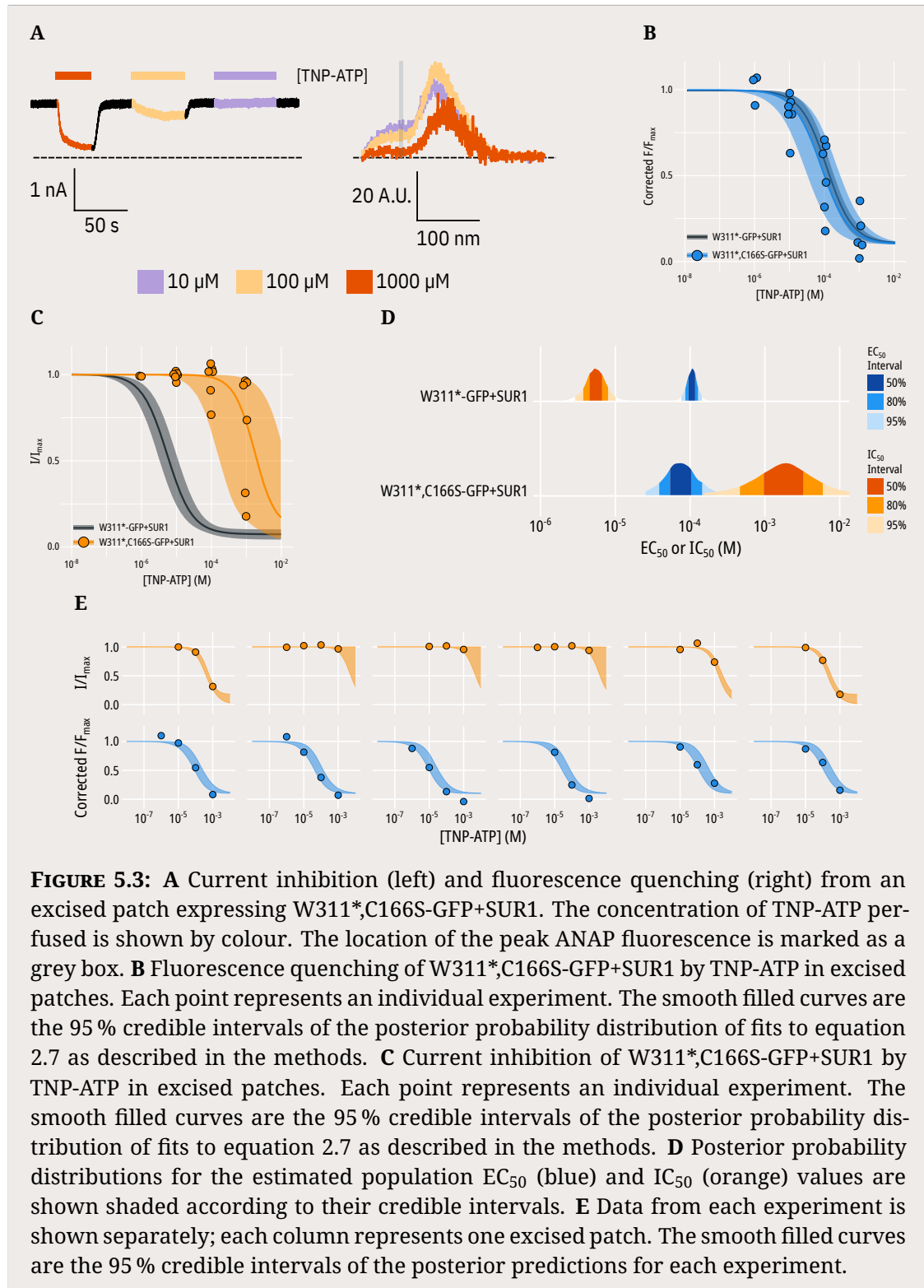
K39 is a residue which may be involved in both nucleotide and PIP<sub>2</sub> binding to Kir6.2, which may explain how mutation to an alanine at this residue appears to reduce both  $P_O$  and sensitivity to nucleotide inhibititon (66, 87). We aimed to elucidate whether K39 was directly involved in nucleotide binding by making three different substitutions with different sidechain charges - alanine, lysine, or glutamic acid - and directly measuring TNP-ATP binding. Unfortunately, we observed differences in the

relative changes in inhibition by ATP and TNP-ATP in the three different constructs, such that the substitution which had the largest effect on ATP inhibition (K39R) had the smallest effect on TNP-ATP inhibition. On examination of the cryo-EM structure of K<sub>ATP</sub>, K39 is in close proximity to the ribose ring of bound ATP (Figure 5.13A). The computational docking of TNP-ATP predicts that the TNP moiety will therefore be in close proximity of K39 (Figure 5.13B). Given this proximity, it is possible that there are extra contacts made between TNP-ATP and the K39 residue, which may go some way towards explaining the increased sensitivity of inhibition of K<sub>ATP</sub> to TNP-ATP. It may also explain why we do not observe consistent relative changes in inhibition by ATP and TNP-ATP for different mutations of the residue.

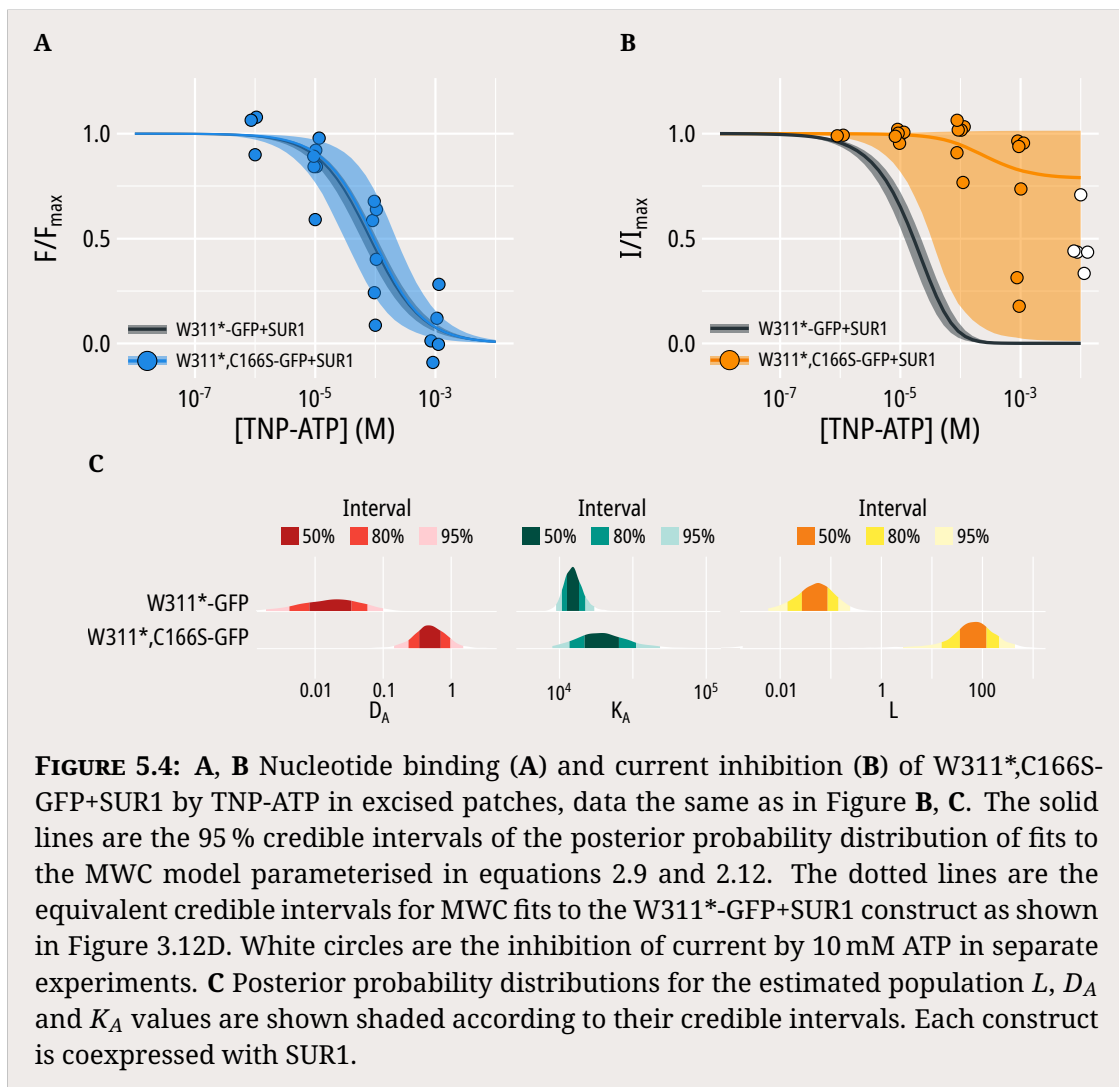
However, given that substitutions of K39 decrease the sensitivity of K<sub>ATP</sub> channels to ATP inhibition, and decrease both the sensitivity to TNP-ATP inhibition and the apparent TNP-ATP binding affinity, we can still conclude that K39 is involved in nucleotide binding to Kir6.2. For TNP-ATP, this involvement manifests mostly as a reduction in the microscopic binding affinity ( $K_A$ ), although substitution with a glutamic acid which has an oppositely-charged side chain also reduces the transduction of TNP-ATP binding to channel closure ( $D_A$ ). Despite the previously observed reduction in open probability for the K39A mutation (66, 87), we did not observe any large changes in our estimates for  $L$  for any of the mutations tested (Figure 5.12B). There is some evidence to suggest that the identity of the amino acid at position 39 affects  $P_O$ , with K39A exhibiting an estimated  $P_O$  range of 0.005 to 0.15 compared to 0.017 to 0.51 for K39E (Figure 5.12B); but given the uncertainty inherent in our data due to patch-to-patch differences in PIP<sub>2</sub> concentrations, rundown over the course of experiments, and having to normalise our data, we cannot confidently suggest there is an effect.

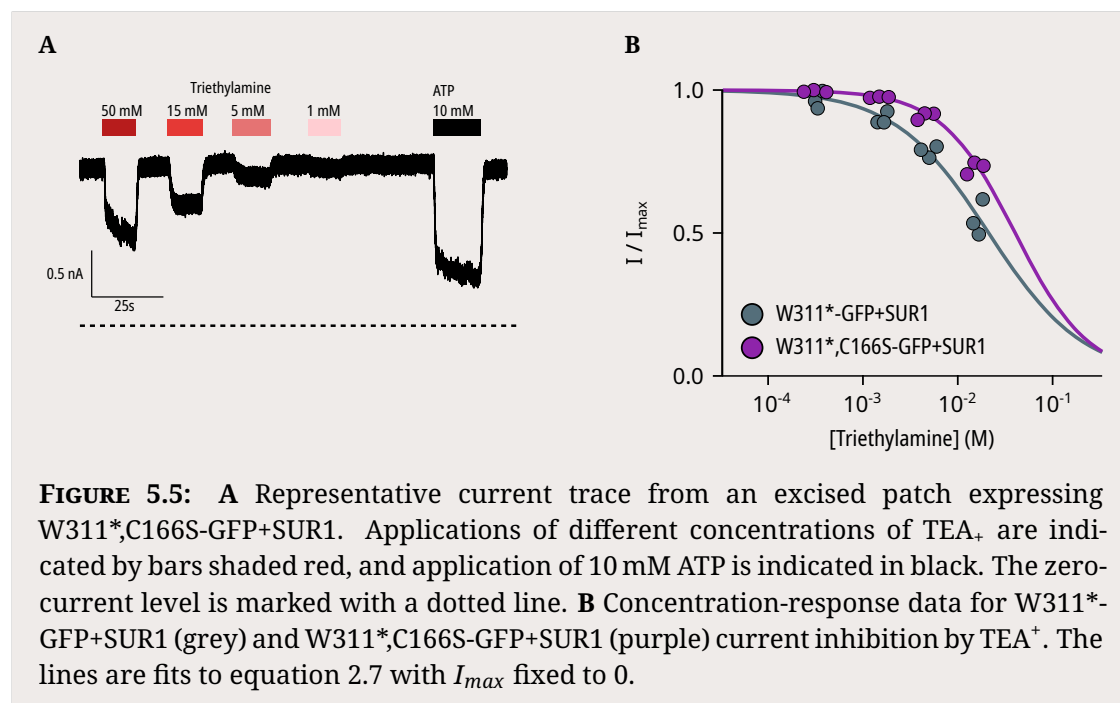




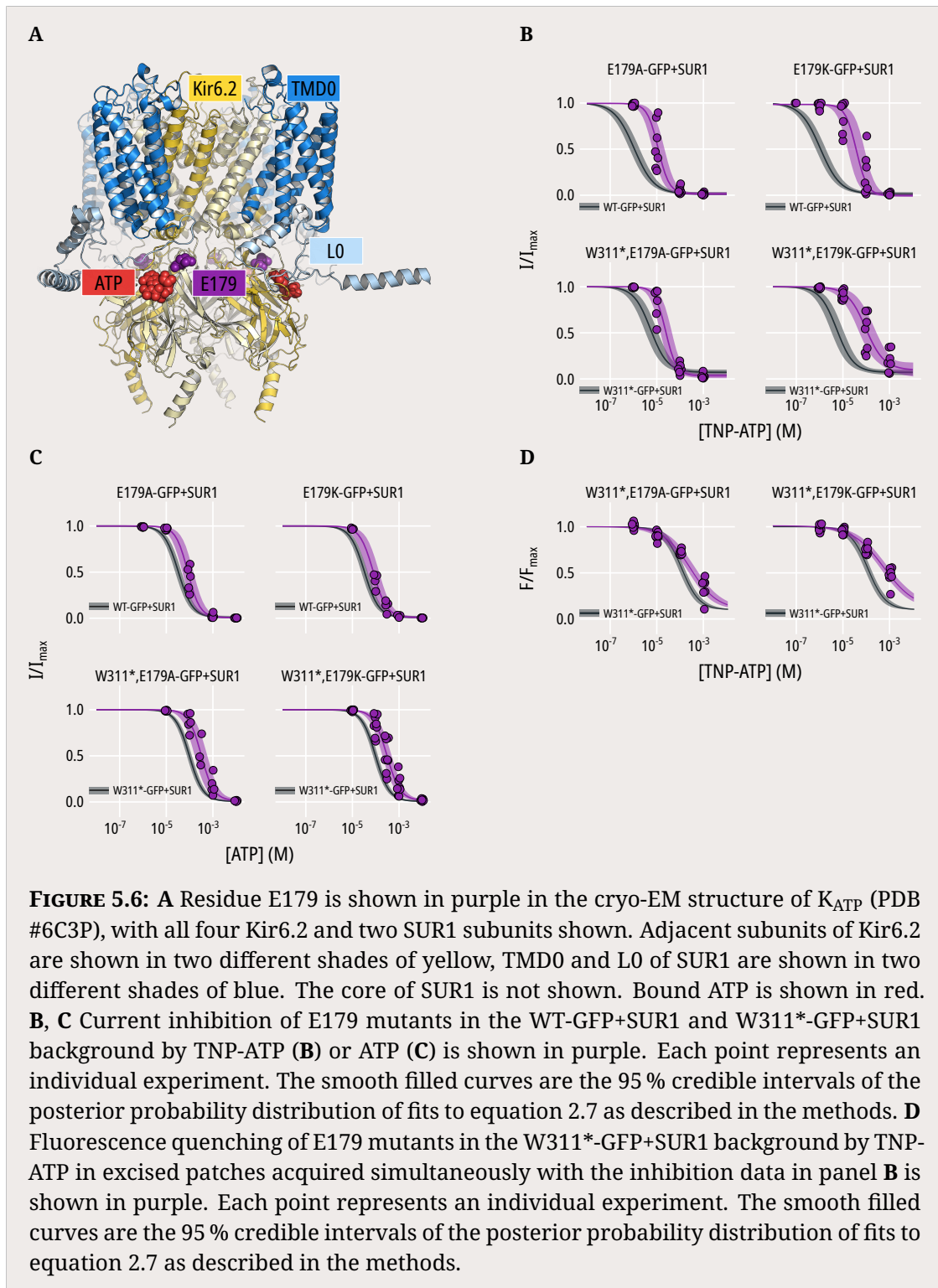


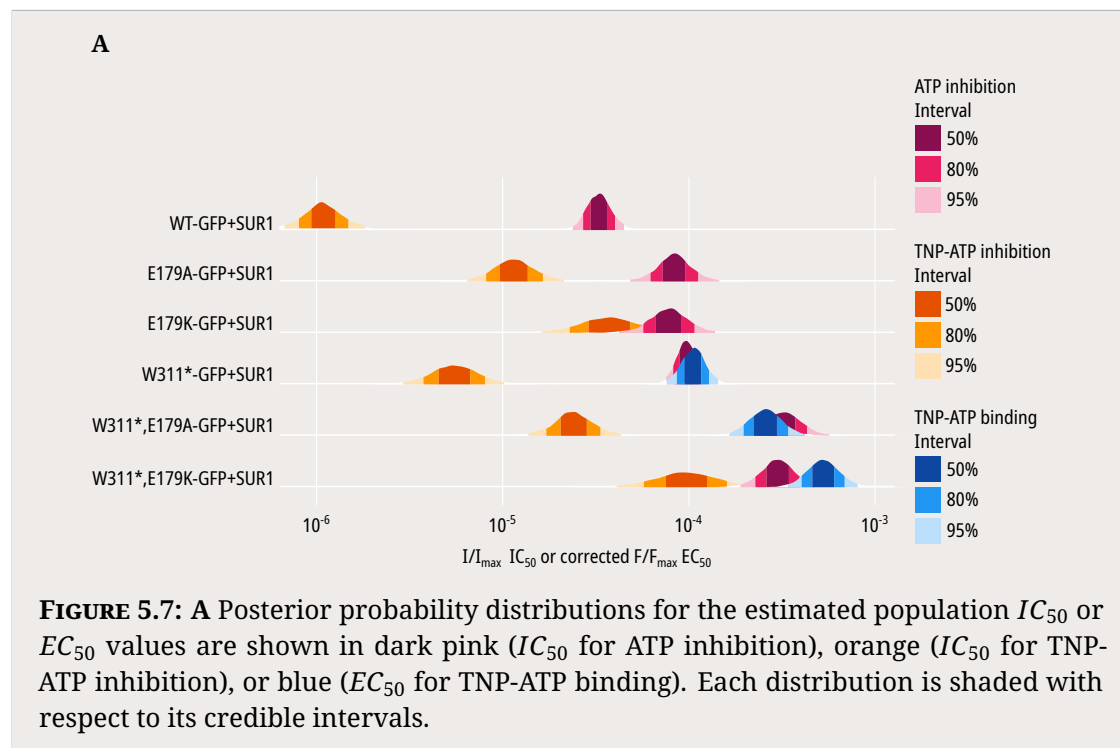
**FIGURE 5.3:** **A** Current inhibition (left) and fluorescence quenching (right) from an excised patch expressing W311\*,C166S-GFP+SUR1. The concentration of TNP-ATP perfused is shown by colour. The location of the peak ANAP fluorescence is marked as a grey box. **B** Fluorescence quenching of W311\*,C166S-GFP+SUR1 by TNP-ATP in excised patches. Each point represents an individual experiment. The smooth filled curves are the 95 % credible intervals of the posterior probability distribution of fits to equation 2.7 as described in the methods. **C** Current inhibition of W311\*,C166S-GFP+SUR1 by TNP-ATP in excised patches. Each point represents an individual experiment. The smooth filled curves are the 95 % credible intervals of the posterior probability distribution of fits to equation 2.7 as described in the methods. **D** Posterior probability distributions for the estimated population  $EC_{50}$  (blue) and  $IC_{50}$  (orange) values are shown shaded according to their credible intervals. **E** Data from each experiment is shown separately; each column represents one excised patch. The smooth filled curves are the 95 % credible intervals of the posterior predictions for each experiment.

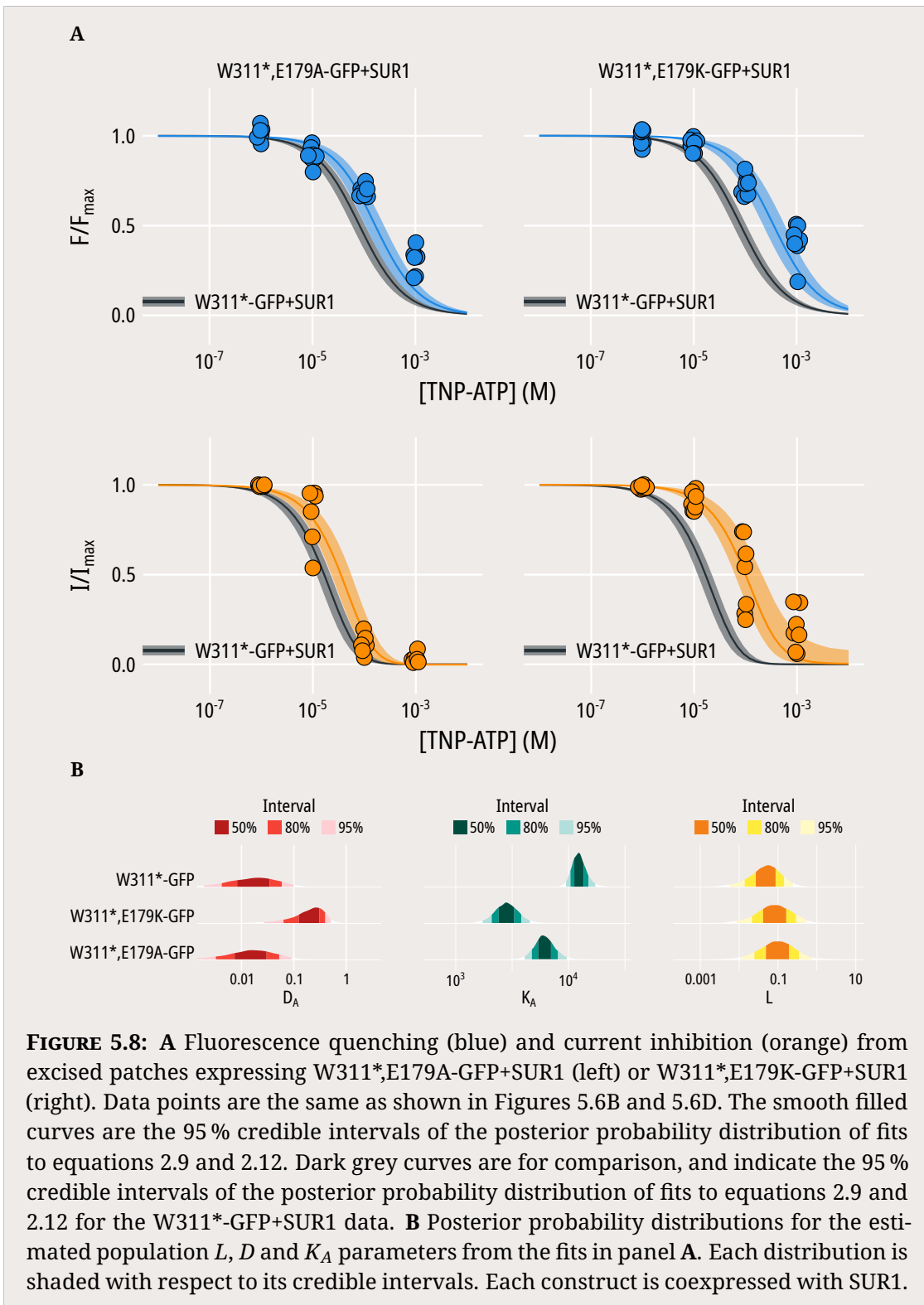


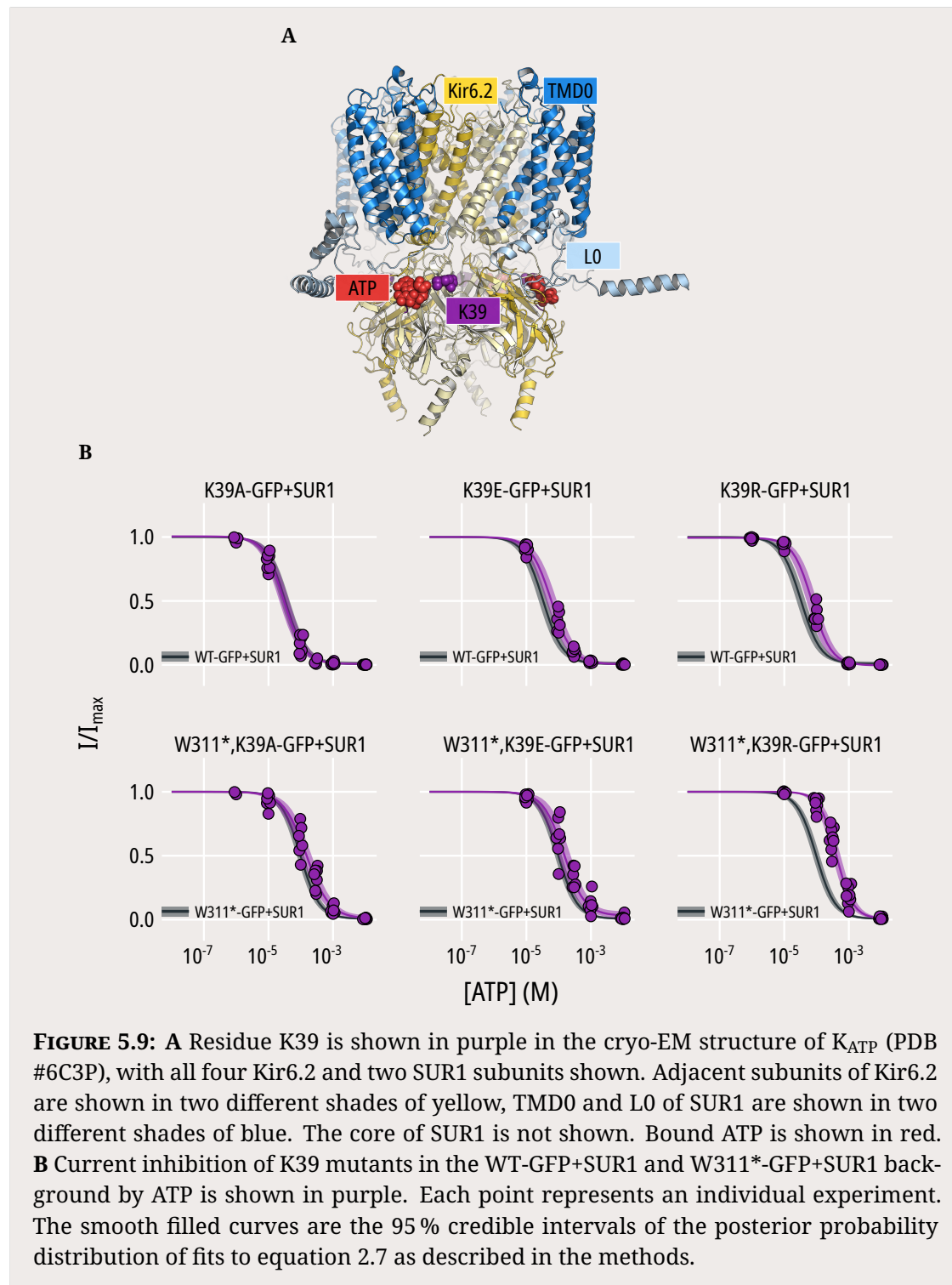


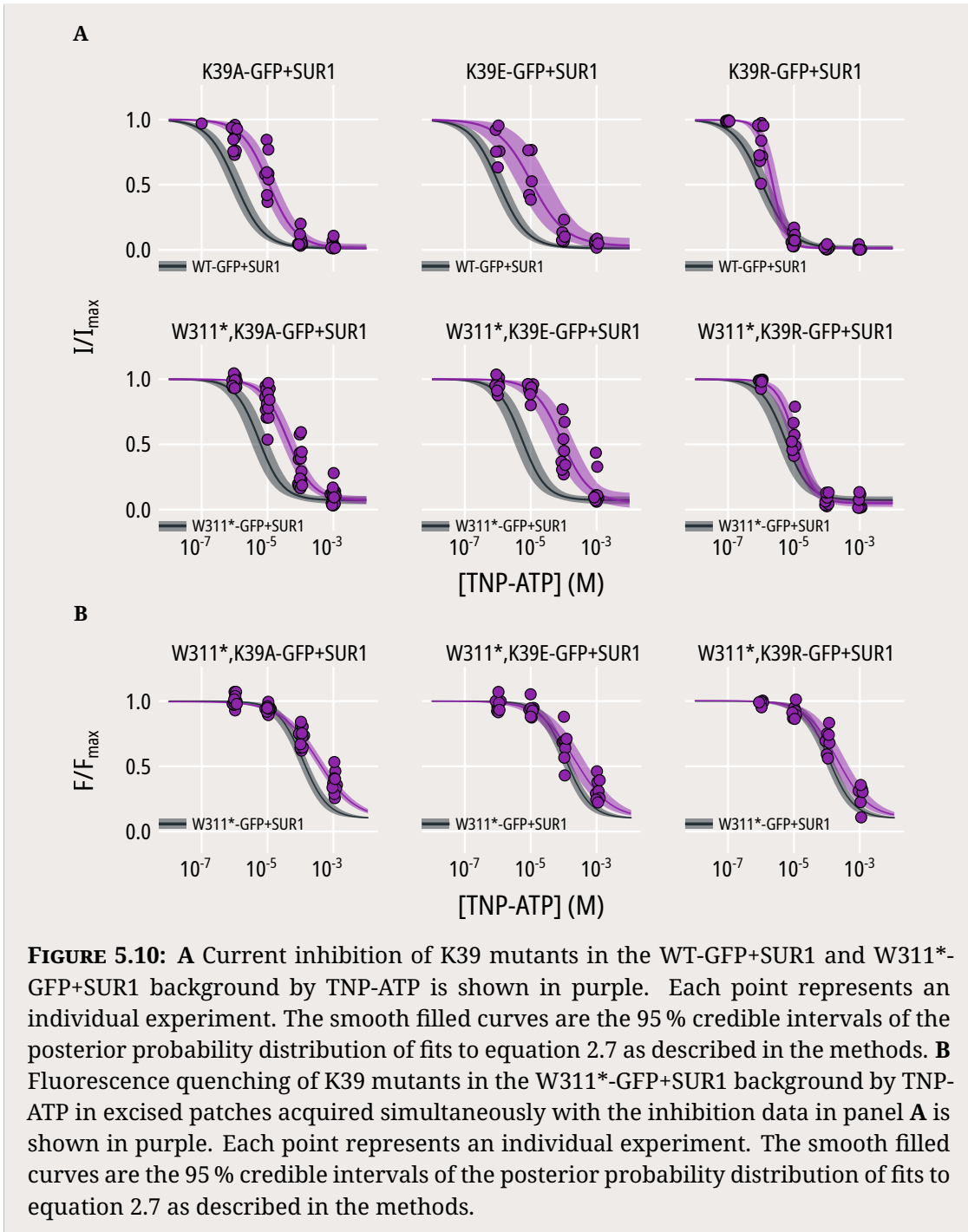
**FIGURE 5.5:** **A** Representative current trace from an excised patch expressing W311\*,C166S-GFP+SUR1. Applications of different concentrations of TEA<sup>+</sup> are indicated by bars shaded red, and application of 10 mM ATP is indicated in black. The zero-current level is marked with a dotted line. **B** Concentration-response data for W311\*-GFP+SUR1 (grey) and W311\*,C166S-GFP+SUR1 (purple) current inhibition by TEA<sup>+</sup>. The lines are fits to equation 2.7 with  $I_{max}$  fixed to 0.

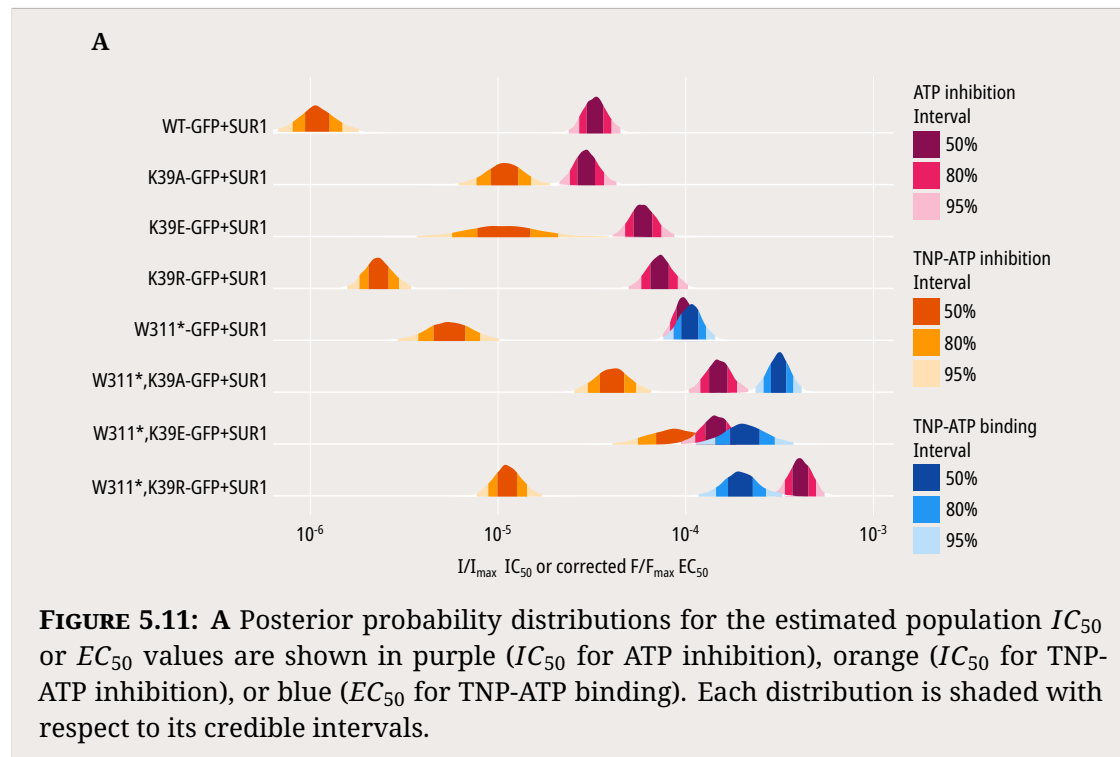


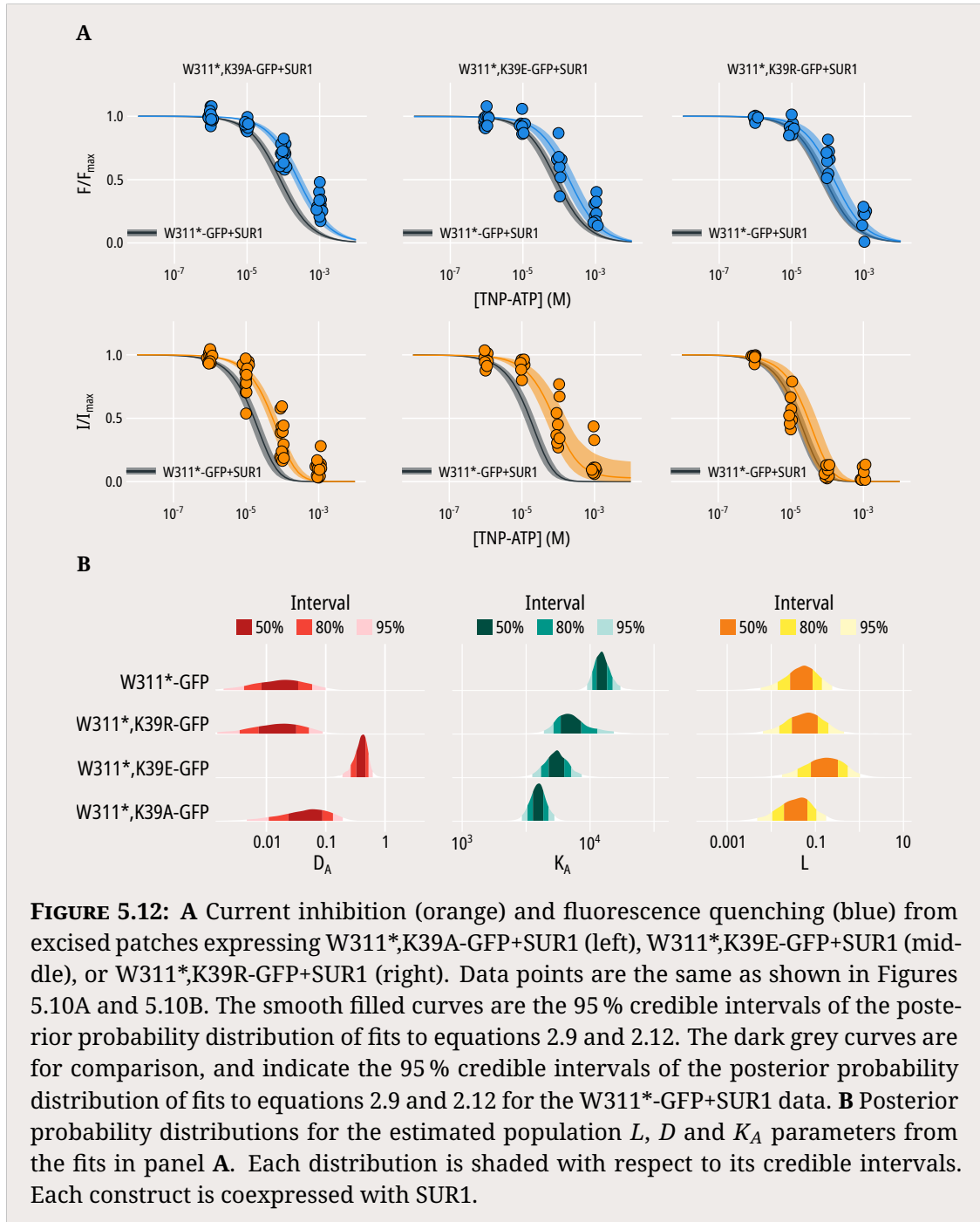


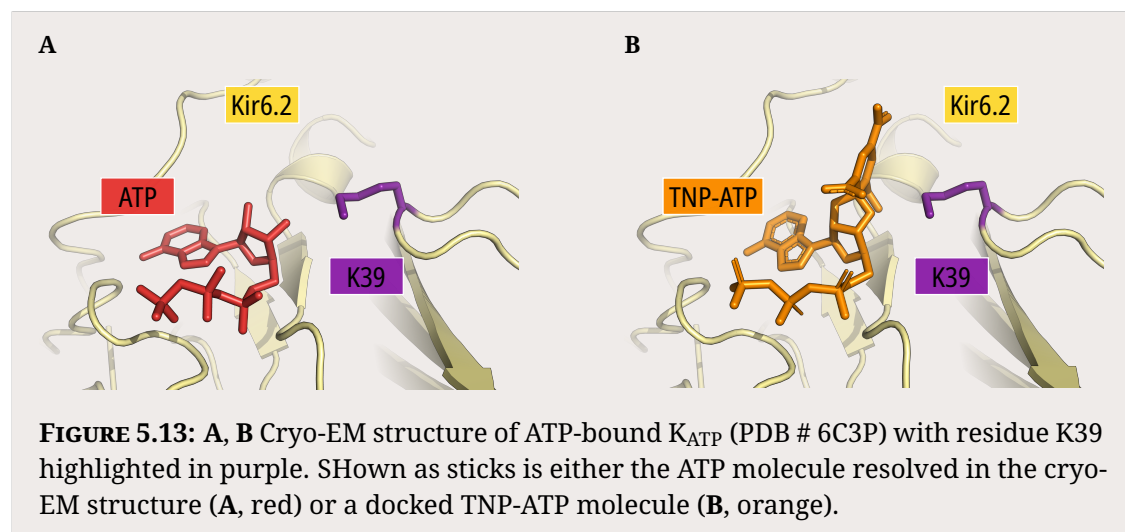












# 6

## Regulation of Kir6.2 by SUR1

### Contents

---

<b>6.1 Introduction</b>	119
<b>6.2 Intrinsic effects of SUR1</b>	120
6.2.1 SUR1 dramatically alters nucleotide inhibition, but only sub-	
tly effects nucleotide binding at Kir6.2	120
6.2.2 Presence of SUR1-TMD0 alone does not dramatically alter	
nucleotide binding at Kir6.2	123
<b>6.3 SUR1 and nucleotide regulation</b>	125
6.3.1 Mutations at SUR1-K205 alter nucleotide binding and inhibi-	
tion at Kir6.2	125
<b>6.4 Discussion</b>	126

---

### 6.1 Introduction

The SUR1 subunit exerts a number of different regulatory effects on the K<sub>ATP</sub> channel. Firstly, it dramatically enhances trafficking of Kir6.2 to the cell membrane by masking the endoplasmic retention motif in Kir6.2 (RKR). Without coexpression with SUR1, Kir6.2 is confined to the endoplasmic reticulum. Truncating the C-terminal by deleting the last 26 (Kir6.2-ΔC26) or 36 (Kir6.2-ΔC36) amino acids (35), mutation of the RKR motif to AAA (153), or addition of a C-terminal GFP tag (215) are sufficient to allow expression of Kir6.2 at the membrane alone without the presence of SUR1.

Comparing the function of these modified Kir6.2 subunits alone to the function of octameric Kir6.2/SUR channels makes it possible to discern the multifaceted roles of SUR1. Crucially, these C-terminal modifications do not appear to alter K<sub>ATP</sub> function when they are coexpressed with SUR1 (35, 212, 215) and the cryo-EM structure solved for C-terminally GFP labelled Kir6.2 (210) was highly similar to those solved without the GFP label (27, 78).

Coexpression of SUR1 has two effects on K<sub>ATP</sub> channel function. Firstly, SUR1 increases the P<sub>O</sub> of the channel (35, 76, 215). Expressing the TMD0 region of SUR1 (residues 1 - 195) alone is sufficient to recapitulate the increase in P<sub>O</sub> observed when full-length SUR1 is coexpressed(76, 216). When TMD0 is coexpressed with Kir6.2, there is additionally a decrease in the sensitivity of Kir6.2 to nucleotide inhibition - allosterically, an increase in P<sub>O</sub> would result in a decrease in apparent ATP affinity due to the reduction in stability of the closed state. However, when full length SUR1 is coexpressed with Kir6.2, there is a marked increase in sensitivity to ATP inhibition (35, 76, 212, 215). This increase in sensitivity has been suggested to be not due to the L0 linker, the other domain of SUR1 postulated to make contacts with Kir6.2. Expression of TMD0-L0 (residues 1 - 232) with Kir6.2 increases the P<sub>O</sub> to nearly saturating, and reduces ATP inhibition even further (216). Increasing the fraction of L0 (up to residue number 256 or 288) attenuates this increase in P<sub>O</sub>, but there is not the dramatic increase in ATP sensitivity observed from expression of full-length SUR1, implicating a role for the core region of SUR1 in regulating nucleotide binding and inhibition (20).

In this chapter, we aim to clarify the role of SUR1 in regulating the inhibitory effect of nucleotides on K<sub>ATP</sub> channel function.

## 6.2 Intrinsic effects of SUR1

### 6.2.1 SUR1 dramatically alters nucleotide inhibition, but only subtly effects nucleotide binding at Kir6.2

Expressing WT-GFP alone without SUR1 results in smaller, noisier currents than when coexpressed with SUR1. Currents are less sensitive to ATP and TNP-ATP by an

order of magnitude (Figure 6.1A, 6.1B. Our surface expression assay suggested that while WT-GFP was able to reach the membrane in the absence of SUR1, W311\*-GFP was not, and when we excised patches from cells expressing W311\*-GFP alone, we were not able to resolve any currents (Figure 3.5B). We were still able to resolve fluorescence in unroofed membranes expressing W311\*-GFP alone, and so we measured binding of TNP-ATP to W311\*-GFP alone in unroofed membranes. We observed very minimal differences in the EC<sub>50</sub> for binding. However, given that we did not observe currents under these experimental conditions, we cannot determine the functional state of these channels and so this finding may not be representative of K<sub>ATP</sub> channels physiologically.

Given that we were able to observe currents when we expressed WT-GFP in the absence of SUR1, we confirmed that when SUR1 was cotransfected with our Kir6.2 constructs we were measuring currents and fluorescence from correctly assembled K<sub>ATP</sub> channels. Firstly, we used tolbutamide to inhibit excised patches from cells expressing either WT-GFP alone, WT-GFP+SUR1 or W311\*-GFP+SUR1. Tolbutamide inhibition occurs at two sites on the K<sub>ATP</sub> channel; a high affinity site on SUR1 and a low affinity site on Kir6.2 (217, 218). Inhibition occurring at these two sites can be well separated, with the high affinity site saturating at ~50 % fractional inhibition with 100 µM tolbutamide . Tolbutamide inhibition of Kir6.2 expressed alone does not display inhibition until concentrations of over 100 µM. When we expressed WT-GFP alone, we saw no inhibition of currents by 100 µM, whereas when we expressed WT-GFP+SUR1 or W311\*-GFP+SUR1, we observed roughly a 50 % fractional inhibition of current as expected when Kir6.2 and SUR1 associate correctly.

While tolbutamide inhibition provides evidence for SUR1 association with our Kir6.2 constructs in excised patches, we cannot perform the same experiment to test for association in unroofed membranes. Instead, we labelled the C-terminus of SUR1 with the fluorophore mOrange (SUR1-mO), and measured FRET between the GFP attached to WT-GFP or W311\*-GFP and the mOrange attached to SUR1. The cryo-EM structures suggest a distance between the C-termini of Kir6.2 and SUR1 of roughly 60 Å, while the GFP-mOrange FRET pair has a theoretical R<sub>0</sub> of 54 Å.

We would therefore expect to see FRET between GFP and mOrange if our Kir6.2 and SUR1 constructs are coassembling.

To measure FRET, we used an approach outlined by Clegg (219) and Selvin (154) whereby FRET is measured as an increase in the emission of the acceptor fluorophore (mOrange) on excitation of the donor fluorophore (GFP) (Figure 6.2). We can directly excite both GFP and mOrange with 490 nm light. When WT-GFP is expressed alone we can measure the resulting emission spectrum as the donor fluorescence alone, and when SUR1-mO is expressed alone we can measure the resulting emission spectrum as the acceptor fluorescence alone (Figure 6.2A). In addition, we can excite mOrange directly with 565 nm light and avoid excitation of GFP. However, in the experimental condition with both WT/W311\*-GFP and SUR1-mO, excitation with 490 nm light results in an emission spectrum which is a mixture of three components: the emission from the donor fluorophore GFP, emission from the acceptor fluorophore mOrange due to direct excitation, and emission from the acceptor fluorophore mOrange due to energy transfer from the donor GFP (Figure 6.2B, 6.2C). To extract the component we are interested in (emission due to energy transfer), we can first remove the contribution of the donor fluorescence to the emission spectrum by subtracting an idealised WT/W311\*-GFP spectrum averaged from multiple cells expressing it alone (Figure 6.2D, 6.2E). We can then take the ratio of the fluorescence intensity of the acceptor mOrange after excitation by 490 nm light (which contains both direct excitation of the acceptor and FRET) to the fluorescence intensity of the acceptor mOrange after excitation by 565 nm light (which contains only direct excitation of the acceptor). Any increase in this ratio over that observed in cells expressing the acceptor alone is evidence for FRET between the fluorophores.

We captured spectra from the membranes of whole cells (rather than unroofed membranes) to improve our signal-to-noise ratio. We observed an increase in the emission ratio when we coexpressed WT-GFP and SUR1-mO, consistent with the two subunits being in close proximity (Figure 6.2F). While we still observed an increase in the emission ratio when we coexpressed W311\*-GFP and SUR1-mO, it was not as large an increase (1.6 to 2.1-fold for WT-GFP+SUR1-mO, 1.3 to 1.6-fold for

W311\*-GFP+SUR1-mO). This could result from three underlying mechanisms. Firstly, W311\*-GFP and SUR1-mO may coassemble differently to WT-GFP and SUR1-mO, and the difference in FRET results from a different distance between the C-termini of the two subunits. We consider this improbable. Secondly, we may be measuring fluorescence from a heterogenous population of channels; some with W311\*-GFP and SUR1-mO coassembled, and some with W311\*-GFP alone. This mixture would result in an intermediate value of FRET when measured from the total population. Finally, this method of calculating FRET is sensitive to the ratio of donor and acceptor fluorophores. If the acceptor fluorophore is present in excess (which we believe to be true as we transfect a molar excess of SUR1 constructs in all our experiments), a decrease in the amount of donor fluorophore present will decrease the proportion of acceptor fluorescence which comes from FRET, and will reduce the measure emission ratio. As our surface expression experiments suggest that W311\*-GFP is present at the membrane in lower quantities than WT-GFP (Figure 3.5C), this is our preferred hypothesis. However, as we cannot discount the possibility that there may be some W311\*-GFP present alone in unroofed membranes even when we coexpress SUR1, our interpretations of binding data acquired from unroofed membranes must be more cautious.

### 6.2.2 Presence of SUR1-TMD0 alone does not dramatically alter nucleotide binding at Kir6.2

We sought to clarify how the TMD0 and L0 regions of SUR1 contribute to inhibitory nucleotide binding at Kir6.2. We used two SUR1 truncation constructs; TMD0 consisting of the N-terminal 1-195 residues of SUR1, and TMD0-L0 consisting of the N-terminal 1-232 residues of SUR1. Firstly, we established whether these constructs were capable of supporting trafficking and expression at the cell membrane as previously reported (76, 216). In our luminescence based cell-surface expression assay, we found that TMD0 and TMD0-L0 increased the expression of WT-GFP approximately 3-fold over the expression of WT-GFP alone (Figure 6.3A, 6.3B). This increase in surface expression is somewhat less than observed when WT-GFP is

coexpressed with full-length SUR1. When we coexpressed either TMD0 or TMD0-L0 with W311\*-GFP, we did not see a convincing increase in surface expression when compared to expression of W311\*-GFP alone (Figure 6.3A, 6.3C). Indeed, when we excised patches from cells coexpressing W311\*-GFP and either TMD0 or TMD0-L0 we were unable to detect currents, while we were able to measure nA currents when WT-GFP was coexpressed with TMD0 or TMD0-L0.

Despite being unable to measure currents in excised patches, we were able to detect ANAP and GFP fluorescence from unroofed membrane patches coexpressing W311\*-GFP with either TMD0 or TMD0-L0. To determine whether this fluorescence was emitted from W311\*-GFP correctly coassembled with the truncated SUR1 constructs, we measured the emission ratio of TMD0-L0 labelled at the C-terminus with mOrange (TMD0-L0-mO) as described previously. We coexpressed either WT-GFP or W311\*-GFP with TMD0-L0-mO and measured the emission ratio of directly excited mOrange to indirectly excited mOrange in whole cells (Figure 6.3D). For WT-GFP+TMD0-L0-mO, we observed an increase in emission ratio over TMD0-L0-mO of a similar magnitude for the increase observed for WT-GFP+SUR1-mO (Figure 6.2F). This is consistent with TMD0-L0-mO coassembling with WT-GFP in unroofed membranes, as an increase in emission ratio requires the two fluorophores to be in close proximity. However, coexpression of W311\*-GFP and TMD0-L0-mO did not result in a convincing increase in the emission ratio (Figure 6.2F). Again, this may be due to decreased expression of W311\*-GFP compared to WT-GFP, but we cannot discount the possibility that we are measuring from a heterogenous population of W311\*-GFP channels and W311\*-GFP+TMD0-L0 channels.

We coexpressed either TMD0 or TMD0-L0 in combination with W311\*-GFP and measured TNP-ATP binding in unroofed membranes (Figure 6.4A). We found that the data were not particularly distinguishable from that collected from TNP-ATP binding to W311\*-GFP expressed alone; although this may be due to measuring from a mixed population of channels. To confirm that we could replicate the functional effects of TMD0-L0 on Kir6.2, we measured currents from excised patches expressing WT-GFP+TMD0-L0 and measured inhibition by ATP (Figure 6.4C). Similarly to Babenko

and Bryan (216) and Chan *et al.* (76), we observed a decrease in sensitivity to nucleotide inhibition in channels formed from WT-GFP and TMD0-L0 to channels formed from WT-GFP alone (Figure 6.4D).

### 6.3 SUR1 and nucleotide regulation

#### 6.3.1 Mutations at SUR1-K205 alter nucleotide binding and inhibition at Kir6.2

Residue K205 of SUR1 is located in the L0 region which links TMD0 and TMD1. While coexpression of Kir6.2 and TMD0-L0 has shown that the region is important in modulating the  $P_O$  of K<sub>ATP</sub> channels (21, 76, 79), it does not confer the high sensitivity to ATP inhibition seen in Kir6.2+SUR1 channels. It has therefore been suggested that the elements of SUR1 which contribute to the higher sensitivity of K<sub>ATP</sub> channels to ATP inhibition lie outside of this region (79, 196). However, the cryo-EM structures of K<sub>ATP</sub> suggest a close proximity between L0 and the ATP binding pocket (27, 78, 210) and mutations in this region reduce the sensitivity of K<sub>ATP</sub> to nucleotide inhibition (196, 220, 221). In particular, mutation of K205 to A (220) or E (222) has resulted in marked reduction of K<sub>ATP</sub> channel sensitivity to nucleotide inhibition.

We excised patches expressing W311\*-GFP+SUR1-K205A or W311\*-GFP+SUR1-K205E and measured current inhibition and fluorescence quenching by TNP-ATP simultaneously. We found that both substitutions resulted in an increased IC<sub>50</sub> for TNP-ATP inhibition and an increased EC<sub>50</sub> for TNP-ATP binding, with K205E exhibiting a more pronounced effect than K205A. Fitting the data to our MWC model gave parameter estimates for  $K_A$  which were reduced when compared to wild-type SUR1; with the neutral mutation K205A not affecting  $K_A$  quite as much as the charge reversal mutation K205E. In addition, both mutations led to similar increases in  $D_A$ . Thus, the reduced sensitivity to nucleotide inhibition is due to a combination of reduced apparent binding affinity in addition to reduced stabilisation of the closed state of the channel by nucleotides.

## 6.4 Discussion

Expression of W311\*-GFP in the absence of SUR1 reduces the apparent TNP-ATP binding affinity by only a small amount in unroofed membranes; approximately 2-fold. This is in contrast to the dramatic 10-fold reduction in sensitivity to inhibition by ATP observed when WT-GFP is expressed in the absence of SUR1; and the near 100-fold reduction in sensitivity to inhibition by TNP-ATP observed when WT-GFP is expressed in the absence of SUR1. The difference in the relative sensitivity to inhibition by ATP and TNP-ATP when WT-GFP is expressed alone and when it is coexpressed with SUR1 is difficult to explain. Two possible explanations are (i) that SUR1 increases the binding affinity for TNP-ATP more than it increases the binding affinity for ATP, and (ii) that SUR1 enhances the transduction of TNP-ATP binding to channel closure to a greater extent than ATP. Our computational docking of TNP-ATP does not predict any contacts between the TNP-moiety and SUR1 (Figure 5.13B), but that does not necessarily mean that there explanation (i) cannot be true.

We also found that coexpression of W311\*-GFP with TMD0 or TMD0-L0 did not result in an increase in apparent nucleotide binding affinity, although this finding is caveated by the possible mixture of correctly complexed mini-K<sub>ATP</sub> channels and W311\*-GFP subunits alone in the unroofed membranes.

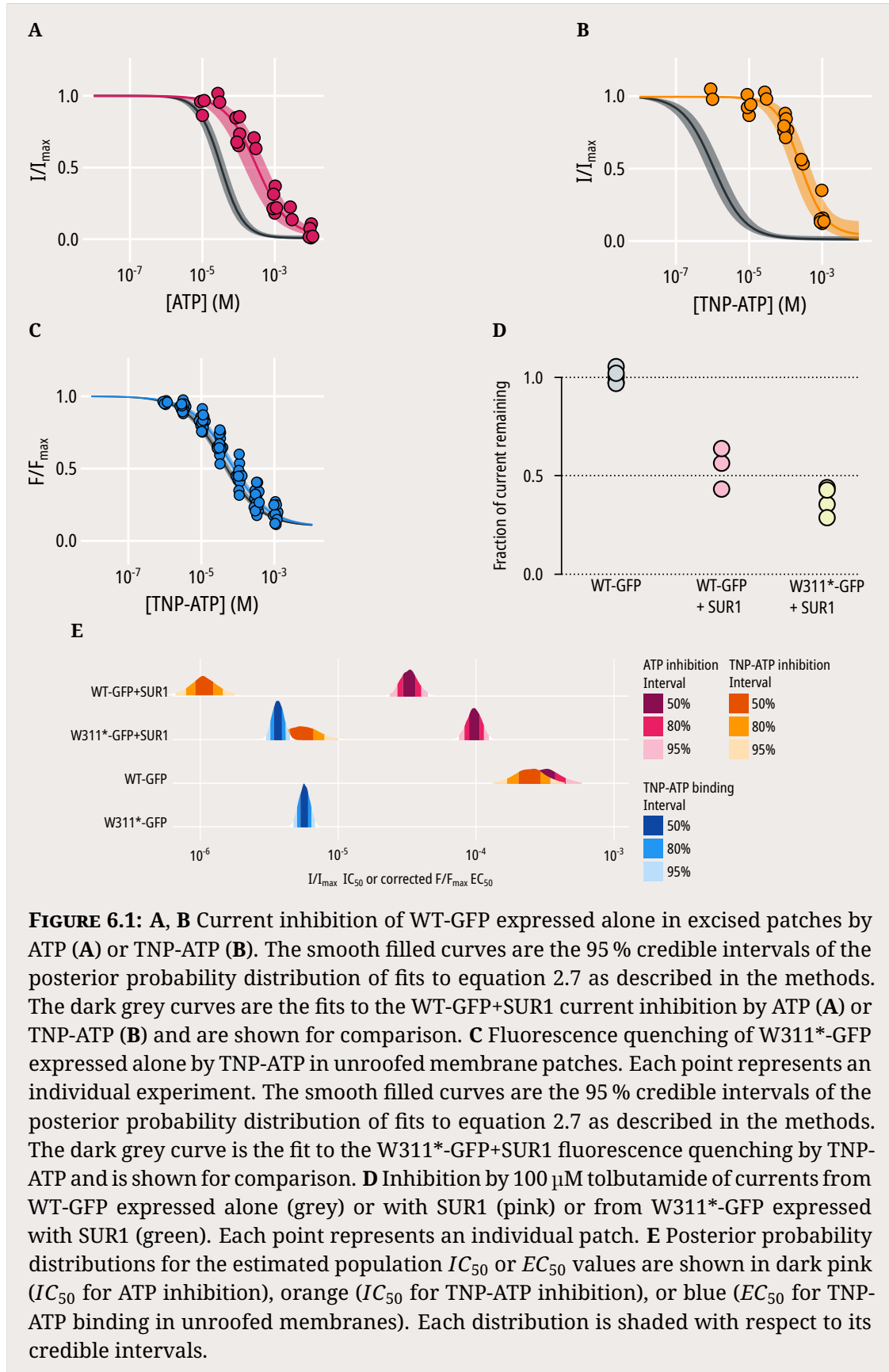
Despite these somewhat inconclusive findings, we saw a clear effect of mutating residue K205 in the L0 loop of SUR1. Similar to the findings of Ding *et al.* (220), we observed a marked reduction in sensitivity to TNP-ATP inhibition when the residue was mutated to an alanine, and a further reduction when it was mutated to glutamic acid. Fitting the data to the MWC model reveals that the reduction in sensitivity is due to both a reduction in the microscopic binding affinity for TNP-ATP, and a decrease in the transduction of nucleotide binding to channel closure.

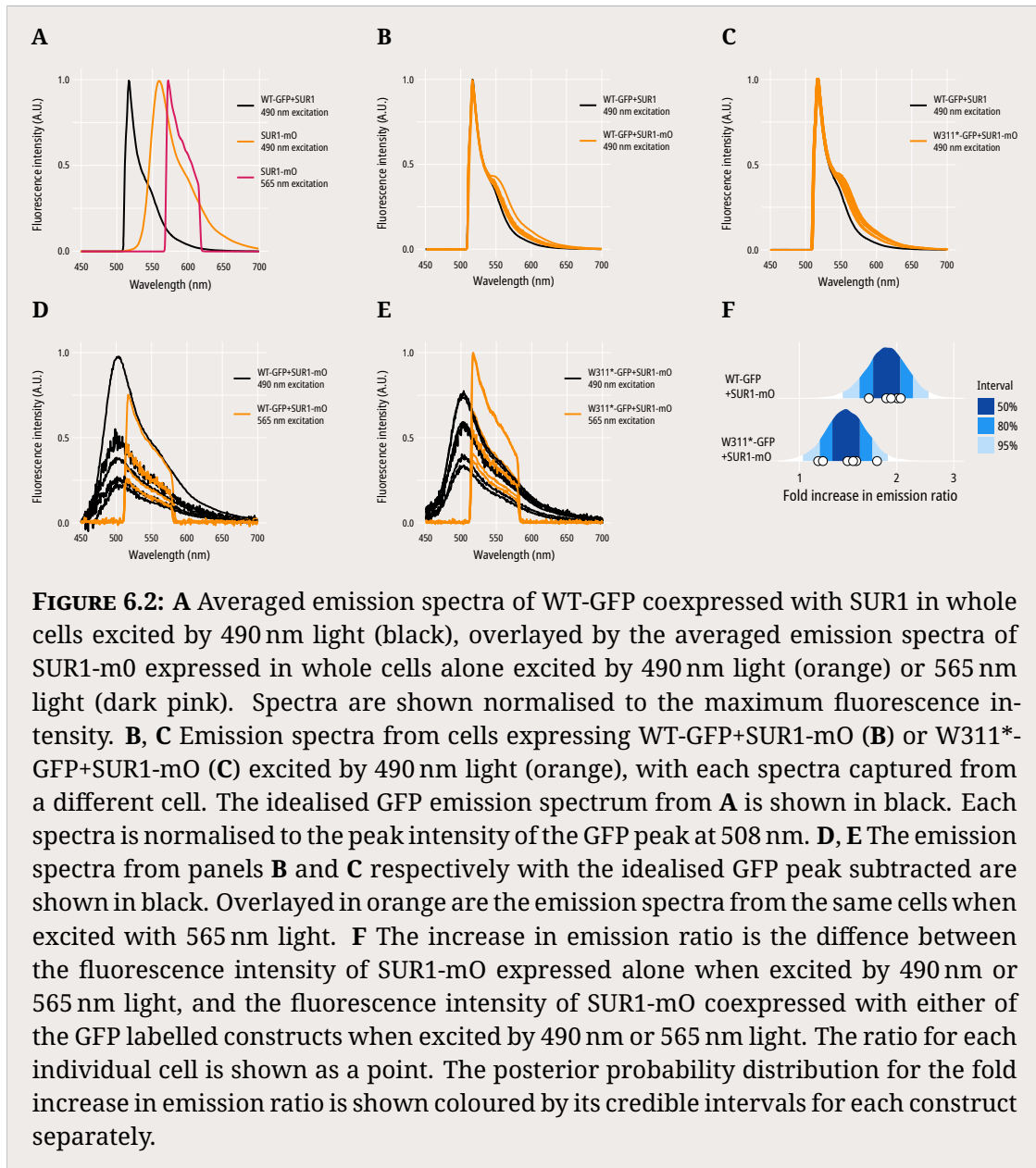
The structure of K205 resolved by Ding *et al.* (220) suggested that the long, positively charged side chain directly coordinates the  $\beta$ - and  $\gamma$ -phosphates of bound ATP (220). Our results are consistent with the hypothesis that mutation to an alanine, thus removing the positive charge, directly disrupts nucleotide binding. We also

observe a further reduction in the microscopic binding affinity upon substitution by glutamic acid, which has a long and negatively charged side chain. Again, this is consistent with the idea that K205 directly coordinates the negatively charged phosphates of ATP, and explains the reduction in sensitivity to ATP inhibition observed by Pratt *et al.* (222) when they made the same mutation.

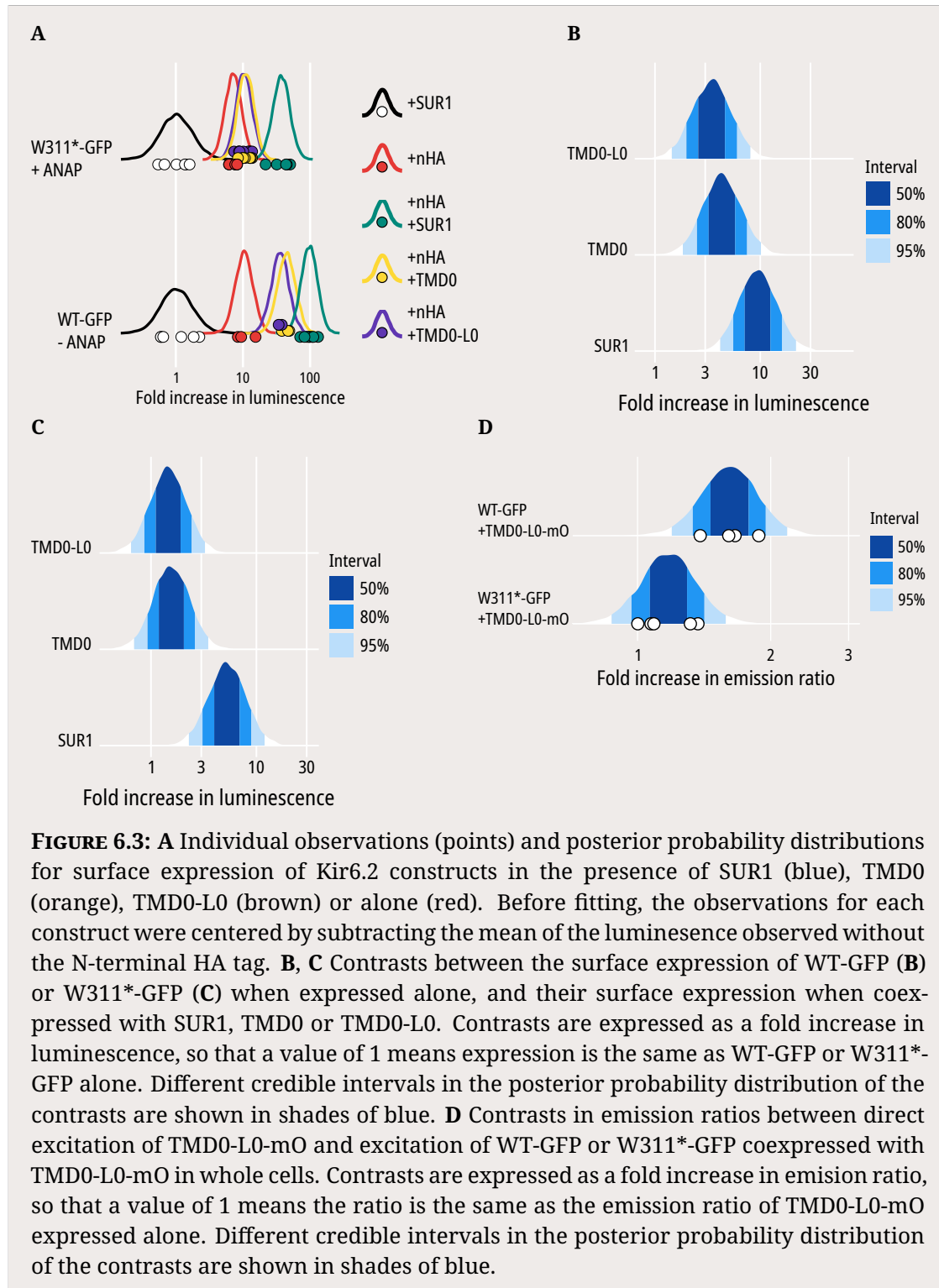
Our MWC fits also suggest that mutation of K205 reduces the ability of nucleotides to close the channel. As we calculated for the C166S mutation in Kir6.2, we can express this reduction in terms of the free energy contributed to the conformational change of closure. For the SUR1-K205A construct, the free energy is  $5.6 \text{ kJ M}^{-1}$  to  $18.3 \text{ kJ M}^{-1}$ , and for the SUR1-K205E construct, the free energy is  $3.3 \text{ kJ M}^{-1}$  to  $13.9 \text{ kJ M}^{-1}$ , much reduced from that of wild-type SUR1 which is  $23.0 \text{ kJ M}^{-1}$  to  $63.4 \text{ kJ M}^{-1}$ . This suggests that the positive charge K205 contributes to the inhibitory binding site is important for transduction of nucleotide binding to channel closure.

This finding does not explain why TMD0-L0 expression alone is not enough to restore full-length SUR1 like nucleotide inhibition. Coexpression of TMD0-L0 with WT-GFP exhibits decreased sensitivity to nucleotide inhibition when compared to full length SUR1, as seen in previous studies (21, 76, 79). Our findings are consistent with the hypothesis that the elements of the L0 linker which enhance the binding affinity of nucleotides for Kir6.2 and which increase the intrinsic open probability of the  $K_{ATP}$  channel are separate; and also suggest that the linker plays an active role in transducing binding to closure.

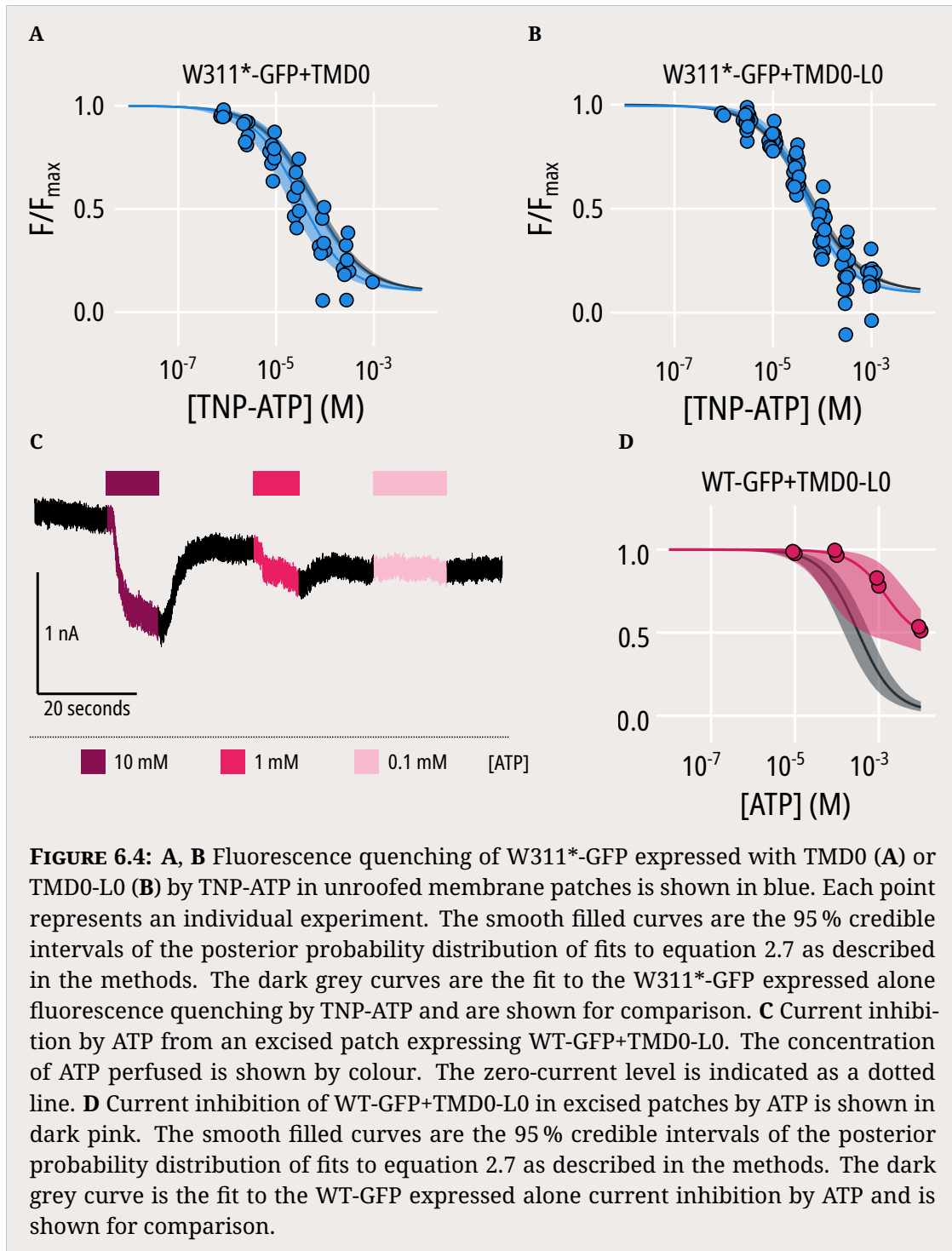


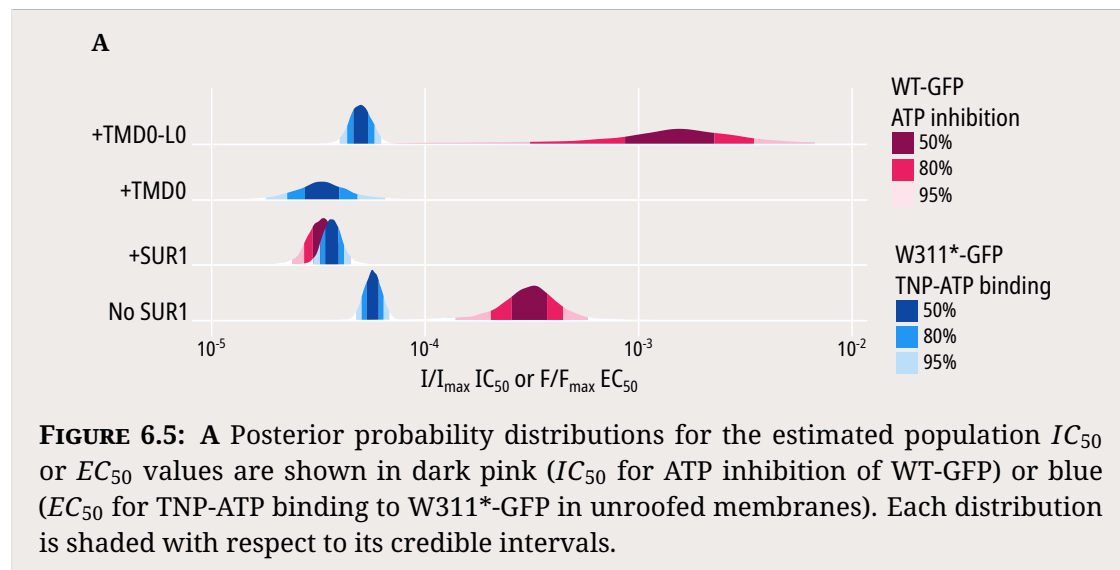


**FIGURE 6.2:** **A** Averaged emission spectra of WT-GFP coexpressed with SUR1 in whole cells excited by 490 nm light (black), overlayed by the averaged emission spectra of SUR1-mO expressed in whole cells alone excited by 490 nm light (orange) or 565 nm light (dark pink). Spectra are shown normalised to the maximum fluorescence intensity. **B, C** Emission spectra from cells expressing WT-GFP+SUR1-mO (**B**) or W311\*-GFP+SUR1-mO (**C**) excited by 490 nm light (orange), with each spectra captured from a different cell. The idealised GFP emission spectrum from **A** is shown in black. Each spectra is normalised to the peak intensity of the GFP peak at 508 nm. **D, E** The emission spectra from panels **B** and **C** respectively with the idealised GFP peak subtracted are shown in black. Overlayed in orange are the emission spectra from the same cells when excited with 565 nm light. **F** The increase in emission ratio is the difference between the fluorescence intensity of SUR1-mO expressed alone when excited by 490 nm or 565 nm light, and the fluorescence intensity of SUR1-mO coexpressed with either of the GFP labelled constructs when excited by 490 nm or 565 nm light. The ratio for each individual cell is shown as a point. The posterior probability distribution for the fold increase in emission ratio is shown coloured by its credible intervals for each construct separately.

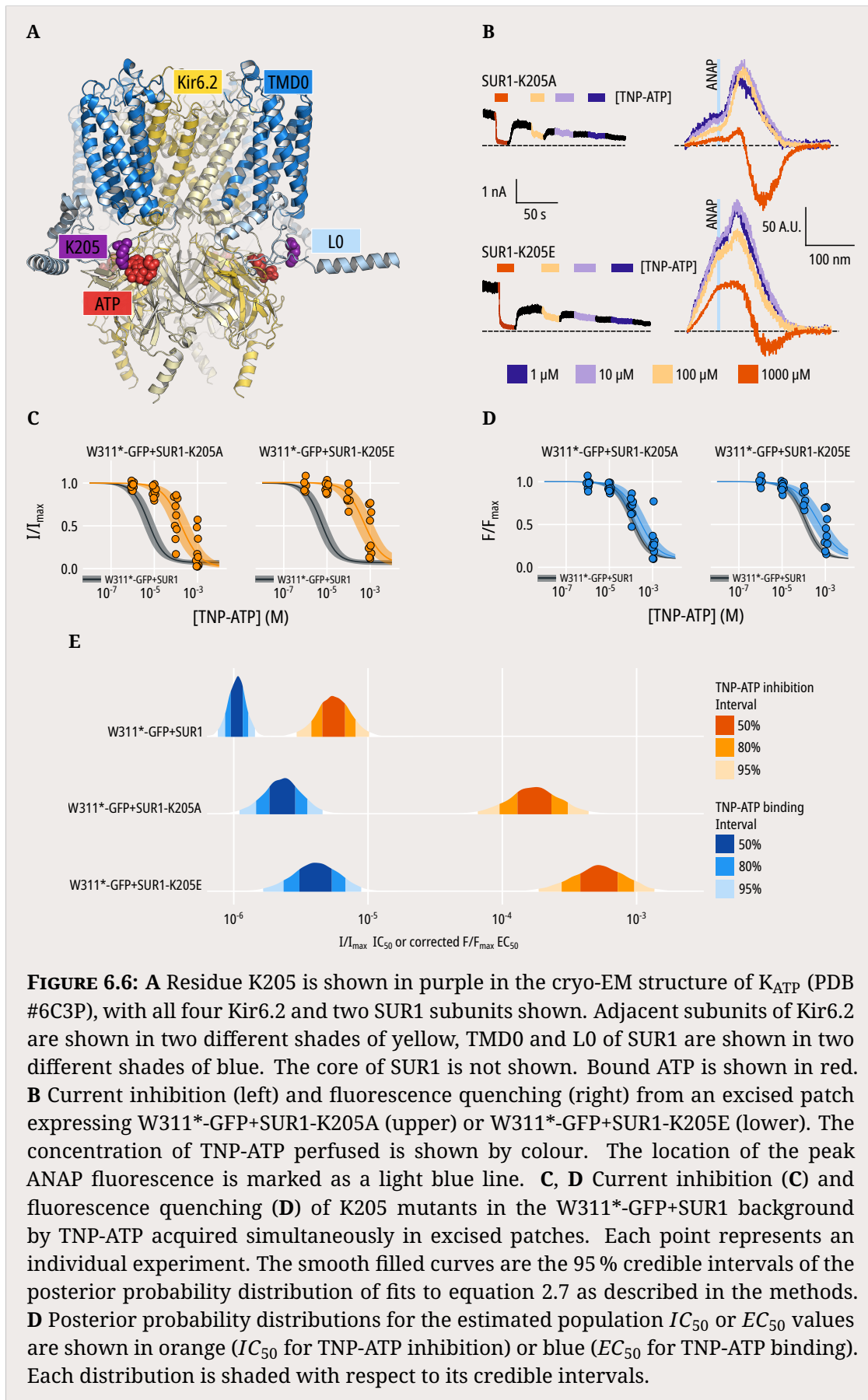


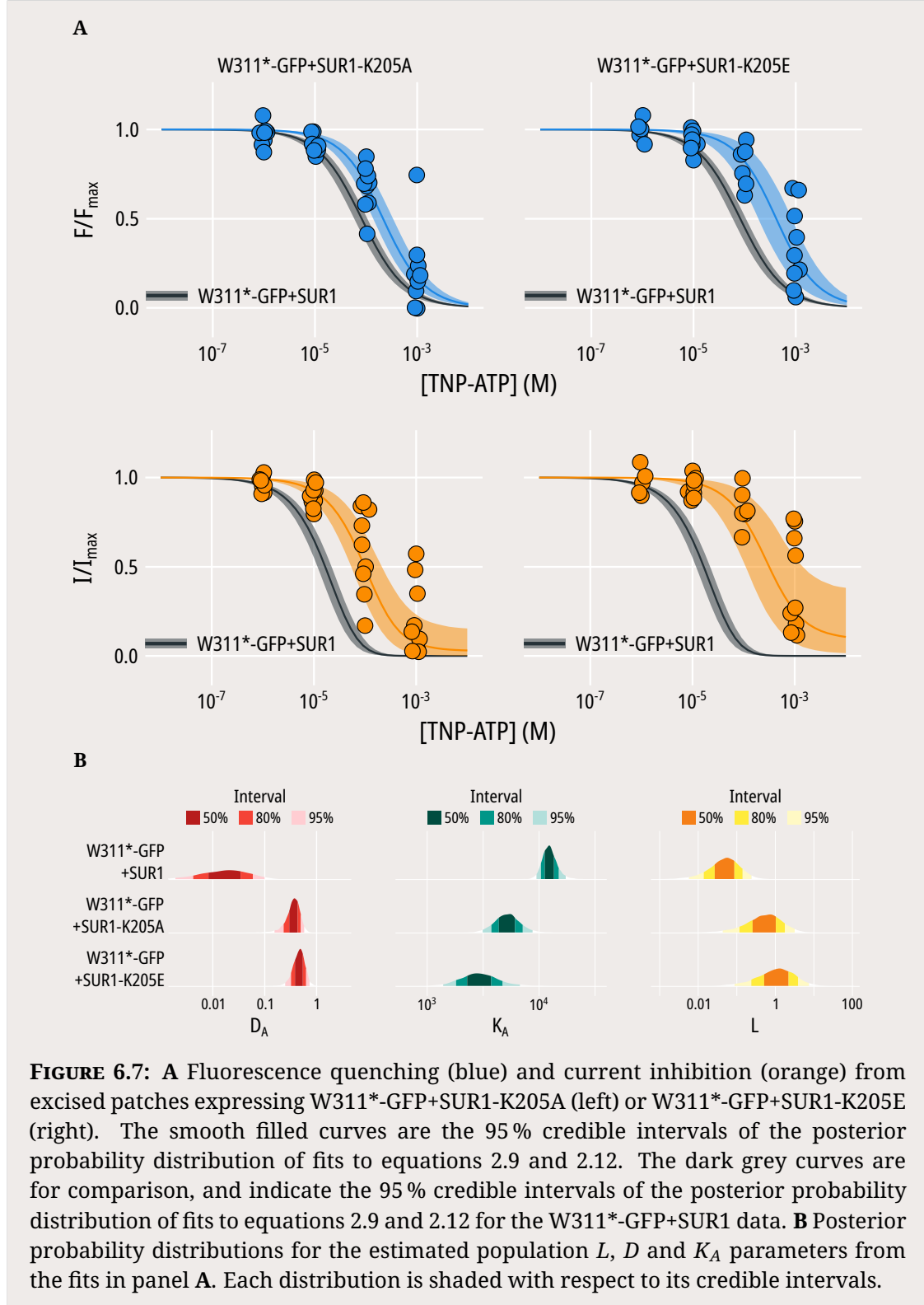
**FIGURE 6.3:** **A** Individual observations (points) and posterior probability distributions for surface expression of Kir6.2 constructs in the presence of SUR1 (blue), TMD0 (orange), TMD0-L0 (brown) or alone (red). Before fitting, the observations for each construct were centered by subtracting the mean of the luminescence observed without the N-terminal HA tag. **B, C** Contrasts between the surface expression of WT-GFP (**B**) or W311\*-GFP (**C**) when expressed alone, and their surface expression when coexpressed with SUR1, TMD0 or TMD0-L0. Contrasts are expressed as a fold increase in luminescence, so that a value of 1 means expression is the same as WT-GFP or W311\*-GFP alone. Different credible intervals in the posterior probability distribution of the contrasts are shown in shades of blue. **D** Contrasts in emission ratios between direct excitation of TMD0-L0-mO and excitation of WT-GFP or W311\*-GFP coexpressed with TMD0-L0-mO in whole cells. Contrasts are expressed as a fold increase in emision ratio, so that a value of 1 means the ratio is the same as the emission ratio of TMD0-L0-mO expressed alone. Different credible intervals in the posterior probability distribution of the contrasts are shown in shades of blue.





**FIGURE 6.5: A** Posterior probability distributions for the estimated population  $IC_{50}$  or  $EC_{50}$  values are shown in dark pink ( $IC_{50}$  for ATP inhibition of WT-GFP) or blue ( $EC_{50}$  for TNP-ATP binding to W311\*-GFP in unroofed membranes). Each distribution is shaded with respect to its credible intervals.





# 7

## Discussion

### Contents

---

7.1 Summary of findings . . . . .	135
7.2 Inhibition in the context of K <sub>ATP</sub> regulation . . . . .	138
7.3 Nucleotide inhibition of the K <sub>ATP</sub> channel in the context of other ligand-gated ion channels . . . . .	140

---

### 7.1 Summary of findings

David Colquhoun wrote the following in 1998: "Distinguishing between effects on binding and effects on conformation change is arguably the fundamental problem of modern molecular studies of receptors. It is not an easy distinction to make, but unless it can be solved, the interpretation of structure-function studies is quite likely to be nonsense" (209). A few months earlier, the first crystal structure of an ion channel (the K<sup>+</sup> channel from *Streptomyces lividans*, KcsA) was published by a team from Roderick MacKinnon's group (223). While Colquhoun acknowledged that such structures would resolve many questions about the location of ligand binding sites, he emphasised that knowledge of structure does not preclude the search for mechanisms and dynamics: "Structures are static but receptors are not" (209).

It took nearly two decades after solving KcsA for structures of the  $K_{ATP}$  channel to be resolved through cryo-EM (26–29). Impressively, many of the predictions made from detailed electrophysiological experiments and molecular modelling about the inhibitory nucleotide binding site of Kir6.2 were validated by the structures (66, 69, 87, 107, 110, 113, 129, 164, 180). As the structures were solved in complex with ATP and in the absence of lipids, we can assume that they resemble the physiological closed state of the  $K_{ATP}$  channel. The difficulty of obtaining open states of ion channels means that relating the captured structures to the function of  $K_{ATP}$  is not trivial, and many open questions remain (20).

In this thesis, I have aimed to show four things:

- We can directly measure nucleotide binding to Kir6.2 by site-specifically inserting ANAP at position W311 and measuring its quenching by TNP-ATP.
- Measuring binding in combination with  $K_{ATP}$  channel current inhibition allows us to confirm that an MWC model is able to describe  $K_{ATP}$  inhibition by nucleotides.
- Effects on nucleotide binding and effects on conformational change can be well distinguished by fitting combined binding and inhibition data to an MWC model.
- SUR1 directly contributes to nucleotide binding to Kir6.2.

In doing so, I have built directly on the work of numerous studies using a variety of electrophysiological approaches to provide answers to the above questions. Where this work differs, and - I believe - adds value, is in two aspects of the approach. Firstly, while the use of fluorescence to study ligand binding to ion channels is far from novel, the site-specific nature of ANAP incorporation is a development which crucially allows for the separation of nucleotide binding to Kir6.2 from binding to the NBDs of SUR1. In addition, measuring the quenching of ANAP fluorescence rather than an increase in ligand fluorescence allows us to directly translate our

observations into the bound fraction of Kir6.2 subunits, without having to assume that at saturation each subunit is bound.

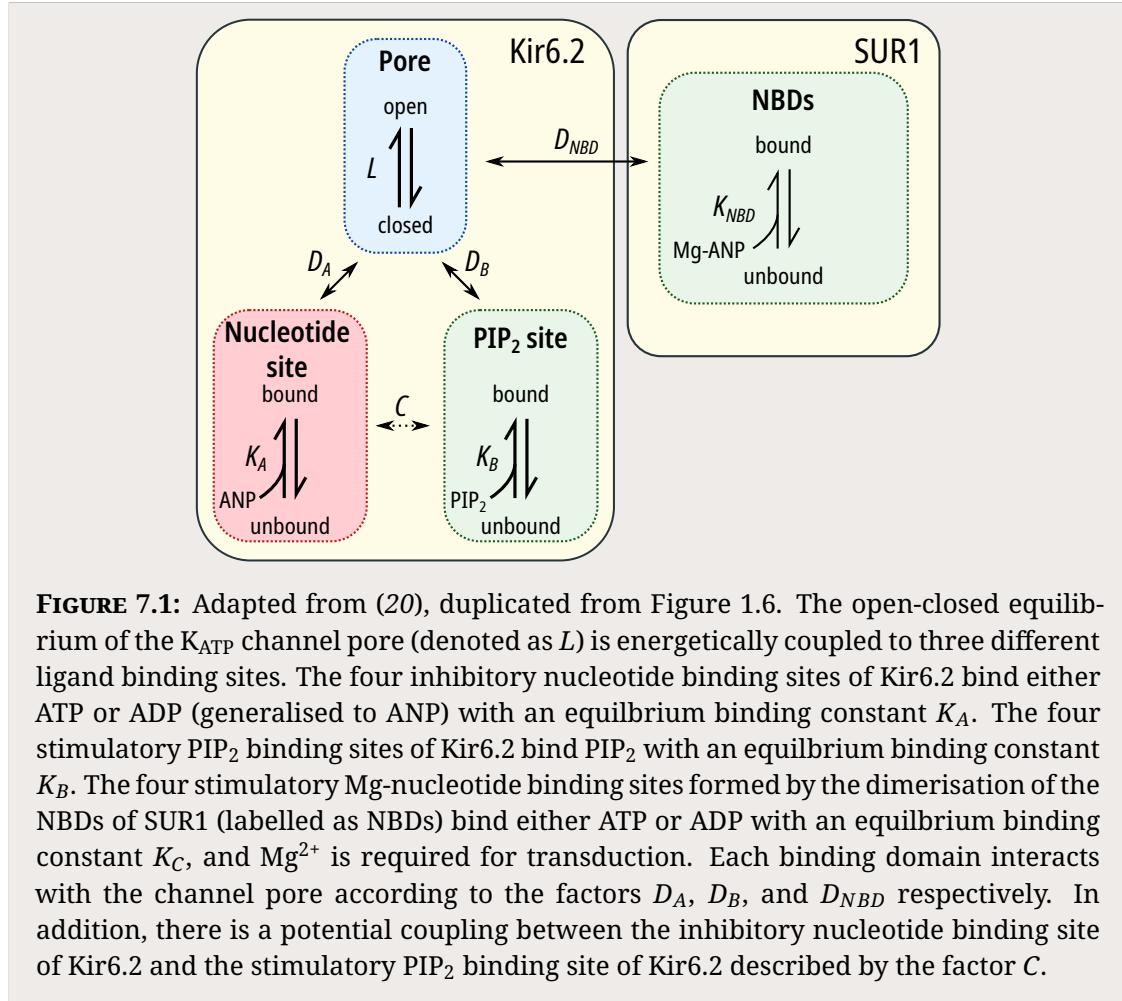
Secondly, formulating the MWC model in a Bayesian fashion allows us to determine whether the parameters in the models we fit are practically identifiable. In other words, are the parameters we estimate uniquely constrained by the data we can collect? The problem of parameter identifiability has been discussed in much greater detail elsewhere (224–227). Briefly, even seemingly simple binding or inhibition curves may often be fit arbitrarily well by many combinations of parameter values. This is further complicated by the inescapable noise present in experimental data.

Here, we address this issue in two ways. Firstly, collecting simultaneous binding and inhibition data allows us to constrain the parameters of a more complex model than would be possible based on either alone. Secondly, the Bayesian MCMC fitting procedure allows us to visualise the full posterior probability distribution of parameter estimates for fits to a given model. It is then trivial to determine whether parameter estimates are unique by visually inspecting the cross-correlation plots of paired parameters (225), which for all the constructs tested yield well bounded ellipses (Figure A.14).

Applying this approach to a series of residue substitutions in Kir6.2 shows that we are able to discriminate not only between effects on binding and effects on conformational change, but that we can further distinguish between effects on intrinsic and ligand-dependent regulation of conformational change. We have demonstrated this for a number of different substitutions at residues on Kir6.2; C166, E179 and K39. In addition, while our attempts to measure TNP-ATP binding to Kir6.2 in the absence of SUR1 (or in the presence of truncated forms of SUR1) were limited in their success, we were able to identify K205 as a residue in L0 which directly contributes to binding of nucleotides to Kir6.2, and plays a role in the transduction of binding to channel closure.

## 7.2 Inhibition in the context of $K_{ATP}$ regulation

Nucleotide inhibition of the  $K_{ATP}$  channel does not occur in isolation in the physiological context, and must be considered in the context of nucleotide stimulation by SUR1 and  $PIP_2$  (Figure 7.1, duplicated from Figure 1.6 for ease of reference).



How does inhibitory nucleotide binding to Kir6.2 interplay with the stimulatory nucleotide binding to the NBDs of SUR1? In parallel work published in Puljung *et al.* (3), we established a similar experimental paradigm to measure MgTNP-ADP binding to NBS2 of SUR1 in unroofed membranes. While we were unable to measure current activation and nucleotide binding simultaneously, we collected data separately for the two processes. Here we refit that data in combination with the inhibition data presented in Figure 3.12D to an MWC model which comprises both inhibition at Kir6.2

by TNP-ATP and activation at SUR1 by MgTNP-ADP with a shared open probability (Figure 7.2). Comparison of the binding association constants for TNP-nucleotides at Kir6.2 and NBS2 shows that MgTNP-ADP binds more readily to NBS2 than TNP-ATP binds to Kir6.2 (Figure 7.2B). In contrast, the transduction of binding is far stronger for TNP-ATP bound to Kir6.2 than for MgTNP-ADP bound to NBS2. In terms of free energy, binding to Kir6.2 contributes  $32.7 \text{ kJ M}^{-1}$  to  $68.0 \text{ kJ M}^{-1}$  to the closed state of the channel (slightly higher than the  $23.0 \text{ kJ M}^{-1}$  to  $63.4 \text{ kJ M}^{-1}$  estimated from fitting the inhibition data alone), whereas binding to NBS2 contributes  $0.6 \text{ kJ M}^{-1}$  to  $33.9 \text{ kJ M}^{-1}$  to the open state of the channel.

Assuming that the excitatory and inhibitory processes are independent, inhibition would be expected to dominate under conditions at which all the nucleotide binding sites of  $K_{ATP}$  are occupied. This is consistent with published measurements of wild-type KATP in the presence of  $Mg^{2+}$  (228). The ability of MgADP to increase  $K_{ATP}$  currents in the presence of ATP (102) and the bell-shaped MgADP concentration response curve for  $K_{ATP}$  (90, 228) can then be explained by the higher binding affinity of NBS2 resulting in an increase in current at low nucleotide concentrations, followed by inhibition at higher concentrations due to stronger transduction from nucleotides binding to Kir6.2.

Of course, this interpretation relies on data which has been obtained from different constructs and under different conditions. Ideally, we would explore this further by carrying out patch-clamp fluorometry experiments under conditions where all three nucleotide binding sites simultaneously affect channel gating (in the presence of  $Mg^{2+}$ ). Our initial attempts to do so were limited by the rapid rate of rundown of  $K_{ATP}$  currents in the presence of divalent ions, which made it difficult to collect useable data with simultaneous current and fluorescence recordings. Introducing mutations which slow the rate of rundown may be one method to ameliorate this problem and synthesise a more complete model of  $K_{ATP}$  function.

How does inhibitory nucleotide binding to Kir6.2 interplay with  $PIP_2$  regulation of the  $K_{ATP}$  channel? As described in Chapter 1, directly measuring or varying the  $PIP_2$  concentration in the membrane is challenging, and in the experiments

presented here we have tried as far as possible to keep  $PIP_2$  constant. Our simplifying assumption which assumes  $PIP_2$  acts solely on the open probability of the channel and does not vary significantly in our recordings seem sufficient to explain the variety of effects we see from the mutations studied in Kir6.2 and SUR1.

However, it remains an open question as to whether  $PIP_2$  binding to Kir6.2 only affects the channel through increasing the open probability (Figure 7.1, *D<sub>B</sub>*) or whether there is a mechanism which directly couples the  $PIP_2$  binding site to the inhibitory nucleotide binding site (Figure 7.1, *C*). Our experiments with substitutions at E179 on Kir6.2, predicted to be in the  $PIP_2$  binding pocket, do not rule out the existence of a direct coupling. However, the observed reduction in the binding affinity for TNP-ATP is only circumstantial evidence as it may also be explained by the two substitutions examined (E179A and E179K) altering the nucleotide binding pocket instead. Experiments to directly test for the existence of direct coupling would need to involve manipulation and measurement of  $PIP_2$  levels.

### 7.3 Nucleotide inhibition of the $K_{ATP}$ channel in the context of other ligand-gated ion channels

The  $K_{ATP}$  channel is one of many ion channels regulated by ligands. The MWC model used here to fit TNP-ATP inhibition of  $K_{ATP}$  allows us to compare nucleotide regulation of the  $K_{ATP}$  channel to other ion channels which are well described by such models. One particularly well studied channel is the nicotinic acetylcholine receptor (nAChR). The binding of acetlycholine (ACh) to the nAChR increases the open probability of the channel in a similar fashion as the binding of nucleotides to Kir6.2 decreases the open probability of the  $K_{ATP}$  channel. Auerbach (229) estimated that the transduction energy which saturating concentrations of ACh contribute to the open state of the nAChR is approximately  $25\text{ kJ M}^{-1}$ , remarkably similar to the  $23.0\text{ kJ M}^{-1}$  to  $63.4\text{ kJ M}^{-1}$  we estimate saturating concentrations of TNP-ATP contribute to the closed state of the  $K_{ATP}$  channel. Similarly, Horrigan and Aldrich (230) characterised the regulation of the large conductance  $K^+$  (BK) channel by voltage and  $Ca^{2+}$  using an MWC framework, and estimated a transduction energy of

approximately  $21 \text{ kJ M}^{-1}$  in favour of the open state at saturating  $\text{Ca}^{2+}$  concentrations. As a final comparison, Varnum and Zagotta (231) investigated the regulation of the cyclic-nucleotide gated (CNG) channel by cGMP, cIMP and cAMP and estimated transduction energies of  $34 \text{ kJ M}^{-1}$ ,  $29 \text{ kJ M}^{-1}$ , and  $15 \text{ kJ M}^{-1}$  to the open state respectively. It appears that the energy ligand binding contributes to conformational change is broadly similar across diverse ion channel families regulated by structurally dissimilar ligands.

Moving forwards, it would be particularly interesting to apply similar binding assays and MWC functional modelling to other ATP-regulated ion channels such as the P2X receptor family (232). While  $\text{K}_{\text{ATP}}$  channels are inhibited by intracellular ATP, the P2X receptor family are activated by extracellular ATP, and differences in the ATP concentrations and dynamics in these two spaces suggest there may be other biophysical differences in nucleotide regulation, upon which direct measurements of nucleotide binding may be able to shed light (233).

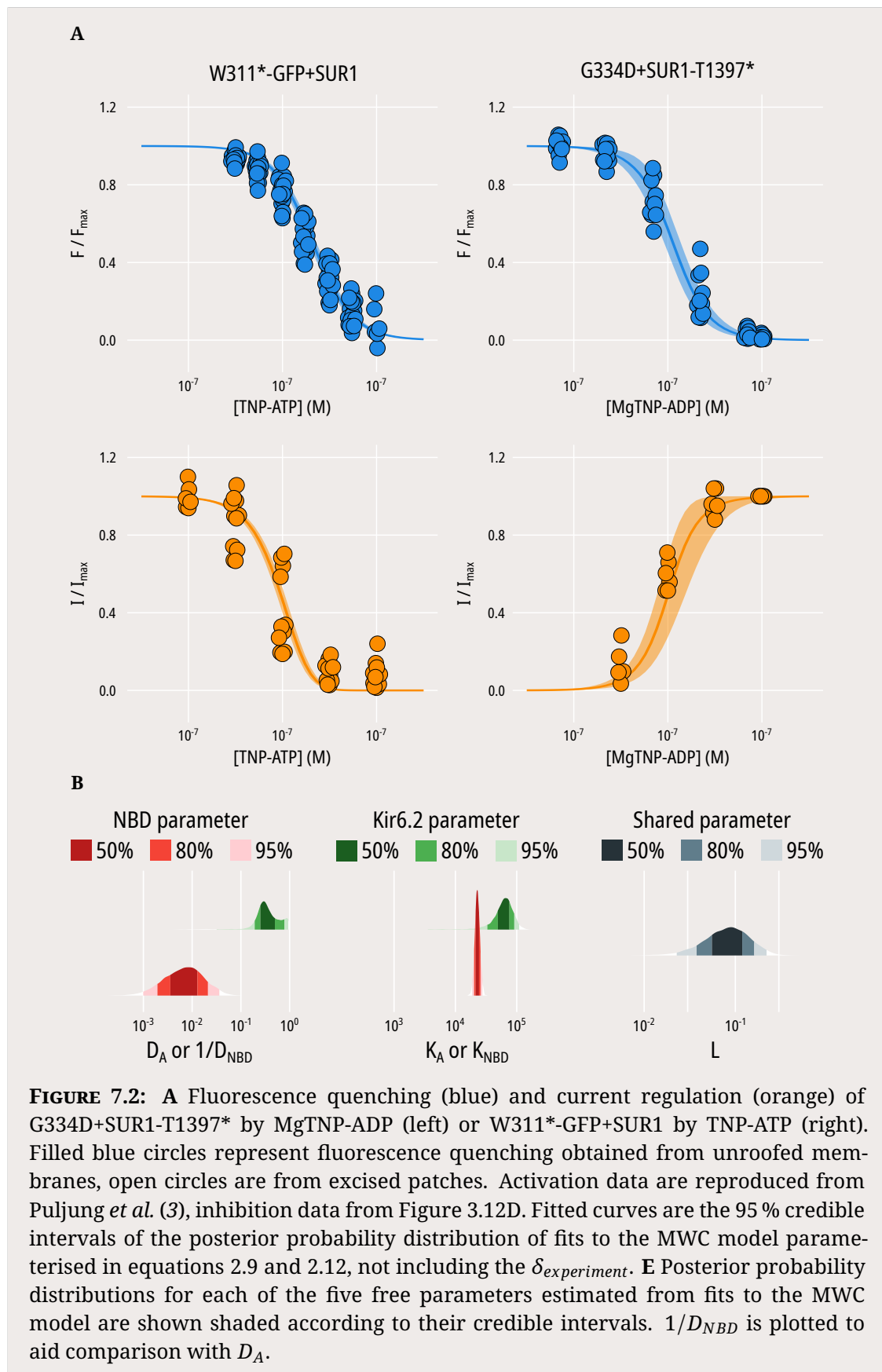


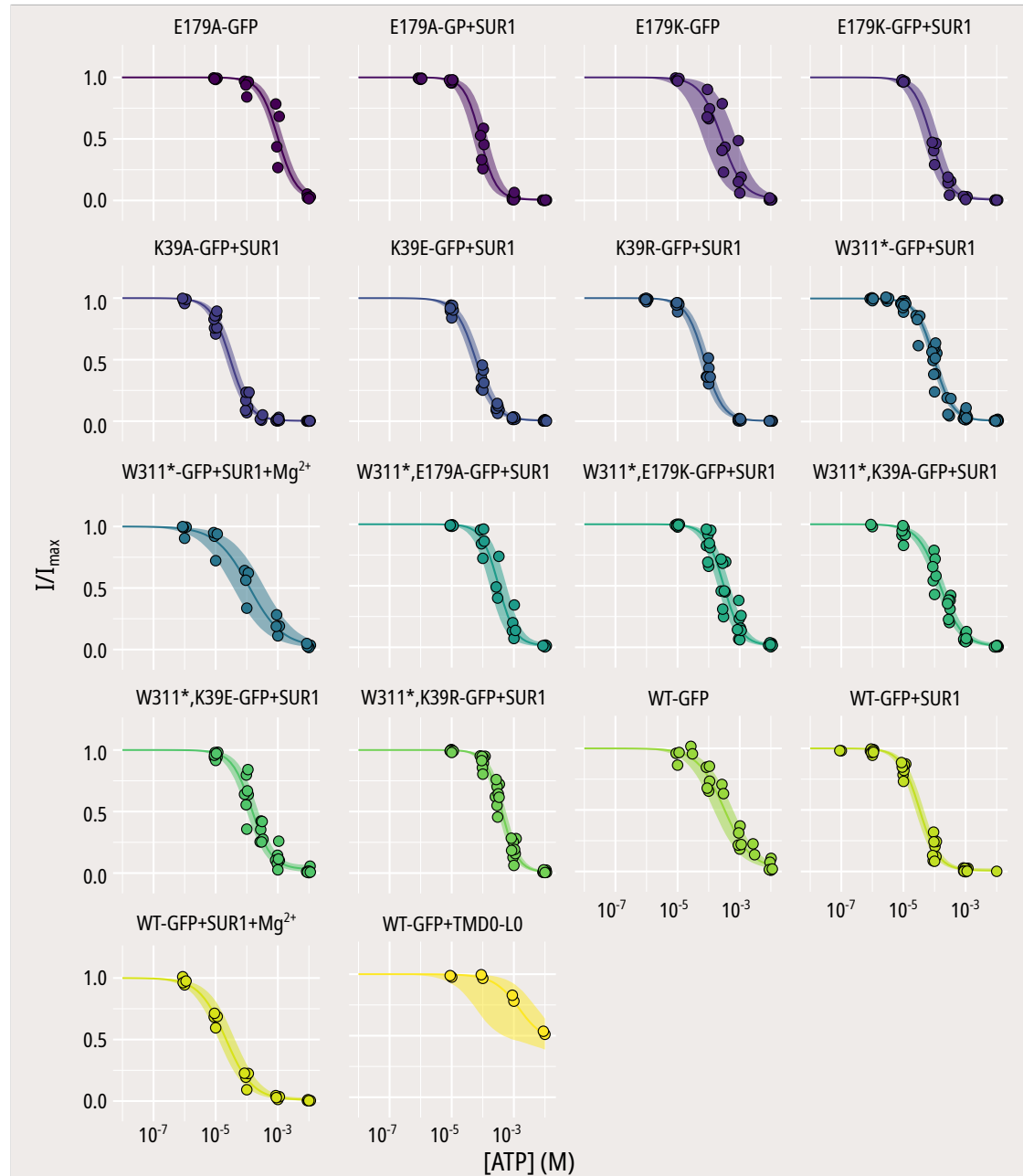
**FIGURE 7.2:** A Fluorescence quenching (blue) and current regulation (orange) of G334D+SUR1-T1397\* by MgTNP-ADP (left) or W311\*-GFP+SUR1 by TNP-ATP (right). Filled blue circles represent fluorescence quenching obtained from unroofed membranes, open circles are from excised patches. Activation data are reproduced from Puljung *et al.* (3), inhibition data from Figure 3.12D. Fitted curves are the 95 % credible intervals of the posterior probability distribution of fits to the MWC model parameterised in equations 2.9 and 2.12, not including the  $\delta_{\text{experiment}}$ . E Posterior probability distributions for each of the five free parameters estimated from fits to the MWC model are shown shaded according to their credible intervals.  $1/D_{NBD}$  is plotted to aid comparison with  $D_A$ .

# **Appendices**

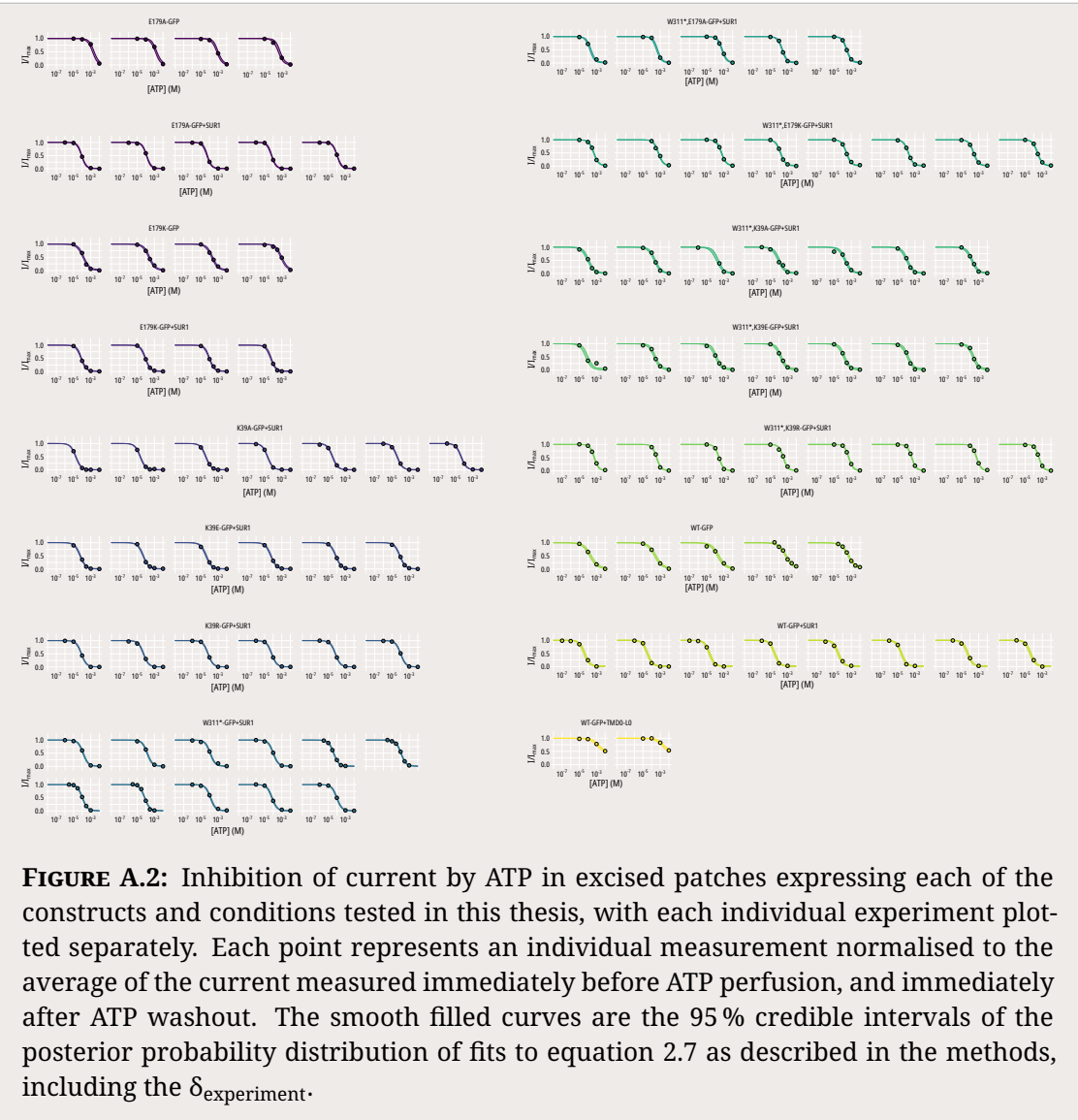


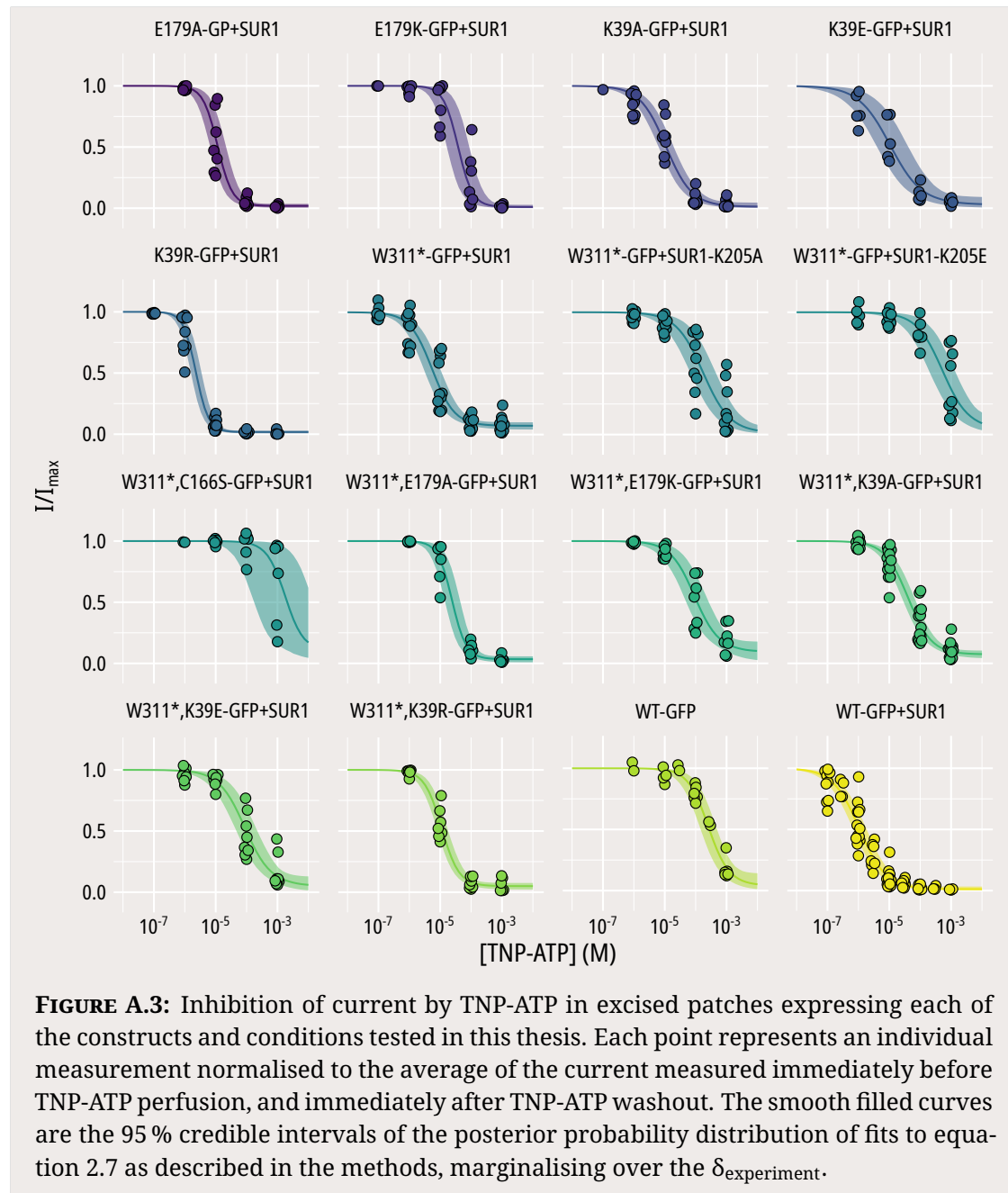
# A

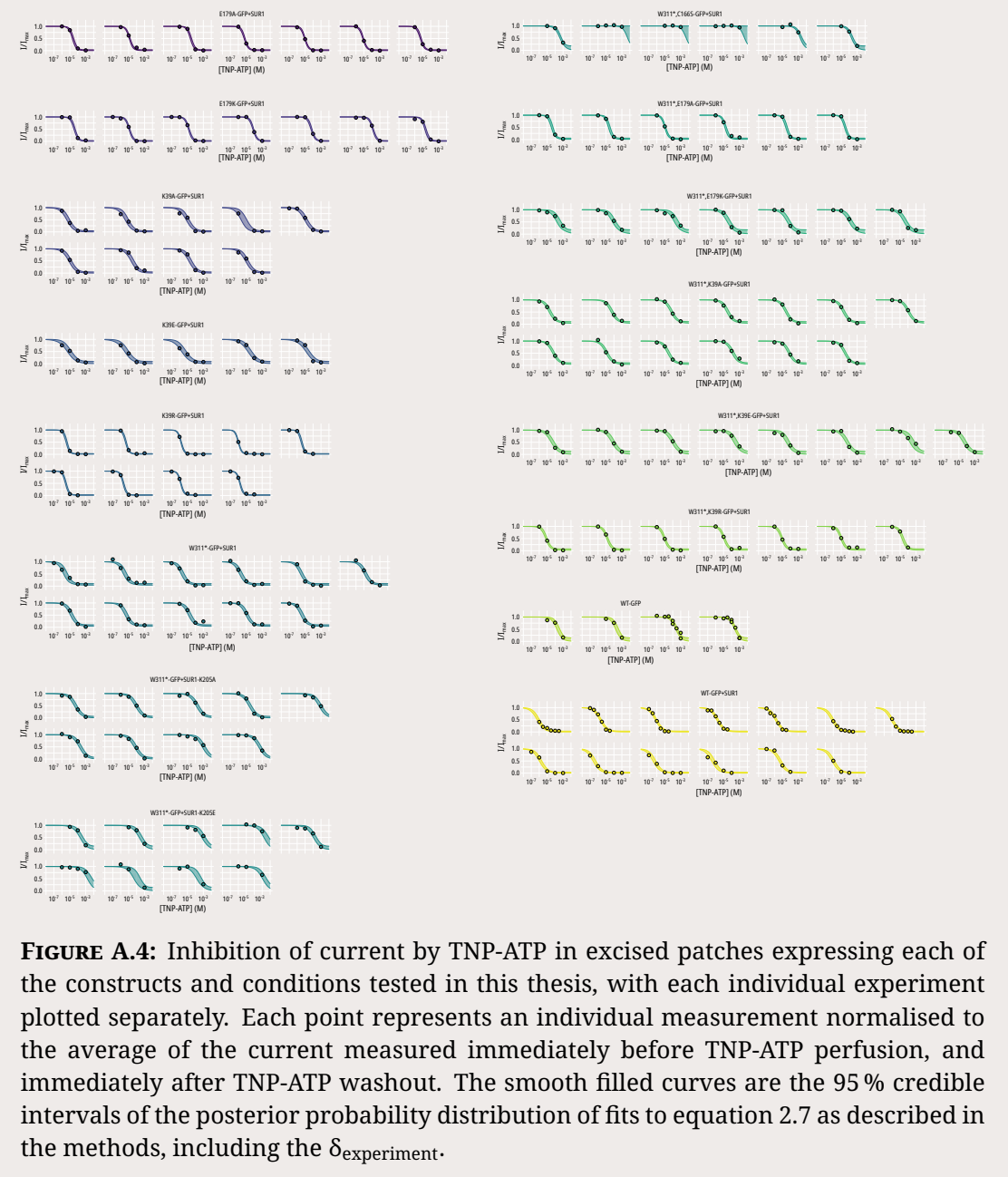
## Appendices

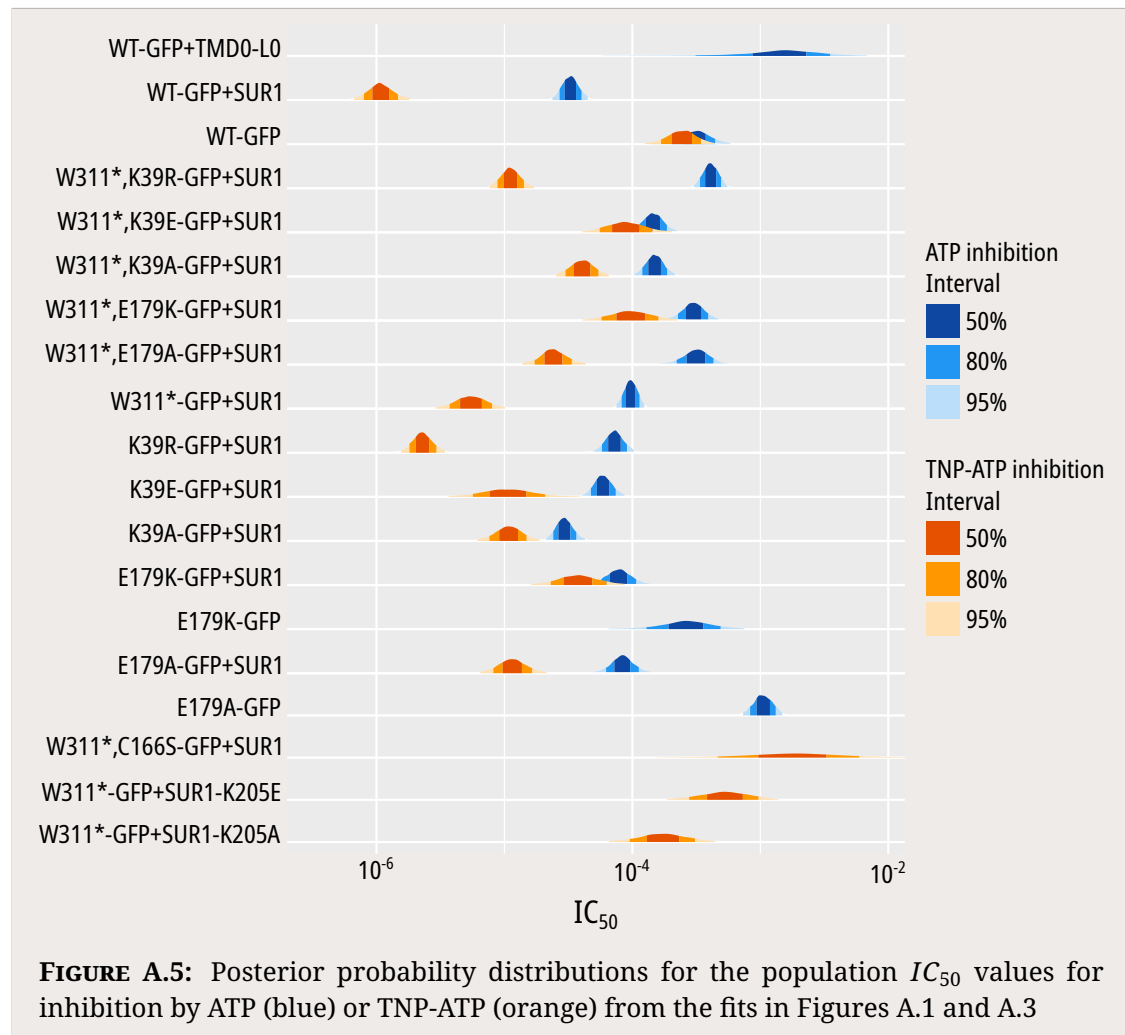


**FIGURE A.1:** Inhibition of current by ATP in excised patches expressing each of the constructs and conditions tested in this thesis. Each point represents an individual measurement normalised to the average of the current measured immediately before ATP perfusion, and immediately after ATP washout. The smooth filled curves are the 95 % credible intervals of the posterior probability distribution of fits to equation 2.7 as described in the methods, marginalising over the  $\delta_{\text{experiment}}$ .

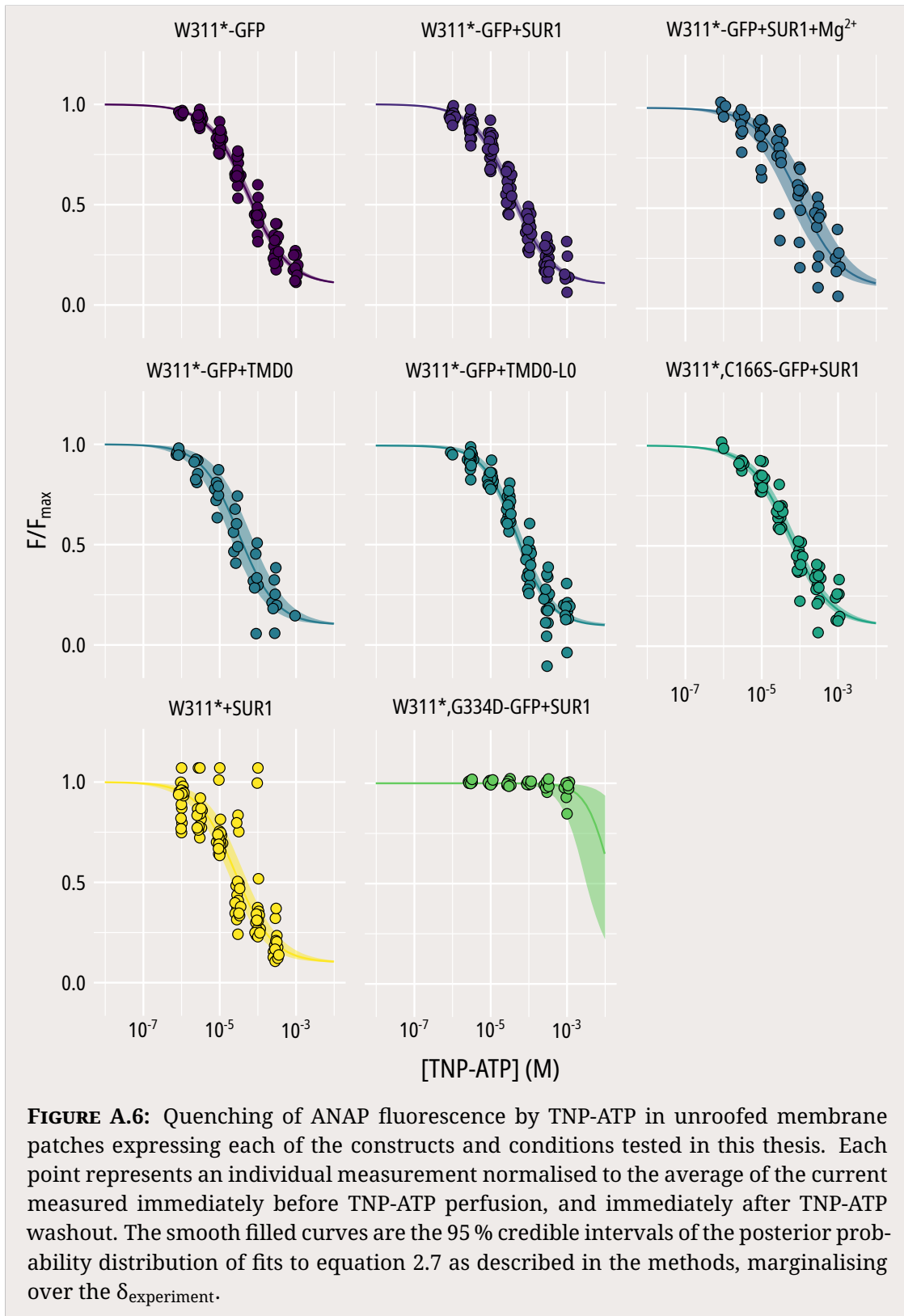


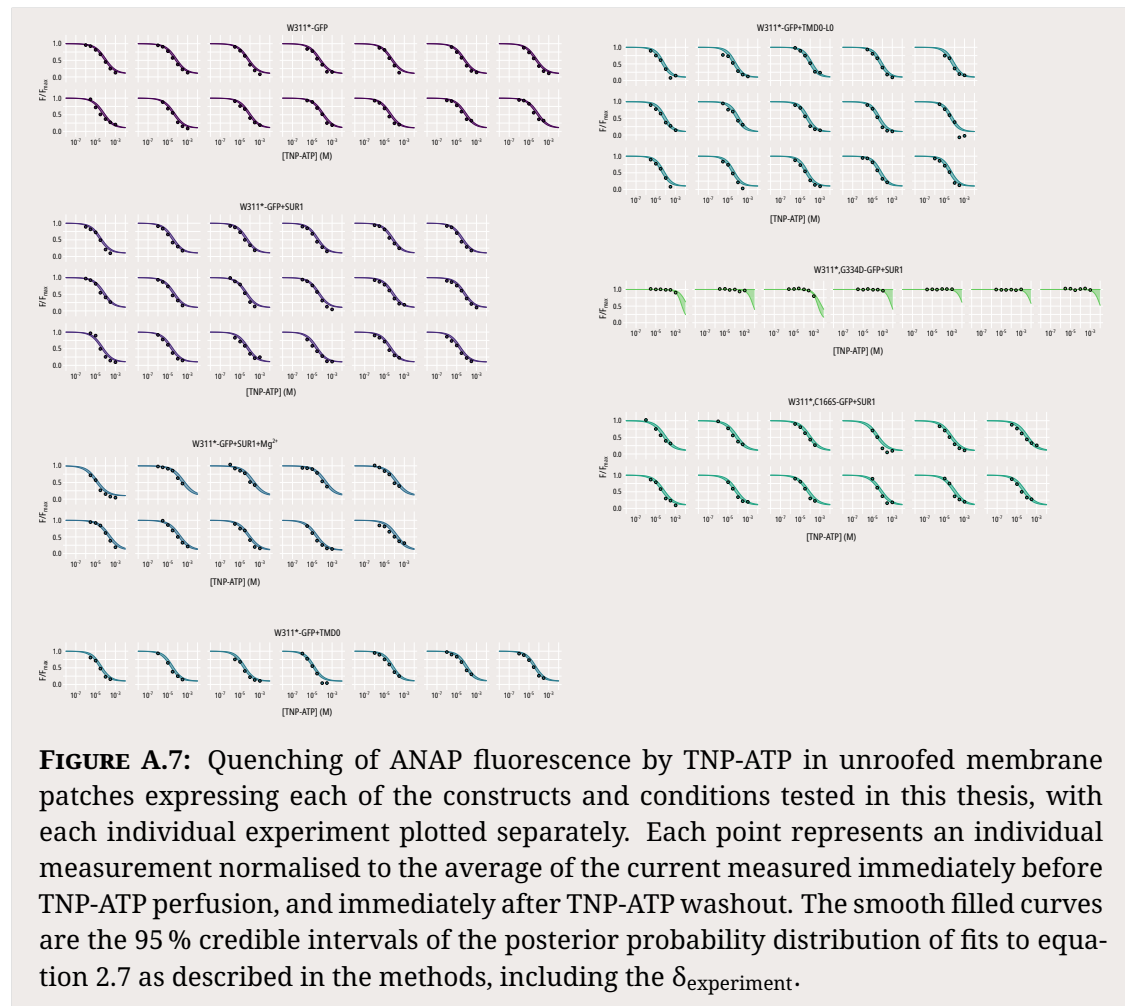


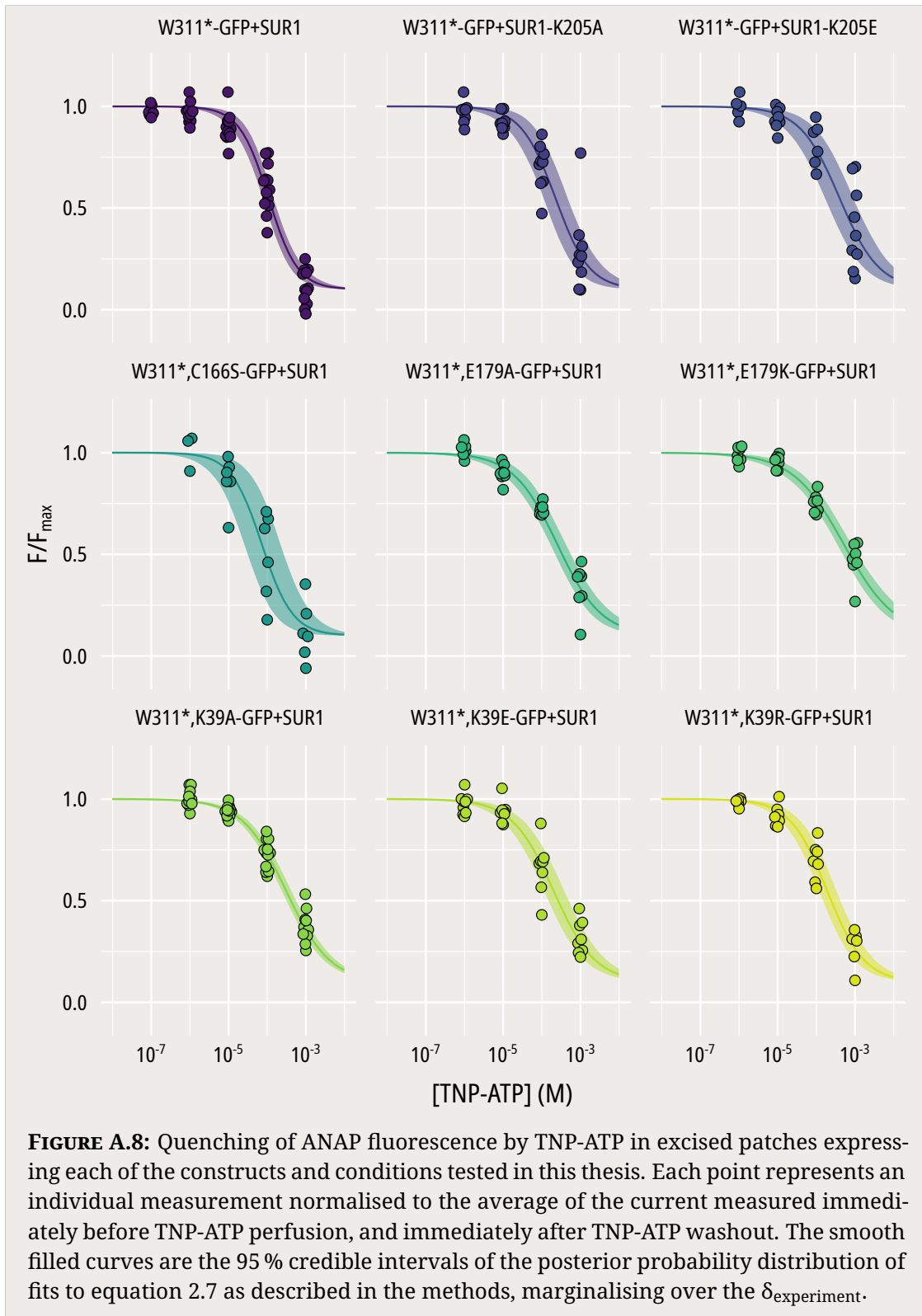




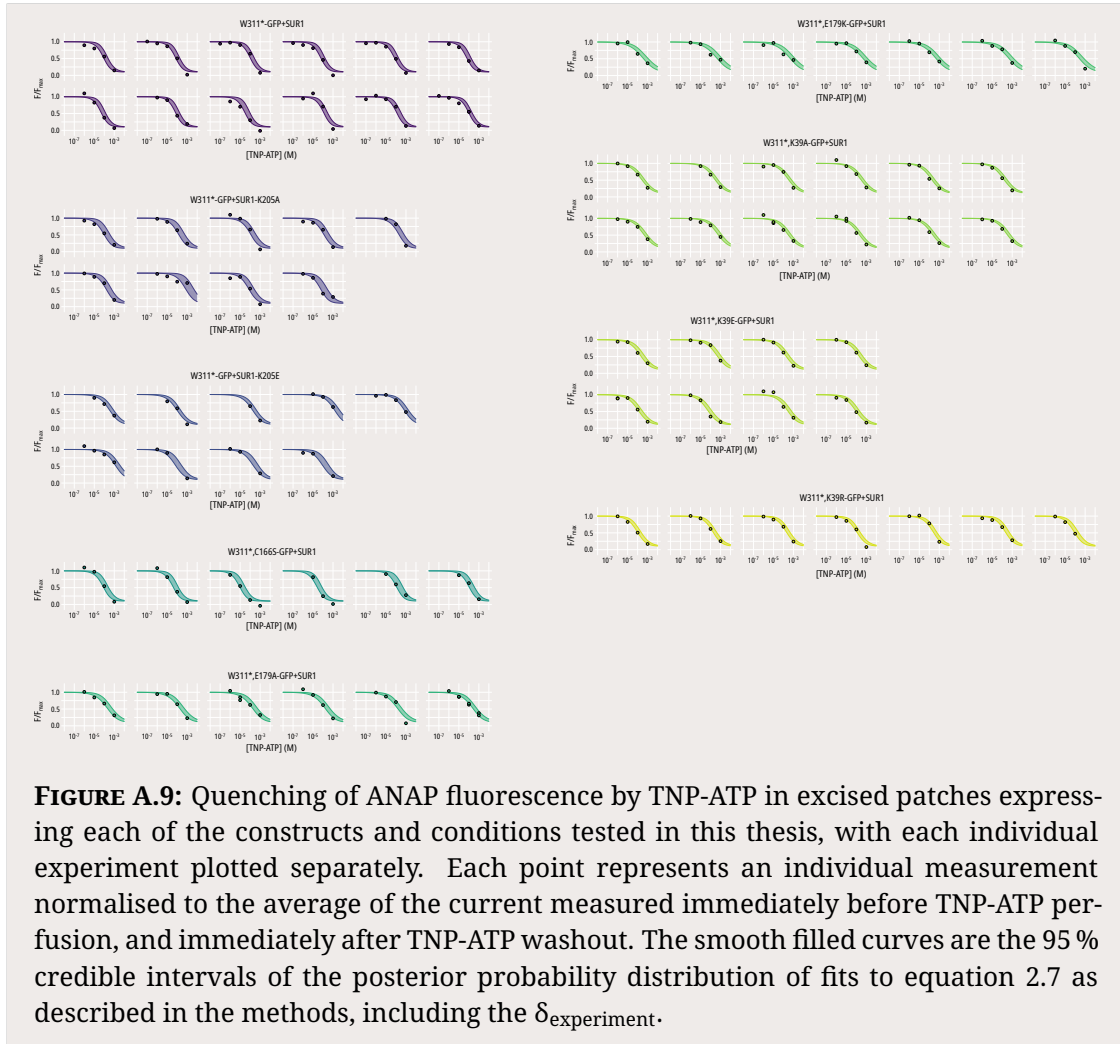
**FIGURE A.5:** Posterior probability distributions for the population  $IC_{50}$  values for inhibition by ATP (blue) or TNP-ATP (orange) from the fits in Figures A.1 and A.3

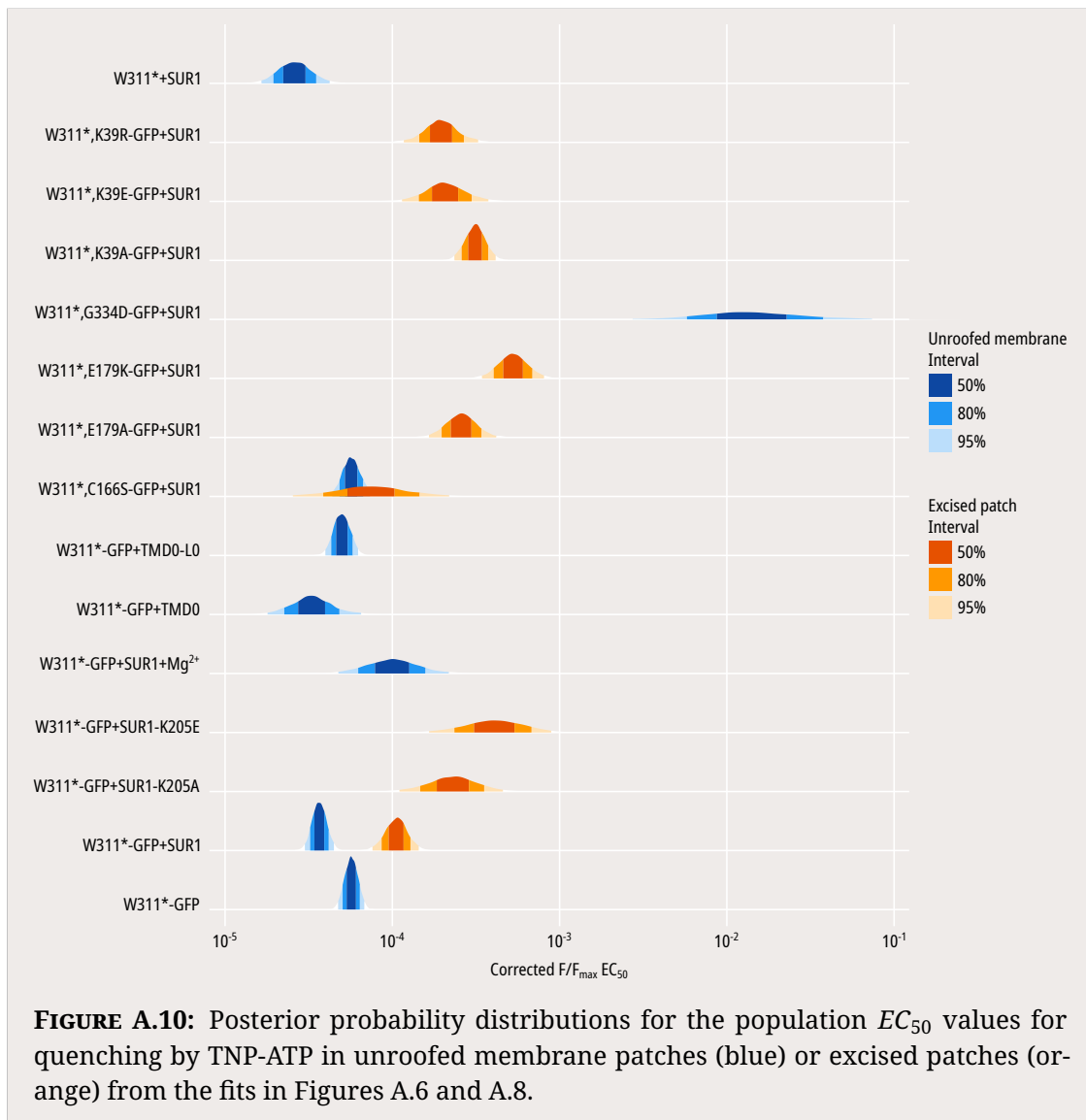




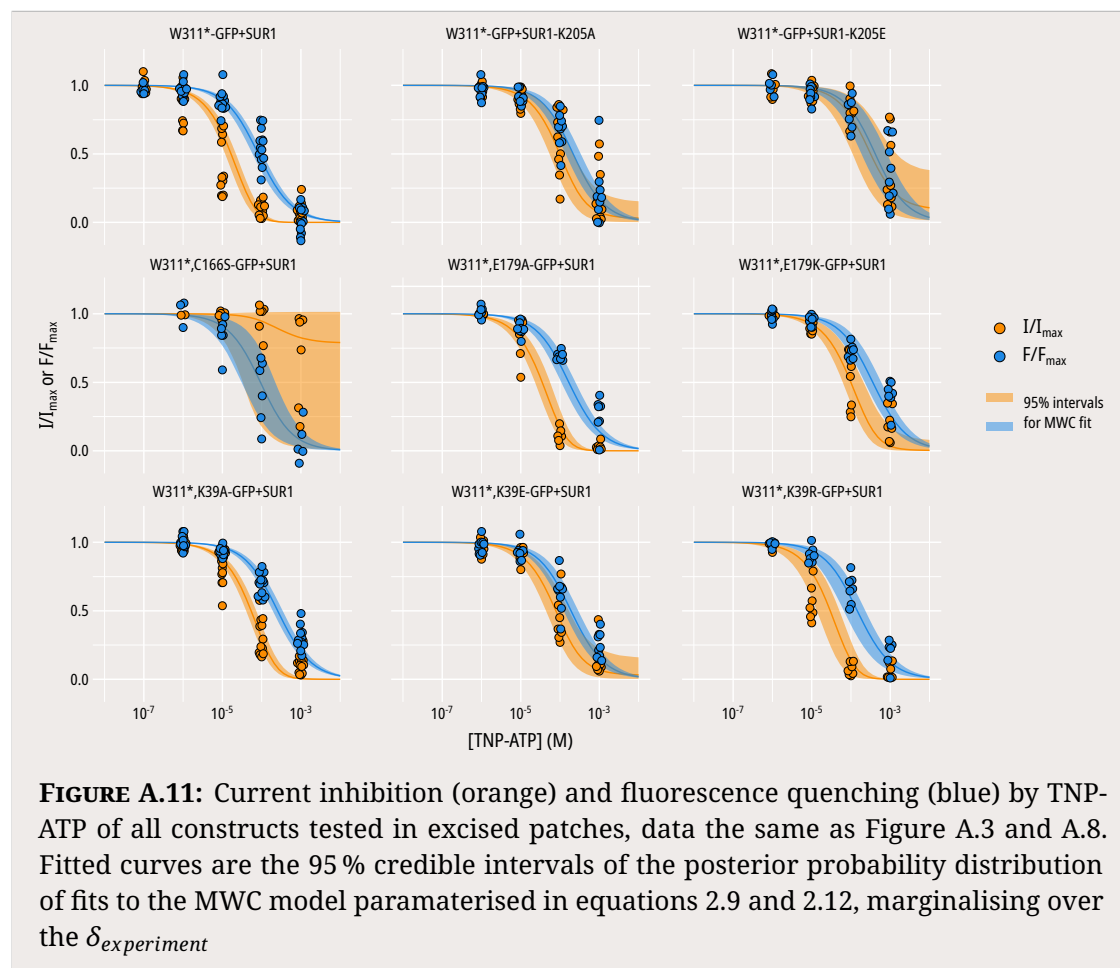


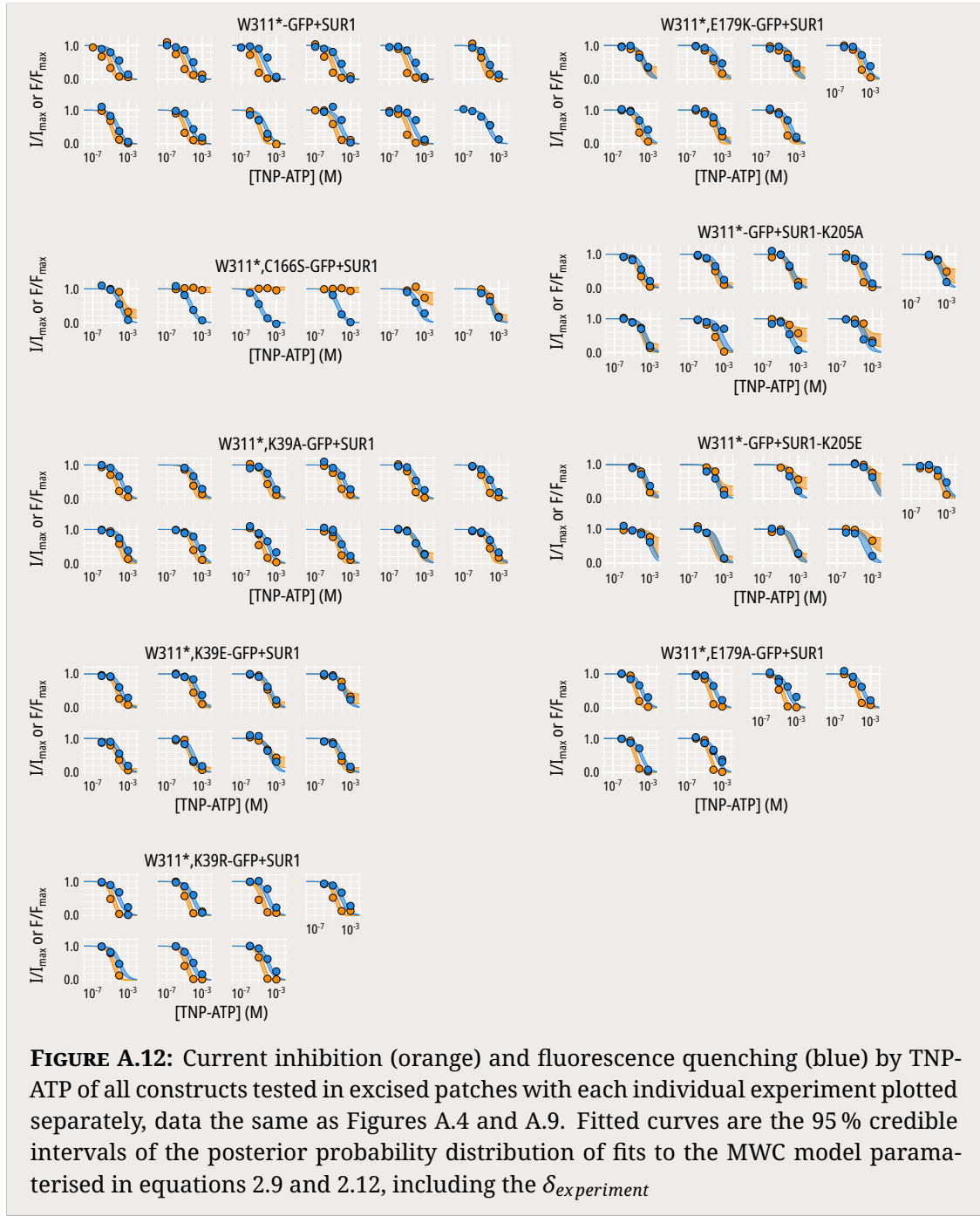
**FIGURE A.8:** Quenching of ANAP fluorescence by TNP-ATP in excised patches expressing each of the constructs and conditions tested in this thesis. Each point represents an individual measurement normalised to the average of the current measured immediately before TNP-ATP perfusion, and immediately after TNP-ATP washout. The smooth filled curves are the 95 % credible intervals of the posterior probability distribution of fits to equation 2.7 as described in the methods, marginalising over the  $\delta_{\text{experiment}}$ .

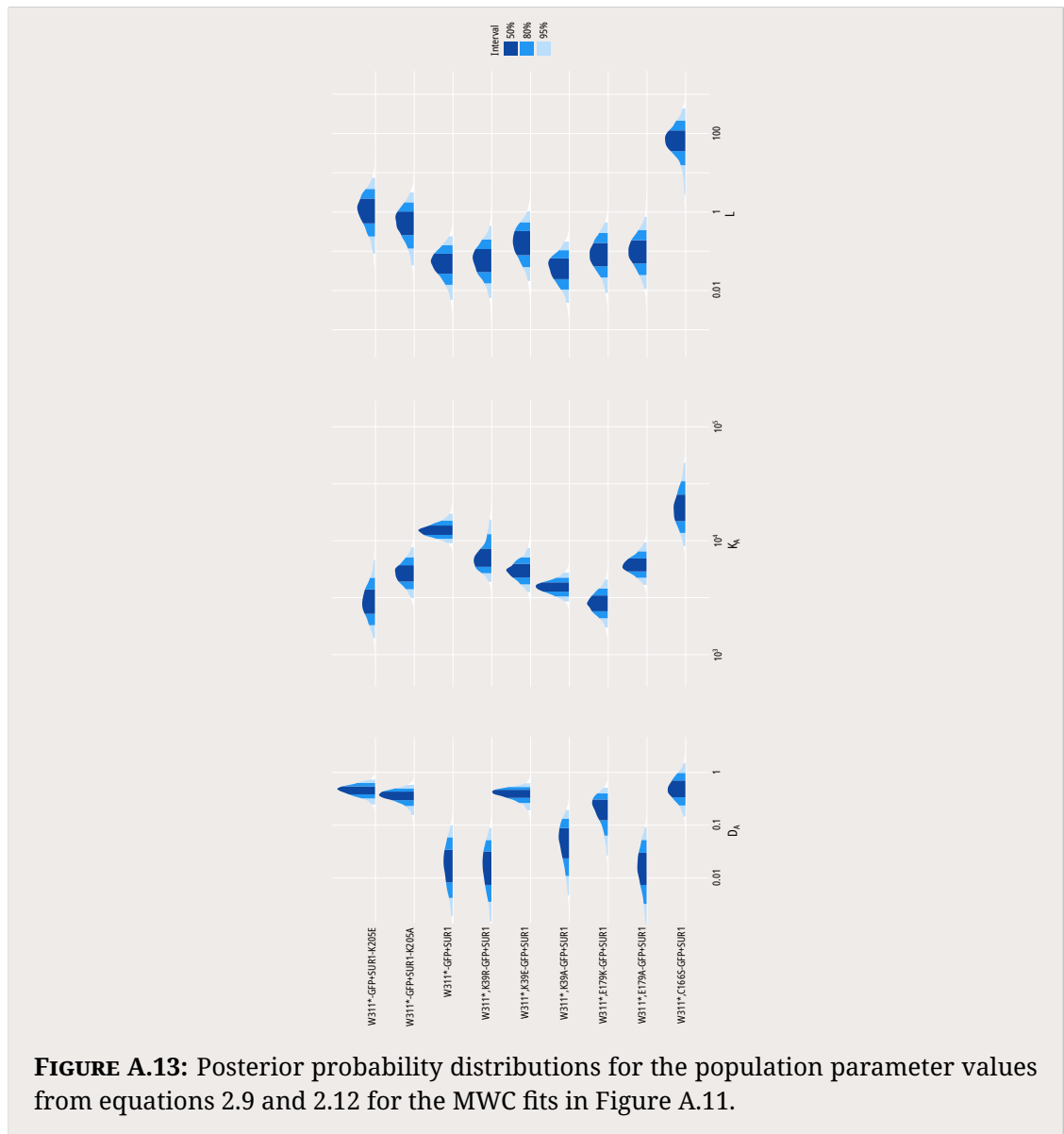




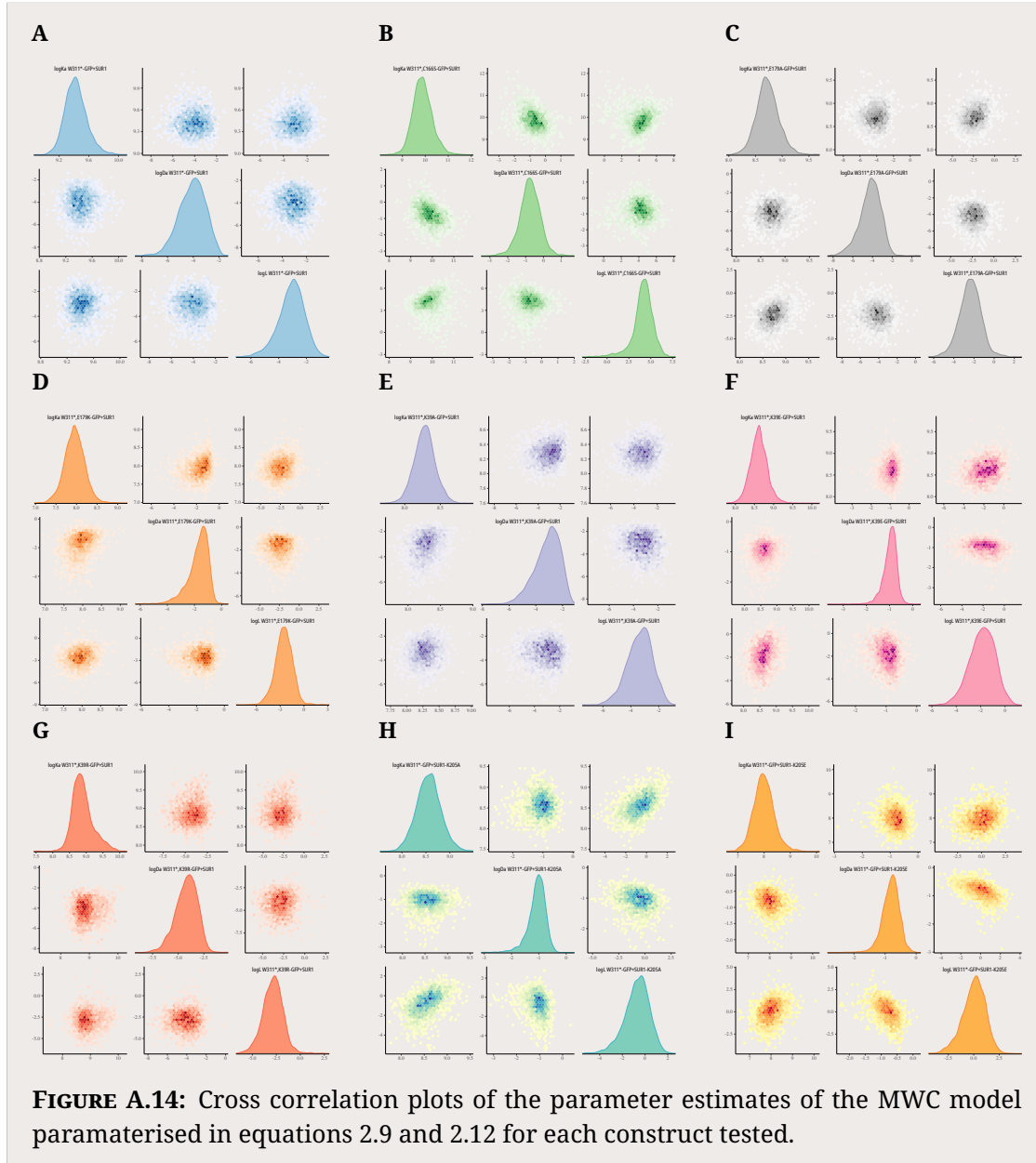
**FIGURE A.10:** Posterior probability distributions for the population  $EC_{50}$  values for quenching by TNP-ATP in unroofed membrane patches (blue) or excised patches (orange) from the fits in Figures A.6 and A.8.

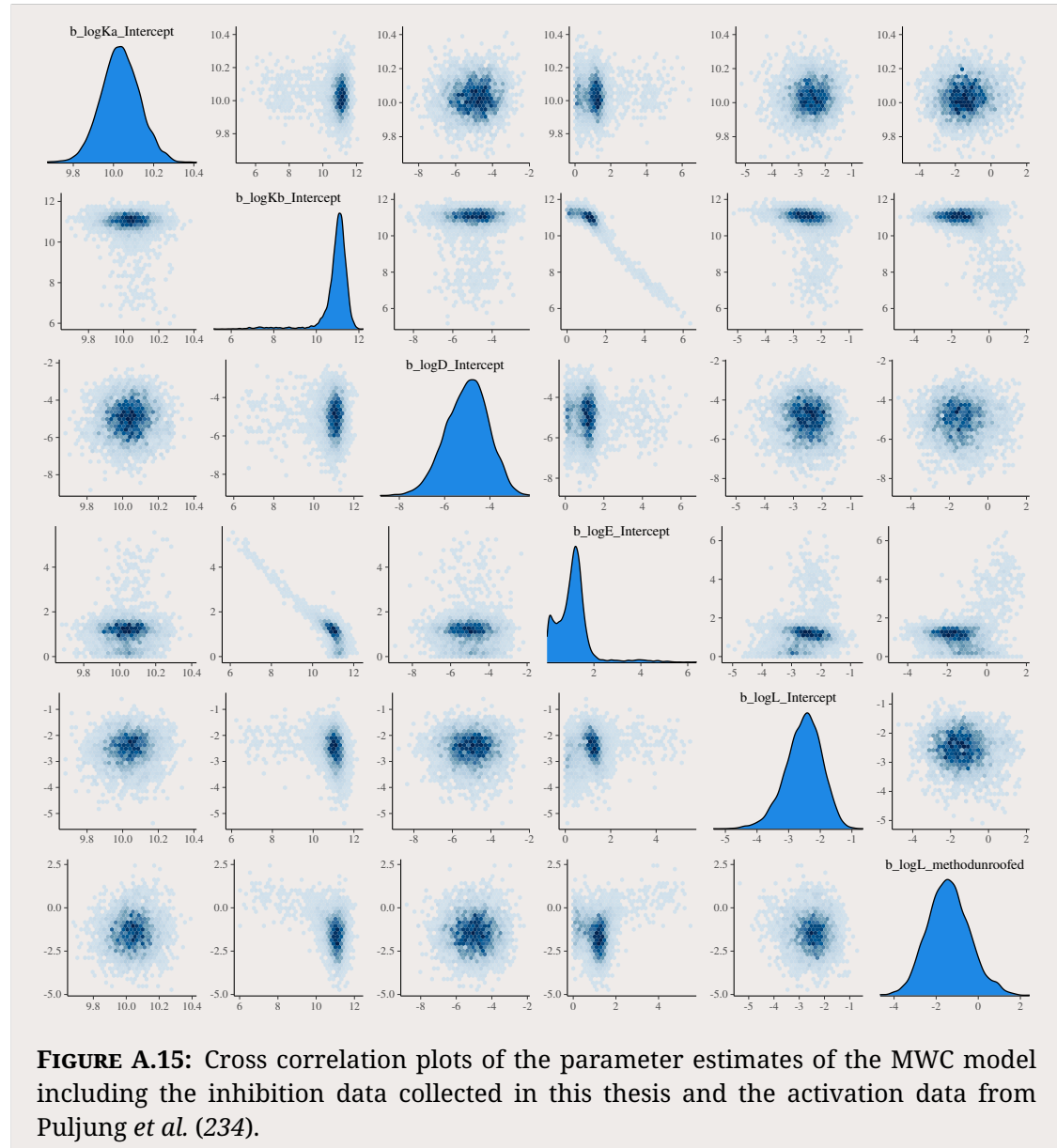






**FIGURE A.13:** Posterior probability distributions for the population parameter values from equations 2.9 and 2.12 for the MWC fits in Figure A.11.





## References

1. S. G. Usher, F. M. Ashcroft, M. C. Puljung, *eLife* **9**, ed. by G. Yellen, R. W. Aldrich, Publisher: eLife Sciences Publications, Ltd, e52775, (2021; <https://doi.org/10.7554/eLife.52775>) (Jan. 7, 2020).
2. T. Pipatpolkai, S. G. Usher, N. Vedovato, F. M. Ashcroft, P. J. Stansfeld, *bioRxiv*, 2021.05.06.442933, (2021; <https://www.biorxiv.org/content/10.1101/2021.05.06.442933v1>) (May 6, 2021).
3. M. Puljung, N. Vedovato, S. Usher, F. Ashcroft, *eLife* **8**, ed. by J. Kuriyan, K. J. Swartz, K. J. Swartz, S.-L. Shyng, M. P. Goldschen-Ohm, Publisher: eLife Sciences Publications, Ltd, e41103, (2021; <https://doi.org/10.7554/eLife.41103>) (Feb. 21, 2019).
4. G. Da Silva Xavier, *Journal of Clinical Medicine* **7**, (2021; <https://www.ncbi.nlm.nih.gov/pmc/articles/PMC5867580/>) (Mar. 12, 2018).
5. F. M. Ashcroft, P. Rorsman, *Nat Rev Endocrinol* **9**, Type: Journal Article, 660–9, (<https://www.ncbi.nlm.nih.gov/pubmed/24042324>) (2013).
6. F. M. Ashcroft, D. E. Harrison, S. J. H. Ashcroft, *Nature* **312**, 446–448, (2021; <https://www.nature.com/articles/312446a0>) (Nov. 1984).
7. P. Rorsman, G. Trube, *Pflügers Archiv* **405**, 305–309, (2021; <https://doi.org/10.1007/BF00595682>) (Dec. 1, 1985).
8. P. Rorsman, G. Trube, *The Journal of Physiology* **374**, 531–550, (2021; <https://physoc.onlinelibrary.wiley.com/doi/abs/10.1113/jphysiol.1986.sp016096>) (1986).
9. C. G. Nichols, *Nature* **440**, 470–476, (2021; <https://www.nature.com/articles/nature04711>) (Mar. 2006).
10. N. Inagaki *et al.*, *Neuron* **16**, 1011–1017, (2021; <https://www.sciencedirect.com/science/article/pii/S0896627300801245>) (May 1, 1996).
11. M. Yamada *et al.*, *The Journal of Physiology* **499**, 715–720, (2021; <https://physoc.onlinelibrary.wiley.com/doi/abs/10.1113/jphysiol.1997.sp021963>) (1997).
12. S.-L. Shyng, C. Nichols, *Journal of General Physiology* **110**, 655–664, (2021; <https://doi.org/10.1085/jgp.110.6.655>) (Dec. 1, 1997).
13. J. P. Clement *et al.*, *Neuron* **18**, 827–838, (2021; <https://www.sciencedirect.com/science/article/pii/S0896627300803219>) (May 1, 1997).

14. N. Inagaki *et al.*, *Science* **270**, Publisher: American Association for the Advancement of Science Section: Research Article, 1166–1170, (2021); <https://science.sciencemag.org/content/270/5239/1166> (Nov. 17, 1995).
15. B. Hille, *Ion Channels of Excitable Membranes* (Sinauer Associates, ed. 3, 2001), (<http://gen.lib.rus.ec/book/index.php?md5=e320aefcf11b0c93b8ecc5db4dfadac>).
16. J. Zheng, M. C. Trudeau, *Handbook of Ion Channels* (Taylor and Francis, ed. 1, 2015).
17. T. Baukrowitz *et al.*, *Science* **282**, 1141–1144, (2021); <https://science.sciencemag.org/content/282/5391/1141> (Nov. 6, 1998).
18. S.-L. Shyng, C. G. Nichols, *Science* **282**, 1138–1141, (2021); <https://science.sciencemag.org/content/282/5391/1138> (Nov. 6, 1998).
19. D. Enkvetchakul, I. Jeliazkova, C. G. Nichols, *Journal of Biological Chemistry* **280**, 35785–35788, (2021); <https://www.sciencedirect.com/science/article/pii/S0021925820593733> (Oct. 28, 2005).
20. M. C. Puljung, *Journal of General Physiology* **150**, 653–669, (2021); <https://doi.org/10.1085/jgp.201711978> (Apr. 23, 2018).
21. E. B. Pratt, P. Tewson, C. E. Bruederle, W. R. Skach, S.-L. Shyng, *Journal of General Physiology* **137**, 299–314, (2021; <https://doi.org/10.1085/jgp.201010557>) (Feb. 14, 2011).
22. L. Aguilar-Bryan *et al.*, *Science* **268**, Publisher: American Association for the Advancement of Science Section: Reports, 423–426, (2021); <https://science.sciencemag.org/content/268/5209/423> (Apr. 21, 1995).
23. G. E. Tusnády, É. Bakos, A. Váradi, B. Sarkadi, *FEBS Letters* **402**, \_eprint: <https://febs.onlinelibrary.wiley.com/doi/pdf/10.1016/S0014-5793%2896%2901478-0>, 1–3, (2021; <https://febs.onlinelibrary.wiley.com/doi/abs/10.1016/S0014-5793%2896%2901478-0>) (1997).
24. P. Vergani, S. W. Lockless, A. C. Nairn, D. C. Gadsby, *Nature* **433**, 876–880, (2021); <https://www.nature.com/articles/nature03313> (Feb. 2005).
25. J. ter Beek, A. Guskov, D. J. Slotboom, *Journal of General Physiology* **143**, 419–435, (2021; <https://doi.org/10.1085/jgp.201411164>) (Mar. 17, 2014).
26. K. P. K. Lee, J. Chen, R. MacKinnon, *eLife* **6**, Type: Journal Article, (<https://www.ncbi.nlm.nih.gov/pubmed/29286281>) (2017).
27. G. M. Martin, B. Kandasamy, F. DiMaio, C. Yoshioka, S.-L. Shyng, *eLife* **6**, ed. by K. J. Swartz, e31054, (2021; <https://doi.org/10.7554/eLife.31054>) (Oct. 16, 2017).
28. N. Li *et al.*, *Cell* **168**, 101–110.e10, (2021); <https://www.sciencedirect.com/science/article/pii/S0092867416317445> (Jan. 12, 2017).
29. G. M. Martin *et al.*, *eLife* **8**, ed. by R. Aldrich, G. Yellen, V. Y. Moiseenkova-Bell, C. G. Nichols, J. Agar, e46417, (2021; <https://doi.org/10.7554/eLife.46417>) (July 25, 2019).

30. M. Matsuo, N. Kioka, T. Amachi, K. Ueda, *Journal of Biological Chemistry* **274**, Publisher: Elsevier, 37479–37482, (2021); [https://www.jbc.org/article/S0021-9258\(19\)53119-2/abstract](https://www.jbc.org/article/S0021-9258(19)53119-2/abstract) (Dec. 24, 1999).
31. L. V. Zingman *et al.*, *Neuron* **31**, Publisher: Elsevier, 233–245, (2021); [https://www.cell.com/neuron/abstract/S0896-6273\(01\)00356-7](https://www.cell.com/neuron/abstract/S0896-6273(01)00356-7) (Aug. 2, 2001).
32. H. de Wet *et al.*, *FEBS J* **274**, Type: Journal Article, 3532–44, (<https://www.ncbi.nlm.nih.gov/pubmed/17561960>) (2007).
33. N. Zerangue, B. Schwappach, Y. N. Jan, L. Y. Jan, *Neuron* **22**, 537–548, (2021); <https://www.sciencedirect.com/science/article/pii/S0896627300807084> (Mar. 1, 1999).
34. G. M. Martin, P.-C. Chen, P. Devaraneni, S.-L. Shyng, *Frontiers in Physiology* **4**, (2021); <https://www.frontiersin.org/articles/10.3389/fphys.2013.00386/full> (2013).
35. S. J. Tucker, F. M. Gribble, C. Zhao, S. Trapp, F. M. Ashcroft, *Nature* **387**, 179–183, (2021; <https://www.nature.com/articles/387179a0>) (May 1997).
36. S. A. John, J. R. Monck, J. N. Weiss, B. Ribalet, *The Journal of Physiology* **510**, 333–345, (2021; <https://physoc.onlinelibrary.wiley.com/doi/abs/10.1111/j.1469-7793.1998.333bk.x>) (1998).
37. L. R. Conti, C. M. Radeke, C. A. Vandenberg, *Journal of Biological Chemistry* **277**, 25416–25422, (2021); <https://www.sciencedirect.com/science/article/pii/S0021925819665026> (July 12, 2002).
38. N. Sharma *et al.*, *Journal of Biological Chemistry* **274**, 20628–20632, (2021); [https://www.jbc.org/article/S0021-9258\(19\)72695-7/abstract](https://www.jbc.org/article/S0021-9258(19)72695-7/abstract) (July 16, 1999).
39. N. Vedovato, O. Rorsman, K. Hennis, F. M. Ashcroft, P. Proks, *The Journal of Physiology* **596**, 6205–6217, (2021); <https://physoc.onlinelibrary.wiley.com/doi/abs/10.1113/JP276708> (2018).
40. J. P. Giblin, K. Quinn, A. Tinker, *European Journal of Biochemistry* **269**, 5303–5313, (2021; <https://febs.onlinelibrary.wiley.com/doi/abs/10.1046/j.1432-1033.2002.03249.x>) (2002).
41. B. Schwappach, N. Zerangue, Y. N. Jan, L. Y. Jan, *Neuron* **26**, 155–167, (2021); <https://www.sciencedirect.com/science/article/pii/S0896627300811460> (Apr. 1, 2000).
42. H. Sakura, S. Trapp, B. Liss, F. M. Ashcroft, *The Journal of Physiology* **521**, 337–350, (2021; <https://physoc.onlinelibrary.wiley.com/doi/abs/10.1111/j.1469-7793.1999.00337.x>) (1999).
43. J. S. Bonifacino, A. M. Weissman, *Annual Review of Cell and Developmental Biology* **14**, 19–57, (2021; <https://doi.org/10.1146/annurev.cellbio.14.1.19>) (1998).

44. F.-F. Yan, C.-W. Lin, E. A. Cartier, S.-L. Shyng, *American Journal of Physiology-Cell Physiology* **289**, C1351–C1359, (2021);  
<https://journals.physiology.org/doi/full/10.1152/ajpcell.00240.2005>) (Nov. 1, 2005).
45. F. Yan *et al.*, *Journal of Biological Chemistry* **279**, 11096–11105, (2021);  
<http://www.sciencedirect.com/science/article/pii/S0021925819643140>) (Mar. 19, 2004).
46. F.-F. Yan, J. Casey, S.-L. Shyng, *Journal of Biological Chemistry* **281**, 33403–33413, (2021);  
<https://www.sciencedirect.com/science/article/pii/S0021925820705247>) (Nov. 3, 2006).
47. F. F. Yan *et al.*, *Diabetes* **56**, Type: Journal Article, 2339–48,  
(<https://www.ncbi.nlm.nih.gov/pubmed/17575084>) (2007).
48. F.-F. Yan *et al.*, *Diabetes* **56**, 2339–2348, (2021);  
<https://diabetes.diabetesjournals.org/content/56/9/2339>) (Sept. 1, 2007).
49. G. M. Martin *et al.*, *Journal of Biological Chemistry* **291**, 21971–21983, (2021);  
<https://www.sciencedirect.com/science/article/pii/S0021925820357811>) (Oct. 1, 2016).
50. K. Yang, K. Fang, L. Fromondi, K. W. Chan, *FEBS Letters* **579**, 4113–4118, (2021);  
<https://www.sciencedirect.com/science/article/pii/S0014579305007763>) (Aug. 1, 2005).
51. A. E. Alekseev, P. A. Brady, A. Terzic, *Journal of General Physiology* **111**, 381–394, (2021; <https://doi.org/10.1085/jgp.111.2.381>) (Feb. 1, 1998).
52. A. P. Babenko, G. Gonzalez, J. Bryan, *Journal of Biological Chemistry* **274**, 11587–11592, (2021);  
<https://www.sciencedirect.com/science/article/pii/S002192581973467X>) (Apr. 23, 1999).
53. L. Li, X. Geng, P. Drain, *Journal of General Physiology* **119**, 105–116, (2021);  
<https://doi.org/10.1085/jgp.119.1.105>) (Jan. 2, 2002).
54. P. Proks, F. M. Ashcroft, *Progress in Biophysics and Molecular Biology* **99**, 7–19, (2021);  
<http://www.sciencedirect.com/science/article/pii/S0079610708000679>) (Jan. 1, 2009).
55. D. Enkvetchakul, G. Loussouarn, E. Makhina, S. L. Shyng, C. G. Nichols, *Biophysical Journal* **78**, 2334–2348, (2021);  
<http://www.sciencedirect.com/science/article/pii/S0006349500767798>) (May 1, 2000).
56. I. Benz, K. Haverkampf, M. Kohlhardt, *The Journal of Membrane Biology* **165**, 45–52, (2021; <https://doi.org/10.1007/s002329900419>) (Sept. 1, 1998).
57. A. Alekseev, M. Kennedy, B. Navarro, A. Terzic, *The Journal of Membrane Biology* **159**, 161–168, (2021; <https://doi.org/10.1007/s002329900279>) (Sept. 1, 1997).
58. S. Trapp, P. Proks, S. J. Tucker, F. M. Ashcroft, *Journal of General Physiology* **112**, 333–349, (2021; <https://doi.org/10.1085/jgp.112.3.333>) (Sept. 1, 1998).

59. B. Sakmann, G. Trube, *The Journal of Physiology* **347**, 659–683, (2021; <https://physoc.onlinelibrary.wiley.com/doi/abs/10.1113/jphysiol.1984.sp015089>) (1984).
60. Y. Zilberman, N. Burnashev, A. Papin, V. Portnov, B. Khodorov, *Pflügers Archiv* **411**, 584–589, (2021; <https://doi.org/10.1007/BF00582382>) (May 1, 1988).
61. M. L. Chapman, M. L. Blanke, H. S. Krovetz, A. M. VanDongen, *Pflügers Archiv* **451**, 776–792, (2021; <https://doi.org/10.1007/s00424-005-1515-2>) (Mar. 1, 2006).
62. Q. Kuang, P. Purhonen, H. Hebert, *Cellular and Molecular Life Sciences* **72**, 3677–3693, (2021; <https://www.ncbi.nlm.nih.gov/pmc/articles/PMC4565861/>) (2015).
63. L. Heginbotham, Z. Lu, T. Abramson, R. MacKinnon, *Biophysical Journal* **66**, 1061–1067, (2021; <https://www.sciencedirect.com/science/article/pii/S0006349594808872>) (Apr. 1, 1994).
64. P. Proks, C. E. Capener, P. Jones, F. M. Ashcroft, *Journal of General Physiology* **118**, 341–353, (2021; <https://doi.org/10.1085/jgp.118.4.341>) (Sept. 18, 2001).
65. S.-L. Shyng, T. Ferrigni, C. Nichols, *Journal of General Physiology* **110**, 141–153, (2021; <https://doi.org/10.1085/jgp.110.2.141>) (Aug. 1, 1997).
66. S. J. Tucker *et al.*, *The EMBO Journal* **17**, 3290–3296, (2021; <https://www.embopress.org/doi/full/10.1093/emboj/17.12.3290>) (June 15, 1998).
67. G. Loussouarn, E. N. Makhina, T. Rose, C. G. Nichols, *Journal of Biological Chemistry* **275**, 1137–1144, (2021; <https://www.sciencedirect.com/science/article/pii/S0021925818312286>) (Jan. 14, 2000).
68. P. Tammaro *et al.*, *Diabetologia* **51**, 802–810, (2021; <https://doi.org/10.1007/s00125-008-0923-1>) (May 1, 2008).
69. P. Drain, L. Li, J. Wang, *Proceedings of the National Academy of Sciences* **95**, Publisher: National Academy of Sciences Section: Biological Sciences, 13953–13958, (2021; <https://www.pnas.org/content/95/23/13953>) (Nov. 10, 1998).
70. P. Proks *et al.*, *Proceedings of the National Academy of Sciences* **101**, 17539–17544, (2021; <https://www.pnas.org/content/101/50/17539>) (Dec. 14, 2004).
71. J. C. Koster, H. T. Kurata, D. Enkvetchakul, C. G. Nichols, *Biophysical Journal* **95**, 4689–4697, (2021; <https://www.sciencedirect.com/science/article/pii/S0006349508786089>) (Nov. 15, 2008).
72. R. Männikkö *et al.*, *Human Molecular Genetics* **19**, 963–972, (2021; <https://doi.org/10.1093/hmg/ddp554>) (Mar. 15, 2010).
73. J. B. W. Li *et al.*, *Journal of Biological Chemistry* **288**, 23038–23049, (2021; <https://www.sciencedirect.com/science/article/pii/S002192582045330X>) (Aug. 9, 2013).

74. P. E. Cooper, C. McClenaghan, X. Chen, A. Stary-Weinzinger, C. G. Nichols, *Journal of Biological Chemistry* **292**, 17387–17398, (2021);  
<https://www.sciencedirect.com/science/article/pii/S0021925820338965>) (Oct. 20, 2017).
75. T. Pipatpolkai, R. A. Corey, P. Proks, F. M. Ashcroft, P. J. Stansfeld, *Communications Chemistry* **3**, 1–10, (2021);  
<https://www.nature.com/articles/s42004-020-00391-0>) (Oct. 30, 2020).
76. K. W. Chan, H. Zhang, D. E. Logothetis, *The EMBO Journal* **22**, 3833–3843, (2021);  
<https://www.embopress.org/doi/full/10.1093/emboj/cdg376>) (Aug. 1, 2003).
77. G. M. Martin, B. Kandasamy, F. DiMaio, C. Yoshioka, S. L. Shyng, *eLife* **6**, Type: Journal Article, (<https://www.ncbi.nlm.nih.gov/pubmed/29035201>) (2017).
78. K. P. K. Lee, J. Chen, R. MacKinnon, *eLife* **6**, ed. by K. J. Swartz, e32481, (2021);  
<https://doi.org/10.7554/eLife.32481>) (Dec. 29, 2017).
79. A. P. Babenko, J. Bryan, *J Biol Chem* **278**, Type: Journal Article, 41577–80,  
(<https://www.ncbi.nlm.nih.gov/pubmed/12941953>) (2003).
80. K. W. Chan, H. Zhang, D. E. Logothetis, *EMBO J* **22**, Type: Journal Article, 3833–43,  
(<https://www.ncbi.nlm.nih.gov/pubmed/12881418>) (2003).
81. K. Fang, L. Csanady, K. W. Chan, *J Physiol* **576**, Type: Journal Article, 379–89,  
(<https://www.ncbi.nlm.nih.gov/pubmed/16887879>) (Pt 2 2006).
82. M. C. Puljung, *J Gen Physiol* **150**, Type: Journal Article, 653–669,  
(<https://www.ncbi.nlm.nih.gov/pubmed/29685928>) (2018).
83. J. C. Koster, Q. Sha, S.-L. Shyng, C. G. Nichols, *The Journal of Physiology* **515**, 19–30,  
(2021; <https://physoc.onlinelibrary.wiley.com/doi/abs/10.1111/j.1469-7793.1999.019ad.x>) (1999).
84. A. P. Babenko, G. Gonzalez, J. Bryan, *Biochemical and Biophysical Research Communications* **255**, 231–238, (2021);  
<https://www.sciencedirect.com/science/article/pii/S0006291X99901729>) (Feb. 16, 1999).
85. F. Reimann, S. J. Tucker, P. Proks, F. M. Ashcroft, *The Journal of Physiology* **518**, 325–336, (2021);  
<https://physoc.onlinelibrary.wiley.com/doi/abs/10.1111/j.1469-7793.1999.0325p.x>) (1999).
86. A. P. Babenko, J. Bryan, *Journal of Biological Chemistry* **277**, 43997–44004, (2021);  
<https://www.sciencedirect.com/science/article/pii/S0021925819717451>) (Nov. 15, 2002).
87. C. Cukras, I. Jeliazkova, C. Nichols, *Journal of General Physiology* **120**, 437–446, (2021);  
<https://doi.org/10.1085/jgp.20028621>) (Aug. 26, 2002).
88. T. J. Craig *et al.*, *The Journal of Clinical Endocrinology & Metabolism* **94**, 2551–2557,  
(2021; <https://doi.org/10.1210/jc.2009-0159>) (July 1, 2009).
89. C. G. Nichols *et al.*, *Science* **272**, 1785–1787, (2021);  
<https://science.scienmag.org/content/272/5269/1785>) (June 21, 1996).

90. N. Vedovato, F. M. Ashcroft, M. C. Puljung, *Biophysical Journal* **109**, 2452–2460, (2021); <http://www.sciencedirect.com/science/article/pii/S0006349515011005> (Dec. 15, 2015).
91. Z. Fan, J. C. Makielski, *Journal of Biological Chemistry* **272**, 5388–5395, (2021); <https://www.sciencedirect.com/science/article/pii/S0021925818412185> (Feb. 28, 1997).
92. H. Hibino *et al.*, *Physiological Reviews* **90**, 291–366, (2021); <https://journals.physiology.org/doi/full/10.1152/physrev.00021.2009> (Jan. 1, 2010).
93. P. Proks *et al.*, *Philosophical Transactions of the Royal Society B: Biological Sciences* **371**, 20150426, (2021); <https://royalsocietypublishing.org/doi/full/10.1098/rstb.2015.0426> (Aug. 5, 2016).
94. D. D. Boehr, R. Nussinov, P. E. Wright, *Nature Chemical Biology* **5**, 789–796, (2021); <https://www.nature.com/articles/nchembio.232> (Nov. 2009).
95. A. Mittermaier, L. E. Kay, *Science* **312**, 224–228, (2021); <https://science.sciencemag.org/content/312/5771/224> (Apr. 14, 2006).
96. B. Ribalet, S. A. John, J. N. Weiss, *Journal of General Physiology* **116**, 391–410, (2021); <https://doi.org/10.1085/jgp.116.3.391> (Aug. 28, 2000).
97. J. Monod, J. Wyman, J.-P. Changeux, *Journal of Molecular Biology* **12**, 88–118, (2021); <https://www.sciencedirect.com/science/article/pii/S0022283665802856> (May 1, 1965).
98. M. M. Rubin, J.-P. Changeux, *Journal of Molecular Biology* **21**, 265–274, (2021); <https://www.sciencedirect.com/science/article/pii/0022283666900970> (Nov. 14, 1966).
99. H. G. Garcia, J. Kondev, N. Orme, J. A. Theriot, R. Phillips, in *Methods in Enzymology*, ed. by M. L. Johnson, J. M. Holt, G. K. Ackers (Academic Press, Jan. 1, 2011), vol. 492, pp. 27–59, (2021); <https://www.sciencedirect.com/science/article/pii/B9780123812681000148>.
100. S. Marzen, H. G. Garcia, R. Phillips, *Journal of Molecular Biology*, Allosteric Interactions and Biological Regulation (Part I) **425**, 1433–1460, (2021); <https://www.sciencedirect.com/science/article/pii/S0022283613001617> (May 13, 2013).
101. C. G. Nichols *et al.*, *Science* **272**, Publisher: American Association for the Advancement of Science Section: Reports, 1785–1787, (2021); <https://science.sciencemag.org/content/272/5269/1785> (June 21, 1996).
102. F. M. Gribble, S. J. Tucker, T. Haug, F. M. Ashcroft, *Proceedings of the National Academy of Sciences* **95**, 7185–7190, (2021); <https://www.pnas.org/content/95/12/7185> (June 9, 1998).
103. P. Proks, H. de Wet, F. M. Ashcroft, *Journal of General Physiology* **136**, 389–405, (2021); <https://doi.org/10.1085/jgp.201010475> (Sept. 27, 2010).

104. P. Proks, F. M. Gribble, R. Adhikari, S. J. Tucker, F. M. Ashcroft, *The Journal of Physiology* **514**, 19–25, (2021); <https://physoc.onlinelibrary.wiley.com/doi/abs/10.1111/j.1469-7793.1999.019af.x> (1999).
105. S. A. John, J. N. Weiss, L.-H. Xie, B. Ribalet, *The Journal of Physiology* **552**, 23–34, (2021; <https://physoc.onlinelibrary.wiley.com/doi/abs/10.1113/jphysiol.2003.048843>) (2003).
106. B. Ribalet, S. A. John, J. N. Weiss, *Biophysical Journal* **84**, 266–276, (2021; <http://www.sciencedirect.com/science/article/pii/S0006349503748474>) (Jan. 1, 2003).
107. S. Trapp, S. Haider, P. Jones, M. S. Sansom, F. M. Ashcroft, *The EMBO Journal* **22**, 2903–2912, (2021; <https://www.embopress.org/doi/full/10.1093/emboj/cdg282>) (June 16, 2003).
108. K. Shimomura *et al.*, *Diabetes* **55**, 1705–1712, (2021; <https://diabetes.diabetesjournals.org/content/55/6/1705>) (June 1, 2006).
109. J. C. Koster, M. S. Remedi, C. Dao, C. G. Nichols, *Diabetes* **54**, 2645–2654, (2021; <https://diabetes.diabetesjournals.org/content/54/9/2645>) (Sept. 1, 2005).
110. L. Li, J. Wang, P. Drain, *Biophys J* **79**, Type: Journal Article, 841–52, (<https://www.ncbi.nlm.nih.gov/pubmed/10920016>) (2000).
111. P. Tammaro, C. Girard, J. Molnes, P. R. Njolstad, F. M. Ashcroft, *EMBO J* **24**, Type: Journal Article, 2318–30, (<https://www.ncbi.nlm.nih.gov/pubmed/15962003>) (2005).
112. R. Masia *et al.*, *Diabetes* **56**, 328–336, (2021; <https://diabetes.diabetesjournals.org/content/56/2/328>) (Feb. 1, 2007).
113. J. F. Antcliff, S. Haider, P. Proks, M. S. Sansom, F. M. Ashcroft, *The EMBO Journal* **24**, 229–239, (2021; <https://www.embopress.org/doi/full/10.1038/sj.emboj.7600487>) (Jan. 26, 2005).
114. P. Tammaro, P. Proks, F. M. Ashcroft, *The Journal of Physiology* **571**, 3–14, (2021; <https://physoc.onlinelibrary.wiley.com/doi/abs/10.1113/jphysiol.2005.099168>) (2006).
115. S.-L. Shyng, C. A. Cukras, J. Harwood, C. G. Nichols, *Journal of General Physiology* **116**, 599–608, (2021; <https://doi.org/10.1085/jgp.116.5.599>) (Oct. 16, 2000).
116. F. M. Gribble, S. J. Tucker, F. M. Ashcroft, *EMBO J* **16**, Type: Journal Article, 1145–52, (<https://www.ncbi.nlm.nih.gov/pubmed/9135131>) (1997).
117. D. C. Rees, E. Johnson, O. Lewinson, *Nature Reviews Molecular Cell Biology* **10**, 218–227, (2021; <https://www.nature.com/articles/nrm2646>) (Mar. 2009).
118. L. Csanády, P. Vergani, D. C. Gadsby, *Proceedings of the National Academy of Sciences* **107**, 1241–1246, (2021; <https://www.pnas.org/content/107/3/1241>) (Jan. 19, 2010).
119. H. d. Wet *et al.*, *The FEBS Journal* **274**, 3532–3544, (2021; <https://febs.onlinelibrary.wiley.com/doi/abs/10.1111/j.1742-4658.2007.05879.x>) (2007).

120. L. V. Zingman *et al.*, *Neuron* **31**, 233–245, (2021);  
<https://www.sciencedirect.com/science/article/pii/S0896627301003567> (Aug. 2, 2001).
121. K.-H. Choi, M. Tantama, S. Licht, *The Journal of Physical Chemistry B* **112**, Publisher: American Chemical Society, 10314–10321, (2021);  
<https://doi.org/10.1021/jp712088v> (Aug. 1, 2008).
122. B. S. Rothberg, K. L. Magleby, *Biophysical Journal* **80**, 3025–3026, (2021);  
<https://www.ncbi.nlm.nih.gov/pmc/articles/PMC1301486/> (June 2001).
123. T. Rohács *et al.*, *Proceedings of the National Academy of Sciences* **100**, 745–750, (2021);  
<https://www.pnas.org/content/100/2/745> (Jan. 21, 2003).
124. D. Schulze, T. Krauter, H. Fritzenschaft, M. Soom, T. Baukrowitz, *Journal of Biological Chemistry* **278**, 10500–10505, (2021);  
<https://www.sciencedirect.com/science/article/pii/S0021925819325347> (Mar. 21, 2003).
125. Z. Fan, J. C. Makielski, *Journal of General Physiology* **114**, 251–270, (2021);  
<https://doi.org/10.1085/jgp.114.2.251> (Aug. 1, 1999).
126. D. Enkvetchakul, G. Loussouarn, E. Makhina, S. L. Shyng, C. G. Nichols, *Biophys J* **78**, Type: Journal Article, 2334–48,  
(<https://www.ncbi.nlm.nih.gov/pubmed/10777731>) (2000).
127. C. Wang, K. Wang, W. Wang, Y. Cui, Z. Fan, *FEBS Letters* **532**, 177–182, (2021);  
<https://www.sciencedirect.com/science/article/pii/S0014579302036712> (Dec. 4, 2002).
128. G. G. MacGregor *et al.*, *Proceedings of the National Academy of Sciences* **99**, 2726–2731, (2021; <https://www.pnas.org/content/99/5/2726>) (Mar. 5, 2002).
129. S. Haider, A. I. Tarasov, T. J. Craig, M. S. Sansom, F. M. Ashcroft, *The EMBO Journal* **26**, 3749–3759, (2021);  
<https://www.embopress.org/doi/full/10.1038/sj.emboj.7601809> (Aug. 22, 2007).
130. S. B. Hansen, X. Tao, R. MacKinnon, *Nature* **477**, 495–498, (2021);  
<https://www.nature.com/articles/nature10370> (Sept. 2011).
131. D. Enkvetchakul, C. Nichols, *Journal of General Physiology* **122**, 471–480, (2021);  
<https://doi.org/10.1085/jgp.200308878> (Oct. 27, 2003).
132. A. Cha, F. Bezanilla, *Neuron* **19**, 1127–1140, (2021);  
[https://www.cell.com/neuron/abstract/S0896-6273\(00\)80403-1](https://www.cell.com/neuron/abstract/S0896-6273(00)80403-1) (Nov. 1, 1997).
133. N. Marmé, J.-P. Knemeyer, M. Sauer, J. Wolfrum, *Bioconjugate Chemistry* **14**, 1133–1139, (2021; <https://doi.org/10.1021/bc0341324>) (Nov. 1, 2003).

134. J. R. Lakowicz, *Principles of fluorescence spectroscopy*, Type: Book (Springer, New York, 3rd, 2006), xxvi, 954 p.  
(Contributor%20biographical%20information%20http://www.loc.gov/catdir/enhancements/fy0824/2006920796-b.html%20Publisher%20description%20http://www.loc.gov/catdir/enhancements/fy0824/2006920796-d.html%20Table%20of%20contents%20only%20http://www.loc.gov/catdir/enhancements/fy0824/2006920796-t.html).
135. S. E. Mansoor, M. A. DeWitt, D. L. Farrens, *Biochemistry* **49**, 9722–9731, (2021; <https://www.ncbi.nlm.nih.gov/pmc/articles/PMC3938424/>) (Nov. 16, 2010).
136. S. E. Mansoor, H. S. Mchaourab, D. L. Farrens, *Biochemistry* **38**, 16383–16393, (2021; <https://doi.org/10.1021/bi991331v>) (Dec. 1, 1999).
137. M. F. Priest, E. E. Lee, F. Bezanilla, “The trajectory of discrete gating charges in a voltage-gated potassium channel”, preprint (Biophysics, Apr. 24, 2020), (2021; <http://biorxiv.org/lookup/doi/10.1101/2020.04.23.058818>).
138. L. M. Mannuzzu, M. M. Moronne, E. Y. Isacoff, *Science* **271**, 213–216, (2021; <https://science.sciencemag.org/content/271/5246/213>) (Jan. 12, 1996).
139. J. Cowgill, B. Chanda, *Journal of General Physiology* **151**, 1163–1172, (2021; <https://doi.org/10.1085/jgp.201912372>) (Aug. 20, 2019).
140. N. Braun, Z. P. Sheikh, S. A. Pless, *The Journal of Physiology* **598**, 4455–4471, (2021; <https://physoc.onlinelibrary.wiley.com/doi/abs/10.1113/JP276695>) (2020).
141. M. S. Siegel, E. Y. Isacoff, *Neuron* **19**, 735–741, (2021; [https://www.cell.com/neuron/abstract/S0896-6273\(00\)80955-1](https://www.cell.com/neuron/abstract/S0896-6273(00)80955-1)) (Oct. 1, 1997).
142. T. Giraldez, T. E. Hughes, F. J. Sigworth, *The Journal of General Physiology* **126**, 429–438, (2021; <https://www.ncbi.nlm.nih.gov/pmc/articles/PMC2266602/>) (Nov. 2005).
143. P. Miranda *et al.*, *Proceedings of the National Academy of Sciences* **110**, 5217–5222, (2021; <https://www.pnas.org/content/110/13/5217>) (Mar. 26, 2013).
144. S. A. Pless, C. A. Ahern, *Annual Review of Pharmacology and Toxicology* **53**, 211–229, (2021; <https://doi.org/10.1146/annurev-pharmtox-011112-140343>) (2013).
145. M. C. Puljung, in *Methods in Enzymology* (Academic Press, Mar. 16, 2021), (2021; <https://www.sciencedirect.com/science/article/pii/S0076687921000707>).
146. H. S. Lee, J. Guo, E. A. Lemke, R. D. Dimla, P. G. Schultz, *Journal of the American Chemical Society* **131**, 12921–12923, (2021; <https://doi.org/10.1021/ja904896s>) (Sept. 16, 2009).
147. A. Chatterjee, J. Guo, H. S. Lee, P. G. Schultz, *J Am Chem Soc* **135**, Type: Journal Article, 12540–3, (<https://www.ncbi.nlm.nih.gov/pubmed/23924161>) (2013).
148. T. Kalstrup, R. Blunck, *Proceedings of the National Academy of Sciences* **110**, 8272–8277, (2021; <https://www.pnas.org/content/110/20/8272>) (May 14, 2013).
149. J. Kusch *et al.*, *Neuron* **67**, 75–85 (July 15, 2010).

150. J. Kusch *et al.*, *Nature Chemical Biology* **8**, 162–169, (2021); <https://www.nature.com/articles/nchembio.747> (Feb. 2012).
151. S. Thon, E. Schulz, J. Kusch, K. Benndorf, *Biophysical Journal* **109**, 2268–2276, (2021); <https://www.sciencedirect.com/science/article/pii/S0006349515010085> (Dec. 1, 2015).
152. C. Biskup *et al.*, *Nature* **446**, Number: 7134 Publisher: Nature Publishing Group, 440–443, (2021; <https://www.nature.com/articles/nature05596>) (Mar. 2007).
153. N. Zerangue, B. Schwappach, Y. N. Jan, L. Y. Jan, *Neuron* **22**, Publisher: Elsevier, 537–548, (2021); [https://www.cell.com/neuron/abstract/S0896-6273\(00\)80708-4](https://www.cell.com/neuron/abstract/S0896-6273(00)80708-4) (Mar. 1, 1999).
154. P. R. Selvin, in *Methods in Enzymology* (Academic Press, Jan. 1, 1995), vol. 246, pp. 300–334, (2021); <https://www.sciencedirect.com/science/article/pii/0076687995460152>.
155. W. N. Zagotta, M. T. Gordon, E. N. Senning, M. A. Munari, S. E. Gordon, *J Gen Physiol* **147**, Type: Journal Article, 201–16, (<https://www.ncbi.nlm.nih.gov/pubmed/26755770>) (2016).
156. L. Stryer, *Annual Review of Biochemistry* **47**, 819–846, (2021); <https://doi.org/10.1146/annurev.bi.47.070178.004131> (1978).
157. R. McElreath, *Statistical Rethinking: A Bayesian Course with Examples in R and STAN* (ed. 2, 2020), (<http://gen.lib.rus.ec/book/index.php?md5=36E9C767D9FE968335E0A93B71087C48>).
158. A. Gelman, *Bayesian Data Analysis* (Chapman and Hall/CRC, ed. 3, 2014), (<http://gen.lib.rus.ec/book/index.php?md5=2e9d2df246cb144c7224d1e6db53466f>).
159. K. Tanabe *et al.*, *Journal of Biological Chemistry* **274**, 3931–3933, (2021); <https://www.sciencedirect.com/science/article/pii/S0021925819878626> (Feb. 12, 1999).
160. T. Hiratsuka, K. Uchida, *Biochimica et Biophysica Acta (BBA) - General Subjects* **320**, 635–647, (2021); <http://www.sciencedirect.com/science/article/pii/0304416573901438> (Oct. 5, 1973).
161. T. Hiratsuka, *Biochimica et Biophysica Acta (BBA) - General Subjects* **719**, 509–517, (2021); <https://www.sciencedirect.com/science/article/pii/0304416582902409> (Dec. 17, 1982).
162. C. G. Vanoye *et al.*, *J Biol Chem* **277**, Type: Journal Article, 23260–70, (<https://www.ncbi.nlm.nih.gov/pubmed/11956191>) (2002).
163. X.-L. Wang, T. Lu, S. Cao, V. H. Shah, H.-C. Lee, *Biochimica et Biophysica Acta (BBA) - Molecular and Cell Biology of Lipids* **1761**, 1041–1049, (2021); <https://www.sciencedirect.com/science/article/pii/S1388198106001855> (Sept. 1, 2006).
164. C. A. Cukras, I. Jeliazkova, C. G. Nichols, *Journal of General Physiology* **119**, 581–591, (2021; <https://doi.org/10.1085/jgp.20028562>) (May 28, 2002).

165. J. W. Chin, *Nature* **550**, 53–60, (2021);  
<https://www.nature.com/articles/nature24031> (Oct. 2017).
166. A. G. Cridge, C. Crowe-McAuliffe, S. F. Mathew, W. P. Tate, *Nucleic Acids Research* **46**, 1927–1944, (2021; <https://doi.org/10.1093/nar/gkx1315>) (Feb. 28, 2018).
167. R. S. Zhang *et al.*, *Journal of Biological Chemistry* **290**, 15450–15461, (2021);  
<https://www.sciencedirect.com/science/article/pii/S0021925820350468> (June 19, 2015).
168. P. K. Devaraneni, G. M. Martin, E. M. Olson, Q. Zhou, S.-L. Shyng, *Journal of Biological Chemistry* **290**, 7980–7991, (2021);  
<https://www.sciencedirect.com/science/article/pii/S0021925820649055> (Mar. 20, 2015).
169. W. H. Schmied, S. J. Elsasser, C. Uttamapinant, J. W. Chin, *J Am Chem Soc* **136**, Type: Journal Article, 15577–83, (<https://www.ncbi.nlm.nih.gov/pubmed/25350841>) (2014).
170. E. Deplazes, D. Jayatilaka, B. Corry, *Journal of Biomedical Optics* **17**, Publisher: International Society for Optics and Photonics, 011005, (2021);  
<https://www.spiedigitallibrary.org/journals/journal-of-biomedical-optics/volume-17/issue-1/011005/ExiFRET-flexible-tool-for-understanding-FRET-in-complex-geometries/10.1117/1.JBO.17.1.011005.short> (Feb. 2012).
171. W. N. Zagotta, M. T. Gordon, E. N. Senning, M. A. Munari, S. E. Gordon, *The Journal of General Physiology* **147**, 201–216, (2021);  
<https://www.ncbi.nlm.nih.gov/pmc/articles/PMC4727949/> (Feb. 2016).
172. J. Y. Ye, M. Yamauchi, O. Yogi, M. Ishikawa, *The Journal of Physical Chemistry B* **103**, 2812–2817, (2021; <https://doi.org/10.1021/jp984232k>) (Apr. 1, 1999).
173. M. Ishikawa, Y. Maruyama, J. Y. Ye, M. Futamata, *Journal of Luminescence, Proceedings of the Seventh International Meeting on Hole Burning, Single Molecules and Related Spectroscopies: Science and Applications* **98**, 81–89, (2021);  
<https://www.sciencedirect.com/science/article/pii/S0022231302002557> (July 1, 2002).
174. Garfinkel, Alan, *Modeling life : the mathematics of biological systems* (Springer, 2017), (<http://gen.lib.rus.ec/book/index.php?md5=5cbd03d9c1c2ab848083a7e1263b0fb>).
175. S. Trapp, P. Proks, S. J. Tucker, F. M. Ashcroft, *J Gen Physiol* **112**, Type: Journal Article, 333–49, (<https://www.ncbi.nlm.nih.gov/pubmed/9725893>) (1998).
176. E. Markworth, C. Schwanstecher, M. Schwanstecher, *Diabetes* **49**, Publisher: American Diabetes Association, 1413–1418, (2021);  
<https://diabetes.diabetesjournals.org/content/49/9/1413> (Sept. 1, 2000).
177. D. Enkvetchakul, G. Loussouarn, E. Makhina, C. G. Nichols, *Biophysical Journal* **80**, 719–728, (2021);  
<https://www.sciencedirect.com/science/article/pii/S0006349501760511> (Feb. 1, 2001).
178. P. Drain, X. Geng, L. Li, *Biophys J* **86**, Type: Journal Article, 2101–12,  
(<https://www.ncbi.nlm.nih.gov/pubmed/15041650>) (2004).

179. P. Proks *et al.*, *EMBO reports* **6**, 470–475, (2021); <https://www.embopress.org/doi/full/10.1038/sj.embor.7400393> (May 1, 2005).
180. L. Li *et al.*, *Journal of General Physiology* **126**, 285–299, (2021); <https://doi.org/10.1085/jgp.200509289> (Aug. 29, 2005).
181. B. Ribalet, S. A. John, L.-H. Xie, J. N. Weiss, *The Journal of Physiology* **571**, 303–317, (2021; <https://physoc.onlinelibrary.wiley.com/doi/abs/10.1113/jphysiol.2005.100719>) (2006).
182. T. J. Craig, F. M. Ashcroft, P. Proks, *The Journal of General Physiology* **132**, 131–144, (2021; <https://www.ncbi.nlm.nih.gov/pmc/articles/PMC2442177/>) (July 2008).
183. D. Enkvetchakul, C. G. Nichols, *J Gen Physiol* **122**, Type: Journal Article, 471–80, (<https://www.ncbi.nlm.nih.gov/pubmed/14581579>) (2003).
184. E. N. (Reinhold Penner (auth.) Bert Sakmann, *Single-Channel Recording* (Springer US, ed. 2, 1995), (<http://gen.lib.rus.ec/book/index.php?md5=19aa82d0f6c84ef003b3712dfa0ee98>).
185. L. Sivilotti, D. Colquhoun, *Journal of General Physiology* **148**, 79–88, (2021; <https://doi.org/10.1085/jgp.201611649>) (July 18, 2016).
186. D. Enkvetchakul, G. Loussouarn, E. Makhina, C. G. Nichols, *Biophysical Journal* **80**, 719–728, (2021; <http://www.sciencedirect.com/science/article/pii/S0006349501760511>) (Feb. 1, 2001).
187. R. Wang *et al.*, *Molecular Pharmacology* **71**, Publisher: American Society for Pharmacology and Experimental Therapeutics Section: Article, 1646–1656, (2021; <https://molpharm.aspetjournals.org/content/71/6/1646>) (June 1, 2007).
188. A. L. Hodgkin, A. F. Huxley, *The Journal of Physiology* **117**, 500–544, (2021; <https://physoc.onlinelibrary.wiley.com/doi/abs/10.1113/jphysiol.1952.sp004764>) (1952).
189. J. Monod, J. Wyman, J.-P. Changeux, *Journal of Molecular Biology* **12**, 88–118, (2021; <http://www.sciencedirect.com/science/article/pii/S0022283665802856>) (May 1, 1965).
190. K. Fang, L. Csandy, K. W. Chan, *The Journal of Physiology* **576**, 379–389, (2021; <https://physoc.onlinelibrary.wiley.com/doi/abs/10.1113/jphysiol.2006.112748>) (2006).
191. S. H. Heinemann, F. Conti, in *Methods in Enzymology* (Academic Press, Jan. 1, 1992), vol. 207, pp. 131–148, (2021; <https://www.sciencedirect.com/science/article/pii/007668799207009D>).
192. O. Alvarez, C. Gonzalez, R. Latorre, *Advances in Physiology Education* **26**, 327–341, (2021; <https://journals.physiology.org/doi/full/10.1152/advan.00006.2002>) (Dec. 1, 2002).
193. F. J. Sigworth, *The Journal of Physiology* **307**, 97–129, (2021; <https://physoc.onlinelibrary.wiley.com/doi/abs/10.1113/jphysiol.1980.sp013426>) (1980).

194. P. Tammaro, F. M. Ashcroft, *The Journal of Physiology* **584**, 743–753, (2021; <https://physoc.onlinelibrary.wiley.com/doi/abs/10.1113/jphysiol.2007.143149>) (2007).
195. E. B. Pratt, F.-F. Yan, J. W. Gay, C. A. Stanley, S.-L. Shyng, *Journal of Biological Chemistry* **284**, 7951–7959, (2021; <https://www.sciencedirect.com/science/article/pii/S0021925820325072>) (Mar. 20, 2009).
196. E. B. Pratt, Q. Zhou, J. W. Gay, S.-L. Shyng, *Journal of General Physiology* **140**, 175–187, (2021; <https://doi.org/10.1085/jgp.201210803>) (July 16, 2012).
197. M. Prakriya, R. S. Lewis, *Journal of General Physiology* **128**, 373–386, (2021; <https://doi.org/10.1085/jgp.200609588>) (Aug. 28, 2006).
198. P. S. Jackson, K. Strange, *Journal of General Physiology* **105**, 643–660, (2021; <https://doi.org/10.1085/jgp.105.5.643>) (May 1, 1995).
199. P. S. Jackson, K. Strange, *Kidney International* **49**, 1695–1699, (2021; <https://www.sciencedirect.com/science/article/pii/S0085253815595446>) (June 1, 1996).
200. Q. F. Gronau, H. Singmann, E.-J. Wagenmakers, *Journal of Statistical Software* **92**, Number: 1, 1–29, (2021; <https://www.jstatsoft.org/index.php/jss/article/view/v092i10>) (Feb. 27, 2020).
201. E.-J. Wagenmakers, *Psychonomic Bulletin & Review* **14**, 779–804, (2021; <https://doi.org/10.3758/BF03194105>) (Oct. 1, 2007).
202. A. Vehtari, A. Gelman, J. Gabry, *Statistics and Computing* **27**, 1413–1432, (2021; <https://doi.org/10.1007/s11222-016-9696-4>) (Sept. 1, 2017).
203. L. Aguilar-Bryan, J. Bryan, *Endocrine Reviews* **29**, 265–291, (2021; <https://doi.org/10.1210/er.2007-0029>) (May 1, 2008).
204. A. T. Hattersley, F. M. Ashcroft, *Diabetes* **54**, 2503–2513, (2021; <https://diabetes.diabetesjournals.org/content/54/9/2503>) (Sept. 1, 2005).
205. F. M. Ashcroft, M. C. Puljung, N. Vedovato, *Trends in Endocrinology & Metabolism* **28**, 377–387, (2021; [http://www.sciencedirect.com/science/article/pii/S104327601730019X](https://www.sciencedirect.com/science/article/pii/S104327601730019X)) (May 1, 2017).
206. S. E. Flanagan *et al.*, *Human Mutation* **30**, 170–180, (2021; <https://onlinelibrary.wiley.com/doi/abs/10.1002/humu.20838>) (2009).
207. F. M. Ashcroft, P. Rorsman, *Cell* **148**, 1160–1171, (2021; [https://www.cell.com/cell/abstract/S0092-8674\(12\)00208-5](https://www.cell.com/cell/abstract/S0092-8674(12)00208-5)) (Mar. 16, 2012).
208. T. Pipatpolkai, S. Usher, P. J. Stansfeld, F. M. Ashcroft, *Nature Reviews Endocrinology* **16**, 378–393, (2021; <https://www.nature.com/articles/s41574-020-0351-y>) (July 2020).
209. D. Colquhoun, *British Journal of Pharmacology* **125**, 923–947, (2021; <https://bpspubs.onlinelibrary.wiley.com/doi/abs/10.1038/sj.bjp.0702164>) (1998).

210. N. Li *et al.*, *Cell* **168**, 101–110.e10, (2021);  
<http://www.sciencedirect.com/science/article/pii/S0092867416317445> (Jan. 12, 2017).
211. A. L. Gloyn *et al.*, *Eur J Hum Genet* **14**, Type: Journal Article, 824–30, (<https://www.ncbi.nlm.nih.gov/pubmed/16670688>) (2006).
212. B. Ribalet, S. A. John, L. H. Xie, J. N. Weiss, *J Physiol* **571**, Type: Journal Article, 303–17, (<https://www.ncbi.nlm.nih.gov/pubmed/16373383>) (Pt 2 2006).
213. H.-Q. Yang *et al.*, *Proceedings of the National Academy of Sciences* **117**, 10593–10602, (2021; <https://www.pnas.org/content/117/19/10593>) (May 12, 2020).
214. S. Trapp, S. J. Tucker, F. M. Ashcroft, *Journal of General Physiology* **112**, 325–332, (2021; <https://doi.org/10.1085/jgp.112.3.325>) (Sept. 1, 1998).
215. S. A. John, J. R. Monck, J. N. Weiss, B. Ribalet, *J Physiol* **510** ( Pt 2), Type: Journal Article, 333–45, (<https://www.ncbi.nlm.nih.gov/pubmed/9705987>) (1998).
216. A. P. Babenko, J. Bryan, *Journal of Biological Chemistry* **278**, 41577–41580, (2021);  
<https://www.sciencedirect.com/science/article/pii/S0021925820826805> (Oct. 24, 2003).
217. F. M. Gribble, S. J. Tucker, S. Seino, F. M. Ashcroft, *Diabetes* **47**, 1412–1418, (2021);  
<https://diabetes.diabetesjournals.org/content/47/9/1412> (Sept. 1, 1998).
218. R. Ashfield, F. M. Gribble, S. J. Ashcroft, F. M. Ashcroft, *Diabetes* **48**, 1341–1347, (2021);  
<https://diabetes.diabetesjournals.org/content/48/6/1341> (June 1, 1999).
219. R. M. Clegg, in *Methods in Enzymology* (Academic Press, Jan. 1, 1992), vol. 211, pp. 353–388, (2021);  
<https://www.sciencedirect.com/science/article/pii/007668799211020J>.
220. D. Ding, M. Wang, J. X. Wu, Y. Kang, L. Chen, *Cell Rep* **27**, Type: Journal Article, 1848–1857 e4, (<https://www.ncbi.nlm.nih.gov/pubmed/31067468>) (2019).
221. R. Masia *et al.*, *Diabetes* **56**, 1357–1362, (2021);  
<https://diabetes.diabetesjournals.org/content/56/5/1357> (May 1, 2007).
222. E. B. Pratt, Q. Zhou, J. W. Gay, S. L. Shyng, *J Gen Physiol* **140**, Type: Journal Article, 175–87, (<https://www.ncbi.nlm.nih.gov/pubmed/22802363>) (2012).
223. D. A. Doyle *et al.*, *Science* **280**, 69–77, (2021);  
<https://science.sciencemag.org/content/280/5360/69> (Apr. 3, 1998).
224. B. Calderhead, M. Epstein, L. Sivilotti, M. Girolami, in *In Silico Systems Biology*, ed. by M. V. Schneider (Humana Press, Totowa, NJ, 2013), pp. 247–272, (2021);  
[https://doi.org/10.1007/978-1-62703-450-0\\_13](https://doi.org/10.1007/978-1-62703-450-0_13).
225. K. E. Hines, T. R. Middendorf, R. W. Aldrich, *Journal of General Physiology* **143**, 401–416, (2021; <https://doi.org/10.1085/jgp.201311116>) (Feb. 10, 2014).
226. K. E. Hines, *Biophysical Journal* **108**, 2103–2113, (2021);  
<https://www.sciencedirect.com/science/article/pii/S0006349515003033> (May 5, 2015).
227. T. R. Middendorf, R. W. Aldrich, *Journal of General Physiology* **149**, 105–119, (2021);  
<https://doi.org/10.1085/jgp.201611702> (Dec. 19, 2016).

228. P. Proks, H. de Wet, F. M. Ashcroft, *J Gen Physiol* **136**, Type: Journal Article, 389–405, (<https://www.ncbi.nlm.nih.gov/pubmed/20876358>) (2010).
229. A. Auerbach, *The Journal of Physiology* **590**, 93–98, (2021; <https://physoc.onlinelibrary.wiley.com/doi/abs/10.1113/jphysiol.2011.214684>) (2012).
230. F. T. Horrigan, R. W. Aldrich, *Journal of General Physiology* **120**, 267–305, (2021; <https://doi.org/10.1085/jgp.20028605>) (Aug. 26, 2002).
231. M. D. Varnum, W. N. Zagotta, *Biophysical Journal* **70**, 2667–2679, (2021; <https://www.sciencedirect.com/science/article/pii/S0006349596798363>) (June 1, 1996).
232. B. S. Khakh, R. Alan North, *Nature* **442**, 527–532, (2021; <https://www.nature.com/articles/nature04886>) (Aug. 2006).
233. S. E. Mansoor *et al.*, *Nature* **538**, 66–71, (2021; <https://www.nature.com/articles/nature19367>) (Oct. 2016).
234. M. Puljung, N. Vedovato, S. Usher, F. Ashcroft, *Elife* **8**, Type: Journal Article, (<https://www.ncbi.nlm.nih.gov/pubmed/30789344>) (2019).